(NASA-CR-137372) PREDICTION OF EXPLOSIVE YIELD AND OTHER CHARACTERISTICS OF LIQUID ROCKET PROPELLANT EXPLOSIONS Final Report (Florida Univ.) 424 p HC $24.25 CSCL 21I G3/33

N74-20589

Unclas 16088

ENGINEERING AND INDUSTRIAL EXPERIMENT STATION

College of Engineering

University of Florida

Gainesville

Final Report

June 30, 1973

Prediction of Explosive Yield and Other Characteristics of Liquid Rocket Propellant Explosions

Contract No. NAS 10-1255

Prepared for

National Aeronautics and Space Administration

John F. Kennedy Space Center

Systems Engineering Division

Design Engineering Directorate

Prepared by

Dr. E. A. Farber, Principal Investigator

Prof. J. H. Smith

Prof. E. H. Watts

University of Florida

Florida Engineering and Industrial Experiment Station

Department of Mechanical Engineering

Gainesville, Florida

Abstract

This report is intended to present the total picture of the work which has been done by Dr. Farber's group at the University of Florida in arriving at credible explosive yield values for liquid rocket propellants.

The results are based upon logical methods which have been well worked out theoretically and verified through experimental procedures.

Three independent methods to predict explosive yield values for liquid rocket propellants will be described. All three give the same end result even though they utilize different parameters and procedures. They are:

I. The Mathematical Model

II. The Seven Chart Approach

III. The Critical Mass Method

A brief description of the methods, how they were derived, how they were applied, and the results which they produced will be given in the text.

The experimental work used to support and verify the above methods both in the laboratory and in the field with actually explosive mixtures will be presented.

In the last two parts of this report the methods developed will be used and their value demonstrated in analyzing real problems, among them the Destruct System of the Saturn V, and the early configurations of the Space Shuttle.

The depth to which the material will be presented here depends upon whether and to what extent some of the material has been presented in previous publications.

There exist about two dozen reports and papers which were presented by Dr. Farber's group and publications in the Annals of the New York Academy of Sciences, various Space Congress Proceedings from both the East and the West Coast, Transactions of the International Cryogenic Engineering Society, Proceedings of the Department of Defense Explosives Safety Board Annual Meetings, The International Fire Institute Bi-Annual Reports, etc.

In addition, some of the material has been presented both formally and informally to NASA groups at NASA Headquarters in Washington, D.C., to NASA groups at Kennedy Space Center, to NASA groups at the Marshall Space Flight Center, to groups at the Air Force Rocket Propulsion Laboratory, at Edwards Air Force Base, to members of the Aerospace Corporationq to the Ballistics Research Laboratory at Aberdeen Proving Grounds, and others.

It is believed that this report presents the only rational approach in existence today to predict explosive yield values of liquid rocket propellants and other characteristics.

This work, carried out over a period of nine years, is presented consistent with the numerous papers and reports produced during this period. It is believed that this produced the clearest presentation even though it created some cosmetic, notation and numeration problems. Quality photocopies can be obtained from the master report residing with NASA.

Acknowledgements

It is with sincere appreciation that the authors thank the many faculty members in Engineering, Mathematics, Statistics, and Chemistry who have worked on this project; the many graduate students who have given assistance with the experimentation; and the many Engineering students who have helped with the computations, preparation of graphs, etc.

The help given by NASA personnel at the Kennedy Space Center and personnel of the Subcontractors made it possible to carry out the auto-ignition experiments at the Kennedy Space Center which verified the Electrostatic Charge Generation and Critical Mass Hypothesis.

Special thanks are due Mr. J.H. Deese who greatly contributed to the execution of this project through active participation in the auto-ignition experiments and through administrative action, and to Mr. W.H. Boggs who took over the duties of NASA's Technical Representative after Mr. Deese's retirement.

Table of Contents

Table of Contents (Continued)

Table of Contents (Continued)

Table of Contents (Continued)

Table of Contents (Continued)

Table of Figures

Table of Figures (Continued)

Table of Figures (Continued)

Table of Figures (Continued)

Table of Figures (Continued)

Table of Figures (Continued)

Table of Figures (Continued)

Table of Figures (Continued)

Table of Figures (Continued)

Table of Tables

DEFINITIONS AND SYMBOLS

O_2 - Oxygen

SO_2 - Solid Oxygen

GO_2 - Gaseous Oxygen

LO_2 - Liquid Oxygen

H_2 - Hydrogen

LH_2 - Liquid Hydrogen

N_2 - Nitrogen

LN_2 - Liquid Nitrogen

F - Fluorine

LF - Liquid Fluorine

LAN - Liquid Argon and Nitrogen

RP_1 - Petroleum Base Rocket Fuel

SRP_1 - Solid Petroleum Base Rocket Fuel

JP - Petroleum Base Jet Engine Fuel

KSC - Kennedy Space Center

MSFC - Marshall Space Flight Center

ln - Logarithm (Base e)

I.D. - Inside Diameter

O.D. - Outside Diameter

SIVB - Third Stage Saturn V Rocket

SII - Second Stage Saturn V Rocket

A - Area

a - Parameter (Function), constant

b - Parameter (Function)

C - Carbon, Capacitance

Definitions and Symbols (Continued)

c - Parameter (Function), constant

c_o - Velocity of sound

D - Diameter, screen separation

d - Parameter (constant), Differential Operator, Diameter

E - Expected Value, Mixing Energy

E_B - Boiling Energy

F - Froude Number, Force, Fluid Plug Motion

F_T - Turbulence Factor

F_B - Boiling Factor

F_F - Freezing Factor

f - Function, Vapor/Volume Fraction

g - Gravitation Constant

H - Height

h - Heat Transfer Film Coefficient

h_{fg} - Heat of Vaporization

i - ith Term

K - Dielectric Constant

K_i - Equilibrium Coefficient

l - Heel of Jump

M - Mass

m - Mass

$\dot{m}$ - Mass Flow Rate

N - Total Number of Moles of Products of Reaction, Number of Molecules

n - Number of Terms, Number of Screens

o - Toe of Jump

Definitions and Symbols (Continued)

P - Pressure, Parameter, Probability

P_i - Partial Pressure

p - Partial Pressure

Q - Volume Flow Rate, Electric Charge

r - Error, Radius

T - Temperature, Time

t - Time

u - Transformation Variable

V - Volume Voltage, Velocity

V_i - Partial Volume

$\bar{V}$ - Velocity Vector

v - Transformation Variable, Velocity

W - Weight

W_i - Partial Weight

x - Mixing Function

Y - Explosive Yield, Displacement

y - Yield Function, Puddle Depth, Displacement

∞ - Infinity

$>$ - Inequality

$<$ - Inequality

$\bar{\ }$ - Average Value ($\bar{Q}$)

$\sqrt{\ }$ - Group Factor

Γ - Gamma Function

γ - Specific Weight

ρ - Density

Definitions and Symbols (Continued)

Σ - Summation sign

τ - Time

Ψ - Buler's Digamma Function

ω - Frequency

Part I

Methods of Analysis for the Prediction of Explosive Yields from Liquid Rocket Propellant Explosions

With the large scale use of liquid propellants in the space programs of this country for the Saturn Rockets, Skylab, projected Space Stations, and the Space Shuttle it became imperative to have knowledge of the characteristics of these liquid rocket propellants.

The yield from liquid propellant explosions as a result of missile failures is of extreme importance in assessing the hazards to astronauts, launch-support personnel, launch-support facilities and surrounding communities. Since explosive tests of large liquid propellant rockets are not practical because of the costs and hazards involved, prediction methods must be used in estimating the expected explosive yields.

For this reason three independent methods have been developed by Dr. Farber and his group at the University of Florida, and all three give essentially the same predictions even though they use different and independent parameters to do this.

The methods are briefly described below with the detail left to other publications dealing specifically with each one of the methods. Only the results from these methods pertinent here will be mentioned. Many other results have been obtained describing the behavior of the liquid rocket propellants

A. The Mathematical Model

A mathematical model[1,4,24,42] was developed by Dr. Farber about

the year 1964, with very limited information available, to describe some of the characteristics of liquid rocket propellants. Because of the limited data and information at hand at that time, it was difficult to evaluate the validity of this model. But since the model was designed to be quite flexible, it was assumed that new information could easily be incorporated into the model.

Considerable information has become available since the development of the model, and it has only supported the original work. Data were obtained by the principal investigator and this group of the University of Florida by instrumenting two 25,000 lb LOX/RP explosive experiments[3], and one 200 lb. LOX/RP cold flow and explosive experiment[75,104] carried out at the Air Force Rocket Propulsion Laboratory at Edwards Air Force Base, California, which established the Yield Function - Spill Function relationship. The data reported by Project PYRO as soon as it became available was also used to check the results predicted by the model.

This information, including the inert mixing experiments carried out in our laboratories, increased the confidence in this model and established it as a very useful tool to describe the liquid rocket propellant behavior.

The basic idea for the model is that in the case of an explosion of liquid rocket propellants only the portions which are actually mixed (fuel and oxidizer) can take part in the explosion. Furthermore, since this must be the case, a definite functional relationship must exist between the mixing of the fuel and oxidizer, the Mixing Function, and the expected explosive yield, the Yield Function.

To make it easier for the reader, a brief description of the model will follow so the references will only be needed if greater detail and insight is needed.

Yield Function

The Yield Function, as used in this work, is defined as the fraction of the theoretical maximum yield which is actually obtained from:

$$y = \frac{Y}{Y \text{ Theor. Max.}} \tag{1}$$

This yield can be expressed as TNT equivalent yield on an energy, or other basis, but care must be exercised in predicting damage, since the pressure-time trace for liquid propellants is considerably different from that of TNT, expecially in the near field.

Mixing Function

The Mixing Function, as used in this report, is defined as the fraction of the total volume of propellants mixed at any time τ, multiplied by some modifying factors.

$$x = \frac{V_M}{V_P} F_T F_B F_F \tag{2}$$

x = Mixing Function

V_M = Propellant Volume Mixed

V_P = Total Propellant Volume

F_T = Turbulence Factor

F_B = Boiling Factor

F_F = Freezing Factor

Inert laboratory experiments utilizing such fluids as water and oil, hot wax and water, hot oil and water, LN_2 and water, LN_2 and kerosene, etc. established the factors F_T, F_B, and F_F.

It was shown that in the early stages of mixing these factors have a value near one, and thus the Mixing Function is essentially the normalized mixing volume. This latter fact was also established by the 25,000 LO_2/RP and the 200 lb. LO_2/RP explosive experiments.

Yield Function - Mixing Function Relationship

In the development of the mathematical model it was assumed that the relationship between y and x can be expressed as

$$y = \frac{b}{b + c} x^d \qquad (3)$$

where b, c, and d are constants. This expression containing three constants is very flexible.

Again the explosive experiments of 25,000 lb. LO_2/RP and the 200 lb. LO_2/RP cold flow and explosive experiments proved the above relationship valid.

The Mathematical Model

With the relationship between the Yield Function (y) and the Mixing

Function (x) established, the mathematical model can be formulated, resulting in a statistical function which is capable of incorporating the above y-x relationship, and is able to provide for the valid estimating procedures of the parameters involved.

The statistical function is a modified Dirichlet bivariate surface with four parameters a, b, c, and d. It is

$$f(x,y) = \frac{d\Gamma(a+b+c)}{\Gamma(a)\,\Gamma(b)\,\Gamma(c)}\; x^{d-1}\,(1-x^{d})^{a-1}y^{b-1}(x^{d}-y)^{c-1} \qquad (4)$$

where Γ is the Gamma Function. The only restrictions on this function are that:

$$y > 0, \quad x > 0, \quad y \leq x^{d}, \quad d \neq 0$$

To fully define the above function, it is necessary to evaluate the parameters a, b, c, and d on the basis of the particular y-x relationship describing the physical phenomena. This can be done by following statistical estimating procedure.

Defining

$$u_i = 1 - x_i^{d}$$
$$v_i = \frac{y_i}{x_i^{d}} \qquad (5)$$

four simultaneous equations can be written for the four parameters a, b, c, and d.

$$\overline{\ln v} = \Psi(b) - \Psi(b + c) \tag{6a}$$

$$\ln \bar{v} = \ln(b) - \ln(b + c) \tag{6b}$$

$$\overline{\ln u} = \Psi(a) - \Psi(a + b + c) \tag{6c}$$

$$\ln \bar{u} = \ln(a) - \ln(a + b + c) \tag{6d}$$

where a bar over an expression indicates the average value of all available values

ln indicates the natural logarithm (base e)

Ψ is Euler's Digamma Function

From the mathematical model, the modified Dirichlet bivariate surface, a wealth of information can be extracted. Some of these are:

A. Probability Distribution of the Yield, P_y

$$P_y(y) = \int_{y^d}^{1} f(x,y)\, dx \tag{7}$$

From this probability distribution, the average yield value can be found as well as the confidence limits, indicating that a certain percentage of all yield values lies below the selected yield value.

B. Probability Distribution for the Mixing Function, P_x

$$P_x(x) = \int_{0}^{x^d} f(x,y)\, dy \tag{8}$$

This distribution can by analyzed the same way as in part (A) above.

C. Confidence Regions for Yield and Mixing

The regions into which a certain percentage of all Yield and Mixing values fall can be obtained by finding the normalized fractional volumes under the probability surface. This requires double integration of the function representing the mathematical model, necessitating the use of a large-scale computer. The integrals for the total volume (and for the sub-volumes with the proper limits) are of the form

$$V_{x,y} = \int_0^1 \int_0^{x^d} f(x,y)\, dy\, dx \qquad (9)$$

Such a plot of y versus x for different volumes gives regions resembling contour lines on a map.

Explosive Yield Estimation

To use the mathematical model for the estimation and the prediction of expected yield values it is necessary to evaluate the parameters a, b, c, and d.

This was done and it was found that by taking the best available information the parameters take on the following values:

$b = 4.0$

$c = 1.1$

$d = 1.5$

a = a free parameter. It can be made a function of the propellant quantity, thus becoming a scaling parameter.

The function for a is a distorted S curve as seen in the references[1,4,24,42,104], which also show how this function is obtained from the best available information.

The only experiments, except the ones in the laboratory, which were fully instrumented to obtain the Yield-Spill Relationship were the two 25,000 lb. LO_2/RP explosion tests and the 200 lb. LO_2/RP cold flow and explosion experiment. The Yield-Mixing relationship which was verified in these experiments was assumed to hold true in the remainder of the experiments and failures.

The effect of parameter a on the yield is rather small in the range of today's liquid propellant rockets, and thus the predictions can be considered very good since large variations in the parameter produce only small changes in the predicted explosive yields.

Figure 1 presents the results from the mathematical model. The main curve presents the average explosive yield values as a function of the propellant weight involved. Also shown is the 95 percent confidence limit. For the Saturn V, the prediction is that in the case of a catastrophic failure the average yield would be 3.5 percent and that in 95 times out of 100 such cases it would be less than 9 percent.

The mathematical model, as used here, included all types of propellants as well as all modes of failures.

It is clear that the mode of failure, as well as the propellant type, has a distinct influence upon the actual yield obtained[2,3,15]. If only a particular type of failure or a particular combination of propellants is to be investigated, then only that information should be used for

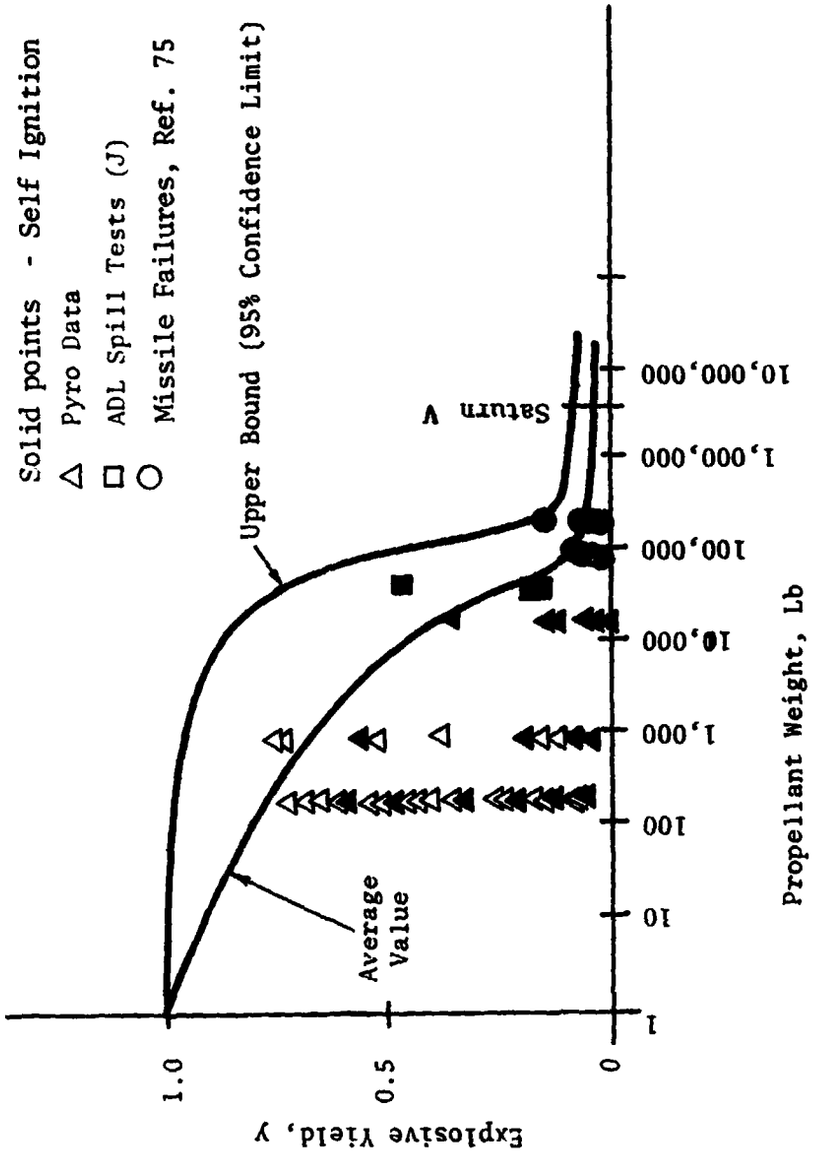

Figure 1 Estimated Explosive Yield as a Function of Propellant Weight

analysis in the mathematical model, and the values of the parameters a, b, c, and d will change. The average explosive yield value should be more accurately determined in such cases and the confidence limits will be found, in general, closer to the average values.

Thus for large-scale liquid propellant rockets it may be desirable to control the mode of failure with a properly designed destruct system to give a minimum explosive yield. With such a procedure, the explosive yield value can be lowered and the explosion yield prediction accuracy increased.

B. The Seven Chart Approach

An approach predicting the most probable yield, the most probable mixing, probability distributions, confidence regions, confidence limits, and so forth, by means of a mathematical model was presented in section A.

The method described there accomplished the ultimate goal of leading to a valid prediction procedure of yield, mixing, etc., of liquid propellant explosions; it did not provide an insight into the physical phenomenon occuring.

The approach in this section suggests a more fundamental method to this problem by considering the physical phenomena in detail. This approach, can, through understanding of the physical processes and phenomena, provide the information necessary to control these processes.

The method presented here and earlier[15,47,75] is referred to by the authors as the "Seven Chart Approach" since the procedure can be summarized in seven charts, constituting a complete, well-planned program,

outlining the necessary steps to be followed.

Furthermore, the "Seven Chart Approach" uses presently available information regarding these poorly understood phenomena producing the liquid propellant explosion yield. It points out where more theoretical and experimental work is needed, and what information it should provide. In this manner the ideal balance is obtained between theory guiding the experimental work and the results from the experiments modifying the theory. For these reasons this procedure is able to reach the desired goals along a more direct route in the shortest possible time and at minimum cost.

Previous theoretical and experimental investigations suggest that the actual phenomena producing the yield in liquid propellant explosions can be divided into groups which lend themselves to separate study. These may be both theoretical and small-scale experimental investigations.

In this method the problem is divided into three groups of phenomena which can be studied separately but when combined allow the desired prediction. The three groups are:

I. The Yield Potential Function

II. The Mixing Function

III. Delay and Detonation Times

These allow the incorporation of the basic characteristics of the particular propellants involved, of the missile design configuration, and of the mode of failure.

The Yield Potential Function (I) is basically controlled by

chemical kinetics, the Mixing Function (II) by the principles of hydrodynamics modified by heat transfer, and the Delay and Detonation Times (III) by characteristic functions for some propellants such as hypergolics or by random processes for others.

The separate studies can be combined by taking the Yield Potential, when expressed as a time function, and multiplying it by the Mixing Function to obtain the expected yield at any time after the start of the failure or after the mixing has begun. This Mixing Function will be different for different modes of failure and missile configurations[15,75].

The actual expected yield can be determined by superimposing the Delay and Detonation Times upon the above obtained expected Yield Function, either as a fixed value where applicable or as a statistically most probable value with proper confidence limits. These Delay and Detonation Times are characteristics of the propellants such as hypergolics or cryogenics, modified by the propellant quantities, missile configurations, modes of failures, and so forth.

The total procedure can be summarized, with the seven charts[15,47,75,104] supplying the necessary information, as the relationship

$$y = (y_p - x)_{\tau^*} \tag{10}$$

where y expected yield

y_p Yield Potential at time τ^*

x Mixing Function at time τ^*

τ^* Most probable detonation time

For the development of the seven chart method, conditions were assumed so that quantitative results could be calculated for cases which were investigated experimentally and for which results are reported in the literature. This gives more meaning to the procedure suggested and allows comparison of results obtained by the "Seven Chart Approach" with actual test results. The approach would be the same if other initial conditions, propellants or configurations were used.

The Yield Potential Function

The Yield Potential Function for any combination of propellants as a function of time can be obtained from theoretical considerations in four steps as follows:

Maximum Theoretical Energy Release (Chart 1)

The maximum amount of energy which can be released from any particular liquid propellant fuel-oxidizer mixture can be calculated employing the basic laws of chemical kinetics.

Figures 2A and 2B (in greater detail) show the results from such calculations for a three-component propellant mixture of $LO_2/LH_2/RP\text{-}1$.

The upper curve in these figures is the result of this three - component mixture with the ratio of LH_2 to RP-1 held constant. In arriving at the numerical values, it was assumed that all LH_2 always reacts, and as much of the RP-1 as can be supplied with LO_2. Atmospheric oxygen could also be included if desired without any particular difficulty.

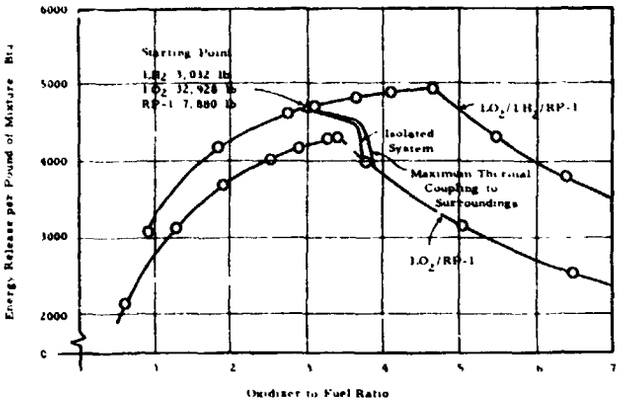

Maximum Amount of Energy Release for a Three Component Liquid Propellant Mixture

Figure 2A
(Chart I)

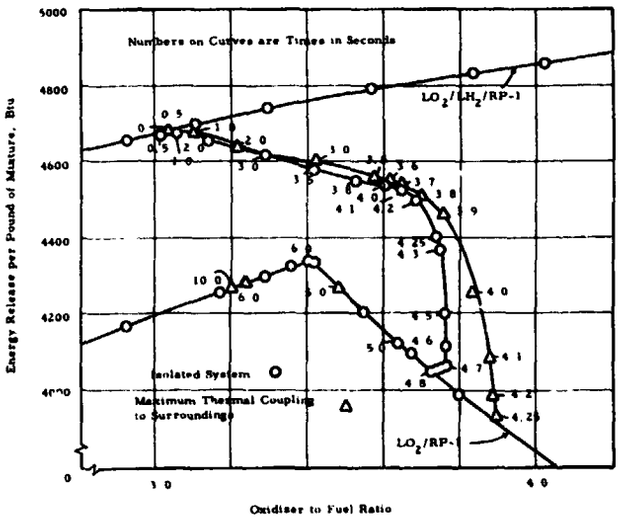

Maximum Amount of Energy Release for a Three Component Liquid Propellant Mixture

Figure 2B
(Chart I Detail)

The lower curve is the result of a two component mixture LO_2/RP-1 again here without atmospheric oxygen contribution. This curve is applicable to a two component mixture or could be considered the condition after all the LH_2 of the three-component mixture has evaporated.

Thus any three-component LO_2/LH_2/RP-1 mixture will have its starting point on the upper curve and will, due to evaporation of both LH_2 and the LO_2, follow a path from the upper to the lower curve toward the origin; this is if the reaction does not occur somewhere along this path terminating this process. The actual path depends upon the changes in the relative quantities of each component present. Two such paths are shown in Figure 2A and in more detail in Figure 2B

How they are calculated will be explained later, but it might be mentioned at this time that they are for a mixture which was actually used in field experiments[6,13,22,75,103,119].

One path assumes that the system is thermally isolated from the surroundings and the other path assumes that maximum thermal interaction between the system and the surroundings occurs.

The two paths are not as different as might be expected, indicating that the effect of the surroundings is minor.

Yield Potential as a Function of Oxidizer to Fuel Ratio (Chart 2)

The explosive yield of the liquid propellants will depend not only on the quantity of energy released, but also upon the rate at which this energy is released. Because of lack of information as to the variation in the reaction rates as a function of the propellant

composition, it was assumed for these calculations that the reaction rate remains essentially constant throughout the LO_2/fuel ratios under consideration here.

With this assumption which can, however, be replaced by reaction rate information as soon as it becomes available, and the information of Figure 2, the yield potential can be calculated and normalized in terms of the theoretical maximum. The results are presented in Figure 3.

Mass-Fraction Time Relationship for LH_2 and LO_2 (Chart 3)

To be able to determine the actual paths as previously discussed and shown in Figures 2A, 2B, and 3, it is necessary to know the time variation of the LH_2/LO_2 ratio. This is easiest to obtain from calculations of the quantities of LH_2 and LO_2 present at any time.

The calculations are more or less standard, involving the principles of thermodynamics and heat transfer, but are very long and tedious. They involve simultaneous heat balance and heat transfer relationships with the proper heat transfer coefficients which allow, through step-by-step iterated calculations, the estimation of the quantities of cryogenics vaporized, escaping, or again condensed in the mixture, the quantities of fuel and oxidizer frozen and portions remelted, and so forth. Some simplifying assumptions were made, wherever it appeared advantageous, in reducing the large amount of computations without appreciably affecting the results. Where quantities were encountered which had the same order of magnitude, but opposite sign and were relatively small, they were sometimes cancelled against each other.

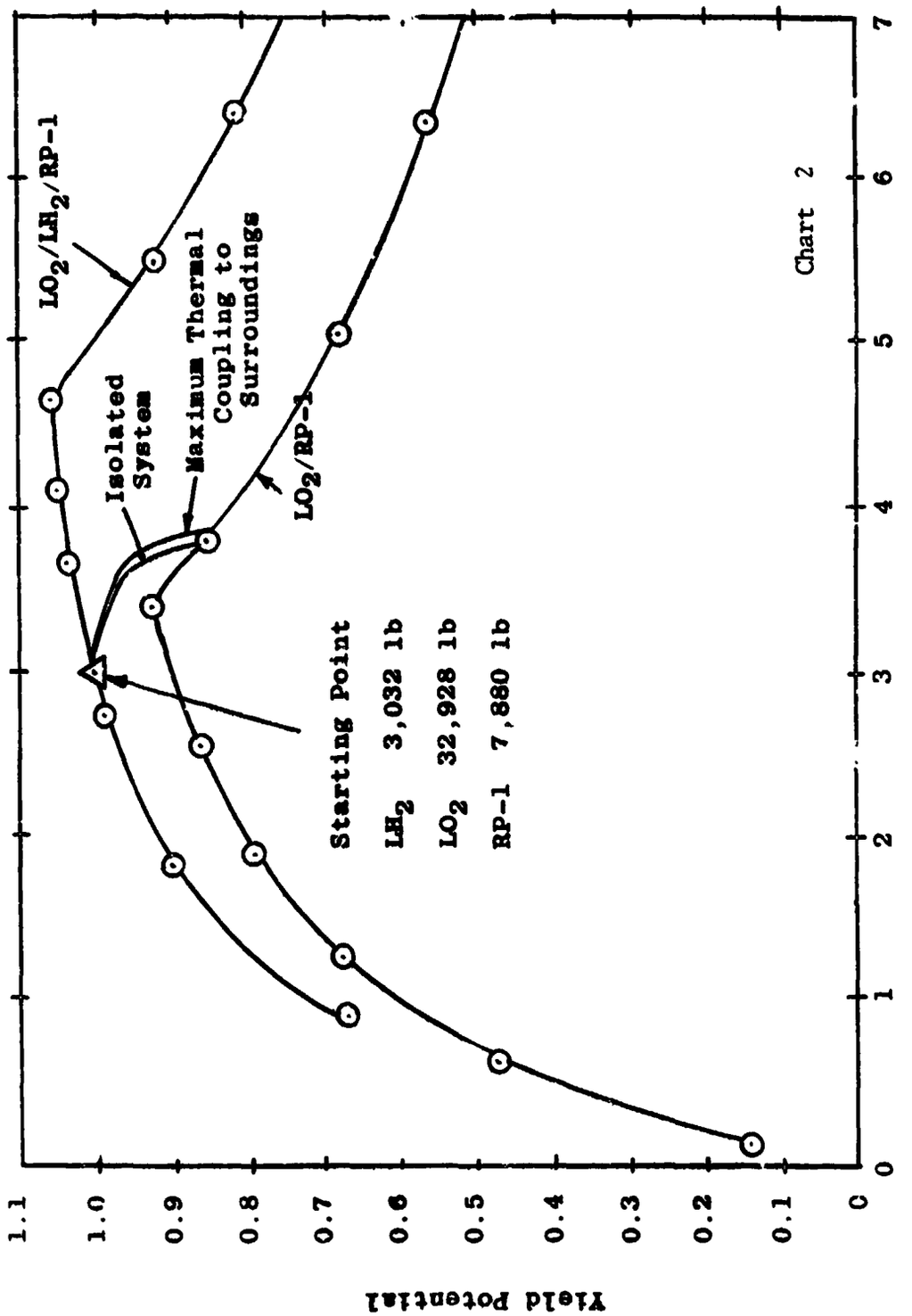

Figure 3 Yield Potential for a Three Component Liquid Propellant Mixture

These actions helped tremendously in reducing the scope of the necessary computations.

Contact area variations based upon mixing studies both at the University of Florida in connection with the study of explosive hazards of liquid propellants, and information found in the literature were used in the heat transfer equations together with the best available heat transfer coefficients to obtain the mass-fraction for LH_2 and LO_2.

The information needed and used, aside from that supplied by supporting studies at the University of Florida, are referred to in Table I; but only the results from the actual calculations can be presented in Figures 4A and 4B.

Yield Potential - Time Relationship (Chart 4)

In the method for the calculation of the yield potential - oxidizer to fuel ratio relationship, time τ was the common variable used; therefore it is possible to put a time scale on the paths as shown in Figure 2B.

With these time scales on the paths of Figure 2B, these curves can be re-plotted, giving the yield potential versus time relationship as seen in Figure 5.

These curves represent the theoretical maximum yield which could be obtained at any time τ from the above propellants due to the quantities of the constituents which are present at that time. One curve again represents the yield potential for the isolated system the other, maximum theoretical thermal coupling with its surroundings.

Table I

List of Literature References Used in Support of the Calculations for the Results Presented in Figures II-1A through II-3B

SUBJECT	REFERENCES
Average Chemical Formulas for Kerosene, RP-1	37, 43, 44, 46
Average Heat of Combustion for Kerosene	37, 38, 45
Heat of Combustion for Hydrogen	38
Propellant Proportion used in Heat Transfer Calculations	6
LAN/RP-1 Contact Area versus Time Data for LO_2/RP-1 Analogy	22
Film Coefficients for LAN/RP-1 Interface	22
Film Coefficients for LN_2/LH_2 Interface and LN_2/LH_2 Contact Area versus Time Data for LO_2/LH_2 Analogy	22
Latent Heat of Evaporation for H_2 and Specific Heat for GO_2	39
Specific Heat for L JP-1 to simulate RP-1	28
Latent Heat of Evaporation for O_2	39, 28
Latent Heat of Fusion for O_2	39
Approximation of Latent Heat of Fusion for RP-1	46
Approximation of Specific Heat of Solid Kerosene	40, 41, 42

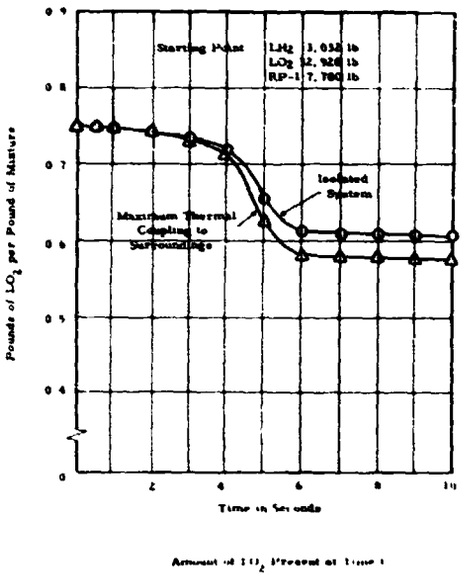

Figure 4A

(Chart 3)

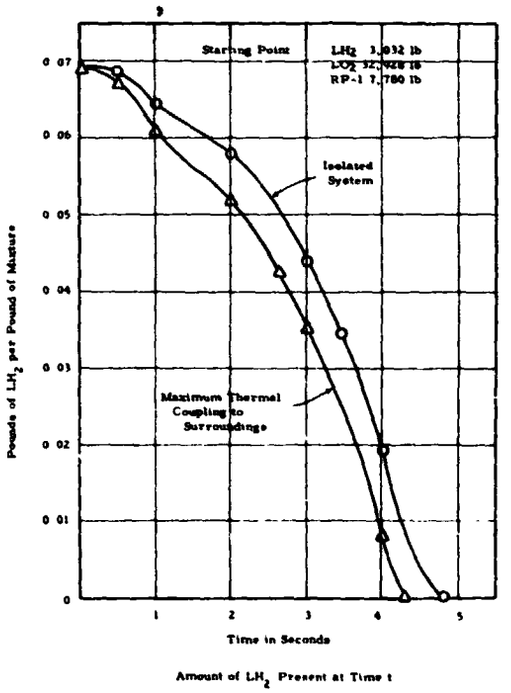

Figure 4B

(Chart 3)

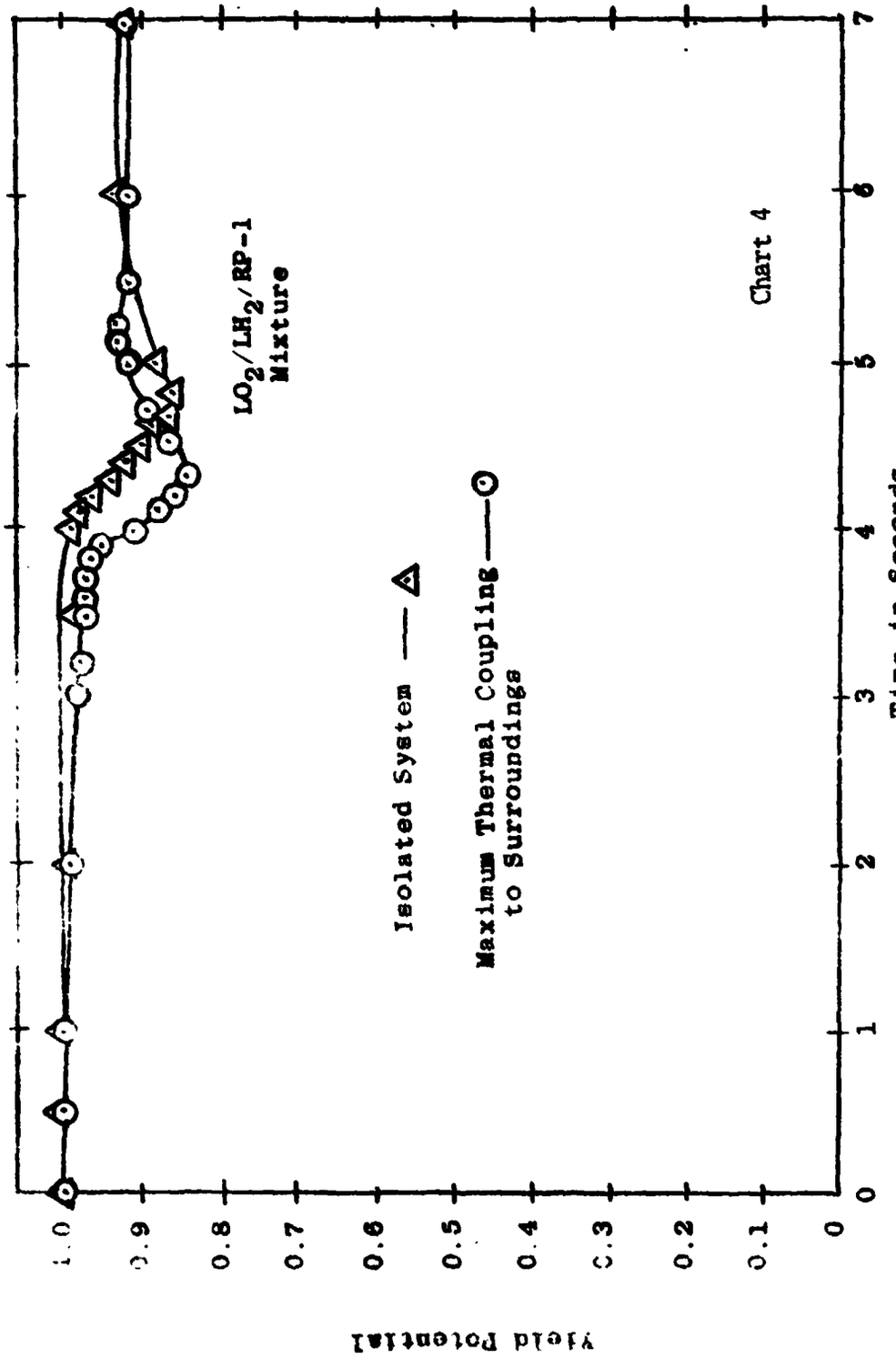

Figure 5 Yield Potential as Time Function

Since the curves of Figure 5 give the yield for propellants when perfectly mixed to produce maximum yield, these results must be modified by the Mixing Function (The ratio of the mixed amounts to the total amount present at any time τ).

The Mixing Function (Chart 5)

While the yield potential function as calculated above for a specific case established the actual quantities of the various constituents present and the maximum theoretical yield, if all these constituents are mixed most effectively, it does not give any information as to the degree of mixing of the constituents.

For example, at time $\tau = 0$ when the constituents just begin to mix, none of them are actually mixed and therefore an explosion could not be produced. Thus the Mixing Function is zero while the yield potential function is near its maximum. The product of the yield potential and the Mixing Function at this time gives the true or expected yield.

The Mixing Function is essentially a hydrodynamic function, however, complicated by high rates of heat transfer. This makes the analytical approach difficult, and at least to start with, an experimental approach for determining this function is more promising. This is true especially since questionable assumptions are not involved.

Four methods have been developed in connection with the over-all systematic approach presented in this section. These four methods allow the detailed study of the mixing process and phenomena producing the Mixing Function of liquid propellants and have been used with

great success. In preliminary studies often applying two methods to the same experiment, these methods have independently produced results which are in excellent agreement.

The detailed description of these methods and the various methods of analysis and the results obtained by them are presented elsewhere[15,75]. Since they implement the approach suggested in this part of the report, they are briefly mentioned here and will be discussed in greater detail later. They are:

1. Film Analysis[15]: A high speed photographic technique, giving by use of mirrors a three-dimensional picture of the mixing process on the same film frame. Special analysis of these frames as to mixing profile, mixing volume, and turbulence factor allow the determination of contact area and degree of mixing.

2. Wax Cast Analysis[15]: By use of hot wax and cold liquids, the mixing process can be "frozen" at different stages of the mixing by varying the hot and cold temperatures. The "frozen" state of the mixing process can then be studied at leisure at any time later. These casts can be analyzed for outside area by projection or coating methods; they can be serially sectioned to give the total contact area, turbulence factors (total contact area over profile area), and so on.

3. Vibration Mixing Analysis[15]: This method consists of mounting a particular configuration on a vibrating table, simulating the various propellant components by particles of different color, size, density, shape, etc., and after removing partitions, partially or completely shaking the system. The components will mix and the degree of mixing can be periodically checked at desired locations. Evaporation and other losses can be simulated by removing programmed quantities or numbers of particles at desired locations and prescribed intervals.

4. Thermocouple Grid Analysis[15]: This method of analysis employs a three-dimensional grid of fine thermocouples with each junction being monitored continuously. The traces give information regarding the mixing front, the degree of mixing at a particular point, the degree of turbulence at a point, the point or points of ignition, the time delay from the start of mixing (or time of failure) to ignition, the propagation of the reaction front, the propagation of the shock front, the separation of the shock front from the reaction front, and so forth.

Results from the above methods can be correlated and compared easily by simultaneously applying the different methods of analysis to the same experiment. These experiments provide information needed for the better understanding of the mixing phenomena of liquid propellants. They provide data as to the statistical reproducibility in seemingly identical experiments, the variation due to test configurations, and so on.

The Thermocouple Grid Analysis method is the most powerful since it directly relates the mixing phenomena and the yield obtained all in one and the same experiment. It is, however, considerably more expensive than the others. Instrumentation for high-speed monitoring of the individual junctions is expensive and the reduction of the data obtained time-consuming.

However, this Thermocouple Grid method is capable of taking measurements in liquid propellant mixtures from the start of failure up to and after ignition. If the grid is extended beyond the original boundaries of the propellant configuration, information can be obtained as to fireball growth rate, extent, temperature, shock wave strength, shock wave velocity, and so on.

Further and more detailed discussion of these four methods of

analysis which can provide the Mixing Function-time relationship is left to a later section when they are used for rather detailed studies of the Saturn V Destruct System, early configurations of the Space Shuttle, etc.

Only one of the results is presented here to show the complete procedure of the Seven Chart Approach corresponding to the spill experiments used as examples for comparison with the calculated numerical results. It is the mixing function presented in Figure 6, in this particular case obtained by method 3, the vibration mixing analysis. Since this method has no absolute time scale, a number of runs were made adjusting the amplitude and frequency so that easily measurable changes were observed in reasonable time intervals (about five seconds). Since from theoretical considerations the maximum should occur at about seven seconds, this time was ascribed to the maximum point of the mixing curve. In this manner the absolute time scale was established.

The reproducibility of this curve was still within plus or minus 4 percent. The reproducibility became better as the mixing violence or quantity of mix increased. This fact was observed in all experiments whether simulated on the vibration table or with real liquids using the other methods.

Delay and Detonation Times

Probably the least understood phenomena of the ones discussed in this section are those controlling the delay and detonation times.

Both these quantities will be discussed in considerable detail in the next section where they are evaluated, and detonation times calculated, based upon the new hypotheses proposed and referred to as

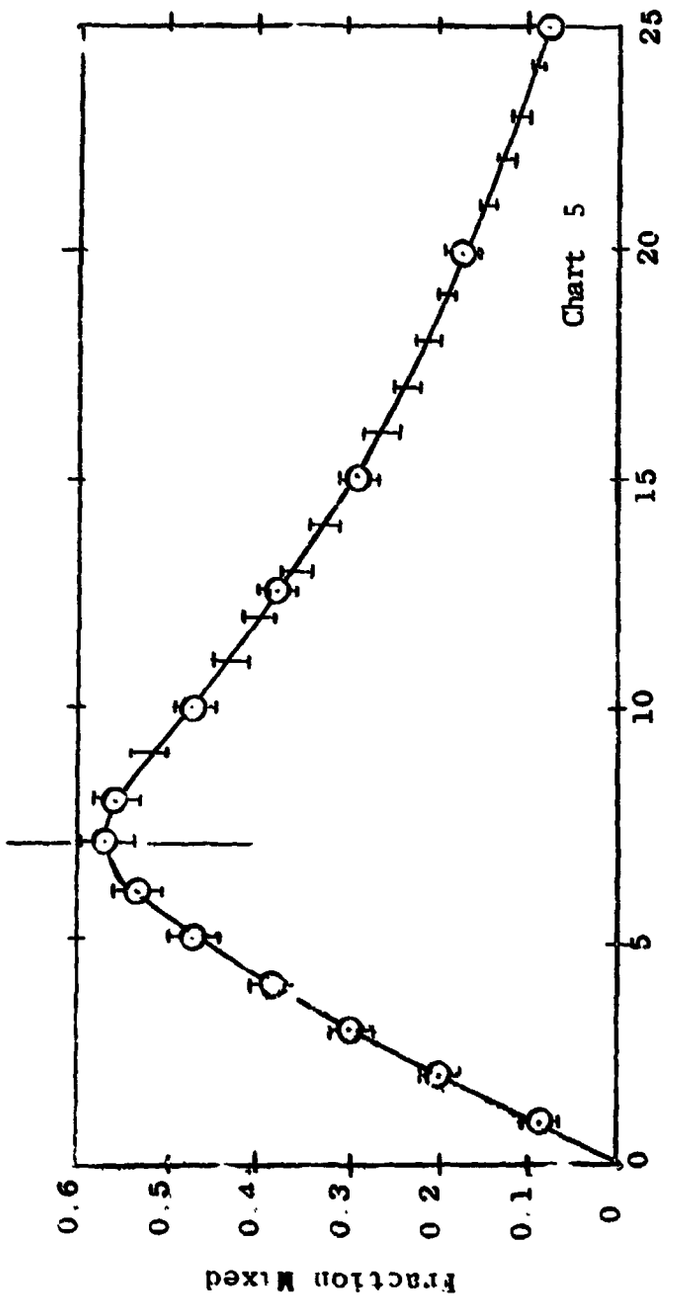

Figure 6 — Mixing Function or Spill Function for Three Component Liquid Propellant Spill Tests

"Fireball Hypothesis" and "Critical Mass Hypothesis".

The delay time is defined as the time from the start of failure to ignition, or the time from the start of mixing to ignition, whichever is preferable.

The detonation time is the time from ignition until the reaction reaches the boundary of the original propellant configuration.

For the purpose of this presentation, actually measured delay times from the experiment are taken and statistically analyzed so as to establish the most probable yield value as well as the 95 percent confidence limits. More data is needed to establish these quantities with greater accuracy.

For the test used for comparison here, the average delay plus detonation time was 3.3 seconds and the standard deviation for fixing confidence limits, 1.1 seconds.

Expected Yield Function - Time Relationship (Chart 6)

Having discussed the three groups of phenomena playing a role in producing the yield of liquid propellant explosions, the results obtained above can now be combined.

Taking the Yield Potential Function calculated and presented in Figure 5 and then the Mixing Function presented in Figure 6, and combining them by multiplying corresponding time ordinates, the expected Yield Function is obtained. This result is presented in Figure 7 which shows the yield which could be expected at any time τ if detonation did occur at that time. Only the curve for the isolated system is presented here but the other is obtained easily in the same manner.

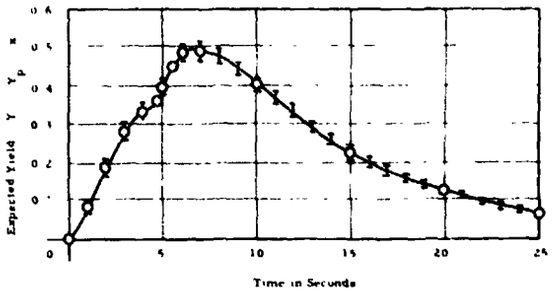

Expected Yield as a Time Function

Figure 7
(Chart 6)

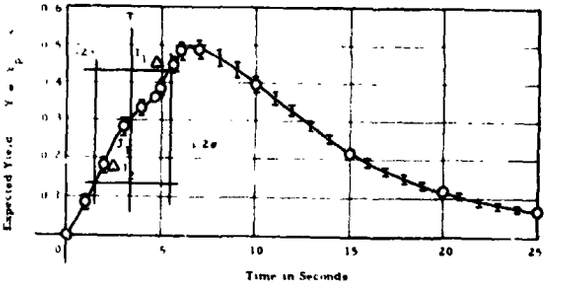

Expected Yield for Random Ignition and Detonation Showing the Upper and Lower Limits of the Statistical Confidence Regions for Liquid Propellant Spill Tests

Figure 8

(Chart 7)

ADL J Test Results plotted

This expected Yield Function has a plus or minus 4 percent variation in yield value due to this variation in the Mixing Function.

The expected Yield Function has a characteristic shape starting at zero, increasing with a dip or double hump to a maximum value and then decreasing again. The dip or double hump is due to the initial proportions of the propellant components.

The maximum is considerably below 100 percent since, with any appreciable quantity of liquid propellants, perfect mixing is almost impossible to achieve and furthermore, due to the time elapsed between the start of mixing, and best mixing, the yield potential falls below one, because of evaporation losses of the propellant components.

Expected Yield (Chart 7)

The last step in this series, to obtain the expected yield for liquid propellant explosions, is to superimpose the information developed above to obtain the combined results.

Figure 8 shows the results, the final step in this systematic approach, with the expected Yield Function of Figure 7 modified by the delay and detonation times fixing an interval within which, statistically, 95 percent of all expected yield values must lie.

The highest value for the expected yield fraction predicted for this test series, using 95 percent confidence limits, should be about 0.43, the lowest 0.13. All values predicted by this approach should fall between 0 and 0.50.

Another theoretical method for predicting the ignition time is presented in the next section and agreement between the theoretical and experimental results is excellent.

The seven steps of this procedure divide the complicated problem into three very distinct parts, which when combined give the following desired results:

1. Maximum Theoretical Energy Release
2. Yield Potential as a Function of Oxidizer to Fuel Ratio
3. Mass-Fraction - Time Relationships
4. Yield Potential - Time Relationships
5. The Mixing Function
6. Expected Yield Function - Time Relationship
7. Expected Yield

The three distinct parts are the determination of the yield potential, the mixing process analysis, and the ignition and detonation phenomena.

The procedure to determine the expected yield for a particular problem is the most detailed of the ones presented here. It gives specific answers but considerable effort is required for this analysis. It will be used extensively in the last two sections of this report for the Saturn V Destruct System Analysis and the analysis of some of the earlier Space Shuttle Configurations.

C. Critical Mass Method

Introduction

When large quantities of liquid fuels and oxidizers are brought together during experiments, or accidentally, the results are liquid propellant explosions.

Many different phenomena can trigger the explosion, such as flames, sparks produced by striking or breaking metal structures, hot materials or hot spots produced by slow chemical reactions of fuel and oxidizer, the breaking of crystals which are formed when one of the liquid components freezes the other and which are broken mechanically or by thermal stresses, or by static electricity which is a result of internal friction and which may produce a spark discharge.

Many more possibilities could be cited but these additional sources do not change the basic picture.

From the above it can be seen that as soon as there is contact or mixing of the fuel and oxidizer, ignition is possible if an ignition source is available. If not, the mixing process may proceed with more and more of the fuel and oxidizer mixing until an ignition source appears, either through external or internal action.

This section discusses the inherent production of an ignition source due to the mixing of oxidizer and fuel, specifically for cryogenic rocket propellants.

It has been well documented[85] over many years that when fluid layers move across each other that electric double layers are produced resulting in electrostatic charges and in very high voltage differences, if the liquids are good dilectrics so that the charges cannot leak off rapidly.

If a gas bubble or other medium of lower dielectric constant is interposed between the highly charged liquid layers, electric breakdown can occur (a spark jumps) which may well act as the source of ignition.

Since this electrostatic build-up is always present within the mixing regions of fuel and oxidizer of dielectric liquid rocket propellants, electric discharge is inevitable when the voltage difference has reached the necessary value for the breakdown to occur across one of the bubbles produced by the boiling of the constituent with the higher boiling point.

This study is rather general but was applied here to mixtures of LO_2/RP-1 and LO_2/LH_2, propellant combinations of main interest at this time.

It will be shown that voltage build-up increases with the quantities or masses or propellants involved and when the ignition probability reaches a value of one (or becomes a certainty) the quantities which have actually been mixed will be referred to as CRITICAL MASS.

Fluid Plug Model

Much work was done with bulkhead type failures since they are likely ones and one of the more gentle methods of bringing the components together. This type was selected in connection with this work since large amounts of experimental data are available involving cryogenics for either fuel, oxidizer, or both. The bulkhead failure mode was then used to formulate the Fluid Plug Model.

When one component of a fuel-oxidizer combination falls into the second, this can be likened to a plug of fluid falling into the other, Figure 9.

When the fluid plug of one component enters the other component

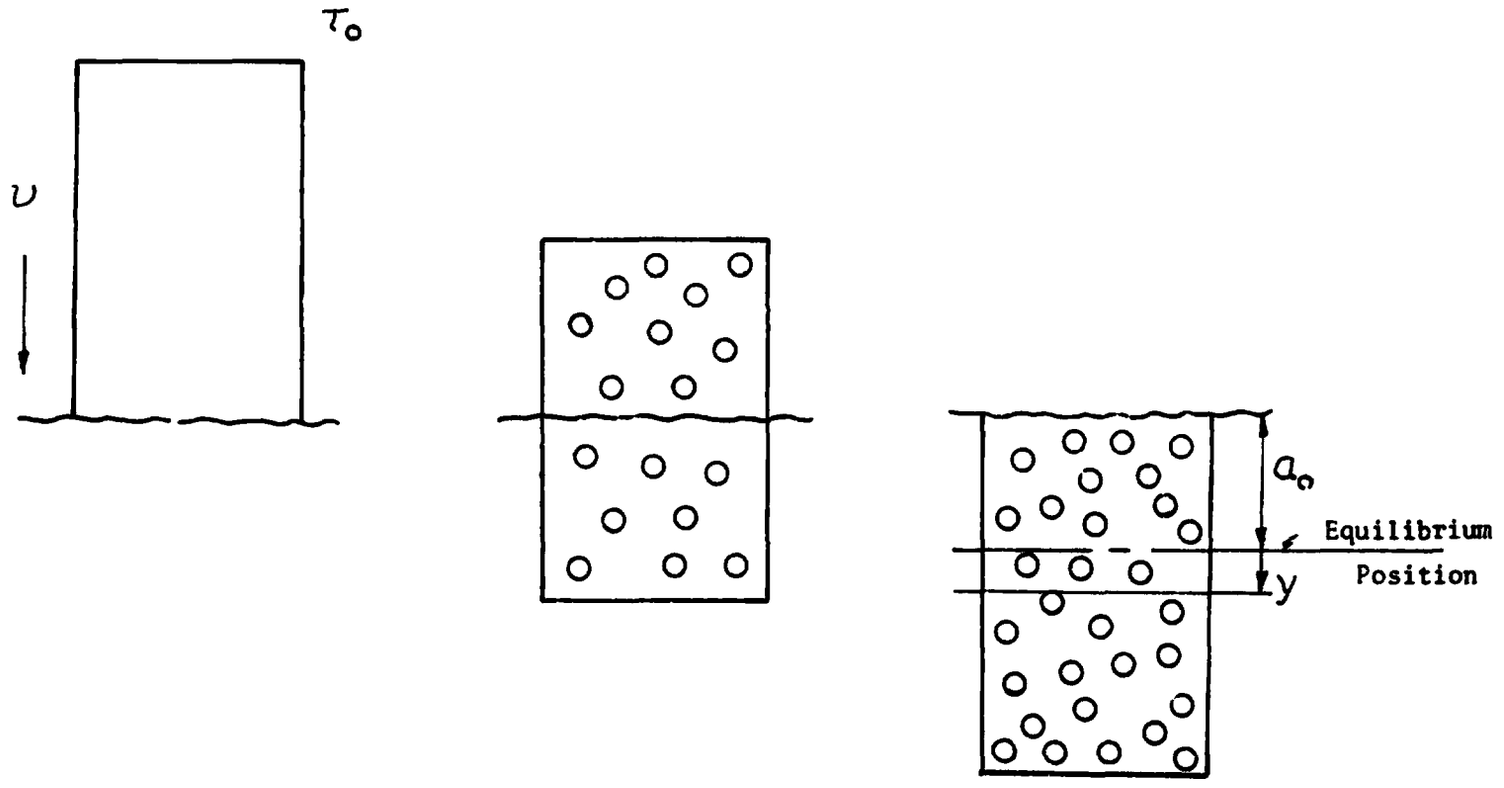

Figure 9 The Fluid Plug Model

heat transfer at the contact surface area, which can be calculated, results in large amounts of vapor being generated. The amount of heat transfer constantly changes since the contact area changes, and the resulting amount of vapor generated as a result varies constantly making the fluid plug bob up and down.

The variable amount of vapor generated with time and the varying fraction of this vapor which is entrained at any one time in the fluid plug, provides the mass of the plug and the force acting on it. The resulting motion is an oscillation with varying and generally decreasing amplitude due to the constantly varying driving force and the constantly varying mass of the fluid plug.

The fluid plug motion can be expressed mathematically as

$$\Sigma F = \frac{d}{d\tau} \left(m \frac{dy}{d\tau} \right) \tag{11}$$

where

$$m = \frac{\rho_L V_{LP}}{g} + \frac{\rho_g V_{gp}}{g}$$

$$= \frac{V_{LP} \rho_L}{g} + f \frac{V_g \rho_L}{g}$$

$$= \frac{\rho_L}{g} (V_p - f V_g) \tag{12}$$

and ΣF is the force acting on the fluid plug, m is the constantly varying mass of the fluid plug, y is the displacement from the instantaneous equilibrium position, and τ the time.

The density of the liquid in the plug is ρ_L, the volume of the liquid in the fluid plug is V_{LP}, the density of the vapor in the

fluid plug is ρ_g , and the volume of the vapor in the fluid plug is V_{GP} , with g being the gravitational constant. V_g is the total volume of vapor generated and f is the fraction of it which is entrained in the fluid plug at time τ .

The volume V_p of the fluid plug can be expressed, if a cylindrical configuration is taken, in terms of the fluid plug radius r_p , and fluid plug height H .

$$V_p = \pi r_p^2 H \tag{13}$$

Considering the heat transfer at the surface of the fluid plug

$$\begin{aligned} q &= h \bar{A} \Delta T \Delta\tau \\ &= V_g \rho_g h_{fg} \end{aligned} \tag{14}$$

with q the heat transfer, h the heat transfer film coefficient, $\bar{A}$ the average area of heat transfer during the interval $\Delta\tau$, ΔT the temperature difference, and h_{fg} the latent heat of vaporization.

From equation (14), the amount of vapor generated can be calculated.

$$V_g = \frac{h \bar{A} \Delta T \Delta\tau}{\rho_g h_{fg}} \tag{15}$$

Using the above equations and relationships, the equation of motion for the fluid plug can be written

$$\Sigma F = -\rho_B \pi r_p^2 y$$

$$\cong \frac{d}{d\tau}\left[\frac{\rho_L}{g} \left(\pi r_p^2 H - f \frac{hA \Delta T \Delta\tau}{\rho_g h_{fg}} \right) \frac{dy}{d\tau} \right] \tag{16}$$

$$\bar{A} = \frac{\int_0^\tau \left[\pi r_p^2 + 2\pi r_p (a_o + v) \right] d\tau}{\int_0^\tau d\iota}$$

$$= \frac{\pi r_p^2 \tau + \int_0^\tau 2\pi r_p (a_o + y) d\tau}{\int_0^\tau d\tau} \tag{17}$$

$$y = \phi(\tau) \tag{18}$$

In the above equations ρ_B is the density of the liquid surrounding the fluid plug, a_o the instantaneous equilibrium position or center of oscillations during $d\tau$ and ϕ is a function which has to satisfy the motion as dictated by the heat transfer and the resulting vapor generation.

The above equation is very complex and for this reason simplifications are made by assuming that H is constant for all the cyclic increments, and that ρ_p, the plug density, is made to vary to compensate for this assumption.

Solutions giving excellent agreement with experimental work can be made by further simplifying the conservation of momentum equation to

$$- \rho_B \pi r_p^2 y = \frac{\rho_L}{g} (V_p - fV_g) \frac{d^2 y}{d\tau^2} \tag{19}$$

or

$$\frac{d^2 y}{d\tau^2} + \frac{g \rho_B \pi r_p^2}{\rho_L (V_p - fV_g)} y = 0 \tag{20}$$

which has solutions of the form

$$y = c' \cos \omega\tau + c'' \sin \omega\tau \tag{21}$$

with

$$\omega = \left[\frac{g\rho_B \pi r_p^2}{\rho_L (V_p - fV_g)}\right]^{\frac{1}{2}} \tag{22}$$

c' and c'' being arbitrary constants, and ω the instantaneous frequency of oscillations of the fluid plug.

The above equations can describe the actual motion of the fluid plug by successive application to fractions of cycles or successive time intervals. This can be indicated by

$$\left.\begin{aligned}
&\frac{d^2y_1}{d\tau_1^2} + \omega_1 y_1 = 0 && \tau_o \leq \tau \leq \tau_1 \\
&\frac{d^2y_2}{d\tau_2^2} + \omega_2 y_2 = 0 && \tau_1 \leq \tau \leq \tau_2 \\
&\text{- - - - - - - - - - -} \\
&\frac{d^2y_n}{d\tau_n^2} + \omega_n y_n = 0 && \tau_{n-1} \leq \tau \leq \tau_n
\end{aligned}\right\} \tag{23}$$

with the solutions of

$$\left.\begin{aligned}
y_1 &= c_1' \cos \omega_1\tau + c_1'' \sin \omega_1\tau \\
y_2 &= c_2' \cos \omega_2\tau + c_2'' \sin \omega_2\tau \\
&\text{- - - - - - - - - - - - - - - -} \\
y_n &= c_n' \cos \omega_n\tau + c_n'' \sin \omega_n\tau
\end{aligned}\right\} \tag{24}$$

and the boundary and initial conditions for each cycle increment.

The final conditions of one cycle increment form the initial conditions for the next.

$$\tau = \tau_i \,, \qquad y = -\bar{a}_i, \qquad \frac{dy}{d} = \upsilon_i \,,$$

$$\bar{a}_i = \frac{\bar{\rho}_{p_i}}{\rho_{B_i}} H_i \tag{25}$$

where the subscript "i" refers to the instantaneous values for the cycle increment under analysis.

From the above the total displacement (submergence) Y_i of the plug is

$$Y_i = a_i + y_i$$

$$= \frac{\bar{\rho}_{p_i}}{\rho_{B_i}} H_i + c'' \sin \omega_i \tau \tag{26}$$

And the volume mixed at time τ_i is

$$V_i = \pi r_{p_i}^2 Y_i \tag{27}$$

And the contact area at time τ_i is

$$A_i = (\pi r_{p_i}^2 + 2\pi r_{p_i} Y_i) F_T \tag{28}$$

where F_T is a turbulence factor which may be added if the contact surface is very turbulent or stirred up.

In using the Fluid Plug Model, the equations can best be solved by trial and error making the necessary assumptions and then varying

them until the loop, which has to satisfy the physical phenomena, closes. The motion of the fluid plug produced by the density changes in the fluid plug must agree with the heat transfer producing these density changes which in turn is a function of the fluid plug motion.

The detailed steps involved in the method are:

a) The determination of r_p, H, υ_o from the physical configuration and failure mode.

b) The selection of $\Delta\tau$ or fraction of cycle to be analyzed

c) The calculation of V_{g_i}

$$h_{LO_2/RP} = 7776 \text{ Btu/hr-ft}^2\text{- °F}$$

$$h_{LO_2/LH_2} = 1140 \text{ Btu/hr-ft}^2\text{- °F}$$

d) The selection of f (or calculation based upon bubble rise velocities).

e) The calculation of ω_i and a_i .

f) The use of the initial and boundary conditions to calculate the amplitude of instantaneous oscillation for the $\Delta\tau$ under consideration.

g) Calculation of the penetration.

h) The determination of the volume mixed V_{mix} during the interval under analysis.

This procedure is then repeated as often as needed or desired to obtain the Mixing Function V_{mix} versus τ .

The analysis described above, using the Fluid Plug Model for approximately half cycle increments is presented in Figure 10.

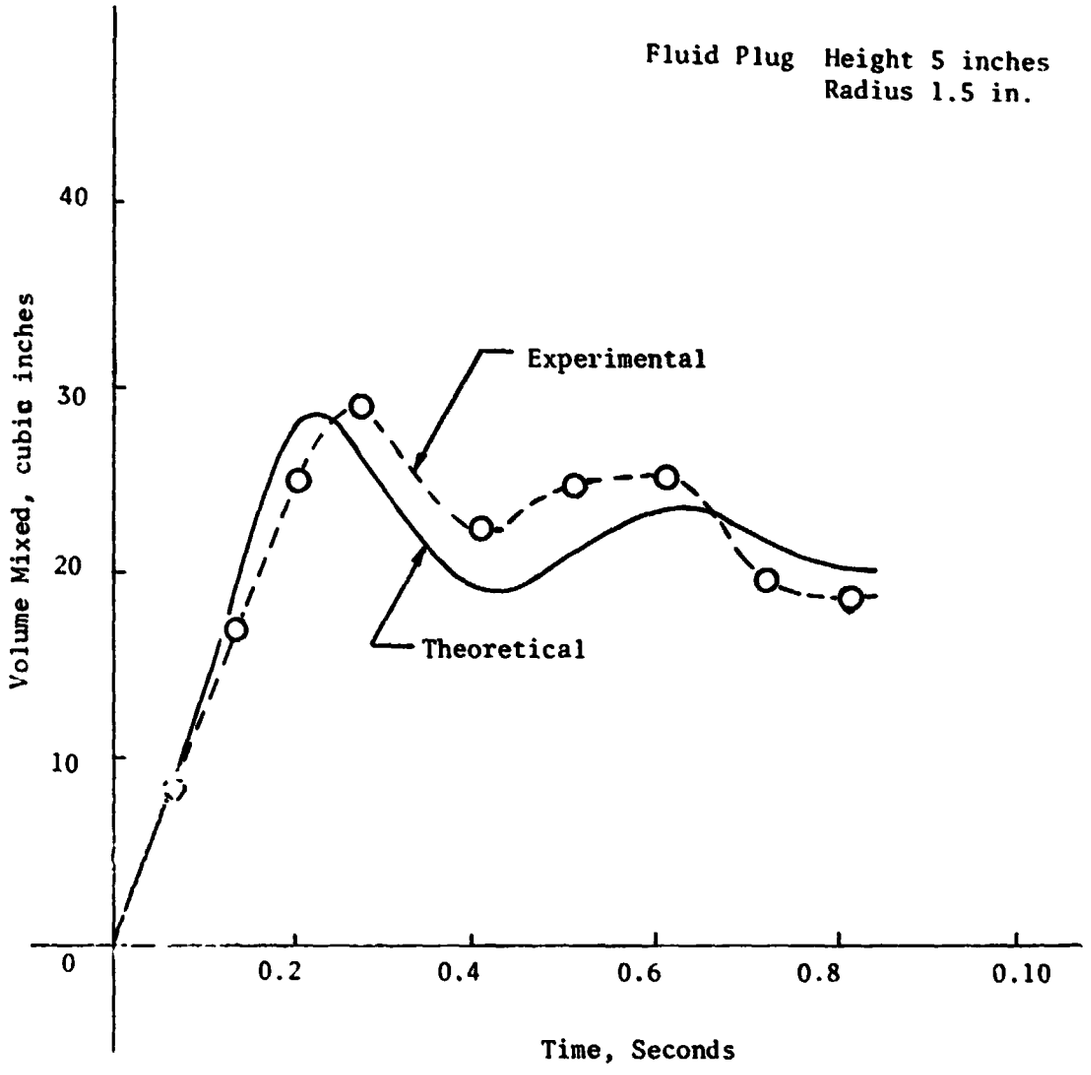

Fig. 10 Fluid Plug Mixing Function

Also plotted on this graph is the experimental result of the Mixing Function for LN_2/RP-1. More discussion on the experimental work will be found in a later section.

Electrical Analogy

As has been discussed in the literature for years, motion of fluid layers will, through the relative motion and friction, produce charged regions and set up potential differences within the fluid if these charges are prevented from leaking off too rapidly.

Since the motion of the fluid plug is described by the Fluid Plug Model developed, this motion should make it possible to describe also the electrostatic charge and voltage generation. Substitution in the equations of motion of the equivalent corresponding electrical quantities for the mechanical ones will provide a relationship between the charges generated and the motion of the fluid plug, the mixing and the heat transfer.

The frequency of the motion in the basic equations remains the same.

While the physical motion, is however, of oscillatory nature, the charge generation and build-up is cumulative, or in other words, independent of the direction of the motion of the fluid layers.

The expression becomes

$$\frac{d^2Q_i}{d\tau^2} + \omega_i^2 Q_i = 0 \qquad (29)$$

when the same basic assumption is made for simplification purposes as before. The general solution is again of the form

$$Q_i = D_i \cos \omega_i \tau + E_i \sin \omega_i \tau \tag{30}$$

Q_i is the instantaneous charge generated and D_i and E_i are arbitrary constants. ω_i is the one determined from the physical motion of the fluid plug.

These equations allow the calculation of the charge generated during each time interval or cyclic increment, with the constants determined from either experiment or physical and electrical properties of the fluids.

The value of the accumulated charge, which is the quantity which eventually provides the ignition source through generation of the required potential, is obtained from

$$Q = \sum_i |Q_i| \tag{31}$$

where Q is the total accumulated charge calculated from the summation of the absolute values of the charges generated for the cyclic increments.

Figure 11 presents two curves of charge generation calculated in this manner from the fluid plug model. The lower curve is calculated for a fluid plug 3 inches in diameter and 5 inches high. It corresponds to the use of 140 in^3 of LN_2 in a 50% bulkhead failure arrangement (d/D = 0.5), where d = diameter of the hole and D = diameter of the tank.

The upper curve represents twice the quantity or a fluid plug twice as high. It is shown that the doubling of the mass produced

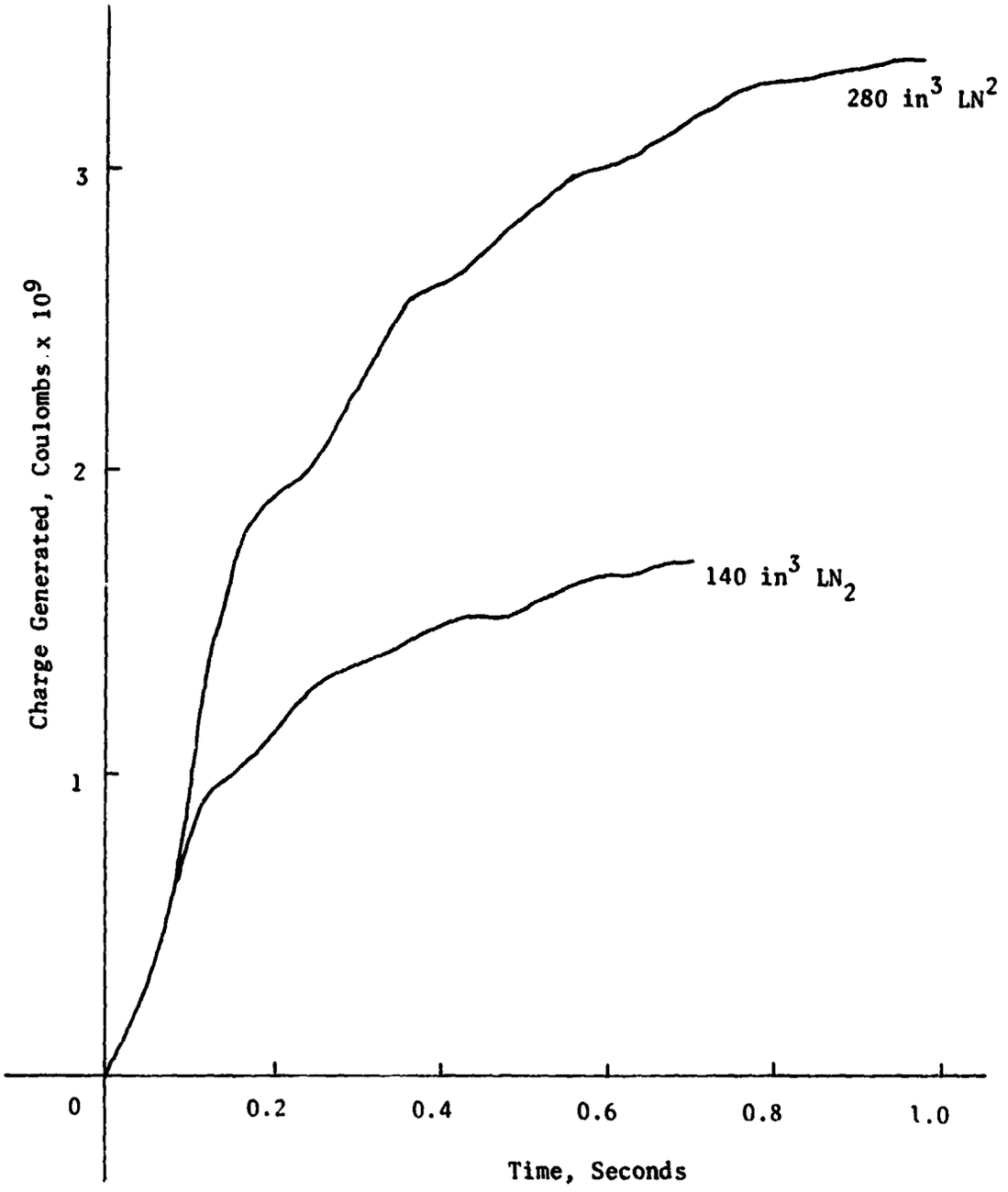

Fig. 11 Theoretical Charge Generation, Fluid Plug Model.

essentially twice the charge. Experiments over two orders of magnitudes demonstrated a linear relationship.

In all the experiments carried out with both organic (hydrocarbon) fuels and LN_2 as well as inorganic liquids such as distilled water and LN_2, it did not seem to make any difference whether the mixing to produce the electrostatic charges was carried out in steps or the total mass was brought together all at once. This is only true if the leakage was negligible since the step by step mixing took much more time to produce the same charges.

Since the fluid layers act as plates of a capacitor, and the electrode screens are imbedded in the fluid layers, the relationship between electrostatic charge, capacitance C, and voltage V can be used

$$Q = CV \tag{32}$$

With the Q calculated from the equations of motion and the electrical equivalencies, and C from the physical configuration, V can be obtained from equation (32).

The voltage build-up obtained in this manner is presented in Figure 12. It is presented here as a function of mass which is the form in which it will be used later for determining the Critical Mass. The experimental verification is presented in the next section.

Critical Mass

The hypothesis proposed here, and believed to have been verified, is that in the absence of any external ignition sources a mixture of fuel and oxidizer will, through the nature of the mixing process, produce electrostatic potentials. These will reach values at which

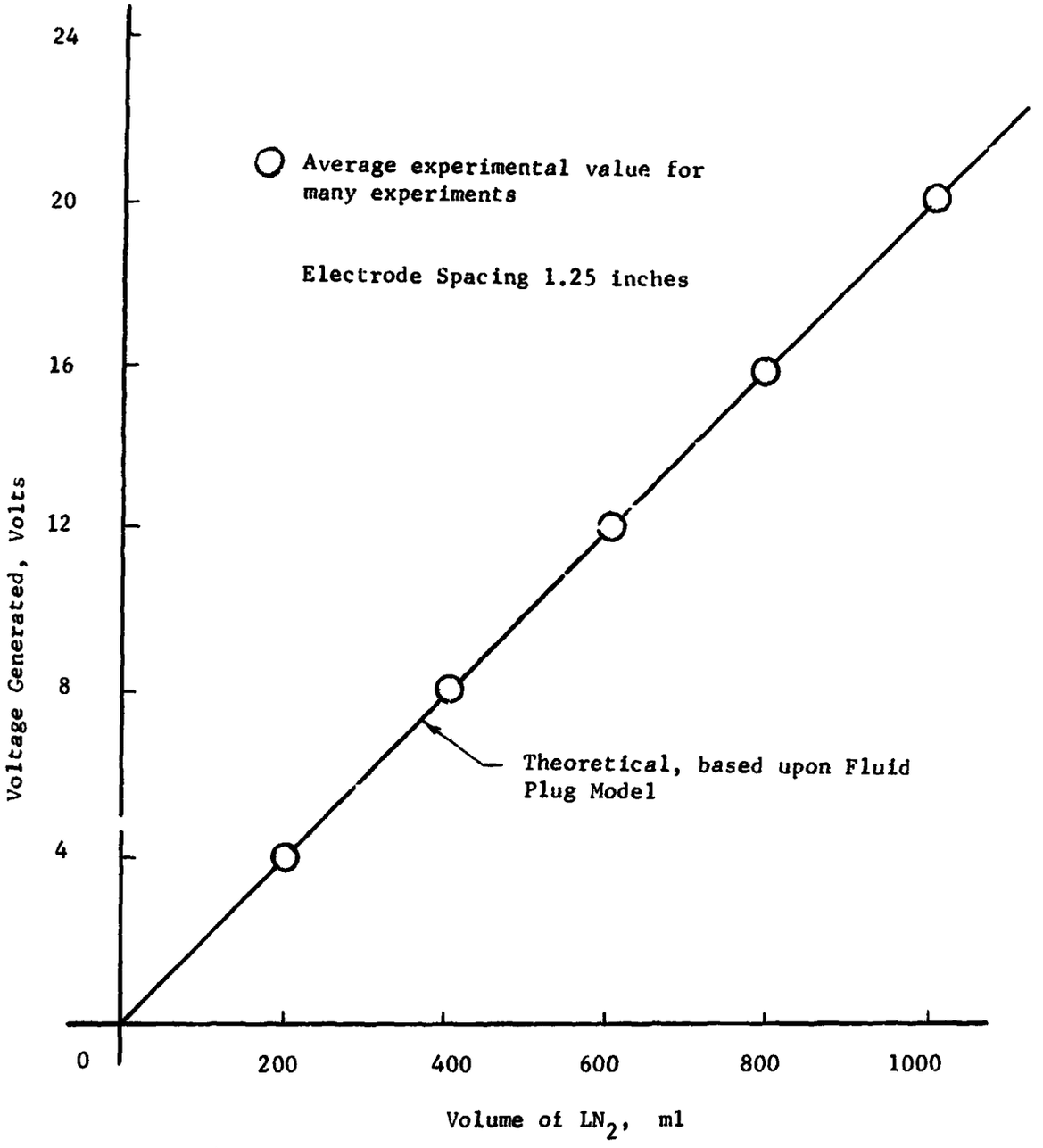

Fig. 12 Voltage Generated as a Function of LN_2 Quantity

breakdown through sparking occurs supplying ignition sources for the explosive mixture.

As a consequence of the above, it is impossible to mix unlimited amounts of cryogenic rocket propellants since the voltage build-up becomes larger as the quantity mixed becomes larger, and finally with a certain limiting quantity mixed, ignition becomes a certainty since breakdown will occur. This quantity is referred to by the writer as CRITICAL MASS.

Basically what this means is that an explosion can occur at any time with any quantity of explosive mixture, but the probability of it occurring increases and finally becomes a certainty at a particular quantity, and it is impossible to mix quantities larger than this limiting value of Critical Mass without an explosion occurring. (The quantity of Critical Mass, however, varies with the energy of the mixing process. This will be discussed later in the report.) Ignition is certain to occur as soon as the Critical Mass is reached.

According to the literature, it takes 0.02 millijoules to ignite hydrogen, and under unusual conditions it has been ignited by 1300 volts[85-94]. Usually it takes higher potential differences, and voltages of 14,000 to 20,000 volts are quoted[85-94]. Some authorities, according to these sources, consider it necessary to have an electric field strength of 76,000 volts per inch before sparking can occur.

Using the last number, one would require about 19,000 volts for discharge across a 1/4 inch bubble, the most prevalent size in the experiments.

Further, using the knowledge that 4 volts are produced at an average, for each 200 ml of LN_2 and recognizing that the physical-electrical properties needed here of LN_2, LH_2, and LO_2 are similar, it can be estimated that for a bulkhead type failure the Critical Mass, or mass which when mixed will produce this voltage, is about 2300 lb. for LO_2/LH_2 and approximately 2800 lb. for LO_2/RP-1.

Trusting that the above results are correct and applicable, one can estimate the maximum expected explosive yields for such failures, obtaining about 3 percent for the S-IVB PYRO experiment and about 11 percent for the 25,000 lb. LO_2/RP-1 bulkhead type explosion experiments. These yield values are in excellent agreement with the reported experimental values[119].

Variation of Critical Mass with Mixing Energy

When LO_2 and RP-1 or LO_2 and LH_2 are brought together the difference in temperature produces rather rapid heat transfer. This heat transfer produces large amounts of vapor which through its sudden displacement of liquid produces rather violent mixing of the fuel and the oxidizer.

With the propellant combinations under these conditions, at least the boiling will always be present, and a fraction of this energy will produce agitation thus contributing to the mixing process.

More gentle mixing is not possible, and mixing energies smaller can only be produced when the propellant components are brought to temperatures less different from each other.

If the mode of failure is changed so that the propellants are driven together with greater energies, the mixing will take place faster. The charge and voltage generation will also occur faster but does not relatively increase as much as the mixing rate.

From these considerations it can be seen that if propellants can be mixed very gently, say drop by drop, infinite quantities could be mixed, which however would take infinite time, without producing ignition. On the other hand, if the propellants could be brought together with infinite energy, they could be completely mixed in zero time, again allowing the mixing of infinite quantities before ignition can occur.

This analysis then indicates that the Critical Mass, when plotted against the Mixing Energy, which is supplied by both the mode of failure and the boiling process, approaches infinity both as the mixing energy approaches zero and also as it approaches infinity. Thus, the plot of Critical Mass versus Mixing Energy is a distorted "U" curve, and all the real values which can be encountered will fall below this curve.

From mathematical analysis, the Critical Mass function can be divided into two characteristic branches, the one to the left of the minimum and the one to the right. The minimum point represents the value of Critical Mass which is the maximum value which could be produced with the boiling energy of the bulkhead type failure. Since this value is easily calculated for any quantity of propellants, all other cases are normalized with respect to this energy value.

From experiments with non-cryogenic mixtures, it is seen that the time it takes for the voltages to be reached which could produce ignition decreases with an increase in the mixing energy; conversely it approaches infinity when the mixing energy approaches zero. The relationship below closely describes this behavior.

$$\tau^* E = C_3 \tag{33}$$

where τ^* is the Critical Time, or time it takes to build up the voltage necessary for ignition, and E is the Mixing Energy. C_3 is an arbitrary constant.

From the Fluid Plug Model the mass mixed at any one time can be expressed as

$$\begin{aligned} M &= C_4 \sin \omega\tau \\ &= C_4\omega\tau - \frac{C_4\omega^3\tau^3}{3!} + \frac{C_4\omega^5\tau^5}{5!} - \cdots \\ &\cong C_4\omega\tau \end{aligned} \tag{34}$$

and therefore

$$M^* = C_4\omega\tau^* \qquad \text{and from (33)}$$

$$\begin{aligned} \tau^* &= \frac{C_3}{E} \\ &= \frac{C_4\omega C_3}{E} \\ &= \frac{C_1}{E} \end{aligned} \tag{35}$$

This equation is seen to give the largest values for Critical Mass at low values of Mixing Energy. Since with cryogenic propellants under normal conditions, the Boiling Energy is the minimum which produces the mixing, Equation (35) is not the most significant contribution.

Again from the Fluid Plug Model and laboratory experiments with cryogenic fluids, it could be seen that twice the energy supplied for the mixing process produced essentially twice the mass mixed for the same time interval, three times the energy produced three times the mass mixed, etc.

This can be stated as

$$M = c_5 E\tau \tag{36}$$

From the previous work at the University of Florida with LN_2/RP-1 and the mixing studies carried out by PYRO with LN_2LH_2 it was found that

$$M = c_6\tau^2 \tag{37}$$

Setting equations (36) and (37) equal, the relationship between and E is obtained.

$$c_5 E = c_6\tau^2$$

$$\tau = \frac{c_5}{c_6} E \tag{38}$$

Substituting this last obtained relationship into equation (36) gives the significant M and E functional relationship for Mixing Energies larger than the Boiling Energy.

$$M = c_5 E \frac{c_5}{c_6} E$$

$$= c_2 E^2 \qquad (39)$$

The two relationships developed (35) and (39) can now be combined for a general equation relating Critical Mass and Mixing Energy.

$$M^* = \frac{c_1}{E} + c_2 E^2 \qquad (40)$$

For the analysis here, the Critical Mass - Mixing Energy relationship was normalized with respect to the Boiling Energy.

$$M^* = \frac{c_1}{\left(\frac{E}{E_B}\right)} + c_2 \left(\frac{E}{E_B}\right)^2 \qquad (41)$$

Evaluating the constants c_1 and c_2 from the Critical Mass determination based upon the charge and voltage generation, the Critical Mass Function takes on the form:

$$M^* = \frac{1870}{\left(\frac{E}{E_B}\right)} + 940 \left(\frac{E}{E_B}\right)^2 \qquad (42)$$

and can be plotted, Figure 13.

Figure 13 presents a plot of Explosion Mass (the amount of mass in any particular case which actually takes part in producing the explosion) versus the Mixing Energy Ratio (Actual Total Energy producing the mixing divided by the boiling energy). On a plot of this sort all explosions of liquid propellants can be recorded for which enough information is available, such as yield values, and in addition

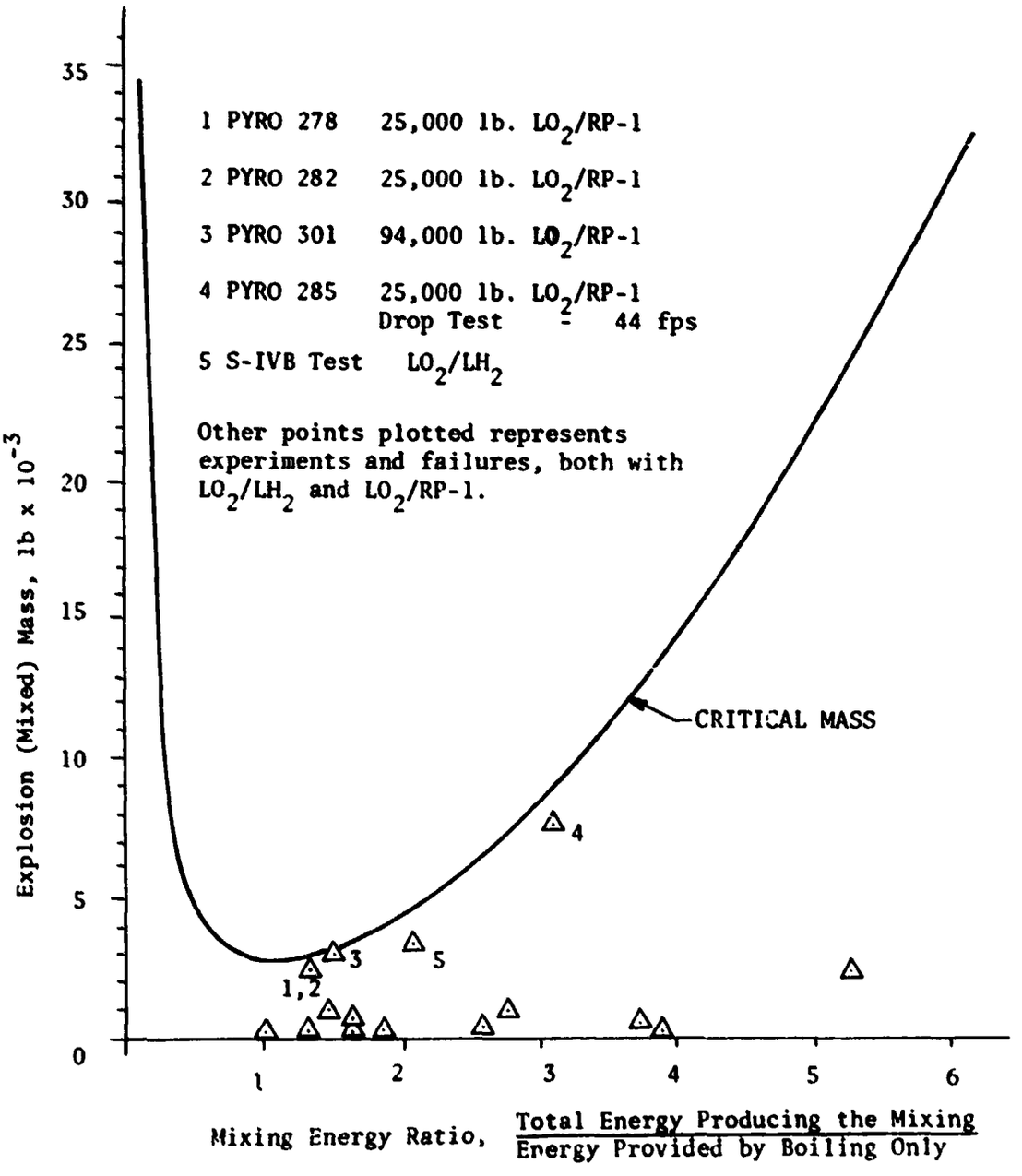

Fig. 13 Explosion Mass - Mixing Energy Relationship

the upper bound of these values can be plotted as the Critical Mass Curve.

All actual masses taking part in an explosion of liquid rocket propellants must fall below this curve.

It is seen from Figure 13 that all known values of explosions for liquid rocket propellants for which data is available fall, when plotted in this manner, below the Critical Mass Curve and only a few values approach the curve.

Many actual cases have been analyzed, but only a sample of them are plotted here. For these cases the boiling energy for a bulkhead failure with equal quantity of propellants was calculated for reference and then the actual boiling, potential, and kinetic energies available for the mixing process were considered.

It is believed that this new concept of Critical Mass for liquid propellants is very useful, indicating that there are self-limiting phenomena in the mixing and explosion processes of liquid rocket propellants and that there exists an upper limit to the size of explosion which can be realized.

For total quantities of propellants less than the Critical Mass explosive yields of 100% are possible, although the absolute size of the explosion is smaller than that produced by the Critical Mass. Furthermore, maximum explosive yield values for liquid propellant explosions depend upon the mode of failure which, in part at least, provides the energy available to bring the propellants together.

With large quantities of propellants it is physically impossible

to get all the propellants involved in an explosion since ignition occurs at the latest as soon as the Critical Mass is reached in the mixing process, while the remainder of the propellants take part only in rapid burning and the formation of the fireball.

The hypothesis of this self-limiting process and the fact that electrostatic charge and voltage generation provide this physical limitation, has been shown in the laboratory. It has further been verified by checks against the explosive yields of large propellant quantities which were produced both by tests and missile failures.

The mathematical Fluid Plug Model presented here demonstrates how the Critical Mass can be predicted from theoretical analyses for a desired mode of failure.

The results and predictions based upon the Critical Mass Hypothesis agree with actual experiments and actual failures and also with results obtained by the Mathematical Model and the Seven Chart Approach.

D. Fireball Hypothesis

Introduction

Sections A, B, C, above give some of the characteristics of liquid rocket propellant explosions. Section A presents the mathematical model which is a statistical treatment of the overall characteristics culminating in prediction of the explosive yield that one can expect. Section B, the Seven Chart Approach, gives details of how the fuel and oxidizer come together, mix for certain modes of

failures, and the expected yield for any time following the failure. Section C, the Critical Mass Method, sets the upper limit for liquid rocket propellant explosions indicating that the mixing process has built-in self-limiting characteristics so that very large explosions with large liquid propellant quantities are not possible.

The present section takes the phenomena from the time of ignition through the formation of a detonation front at the reaction front, which in turn produces a shock front. The reaction front and the shock front behavior which produces a fireball and a following combustion product cloud is discussed.

After ignition occurs, the reaction of fuel and oxidizer produces a reaction front which develops into a detonation front producing a shock wave which has a maximum velocity due to confinement of the surrounding liquid. The velocity then decreases with the decrease in confinement as the fronts come closer to the surface of the container. When the shock front, pushed by the reaction front, reaches the edge of the mixture and enters into the inert liquid, it moves ahead of the reaction front and is reflected back and forth between the wall and the reaction front. Each pressure impulse can actually deflect the walls while this occurs. When finally the reaction front and shock front are at the surface together, they suddenly break through with an increase in velocity due to the transfer of momentum to a lighter fluid and emerge as a shock front and a reaction front which forms the edge of the fireball. The shock front is very rapidly attenuated as it moves through the atmosphere. The reaction front

also is attenuated rather rapidly forming the typical hesitation hump.

For the purpose of this discussion, the problem can be divided into 5 parts which together form the "fireball hypothesis". These 5 parts are:

I. The region where ignition produces phenomena that develop into the detonation phenomemon.

II. The region where the reaction front and the shock front travel together through the propellant mixture.

III. The inert liquid region where the shock front and the reaction front separate and where the shock front is reflected back and forth between the walls of the container and the reaction front.

IV. The liquid propellant-air interface, actually a region where the liquid boundary begins to move and where the velocity of the reaction front forming the fireball and the velocity of the shock wave increase sharply due to the entrance into a lower density medium.

V. The region in which the shock wave travels through the atmosphere and where the fireball grows and develops separately far behind the shock wave.

Figure 14 is a sketch of the hypothesis showing the five regions for one case of confinement and yield, etc. These regions are discussed in detail in the following pages.

It might be well to mention that the scales chosen for presenting the five regions in Figure 14 are different for each so as to be

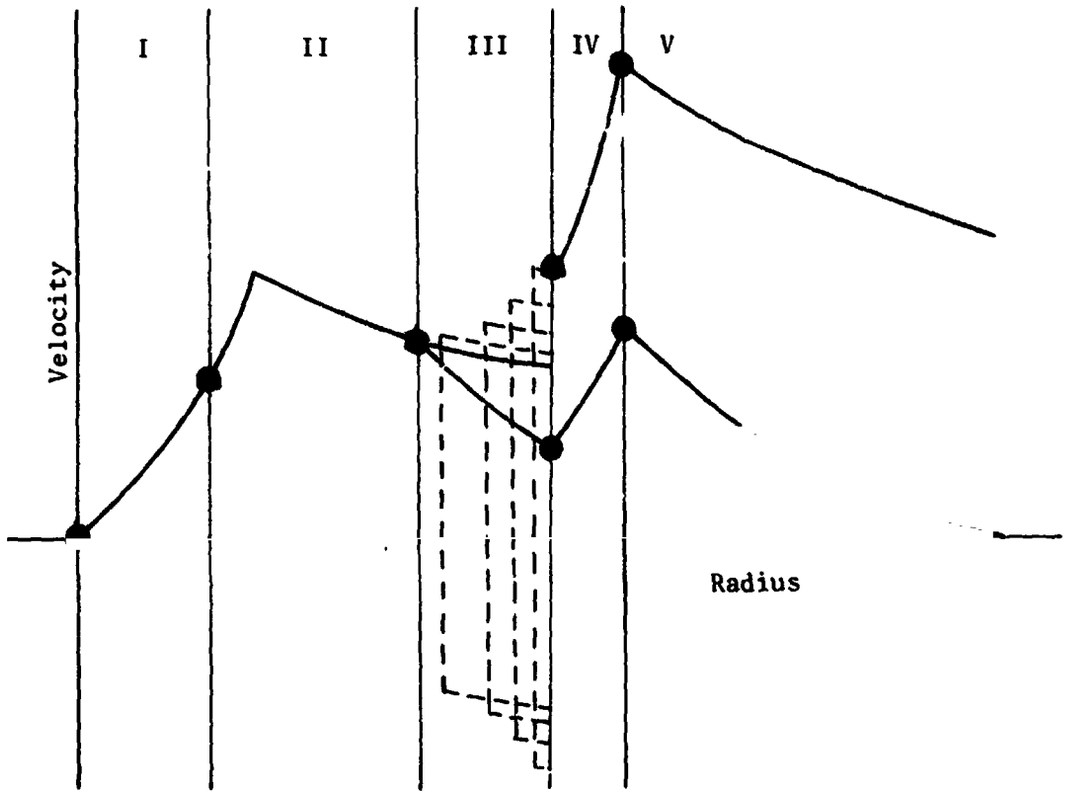

Figure 14 Graphical Representation of Fireball Hypothesis Indicating the Five Distinct Regions

able to show the variations occurring in each region. Region 4 is actually very small; regions 1, 2, and 3 make up the physical space of the liquid propellants, the relative size being a function of the explosive yield obtained from the propellants. Region 5 is by far the largest.

Also on a time scale, the phenomena in regions 1, 2, 3, and 4 will happen in a matter of milli-seconds and the flash in micro-seconds, while those of region 5 ordinarily stretch over many seconds. This last fact is also the reason why measurements are available for a good part of region 5, while they are not for regions 1, 2, 3, and 4.

The other sections report work covering another phase of the problem of liquid propellant explosion hazards, mainly the Mixing Function - an important factor in the prediction of explosive yields, and propose a method which is believed to be able to give experimental information in regions 1, 2, 3, and 4.

The Five Regions

Region I - The Region Where Ignition Produces Phenomena that Develop Into the Detonation Phenomenon.

Some time after liquid propellants are brought together, either intentionally or through failure, ignition may occur. At this time of ignition a certain fraction of the total propellants involved is mixed and ready for reaction. Since mixing continues with time, but also evaporation losses occur where cryogenics are involved, the ignition time has a pronounced effect upon the explosive yield[15,47,75,104]. The time of ignition may be essentially a constant for hypergolics or

or a random function for cryogenic propellants.

The reaction between the propellant components thus initiated will progress rather quickly among those molecules that are ready to react. This may be expressed simply as

$$\frac{dN}{d\tau} = kN \tag{43}$$

N = number of molecules ready to react

τ = time

k = reaction factor

Since the molecules that are ready to react at time, τ , must be in "contact" with each other, they can be thought of as located on a "contact area" or "surface" produced by the mixing process. Thus the above equation can also be expressed as

$$\frac{dA}{d\tau} = kA \tag{44}$$

A = contact area

This contact area, or a surface proportional to it, can be measured experimentally for a particular missile configuration and mode of failure as a function of time. For the purposes here and from a theoretical point of view, it could be considered spherical for a first approximation, thus assuming the reaction progresses in all directions, which will certainly be true in the initial stages. Thus we can write

$$A = \frac{4\pi r_y^2}{y} = 4\pi r^2 \tag{45}$$

r_y = equivalent radius of actually spherical surface

r = radius of actual total contact area of which only a fraction y reacts

y = yield

Little information is available on the reaction factor k in equation (44). Let us assume that it is a function of time and that it can be expressed as

$$k = k_o \tau^a \tag{46}$$

where k_o and a are constants.

With this information and the above assumptions, Equation (44) can be integrated.

(A) For $a = 0$ in equation (46), equation (44) can be integrated, and utilizing equation (45) one obtains;

$$v_{y_2} = \frac{r_1 \sqrt{y_1 k_o}}{2e^{\left(\frac{k_o}{2} \tau_1\right)}} e^{\left(\frac{k_o}{2} \tau_2\right)} \tag{47a}$$

$$r_2 = \frac{r_1}{e^{\left(\frac{k_o}{2} \tau_1\right)} \sqrt{\frac{y_1}{y_2}}} e^{\left(\frac{k_o}{2} \tau_2\right)} \tag{47b}$$

Where v_{y_2} is the velocity in Region I and r_2 the corresponding radius at which this velocity is reached.

Plotting these parametric Equations (47a) and (47b) as v_y versus r, the part of the Fireball Hypothesis falling into Region I

is obtained (Figure 15A).

(B) Repeating the operation of part (A) but with $a = 1$, making the reaction factor a linear function of time instead of leaving it a constant as in (A) we obtain

$$v_{y_2} = \frac{r_1 \sqrt{y_1} k_o}{2e^{\left(\frac{k_o}{2}\tau_1^2\right)}} \tau_2 \, e^{\left(\frac{k_o}{2}\tau_2^2\right)} \tag{48a}$$

$$r_2 = \frac{r_1}{e^{\left(\frac{k_o}{2}\tau_1^2\right)}} \sqrt{\frac{y_1}{y_2}} \, e^{\left(\frac{k_o}{2}\tau_2^2\right)} \tag{48b}$$

Plotting these parametric equations as in (A), Figure 15B is obtained. Other functions can be selected for the reaction factor and with it other velocity rise rate curves can be obtained. The decision as to which relationship represents the true case best (for particular propellants) will have to wait until experimental information, either direct as velocity measurements or indirect in terms of contact area-time measurements for some of these cases, becomes available.

The yield, y, was considered constant or at least an average value in the above calculations. Any other function can be selected in this analysis as soon as there is some justification for it.

It is believed that the above approach gives better insight into the happenings in Region I and allows for the expression of these happenings in a satisfactory manner.

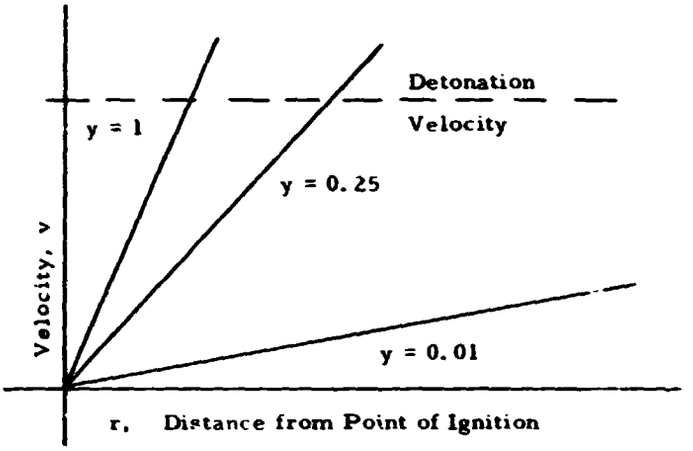

Figure 15A Representation of Fireball Hypothesis in Region I (Reaction Factor = C)

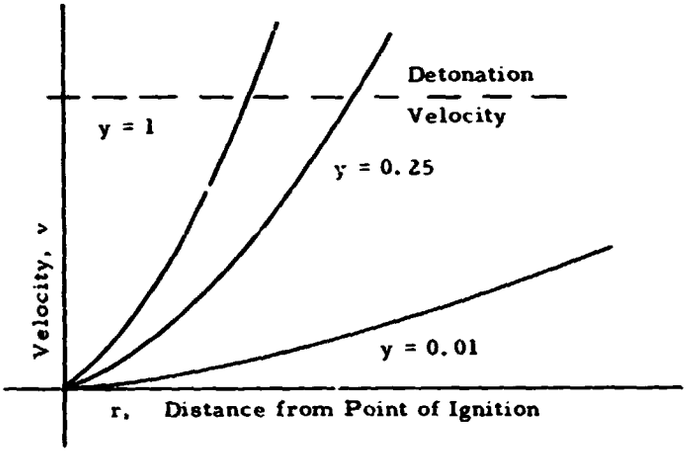

Figure 15B Representation of Fireball Hypothesis in Region I (Reaction Factor = $k_o t$)

Region II - The Region Where the Reaction Front and the Shock Front Travel Through the Liquid Propellants Together.

In Region II, if the propellants were properly mixed, uniform or smooth propagation of the reaction front and the shock wave would occur. Since this is most likely not the case, the traces must be considered average curves since actually they would have small steps, like a stairway, superimposed upon them. These finer points can be added later on, after the overall hypothesis is developed and assuming that enough information is available to do this.

If the physical system is very small or if the system is essentially unconfined, thus not capable of supporting pressure gradients, then the waves would travel with the velocity of sound as soon as these velocities are reached. Under these conditions the velocity could be considered constant in the Region II with the reaction or detonation and shock fronts traveling together.

Actually confinement, especially in the earlier stages, will build up pressure and temperature due to the reaction taking place and will further increase the front velocities. Assuming the degree of confinement in terms of the masses surrounding the reaction, the pressures and temperatures can be estimated, and from them the wave velocities. Studies[7] have shown however that the velocities in liquids do not increase very fast with increase in pressure so that the original assumption of essentially constant velocity in this region seems justified.

As the traveling waves approach the boundary of the liquids,

the confinement decreases, and so the velocity differential between unconfined, or sonic, and the actual velocity decreases. Therefore a maximum velocity will be reached in this region which is a function of confinement, and which is also dependent upon the missile configuration and yield for specific propellants.

Calculations have been made for confinement but seem to be of lesser importance than other considerations.

Figure 16 represents schematically, for a particular condition, the velocity rise and following decrease in Region II.

In Figure 16, detonation velocity is reached at point A. In an unconfined system the velocity may be considered constant until the edge of the mixing region is reached. Thus the line AB would represent this case. If confinement is considered, which is naturally highest on the left hand side of the Region II, the wave velocities will still increase until, due to continuous decrease in confinement, they reach a maximum, and then will decrease to a value above or equal to the unconfined system, depending upon what the confinement is at the liquid-air boundary. Thus the actual case will be more closely represented by the curve A-A'-B'.

The calculations for these curves in Region II are relatively simple. They can be carried out provided the equation of state, heat generation and losses from a certain region, and constant volume processes for complete confinement, or appropriate volume changes for the various degrees of confinement, are considered.

Verification of this part of the hypothesis is presented in the next section.

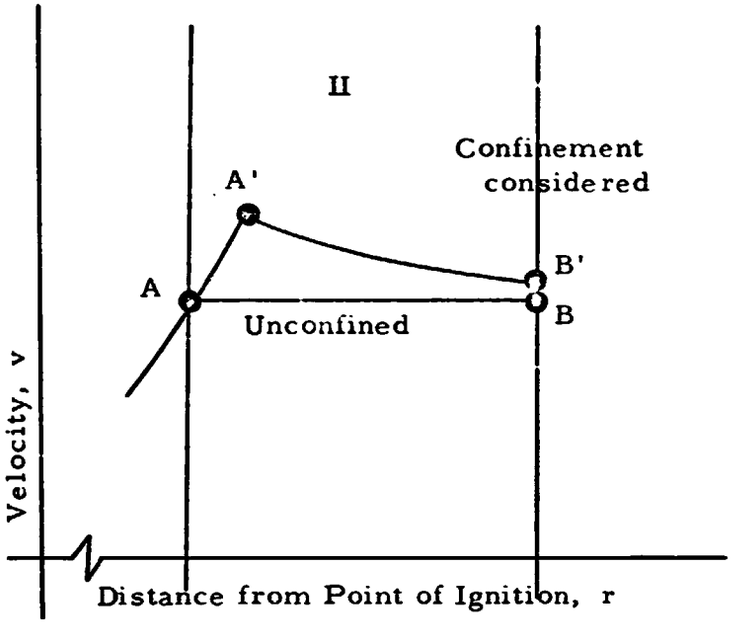

Figure 16 Representation of Fireball Hypothesis in Region II

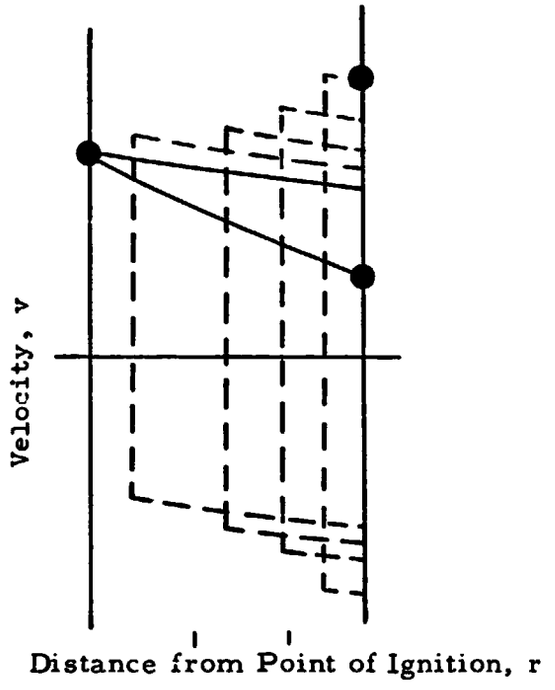

Figure 17 Representation of the Fireball Hypothesis in Region III

Region III - Separation of the Shock Wave and the Reaction Front and Travel of Each Through the Inert Liquid

When the shock wave, driven by the reaction front, arrives at the edge of the mixing region, the shock wave will enter this region being attenuated through the new medium. The reaction front not being driven as it was in the mixing region, will be attenuated much more rapidly. The shock wave moving ahead of the reaction front, will arrive at the container wall giving an impulse to this wall, and upon being reflected it will reverse its direction and move toward the reaction front. When the two fronts meet, the shock front will again be reflected in the original direction and thus will bounce back and forth between the walls and the reaction front. While the shock wave gives continued pressure impulses to the container walls, the wall may actually start expanding and moving out. This phenomemon has been observed in high speed photography of exploding missiles.

Figure 17 shows more detail of Region III and a schematic indication of the phenomenon occurring. The actual velocities of both the shock front and the reaction front can be calculated with the shock front taking up energy from the reaction front every time it is reflected from it. Thus the velocity of the shock wave will increase and the distance traveled between reflections will rapidly decrease. These phenomena continue until both the shock wave and reaction front arrive at the already moving boundary together.

Region IV - The Liquid Propellant-Air Interface, Actually A Region Where the Liquid Boundary Begins to Move and Where the Reaction Front Forming the Fireball and the Shock Wave Emerge.

When the reaction front and shock front reach the liquid propellant-air interface which most probably has begun to move slightly, two distinct phenomena occur.

A. The shock wave in the liquid is transformed into a shock wave in air. This is a wave-to-wave phenomena transition, essentially not involving mass transport.

B. The reaction front, or detonation front, is transformed into a moving mass front. This is a transition from a wave phenomenon to a particle phenomenon.

It seems that this may well be the reason why at this point the two phenomena, as for instance represented by the velocities, follow different paths.

The shock wave experiences an increase in velocity as it crosses from the liquid into the air through possibly a small vapor layer. Very little information could be found about the transition of a shock wave from one medium into another and especially for the case where the compressibility is so different.

The reaction front, when reaching the interface also as a wave phenomenon will now have to change into a particle phenomenon where the propellant particles have to move out forming the fireball boundary, thus involving tremendous amounts of mass transport. This transition must produce a rather abrupt change in the velocity in a rather small region.

These phenomena are represented schematically in Figure 18 for Region IV.

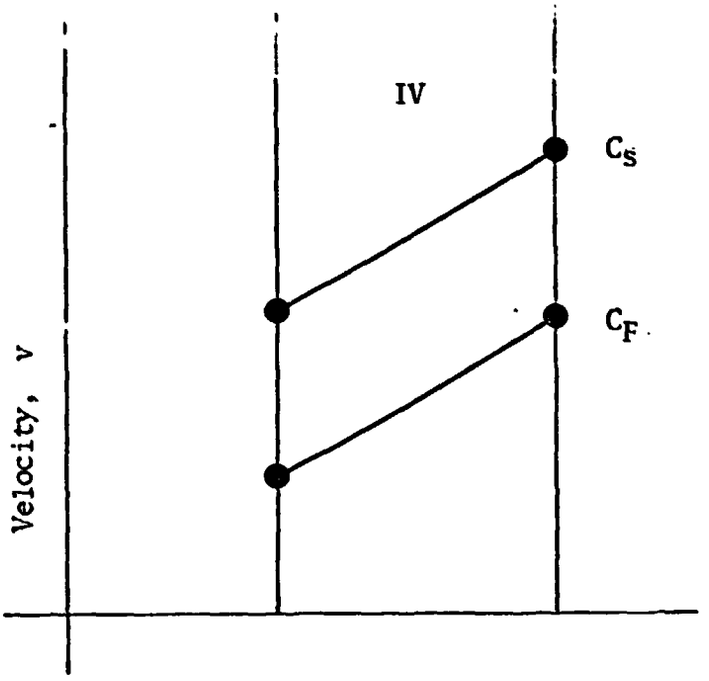

Figure 18 Graphical Representation of Fireball Hypothesis in Region IV

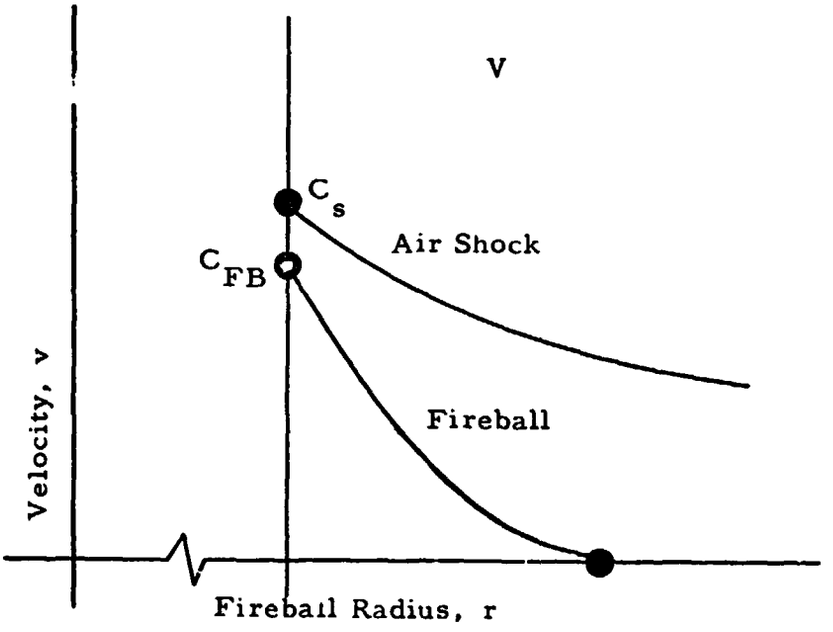

Figure 19 Graphical Representation of Fireball Hypothesis in Region V

Region V - The Region in Which the Shock Wave Travels Through the Atmosphere as an Air Shock and Where the Fireball Grows and Develops Separately Far Behind the Shock Wave.

After separation of the shock wave and the reaction front, each of these phenomena follow their own physical laws and relationships. See Figure 19.

Fortunately some experimental information is available in this region on both the shock and the fireball. All this information, however, is for considerable distances from the liquid-air interface, and theory again will have to bridge this gap.

Air Shock

The attenuation of the air shock can be approximated by the well-known equations of compressible fluid flow and can be expressed in terms of the pressure ratio across the shock.

$$v_s = c_o \left\{ \frac{\gamma + 1}{2\gamma} \left[\frac{P_2}{P_o} + \frac{\gamma - 1}{\gamma + 1} \right] \right\}^{\frac{1}{2}} \tag{49}$$

where

v_s = shock velocity

c_o = velocity of sound at P_o

γ = 1.4 for air

P_2/P_o = pressure ratio across shock

The pressure ratio can also be expressed in terms of the propellant weight, the yield, the distance from the point of ignition and some constants.

$$\frac{P_2}{P_o} = \frac{10^b}{P_o}\left[\frac{(Wy)^{1/3}}{r}\right]^m + 1 \qquad (50)$$

Equation (50) can now be substituted into Equation (49) to obtain the desired relationship, giving the air-shock velocity in terms of the distance from the point of ignition. Spherical geometry was assumed throughout in these derivations and whenever the fireball moved, r was taken as the radius of the fireball. This was necessary since otherwise information like wind velocity, etc. would have to be added into the above equations. Equation (51) is the desired result giving the air-shock relationship for the fireball hypothesis in Region V.

$$v_s = c_o \left\{ \frac{\gamma + 1}{2\gamma} \left[\frac{10^b}{P_o} \left(\frac{(Wy)^{1/3}}{r} \right)^m + \frac{\gamma - 1}{\gamma + 1} + 1 \right] \right\}^{1/2} \qquad (51)$$

The symbols in Equation (51) have the meanings as defined earlier with b and m constants.

Equation (51) now allows the calculation of the velocity of the air shock at any distance from the missile.

Fireball Boundary

The fireball boundary can be calculated by utilizing the perfect gas relationships and considering either the spherical or hemispherical configuration. Then considering the heat generated through the chemical reaction processes and the heat losses, the necessary constants describing the process can be evaluated. Information such

as that found in the literature[16,49,50,51,52] is very helpful in this treatment.

Further considering that the heat or energy released minus the amount used in raising the temperature and minus the amount lost produces the kinetic energy which is observed in terms of the velocity at any time t or at any distance r. This is then the fireball velocity as expressed in Equation (52).

$$v_{FB} = \left(\frac{2Q}{m4/3\pi}\right)^{1/2} \frac{1}{r^{3/2}} = \frac{C}{r^{3/2}} \tag{52}$$

In Equation (52), Q is the energy released and available for acceleration of the mass m. As can be seen the fireball velocity, that is the boundary velocity, is inversely proportional to the 3/2 power of the radius. Q can be expressed in terms of the total weight of the propellants and the thermal yield.

Figure 19 represents schematically the shock velocity and the fireball velocity in Region V indicating the separate paths which they follow.

It might be well to mention again that in the presentation of the fireball velocity the actual center of the fireball was used as reference rather than the original point of ignition.

If that had not been done, then the rise of the fireball and draft due to winds and atmospheric conditions would have complicated the presentation.

Complete Fireball Hypothesis

Having discussed the five parts or regions of the complete fireball hypothesis, they can be combined to give the complete picture, which is presented in graphical form in Figure 20. The different regions are not plotted to the same scale but rather to a scale which allows the presentation of the variations in each ·on. This was done by enlarging Region I, and especially Region IV, and by shrinking Region III, and especially Region V.

Figure 20 presents graphically the complete fireball hypothesis (not all detail shown) for a specific yield. Different yields would change it slightly, specifically the relative sizes of Regions I, II, and III. The higher the yield the smaller is Region I.

The various regions of Figure 20 can be compared with the detailed regions and their discussion under the specific headings, Region I, Region II, Region III, Region IV, and Region V.

Comparison of Results from the Hypothesis and Some Actual Data

To show how thi hypothesis agrees with the sparse experimental information available, films of the S-IV Test were analyzed and analyses from the various reports were used. The hypothesis is plotted in Figure 20 and the available experimental points are superimposed.

The equations used for plotting the calculated curves in Figure 20 were Equations (51) for the air shock velocity and (52) for the fireball velocity.

These equations for the S-IV, where W = 91,200 lb., y = 0.045 avg.,

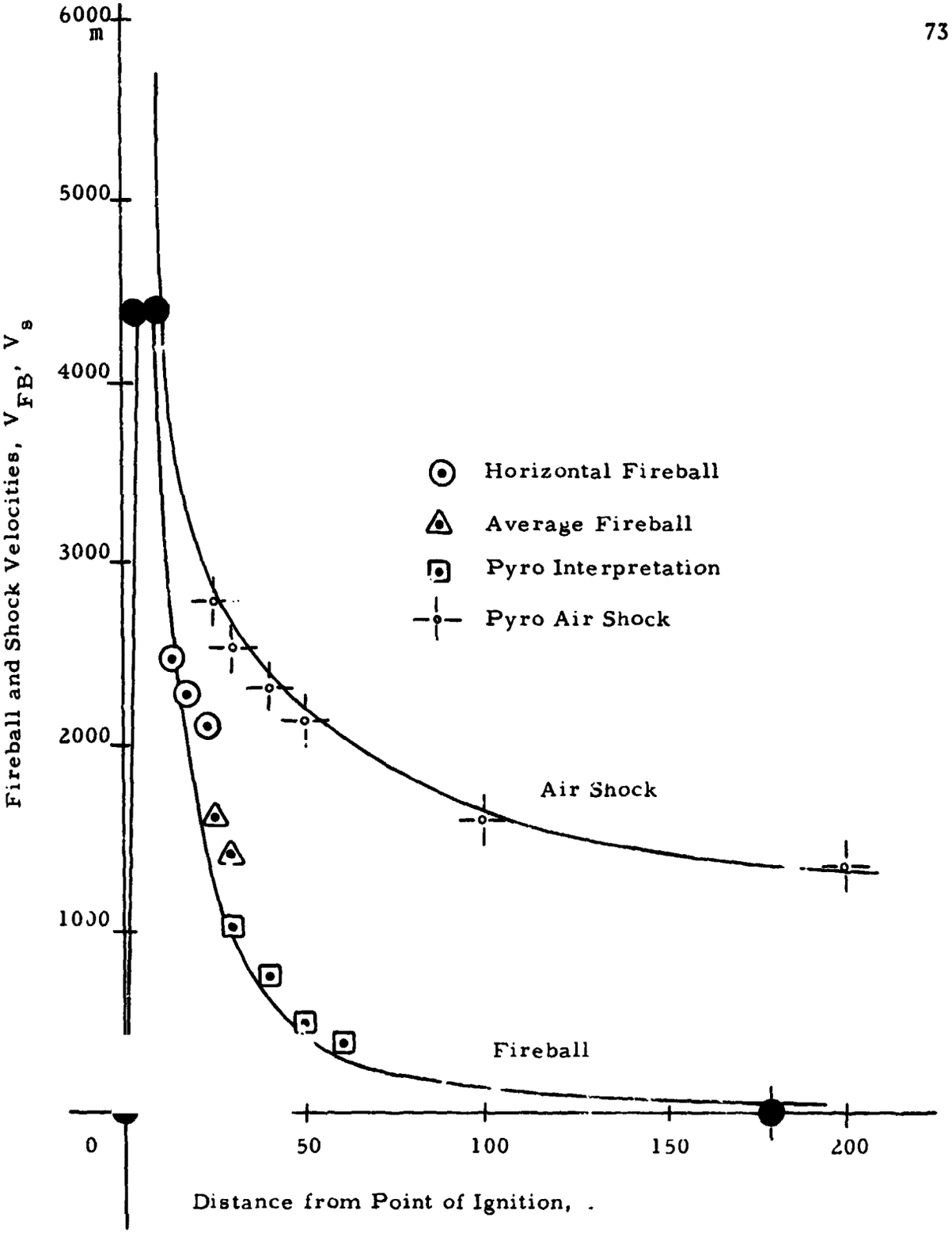

Figure 20 Fireball Hypothesis Applied to the S-IV Experiment with Experimental Points Superimposed upon the Calculated Curves

with their constants evaluated, have the following form:

Shock Velocity:

$$v_s = 1100 \left\{ 14 \left[\frac{(91{,}200 \times 0.045)^{1/3}}{r} \right]^{1.4} + 1.17 \right\}^{1/2} \quad (51a)$$

Fireball Velocity:

$$v_{FB} = \frac{157.500}{r^{3/2}} - 80 \quad (52a)$$

The results from these equations are the solid curves plotted in Figure 20. In this figure which is plotted to scale, Regions I, II, III, and IV are so small that not much detail can be shown.

SUMMARY

In this section a hypothesis was discussed which seems capable of giving insight into the actual processes taking place from the time of ignition in a liquid propellant rocket explosion until the shock and the fireball have separated and dissipated.

This hypothesis makes it possible to calculate curves for particular missile configurations and yield estimates giving a package for complete analysis.

The assumptions going into the analysis have been verified through actual experimental work the results of which are presented in the next section.

The thermocouple grid analysis discussed earlier was the method used to supply the experimentation and verification.

E. Fireball and Post-Fireball Analysis

Introduction

After the detonation has occurred the behavior of the fireball from the explosion which is formed and then gradually changes into a combustion products cloud is of importance. How large a fireball is formed, what is its temperature and what are the pressures inside? To be able to obtain this information the knowledge of how the fireball comes about, how it cools and then changes into a combustion products cloud is essential. Thus, its behavior is really one of the last groups of phenomena or processes in a series.

So for this phase of the work the knowledge of the fireball and combustion products cloud, volume-time, pressure-time and temperature-time histories have been assumed known and then the composition of the combustion phenomena has been determined. The composition of the fireball and of the combustion products cloud are important as well as their interaction with the atmosphere, expecially when toxic materials such as Flourine are used in the propellants.

The volume-time, pressure-time, and temperature-time histories of the explosion from liquid propellants were chosen as input since they may be determined theoretically[20,21] or may be measured in experiments thus giving a check on the theoretically determined information, with its statistical variations, etc.

For this investigation the best information available at this time has been used as input and then rather elaborate computer programs

have been used in obtaining the desired results[22]. Homogeneity of the fireball and of the combustion products cloud have been assumed in all calculations and this seems to be a reasonably good basis since the turbulence of the reaction processes is great enough to tend to mix the different products well.

With the volume-time, pressure-time, and temperature-time history available, the mathematical equations controlling these processes were set up and then computer solutions worked out to give the desired results.

Only a portion of all the information which was generated by this analysis is reported here but it seems ample to show the method of approach and the kind of results which can be obtained.

The fuel-oxidizer combination chosen here as examples for this investigation were ones which are used and some which may become important in the future development of liquid propellant rockets. They are:

LH_2/LO_2

RP-1/LO_2

LH_2/LF_2

RP-1/LF_2

LH_2/RP-1/LO_2

LH_2/LO_2 + 1% F
+ 5% F
+ 10% F

RP-1/LO_2 + 1% F
+ 5% F
+ 10% F

$LH_2/RP\text{-}1/LO_2$ + 1% F
+ 5% F
+ 10% F

For the above combinations of fuel and oxidizer, assuming a quantity of propellants of about 100,000 lbs., the results which are all normalized are presented as follows:

1. Fuel consumption versus time
2. Volume of entrained air versus time
3. Partial Pressures (of combustion products) versus time
   Partial Volumes (of combustion products) versus time
4. Partial Weights (of combustion products) versus time

Both the input information as well as the results are given in graphical form since it is believed that this method of presentation will give the maximum amount of information in the minimum amount of space.

It might be mentioned that the method and computer program developed are rather general and by no means restricted to the above fuel-oxidizer combination.

Theory of Approach

Equilibrium Composition of Chemical Reactions of Liquid Propellants Taking Place in the Atmosphere.

The purpose of this phase of the research program is to theoretically determine the amounts of product gases formed, as a function of time, as the result of a reaction involving liquid propellants and entrained air. This type of reaction is continuous since all of the available fuel does not react immediately and furthermore the resulting

fireball (which grows with time as more fuel reacts) continually entrains air. Given the initial amounts of fuel and oxidant as well as the volume - time history of the fireball (theoretically determined or as observed from high speed films), equilibrium compositions can be determined.

The equilibrium composition for the system of n products of reaction is determined by the simultaneous solution of n+1. equations consisting of the equations of mass balance, pressure balance and the dissociation equations involving equilibrium constants.

Assuming a constant pressure process as well as an instantaneous reaction time and making use of either theoretically obtained or experimentally determined pressure-time and temperature-time histories of the fireball, a solution is found such that the total theoretical volume of the products of reaction is made identically equal to the total experimental volume by adjusting the fuel burning rate and/or adjusting the amount of entrained air. As a first approximation, it is further assumed that no air entrainment exists until all of the available fuel is burned.

To efficiently meet these demands, a computer program has been developed. The program is general but limited here to the following reactants: liquid hydrogen, kerosene (RP-1), liquid oxygen, liquid fluorine, and air. Fifteen products of reaction were considered.

The equations and method of solution follows.

Controlling Equations

Symbol	Description	Reactant
A_1	moles of LH_2	A_1H_2
A_2	moles of RP-1	$A_2C_xH_{2x}$
A_3	moles of LO_2	A_3O_2
A_4	moles of LF_2	A_4F_2
A_5	moles of air	$\frac{A_5}{4.79}(O_2 + 3.79\ N_2)$

The reactants can then be written as:

$$(A_1 + A_2X)H_2 + (A_3 + 0.209A_5)O_2 + A_4F_2 + 0.792A_5N_2 + A_2XC$$

Consider the following products of reaction; such that the right hand side of the equilibrium equation is

$$\frac{N}{P}(p_1H_2O + p_2CO_2 + p_3H_2 + p_4N_2 + p_5F_2 + p_6O_2 + p_7HF + p_8CO + pgNO + p_{10}OH + p_{11}H + p_{12}N + p_{13}F + p_{14}C + p_{15}O) \quad (53)$$

where,

N = total number of moles of products of reaction

P = total pressure

p_i = partial pressure of ith product

The unknowns are $p_i (i = 1, \ldots 15)$, N. Hence 16 equations are necessary for a solution. The balance equations are:

(a) Pressure Balance

$$p - p_i = 0 \tag{54}$$

(b) Hydrogen Balance

$$2(A_1 + A_2X) - \frac{N}{P}(2p_1 + 2p_3 + p_7 + p_{10} + p_{11}) = 0 \tag{55}$$

(c) Oxygen Balance

$$2(A_3 + 0.209A_5) - \frac{N}{P}(p_1 + 2p_2 + 2p_6 + p_8 + p_9 + p_{10} + p_{15}) = 0 \tag{56}$$

(d) Nitrogen Balance

$$1.584\ A_5 - \frac{N}{P}(2p_4 + p_9 + p_{12}) = 0 \tag{57}$$

(e) Carbon Balance

$$A_2X - \frac{N}{P}(p_2 + p_8 + p_{14}) = 0 \tag{58}$$

(f) Flourine Balance

$$2A_4 - \frac{N}{P}(2p_5 + p_7 + p_{13}) = 0 \tag{59}$$

The above 6 equations can be reduced to 5 equations by eliminating $\frac{N}{P}$. Since we will be dealing with hydrogen (either LH_2 and/or RP-1), $\frac{N}{P}$ can be eliminated by dividing the 2nd equation into the last 4 equations. The 5 equations are:

$$P - p_1 - p_2 - \ldots\ldots - p_{15} = 0 \tag{60}$$

$$(2Y_1 - Y_2)\, p_1 - 2Y_2p_2 + 2Y_1p_3 - 2Y_2p_6 + Y_1p_7 - Y_2p_8 - Y_2p_9$$
$$+ (Y_1 - Y_2)\, p_{10} + Y_1p_{11} - Y_2p_{15} = 0 \qquad (61)$$

$$2Y_3p_1 + 2Y_3p_3 - 2Y_2p_4 + Y_3p_7 - Y_2p_9 + Y_3p_{10} + Y_3p_{11} - Y_2p_{12} = 0 \qquad (62)$$

$$2Y_4p_1 - Y_2p_2 + 2Y_4p_3 + Y_4p_7 - Y_2p_8 + Y_4p_{10} + Y_4p_{11} - Y_2p_{14} = 0 \qquad (63)$$

$$2Y_5p_1 + 2Y_5p_3 - 2Y_2p_5 + (Y_5 - Y_2)p_7 + Y_5p_{10} + Y_5p_{11} - Y_2p_{13} = 0 \qquad (64)$$

where

$Y_1 = 2(A_3 + 0.209A_5)$

$Y_2 = 2(A_1 + A_2X)$

$Y_3 = 1.584A_5$

$Y_4 = A_2X$

$Y_5 = 2A_4$

The remaining 10 equations required for a solution are the dissociation equations. Tables of equilibrium coefficients are available (23) in terms of partial pressures rather than concentrations of the products of reaction. The appropriate equations are given below

$2H + O \rightarrow H_2O$ such that $p_1 - K_1p_{11}^2p_{15} = 0$ (65)

$C + 2O \rightarrow CO_2$ such that $p_2 - K_2p_{14}p_{15}^2 = 0$ (66)

$2H \rightarrow H_2$ such that $p_3 - K_3p_{11}^2 = 0$ (67)

$2N \rightarrow N_2$ such that $p_4 - K_4p_{12}^2 = 0$ (68)

$$2F \rightarrow F_2 \qquad \text{such that } p_5 - K_5 p_{13}^2 = 0 \tag{69}$$

$$2O \rightarrow O_2 \qquad \text{such that } p_6 - K_6 p_{15}^2 = 0 \tag{70}$$

$$H + F \rightarrow HF \qquad \text{such that } p_7 - K_7 p_{11} p_{13} = 0 \tag{71}$$

$$C + O \rightarrow CO \qquad \text{such that } p_8 - K_8 p_{14} p_{15} = 0 \tag{72}$$

$$N + O \rightarrow NO \qquad \text{such that } p_9 - K_9 p_{12} p_{15} = 0 \tag{73}$$

$$O + H \rightarrow OH \qquad \text{such that } p_{10} - K_{10} p_{11} p_{15} = 0 \tag{74}$$

The equilibrium coefficients K_i vary systematically with the temperature of the reaction. It is assumed that the products of reaction calculated at a particular temperature and pressure, are formed instantaneously. Hence, one need only solve the above 15 equations for given values of P, T, and the amounts of reactants, to arrive at the equilibrium composition.

Solution of These Equations

Since the dissociation equations are non-linear, there exists no direct solution. The Newton-Raphson method is used to obtain a "trial and error" solution.

(1) Initially, estimates of $p_i (i = 1, \ldots 15)$ are taken and each of the 15 equations is expanded in a Taylor's series about the estimated point, p_i .

(2) Corrections to p_i are then found (Δp_i) and the new estimates of p_i , given by $p_i + \Delta p_i$, are used in place of the initial estimates in (1).

(3) The procedure is repeated until Δp_i becomes negligible.

Consider a solution to two non-linear equations; $f(x,y) = 0$, $g(x,y) = 0$.

Let the initial estimate of the required solution (x,y) by the point (x_1,y_1). Expanding f, g in a Taylor's series about the point (x_1,y_1), then

$$f(x,y) = 0 = f(x_1,y_1) + \frac{\partial f}{\partial x}(x_1,y_1) + \frac{\partial f}{\partial y}(x_1,y_1) \cdot (y - y_1) + \ldots. \quad (75)$$

$$g(x,y) = 0 = g(x_1,y_1) + \frac{\partial g}{\partial x}(x_1,y_1) \cdot (x-x_1) + \frac{\partial g}{\partial y}(x_1,y_1) \cdot (y-y_1) + \ldots. \quad (76)$$

or

$$\Delta f = \frac{\partial f}{\partial x} \cdot x + \frac{\partial f}{\partial y} \cdot y + \ldots \quad (77)$$

$$\Delta g = \frac{\partial g}{\partial x} \cdot x + \frac{\partial g}{\partial y} \cdot y + \ldots \quad (78)$$

where

$$\Delta f = f(x,y) - f(x_1,y_1) = -f(x_1,y_1) \quad (79)$$

$$\Delta g = g(x,y) - f(x_1,y_1) = -g(x_1,y_1) \quad (80)$$

and

$$\Delta x = x - x_1 \quad (81)$$

$$\Delta y = y - y_1 \quad (82)$$

Hence the non-linear equations have been transformed into linear correction equations of the form

$$f(x_1,y_1) + f_x \cdot \Delta x + f_y \cdot \Delta y = 0 \qquad (83)$$

$$g(x_1,y_1) + g_x \cdot \Delta x + g_y \cdot \Delta y = 0 \qquad (84)$$

where $f_x = \frac{\partial f}{\partial x}$, $f_y = \frac{\partial f}{\partial y}$, etc., and the derivatives of second order and higher have been neglected.

The equations are solved for Δx, Δy and new estimates are given by $x_1 + \Delta x$, $y_1 + \Delta y$. The procedure is repeated until the desired accuracy is obtained.

The full procedure can best be demonstrated with an example.

Example

Consider a solution to

$$f(x,y) = x^2y + y^2 + 3 = 0$$

$$g(x,y) = x^3 + 2xy^2 + 4y = 0$$

then

$$f_x = 2xy$$

$$f_y = x^2 + 2y$$

$$g_x = 3x^2 - 2y^2$$

$$g_y = -4xy + 4 = 4(1 - xy)$$

Let $x_1 = 1$, $y_1 = -1$, be the initial estimates.

Then substituting into the linear correction equations

$$3 - 2\Delta x - \Delta y = 0$$

$$-5 + \Delta x - 8\Delta y = 0$$

the solution to the above equations is

$$x = 38/30 \cong 1.3$$

$$y = 7/15 \cong 0.5$$

The new estimates of x, y are given by x_2, y_2 where

$$x_2 = x_1 + \Delta x = 2.3$$

$$y_2 = y_1 + \Delta y = -0.5$$

Substituting into the linear correction equations, then

$$0.6 - 2.5\,\Delta x + 4.3\,\Delta y = 0$$

$$9 + 15.4\,\Delta x + 10\,\Delta y = 0$$

The solution to the above equations is

$$\Delta x \cong -0.4$$

$$\Delta y \cong -0.3$$

The new estimates for x, y become

$$x_2 + \Delta x = 1.9$$

$$y_2 + \Delta y = -0.8 \qquad \text{etc.}$$

The correct solution is (2, -1).

For more than 2 unknowns, the linear correction equations take

the form

$$f(x,y,z,\ldots) + f_x \cdot \Delta x + f_y \cdot \Delta y + f_z \cdot \Delta z + \ldots = 0 \qquad (85a)$$

$$g(x,y,z,\ldots) + g_x \cdot \Delta x + g_y \cdot \Delta y + g_z \cdot \Delta z + \ldots = 0 \qquad (85b)$$

$$h(x,y,z,\ldots) + h_x \cdot \Delta x + h_y \cdot \Delta y + h_z \cdot \Delta z + \ldots = 0 \qquad (85c)$$

$$i(x,y,z,\ldots) + \ldots = 0 \qquad (85d)$$

$$j(x,y,z,\ldots) + \ldots = 0 \qquad (85e)$$

etc.

where the subscripted variable, f_x for example, represents the partial derivative of $f(x,y,z,\ldots)$ with respect to x.

Denoting equations (60) to (74) by B_i ($i = 1, \ldots, 15$); the correction equations are given by

$$B_1 + A_{1,1} \cdot \Delta p_1 + A_{1,2} \cdot \Delta p_2 + \ldots + A_{1,15} \cdot \Delta p_{15} = 0$$

$$\ldots\ldots\ldots\ldots\ldots\ldots\ldots$$

$$\ldots\ldots\ldots\ldots\ldots\ldots\ldots$$

$$B_{15} + A_{15,1} \cdot \Delta p_1 + A_{15,2} \cdot \Delta p_2 + \ldots + A_{15,15} \cdot \Delta p_{15} = 0 \qquad (86)$$

where $A_{i,j}$ is the partial derivative of B_i with respect to p_j. For example, $A_{7,14}$ is the partial derivative of equation (7), i.e. B_7, with respect to p_{14}. The equations are solved for Δp_i ($i = 1$ to 15) by first assuming initial estimates of p_i. Subsequent estimates of p_i are given by $p_i + \Delta p_i$ and the procedure is repeated until Δp_i approaches zero.

The coefficients of the correction equations ($A_{i,j}$) are denoted by matrix A and the constants B_i are denoted by the vector, -B. Hence, in matrix notation, the set of linear correction equations is given by

$$B = A \cdot \Delta p \tag{87}$$

and its solution is given by

$$\Delta p = A^{-1}B \tag{88}$$

where A^{-1} is the inverse matrix.

Outline for the Fortran IV Computer Program

The program is presently designed to handle nine sets of values of pressure, temperature and volume for a given propellant mixture. That is, equilibrium coefficients are incorporated into the program for values of temperature between 3000 K and 1400 K in 200 degree increments.

Input Data

The following information is required:

(a) Weights of reactants, i.e., the total amount of fuel and oxidizer available.

(b) Yield

(c) Temperature of reaction

(d) Pressure at which reaction occurs

(e) Volume of products of reaction

Assumptions

The following assumptions are implied:

(a) Constant pressure process

(b) Instantaneous reaction time

(c) No air entrainment until all of the available propellants are used up.

Procedure

For each data point (i.e. for a given value of P, T, and V) the program determines the partial pressures of the products of reaction such that the theoretical volume of the product gases is identical to the given input volume.

For the first data point, however, since no value of volume is available, the yield is used to determine the initial amounts of propellant burned and the partial pressures are then determined.

For subsequent data points, the fuel burning rate is continually adjusted and partial pressures are calculated in turn so that finally the resultant theoretical volume becomes identical to the given (theoretically determined or experimentally evaluated) volume.

This latter procedure is repeated for subsequent data points until all of the available fuel is used up. From then on, air is added as a reactant combined with all of the available fuel in order to satisfy the "identical volume" condition.

The program also converts the resultant partial pressures into the following:

1. Pound Moles

2. Pressure-Ratios, Mole-Ratios, Volume-Ratios

3. Pound Weights

4. Weight-Ratios

The fuel burning rate, the amount of entrained air, and the theoretical volume for each data point are also determined.

Subroutine Invert

The subroutine solves the set of linear equations

$$\Delta p = A^{-1}B \tag{89}$$

The input data card is

CALL INVERT (A, NA, NAD, B, NB, NBD, DETERM, IERROR)

where

A = matrix of order NA

B = vector having NB = 1 constant vector

NAD = row dimension of A in main program

NBD = row dimension of B in main program

DETERM = dummy

IERROR = dummy

The output consists of A^{-1} placed in A, p placed in B, and the determinant of A placed in DETERM. IERROR is an error signal equal to 0 for successful inversion; equal to -1 for overflow, equal to +1 if no inverse is obtainable.

The maximum size of A can be 100 x 100.

Symbols Used in Main Program

Subscripted Variables

A - coefficients appearing in the correction equations

B - constant appearing in the correction equations

C - equilibrium constants

P - partial pressure

PR - partial pressure-ratio, mole-ratio, volume-ratio

PT - total pressure

T - temperature

TNT - partial moles

V - volume

WMOL - molecular weight

WT - partial weight

WTR - partial weight-ratio

Floating Point Variables

F^2 - weight of liquid fluorine available

H^2 - weight of liquid hydrogen available

O^2 - weight of liquid oxygen available

RP1 - weight of liquid RP-1 available

RNAIR - mole-ratio of entrained air

RWAIR - weight-ratio of entrained air

TN - total theoretical moles of products of reaction

TNE - total experimental moles of products of reaction

TVOL - total theoretical volume of products of reaction

WAIR - weight of entrained air

X - number of carbon atoms in the RP-1 molecule, C_xH_{2x}

YIELD - percentage of fuel burned at time "zero"

The fixed point variable, MA, is the number of experimental runs with combinations of LH_2, RP-1, LO_2 and LF_2.

The Fortran IV program follows with an example of the output data for one of the nine data points using LH_2/RP-1/LO_2/LF_2 and entrained air.

Input Information

Many different quantities could have been chosen for the input information based upon which the desired fireball composition and atmospheric chemistry could be calculated.

For this investigation the

Volume-time history

Pressure-time history

Temperature-time history

were taken as the principal input information.

The reason for this choice was that another phase of this over-all program deals with the theoretical determination of these functions and most of all that it is possible to measure the above quantities and thus verify any theoretical results by actual field experimentation. This latter fact seems to be of extreme importance if theories are developed since without experimental verification they are of little use and certainly not much credence can be given to them.

Other factors such as fuel burning rates, etc. were selected by others[20,21] but the investigators of this project do not see how such quantities could be verified experimentally and therefore would remain assumptions throughout the work.

As mentioned above, much work is being done on the determination of the volume-time, pressure-time, and temperature-time histories of the explosion phenomena from a theoretical point of view. Rather than wait for the results from this separate investigation and because of contract commitments it was decided to present the methods of obtaining the fireball and combustion cloud composition from such input data as mentioned above and for the present combine both theory and experimental information to obtain the most plausible functions at this time.

A brief description of how the volume-time, pressure-time, and temperature-time functions have been determined for this report follows:

Volume-Time History of Fireball and Combustion Products Cloud from Liquid Propellant Explosions

The volume of combustion products produced by liquid propellant explosions transgresses a number of stages with time, changing in shape from one typical configuration into another. These stages can be observed in the high speed film records of such explosions and can be, in part at least, analyzed mathematically or theoretically. These major stages are:

1. Hemisphere

2. Truncated Sphere

3. Sphere

4. Pinched Sphere

5. Toroid

The above 5 stages are distinct and can be observed in at least the larger explosions.

Stage 1. Hemisphere

This stage is the earliest one which can be observed and is of relatively short duration. It involves a very rapid growth of the combustion products both along the ground and up into the atmosphere so that the shape can best be approximated by a hemisphere. The size of this initial hemisphere depends upon the yield of the liquid propellant explosion, the very rapid combination of the fuel and oxidizer so as to form detonation and shock waves. The larger the yield the larger the initial hemispherical fireball.

Stage 2. Truncated Sphere

Following the very rapid formation of the hemispherical fireball from liquid propellant explosions the hot combustion products begin to rise. This upward motion and the convection currents due to the bouyant forces undercut the rising mass thus forming a truncated sphere, in contact with the ground at the flat base.

As the center of the mass rises the fireball changes more and more from the original hemisphere into a sphere, the shape which is attained when the combustion products become essentially tangent to the ground.

This stage in the development is referred to as "Lift Off", at which most of the fuel seems to have been consumed[20,21].

Stage 3. Sphere

Having attained essentially a spherical configuration at "Lift Off" the combustion products continue to rise as a rather turbulent, well mixing sphere which however gradually changes shape from the almost perfect sphere into the first slightly pinched and then rather pronounced pinched sphere.

Stage 4. Pinched Sphere

The change from the spherical configuration to the pinched sphere is rather gradual and then as the indentations become larger and larger, the appearance of the sphere is lost. A cross-section by a vertical plane through the center would give the appearance of a "Bar Bell".

As this process continues the indentations will eventually touch, forming a toroid.

Stage 5. Toroid

From the time the toroid is formed the initial contact point of the indentation becomes a hole with the general configuration of a ring or doughnut.

As this toroid grows in diameter the size of the hole increases but the volume now at this stage of development increases relatively slowly.

Finally this well defined configuration diffuses into the

Figure 21 Typical Development Configuration Stages of Liquid Propellant Explosions

Stage 1-. Hemisphere

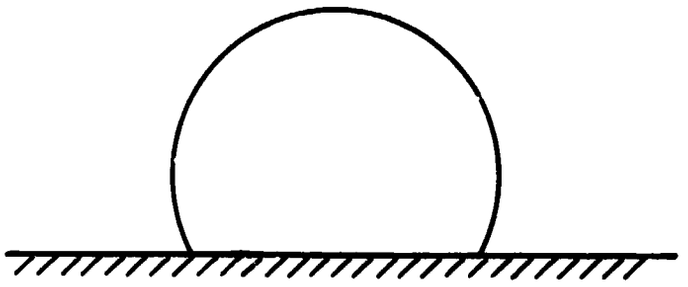

Stage 2-. Truncated Sphere

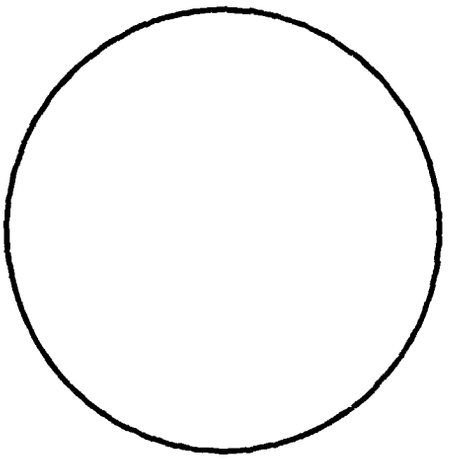

Stage 3-. Sphere

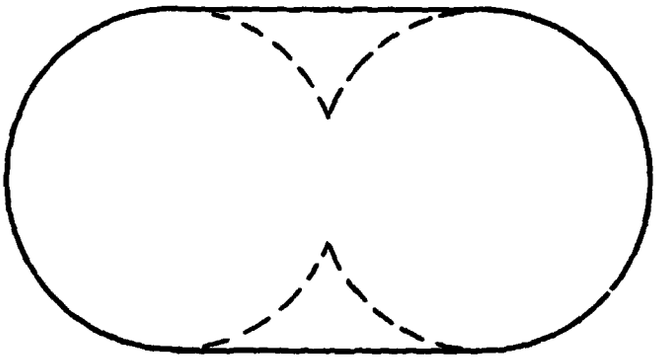

Stage 4-. Pinched Sphere

Stage 5-. Toroid

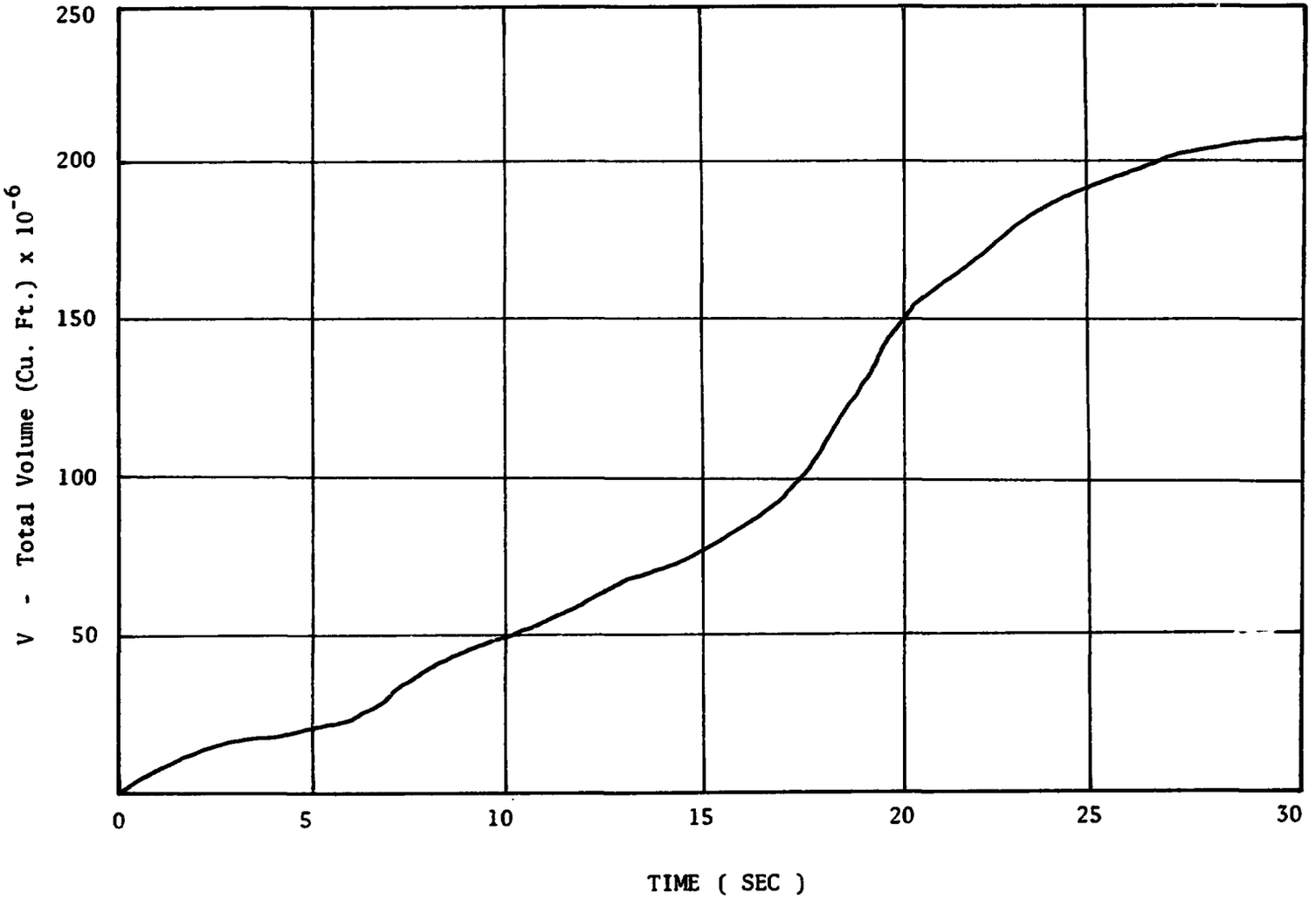

Figure 22 TYPICAL VOLUME-TIME FUNCTION FOR LIQUID PROPELLANT EXPLOSION PRODUCTS (Yield = 4.5 Percent)

atmosphere losing its resemblance to any characteristic shape and being controlled to a great extent by the prevailing atomspheric conditions.

Each of these stages as described above and schematically shown in Figure 21, takes a longer and larger part on the time scale. Stage 1 may occur in fractions of a second while the last stage will be a matter of minutes.

Utilizing this 5 stage concept for the purpose of analysis a volume versus time curve can be obtained, either theoretically by the use of restricting assumptions or by the actual analysis of high speed film records of liquid propellant explosions.

The variation is greatest in Stage 1 which is controlled by the yield while the statistical differences are rather small (but somewhat dependent upon atmospheric conditions) as long as the same quantities of propellants are involved and it is assumed that essentially all the propellants take part in the formation of the fireball and cloud[20,21].

Figure 22 shows the volume versus time curve for the S-IV PYRO experiment. The yield as reported was about 4 1/2% which is in agreement with the predictions of reference (1).

Similar volume versus time curves have been developed for the various fuel oxidizer combinations considered and reported upon here.

Pressure-Time History of Fireball and Combustion Products Cloud from Liquid Propellant Explosions

The pressure-time history as presented here and as used as input

data for the determination of the composition of both the fireball and the combustion products cloud was determined partially from preliminary theoretical considerations[16] and partially from the analysis of field data obtained by the liquid propellant explosion program of project PYRO[22].

The theoretical analysis was necessary for the early time processes since no experimental data is available and the results were then checked and agreed with experimental re , in the later stages.

In general it might be said that the pressure immediately after ignition rises very rapidly to very high values inside the missile due to the confinement of the propellants and the tanks, reaching a maximum somewhere as the reaction front progresses toward the boundary of the missile configuration. After this maximum is reached the pressure falls very rapidly to almost atmospheric conditions.

From the time of "lift-Off" of the fireball which occurs at essentially atmospheric pressure[24] the pressure drops very slowly due to the rise of the explosion products and the effect on atmospheric pressure due to altitude.

The pressure-time history presented here for approximately 100,000 lbs. of propellants was used for all the propellants reported upon here.

Analysis of the sparse experimental information of liquid propellant explosion experiments seems to support this general pressure-time history. The yield produced by the explosion will change the

early values of the pressure. Again for the analysis here a yield of 4 1/2% was taken based upon the most likely value as given in reference (2).

The actual curve used here is presented in Figure 2 . If better information is to be used, an experimental program could be instituted to actually measure these pressures, an important reason for this choice of input information is because it allows theoretical determination and experimental verification.

Temperature-Time History of Fireball and Combustion Products Cloud from Liquid Propellant Explosions

The third and last principal input information needed for the determination of the composition of the fireball and combustion products cloud including air entrainment and atmospheric interaction is the temperature-time relationship.

Again theoretical considerations and the available rough experimental observations of fireball temperature and variations with time indicate that the intial temperature is close to the maximum obtainable by the particular propellants involved. Then, at low yields at least, since only a small part of the propellants take part in the initial stages of the fireball formation the reaction of the remaining fuel and oxidizer, both in the propellants as well as the atmosphere, make the temperature drop with temperature in an almost linear manner. This is observed in theoretical work[20,21] and seems to be closely approximated by the available experimental information[22].

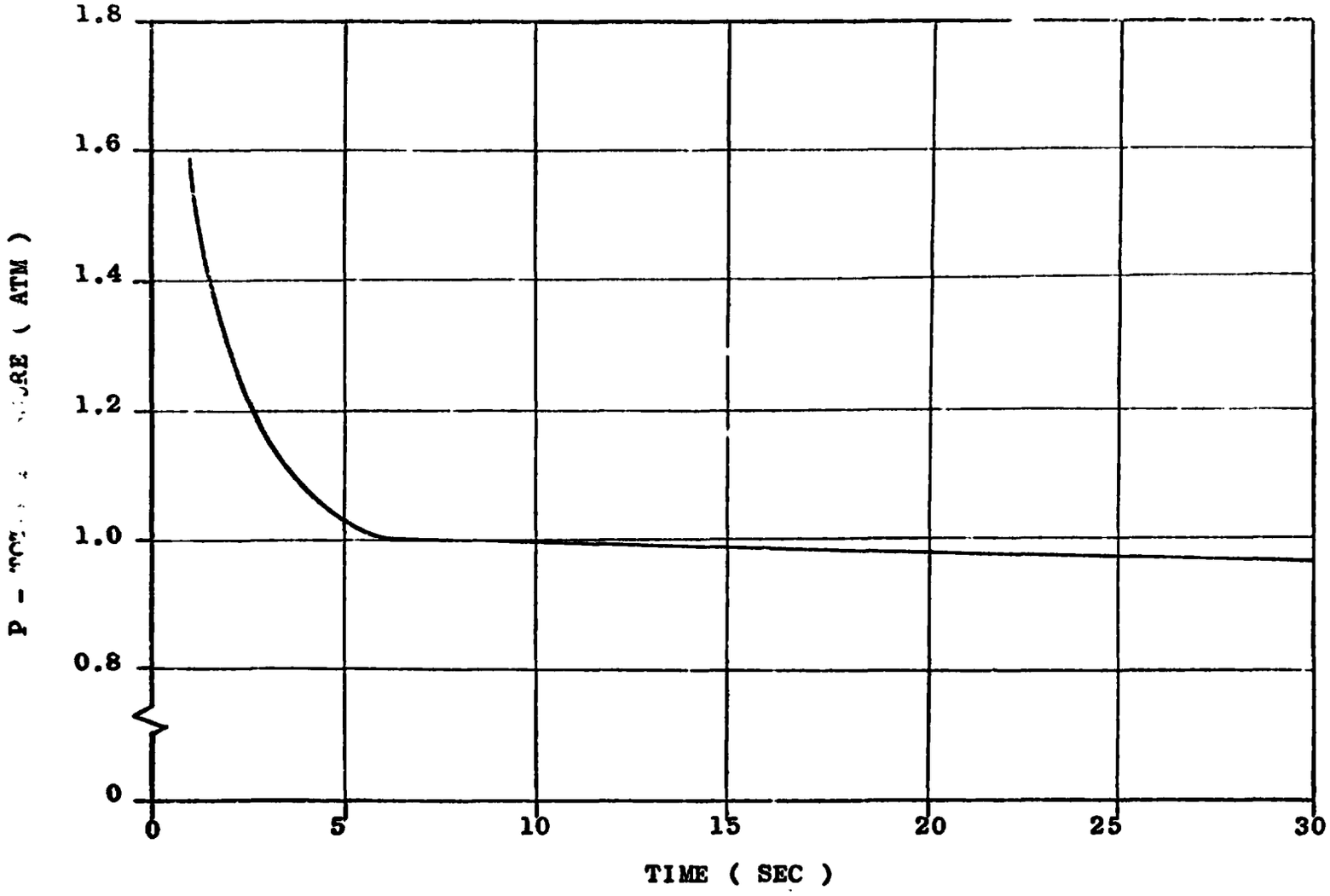

FIGURE 23 - TYPICAL PRESSURE-TIME FUNCTION FOR LIQUID PROPELLANT EXPLOSION PRODUCTS (YIELD = 4.5 PERCENT)

This linear decrease of the temperature with time continues until the incandescence of the fireball ends often referred to as the "duration" which can be approximated as shown in[24].

For the purpose of analysis here it was assumed that the actual variation can be closely approximated by further linear decreases changing the slope to a value 1/2 the previous one for each subsequent "duration" time interval.

By this method a curve representing the temperature-time history of the liquid propellant explosion is obtained which from both theoretical and the available sparse experimental observations seems to approximate the actual conditions. This again is taken here for low yield (4 1/2% in this case) liquid propellant explosions.

Again it is believed that an experimental program can be designed, if desired, to obtain this temperature-time history for various cases and verify or modify the presently used information, which is presented in Figure 2 4 and again was used for all the fuel-oxidizer combinations analyzed and reported upon here.

It should be mentioned again that the volume-time, pressure-time, and temperature-time histories were selected as the principal input data because it is felt by these investigators that this information which can be generated with appropriate assumptions theoretically, can be verified experimentally. In addition these volume-time, pressure-time, and temperature-time histories are of great interest to other investigators for various reasons. A number of groups are presently engaged in trying to measure pressures and temperatures within fireballs and of combustion products clouds produced by liquid propellant explosions.

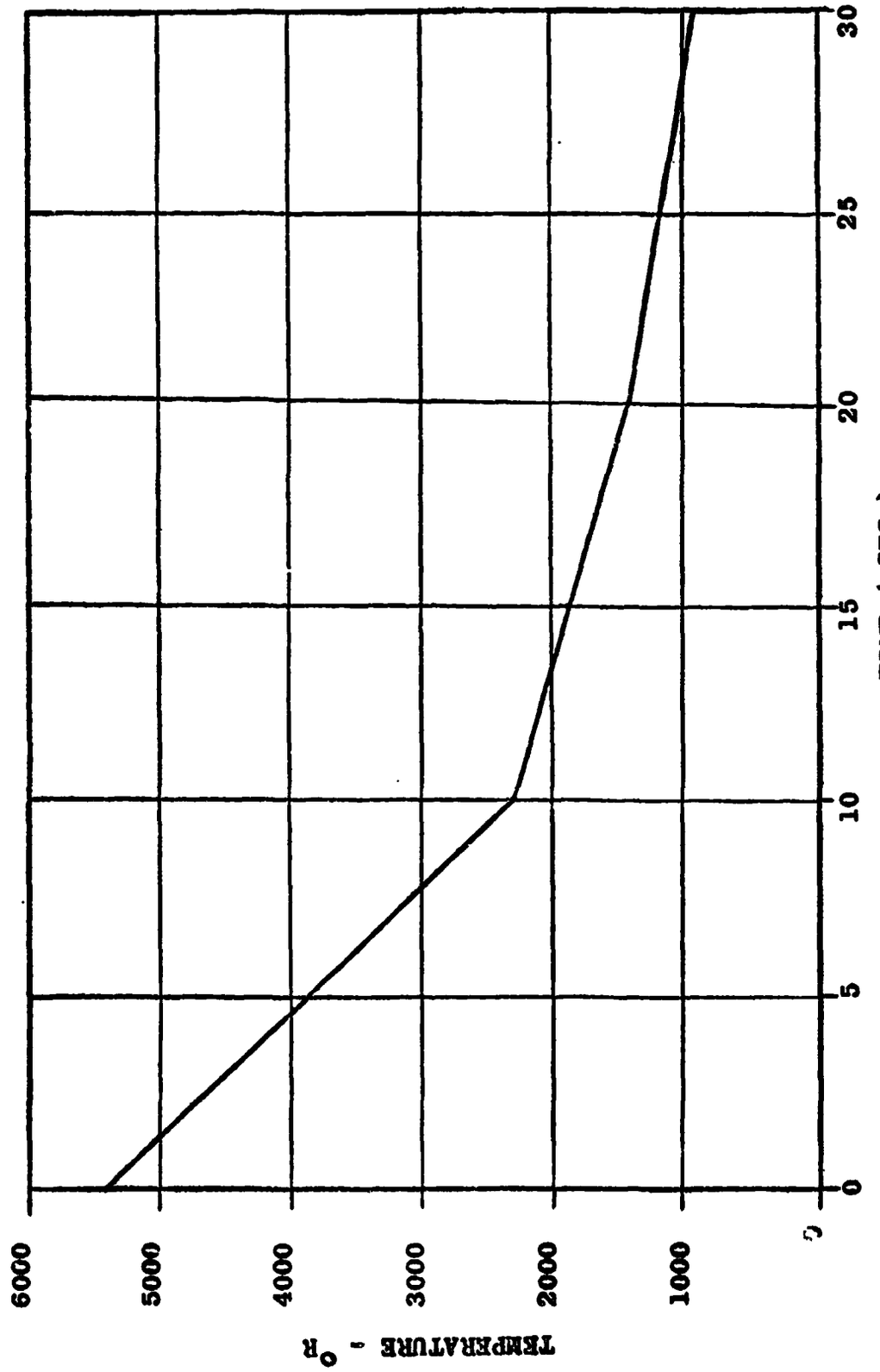

FIGURE 24 . TYPICAL TEMPERATURE-TIME FUNCTION FOR LIQUID PROPELLANT EXPLOSION PRODUCTS (YIELD = 4.5 PERCENT)

It should also again be emphasized that in this investigation homogeneity of the fireball as well as of the combustion products cloud was assumed. These assumptions seem to be reasonably well satisfied because of the tremendous turbulence observed within the fireball which tends to produce thorough mixing with a relatively short time.

In addition to the principal input information, the volume-time, pressure-time, and temperature-time functions it is necessary to know

4. The Type of Propellants
5. Propellant Composition
6. Propellant Quantities
7. Yield

4, 5, and 6 are easily obtainable as original data, while 7 is selected to obtain the results for this particular value of yield, a value which may again be dictated by theoretical considerations.

Type of Propellants

The type of propellants selected for this presentation are combinations of fuel and oxidizers which are presently used in liquid propelled rocket systems or combinations which may become important in the future development of these rockets.

The method however used is perfectly general and any propellant type and combinations could be analyzed in the same manner.

The types selected for this presentation are: Ref. 75

LH_2/LO_2

RP-1/LO_2

LH_2/LF_2

RP-1/LF_2

LH_2/RP-1/LO_2

LH_2/LO_2 + 1% F
+ 5% F
+ 10% F

RP-1/LO_2 + 1% F
+ 5% F
+ 10% F

LH_2/RP-1/LO_2 + 1% F
+ 5% F
+ 10% F

Propellant Composition

The propellant type was outlined above with the composition of fuel to oxidizer chosen as follows:

LH_2/LO_2	1 : 5	by weight
RP-1/LO_2	1 : 2.25	by weight
LH_2/LF_2		
RP-1/LF_2		
LH_2/RP-1/LO_2	1 : 2.6 : 5.86	by weight

In the combinations with Fluorine traces the weight ratios of the main constituents were the same as given above.

The chemical composition of the RP-1 was taken as $C_{11.6}H_{23.2}$ which was obtained from reference (25).

Propellant Quantities

The propellant quantities were taken as 100,000 lbs. in all cases. This allowed the standardization of the pressure-time and temperature-time histories for the present analysis, since it seems that the quantity of propellants used has the major effect on the time axis of pressure and temperature.

Yield

The yield, the energy release as a fraction of the theoretical maximum, for these calculations and analyses was taken as 4 1/2% which from previous theoretical investigations[2] and from experimental observations[2,22] seems to come close to the statistically probable value.

Again it might be mentioned that other values could be taken just as well without changing the method of analysis. The resulting compositions of the fireball and explosion products cloud would, however, be different.

With the input information as described above a number of cases were analyzed and many quantities calculated. Rather elaborate computer programs were developed for this purpose and the main program will be presented in the appendix.

The results which seem to be most pertinent to this investigation are presented in the reference 75 , mostly in graphical form.

Results Obtainable

Utilizing the data information as discussed above and the calculation and analyzing procedures outlined earlier, many important qunatities can be calculated.

Because of the space limitations only one set of the more complicated combinations will be presented here. Many more have been worked out in connection with this work and have been reported by Dr. Farber and his group in the references[75].

As mentioned in earlier work the same pressure-time, and temperature-time history was used for all the propellant combinations but individual volume-time histories had to be worked out for each different propellant combination.

Through a rather large iterative computer program such quantities as partial moles, partial pressures, partial volumes, partial weights, volume of air entrained, weight or air entrained, unburned fuel present, etc., were calculated.

Some of these quantities were then normalized and one set is presented here graphically as a function of time. They are

a.	Fuel and oxidizer consumption wgt.	(normalized)	Fig. 25
b.	Volume of entrained air	"	Fig. 26
c.	Partial Pressures	"	Fig. 27
d.	Total Volumes		Fig. 28
e.	Partial Weights	"	Fig. 29

These results and the manner of presentation, it is believed give a good picture of the composition and its time variation of the fireball and combustion products cloud.

It is believed that the graphs are self-explanatory and the results can easily be compared when different fuel-oxidizer combinations are used.

The Fluorine tracer quantities added seem to have a hypergolic effect upon the cryogenic propellants to render the predictions of the most probable ignition times and delay times, and thus the yield, more certain.

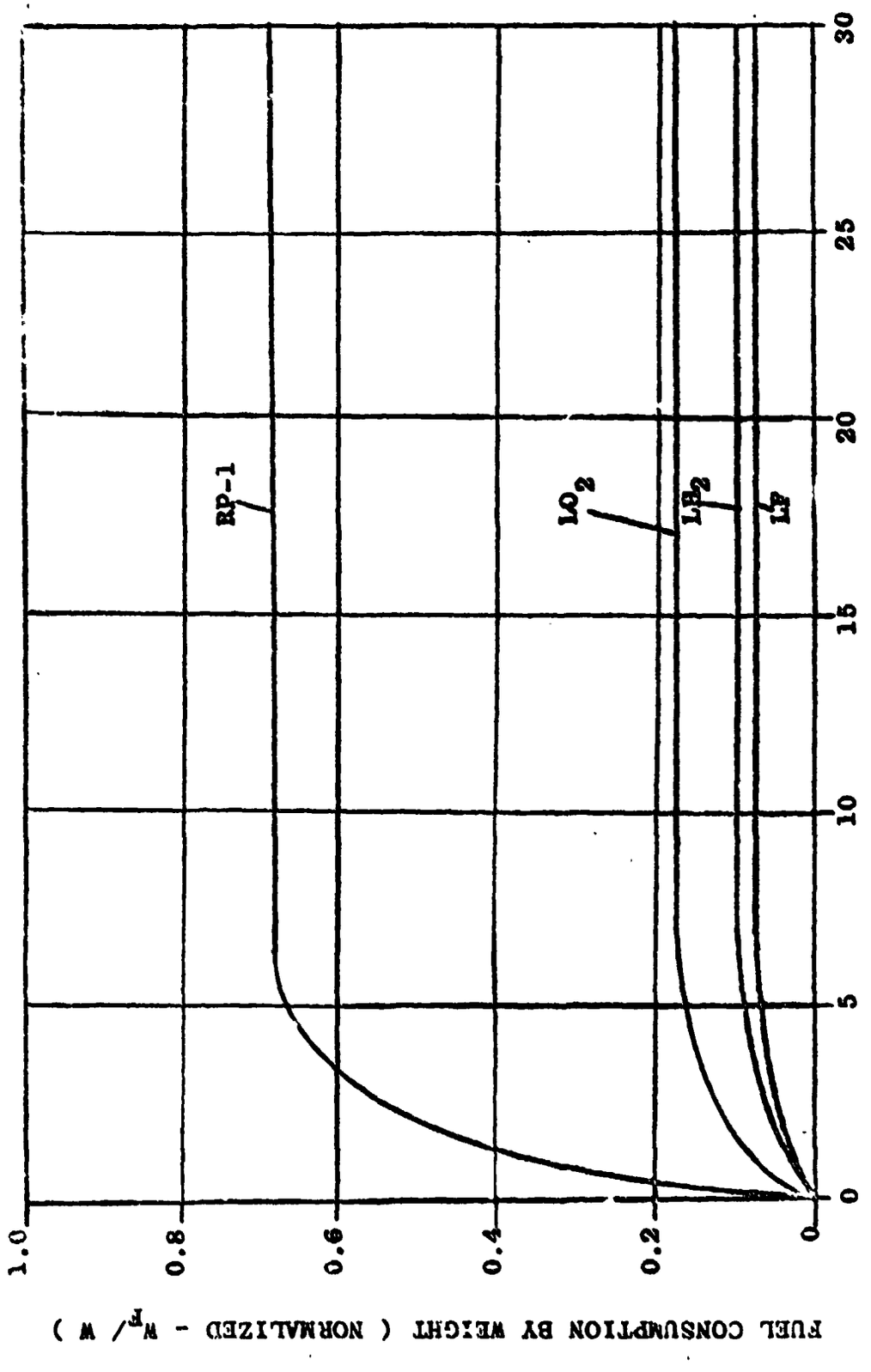

FIGURE 25 . FUEL CONSUMPTION FOR LB_2/RP-1/LO_2 + 10% F LIQUID PROPELLANT EXPLOSION (YIELD = 4.5 PERCENT)

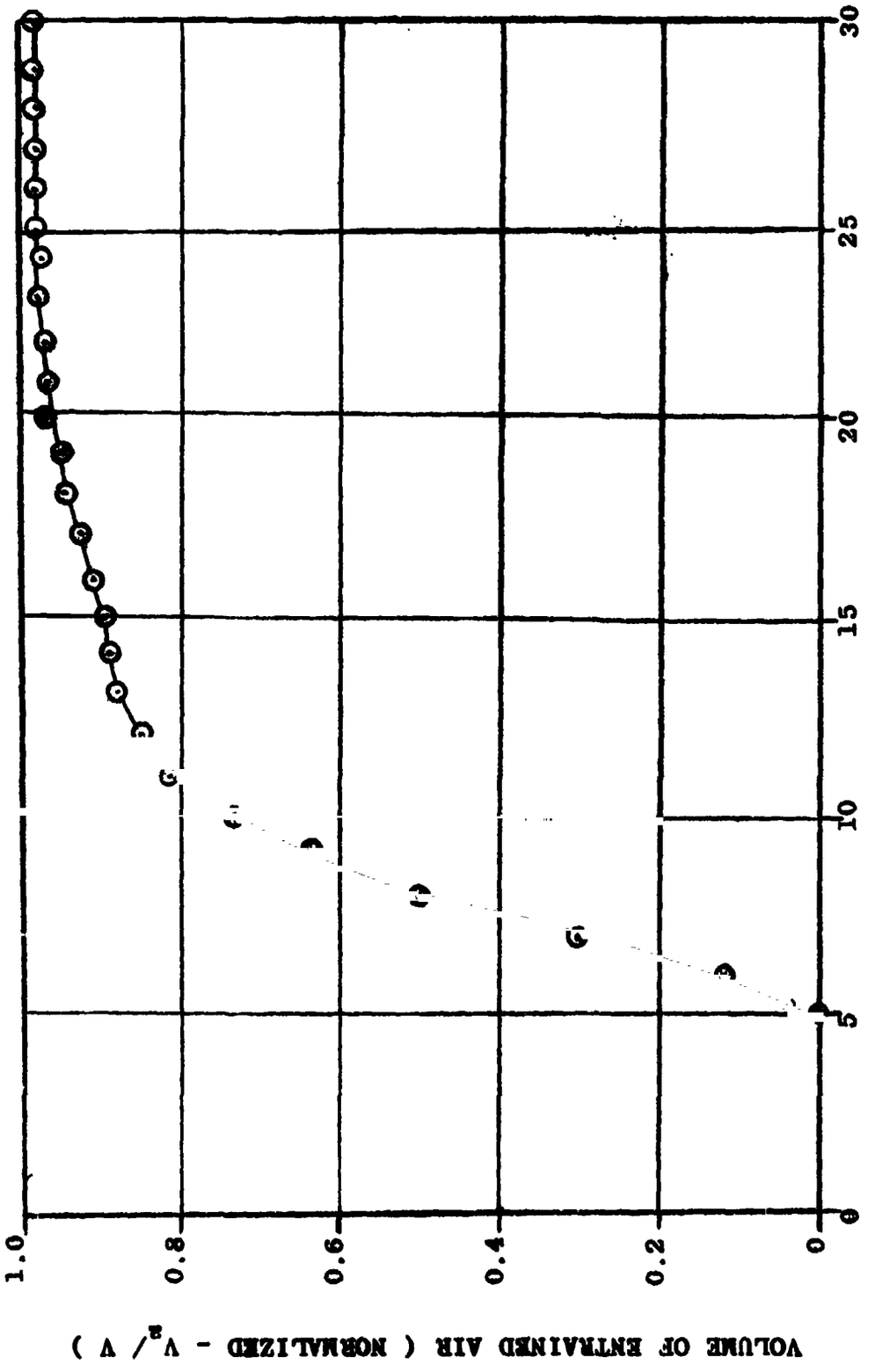

FIGURE 26 . VOLUME OF ENTRAINED AIR FOR LF_2/RP-1/LO_2 + 10% F LIQUID PROPELLANT EXPLOSION (YIELD = 4.5 PERCENT)

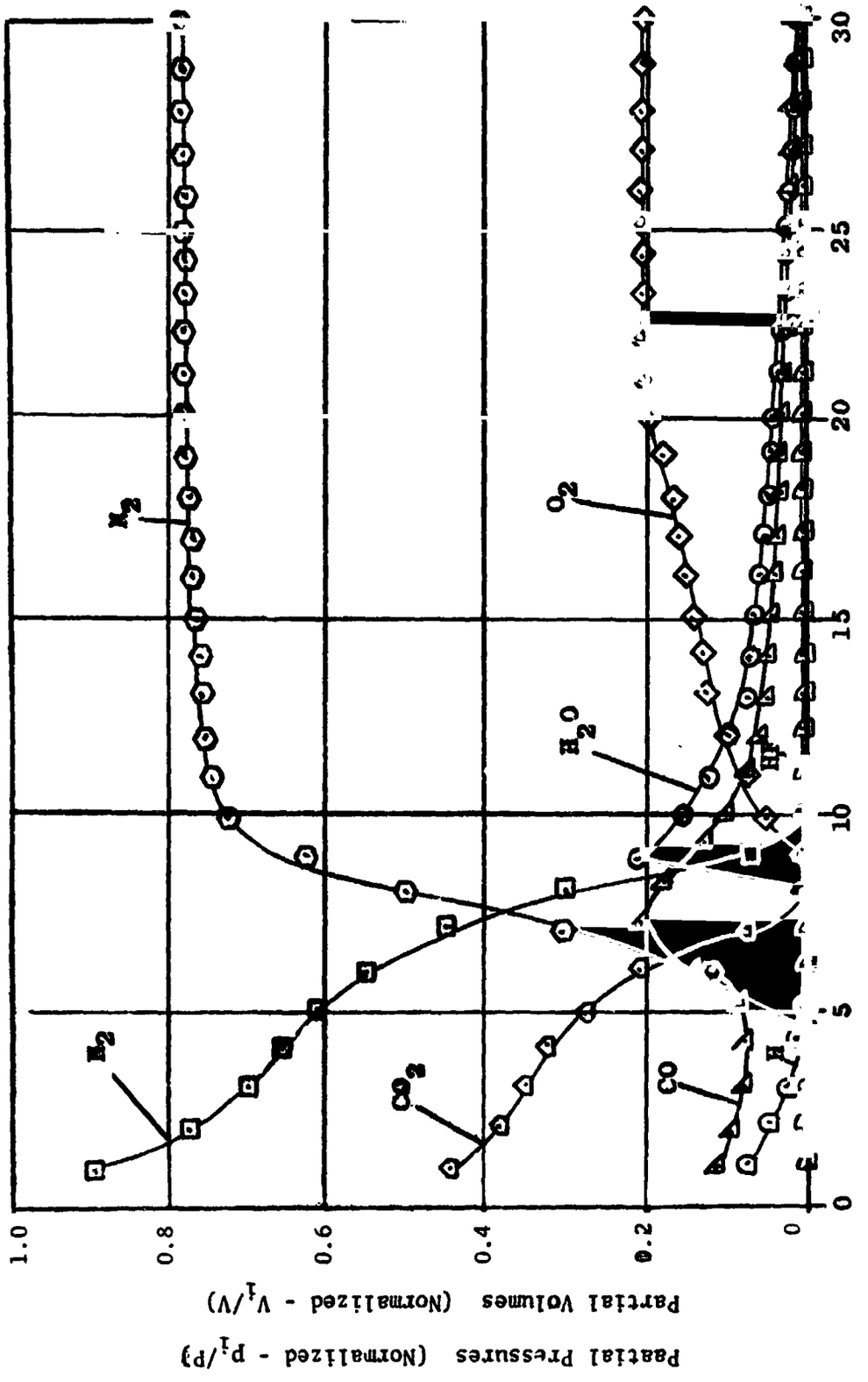

FIGURE 27 - PARTIAL PRESSURES AND PARTIAL VOLUMES FOR $LH_2/RP\text{-}1/LO_2$ + 10%F LIQUID PROPELLANT EXPLOSION PRODUCTS (YIELD = 4.5 PERCENT)

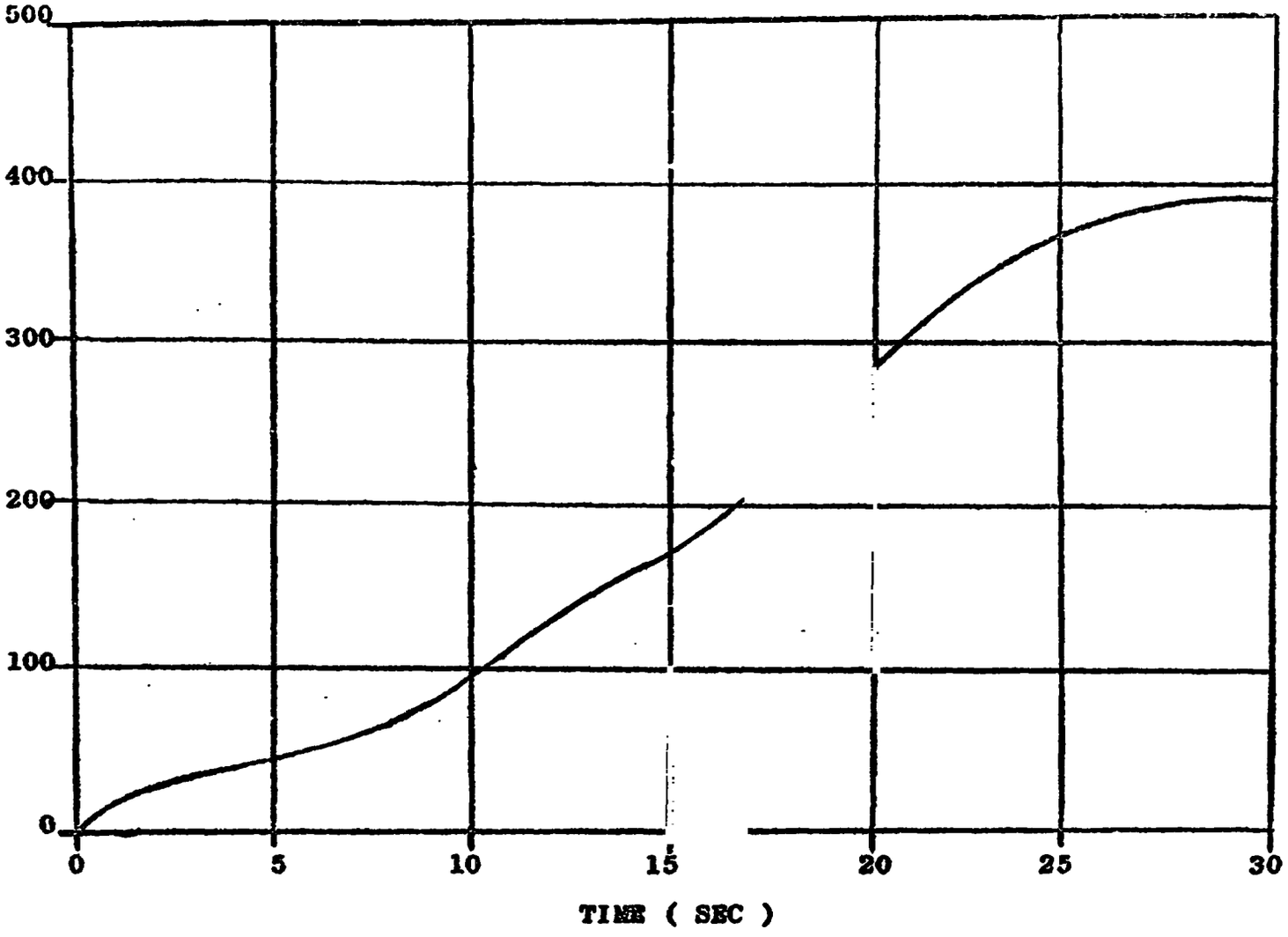

FIGURE 28 . VOLUME-TIME FUNCTION FOR $LH_2/RP\text{-}1/LO_2$ + 10% F LIQUID PROPELLANT EXPLOSION PRODUCTS (YIELD = 4.5 PERCENT)

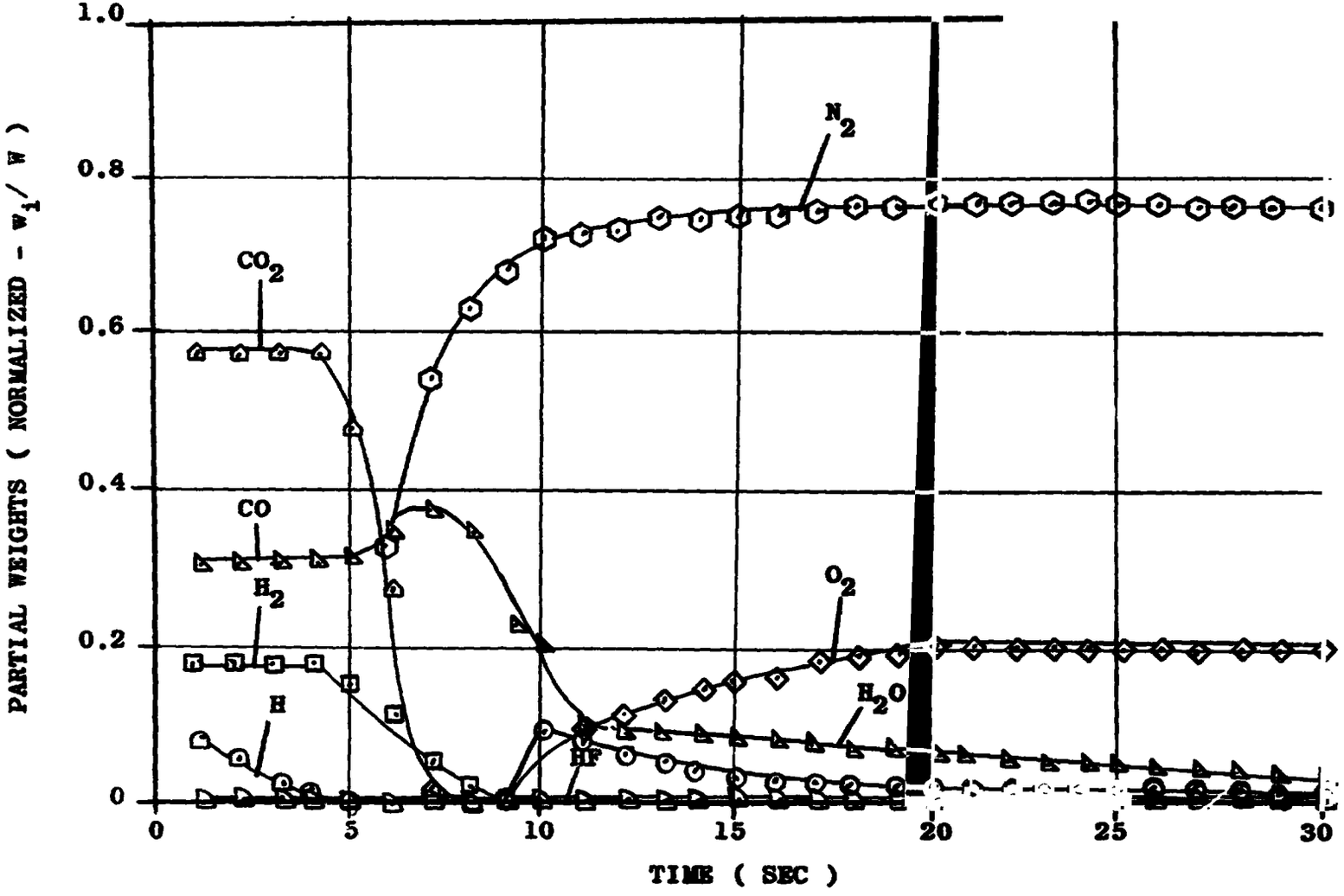

FIGURE 29 . WEIGHT COMPOSITION OF THE COMBUSTION PRODUCTS FROM $LH_2/RP\text{-}1/LO_2$+ 10%F LIQUID PROPELLANT EXPLOSION (YIELD = 4.5 PERCENT)

PART II

EXPERIMENTAL VERIFICATION

In this section the experimental work which was carried out in support and for the purpose of verifying the theoretical work will be discussed. The experiments verified the theoretical predictions of explosive yield and other characteristics of liquid rocket propellants.

All the experiments can be divided into two large classes, laboratory experiments and explosive field experiments.

The laboratory experiments were carried out with inert components to reduce the hazards and only with small quantities of explosive materials so that explosions were not expected.

The laboratory experiments can be further subdivided into Mixing Function development and electrostatic charge generation.

The explosive field experiments were carried out to substantiate the information obtained by theory and then verified in the laboratory. The field experiments were carried out with actual liquid rocket propellants, and substantiated the laboratory data, and in addition provided actual explosion information. They can be grouped as mixing and explosion experiments, electrostatic generation and auto ignition experiments.

The present section will discuss in detail the experimental methods used and the results obtained.

Laboratory Experiments

The first large program carried out in the laboratory was the

development of methods by which the Mixing Function could be determined, either for verification of the theoretical one or as a direct input into the Seven Chart Approach.

Mixing Function Determination (1)

It is always desirable to check any theoretical work with actual experimentation so in this section it will be shown that four methods have been developed which can give the Mixing Function experimentally. The Mixing Function is defined as the proportion or fraction of the propellants mixed at any time τ . This fraction can be expressed in a number of ways as will be seen. It can be defined in terms of contact area or surfaces proportional to this area, in terms of liquid interfaces, of mixing surface profiles, etc.

It will be shown how this was done in various manners by four experimental methods which are independent but complement each other. In many experiments two of these methods were used simultaneously so that the results could be compared for one and the same experiment.

These four methods are:

A. The Film Analysis

B. The Wax Cast Analysis

C. The Vibration Mixing Analysis

D. The Thermocouple Grid Analysis

The film analysis is a method which depends on high-speed photographic coverage of the mixing phenomena, followed by an analysis and proper interpretation of these records.

The Wax Cast Analysis "freezes" the mixing process at different

stages of the mixing so that the solidified image can be analyzed at a later date and at leisure.

The Vibration Mixing Analysis simulates small fluid elements by different density, different color, different shaped particles such as marbles. By shaking them on a vibration table for a certain length of time, and by removing particles periodically, such things as evaporation or spill losses may be simulated.

Thus the mixing phenomena can be studied in small incremental steps, using marbles or particles as fine as powder.

The Thermocouple Grid Analysis, the best and most powerful of the four methods, consists of a three dimensional grid of fine thermocouples, which produces a time record of temperature and its variation at many points in a region in which fluids at different temperatures are being mixed. These readings can be interpreted as will be explained to give insight into the phenomena leading up to and producing the explosive yield.

In the following pages these four methods will be discussed in detail, and some of the results which have been obtained will be presented. These results will give an indication of the value of these study methods in investigating the mixing phenomena of liquid rocket propellants. The results presented here are not intended to simulate a particular missile or missile failure (This will be done in the last two sections of this report) but rather to demonstrate how these methods can be employed in the study of the mixing produced by many different missile configurations and types of failures.

THE METHODS

A. Film Analysis

For the application of this method for analysis, it is necessary to obtain a high-speed pictorial record of the mixing phenomena, involving high-speed photographic equipment. For the present investigation transparent configurations were chosen and then, by placing mirrors at various angles, three-dimensional views were obtained on the same frame of the high-speed recording film. For non-transparent arrangements, X-ray, Gamma-ray, or tracer techniques could be used in a similar manner. Some of the latter techniques have been used by one of the authors in concentration studies and profile interface studies of two- and three-phase mixtures[1,15,49,75,104].

Figure 30 presents an overall view of the experimental apparatus used in the study of the mixing processes between hot or cold oil and water, hot wax and water, LN_2 and kerosene, etc. It consists essentially of a Pyrex glass tube filled to a desired level with one liquid, and another Pyrex tube above filled with the desired amount of the other liquid. A diaphragm between the two glass tubes holds the upper liquid in place. At time zero the diaphragm is pulled out by a quick motion so as to remove it almost instantaneously. Slower removal of the diaphragm according to a programmed input can, if desired, simulate a progressive failure. If a complete diaphragm or bulkhead failure is not desired, a second fixed diaphragm can be inserted in addition to the removable one so that when the latter is removed, a desired size opening at a desired location remains, simulating a particular type of failure.

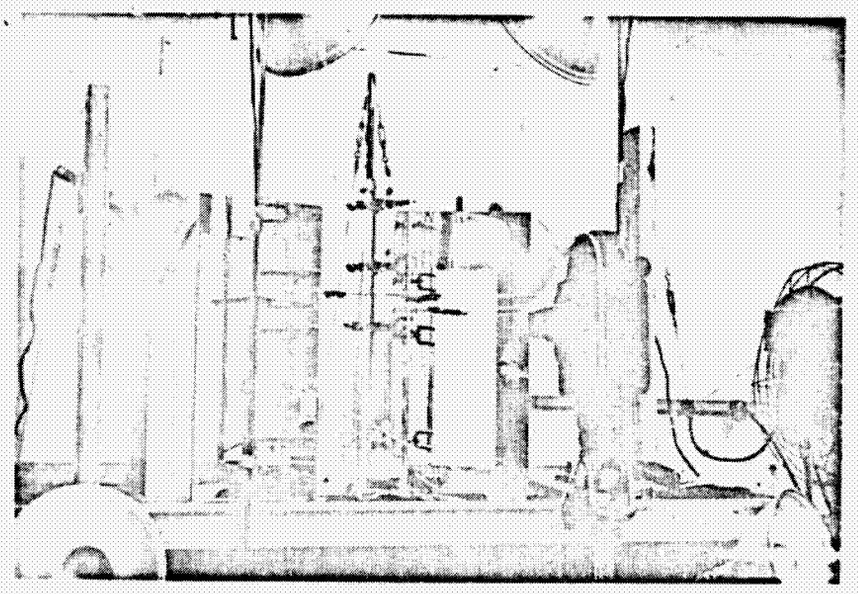

Figure 30 Experimental Arrangement for Film Analysis

Figure 31 shows a number of frames for oil above and water (below) simulating bulkhead failure in a 1 1/2 in. I.D. tube and a ullage space of 4 1/4 in. Successive frames taken at 64 frames per second show the progression of the mixing process from three views, 120 degrees apart.

The analysis can be made directly from the frames as projected on a screen or from a more permanent record by either enlarging them on photographic paper or tracing the outlines of the mixing fronts as shown in Figure 32.

Figure 32 further indicates the reproducibility of the mixing experiments by showing the traces of three identical runs and how close the total profile areas match.

From the three-dimensional views or traces, the total surface areas were determined by first cutting the total volume into thin irregularly shaped discs and then graphically obtaining the peripheral surface of the discs. The resulting outside surface area, or A_o , can then be plotted versus film frame or versus time (see Fig. 33).

Since there are, however, droplets or particles of one liquid (vapor or solid) surrounded by the other within the space circumscribed by the profile, to get the true contact area between the liquids, these additional surfaces must be taken into account. This was accomplished by a tedious method of counting these droplets, determining their size and surface areas, and adding these new areas to the profile areas. The ratio of the total area to the profile or outside area of any particular frame was defined as the "Turbulence Factor" for

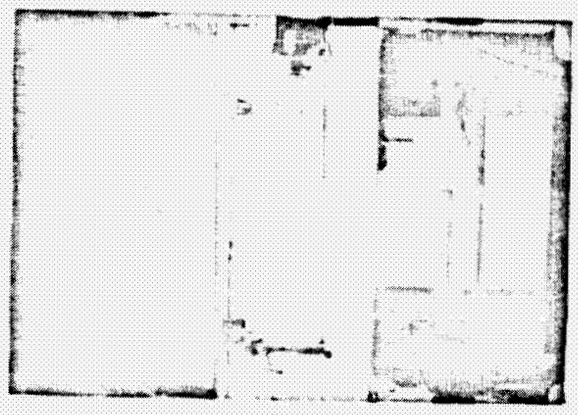

0.015 sec.

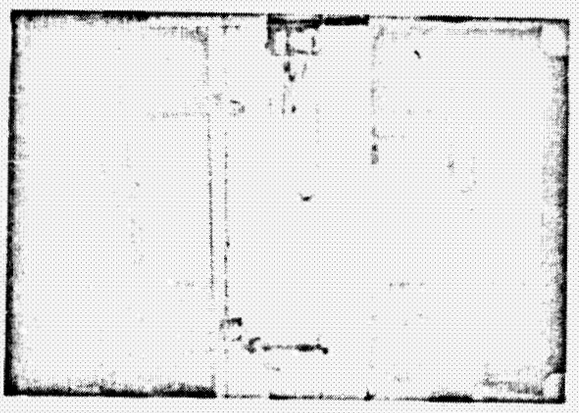

0.063 sec.

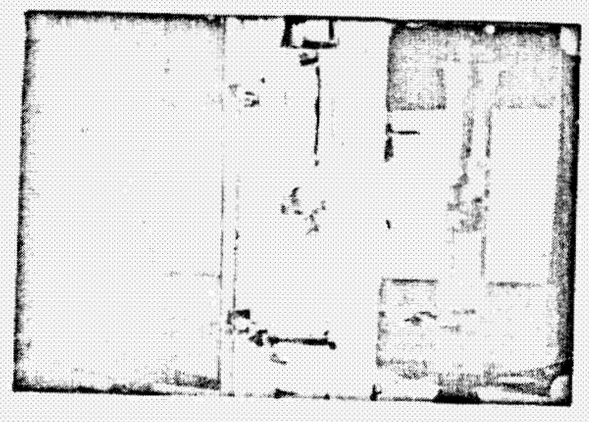

0.14 sec.

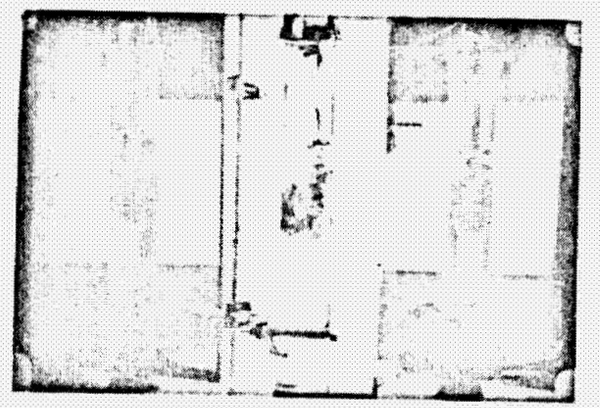

0.22 sec.

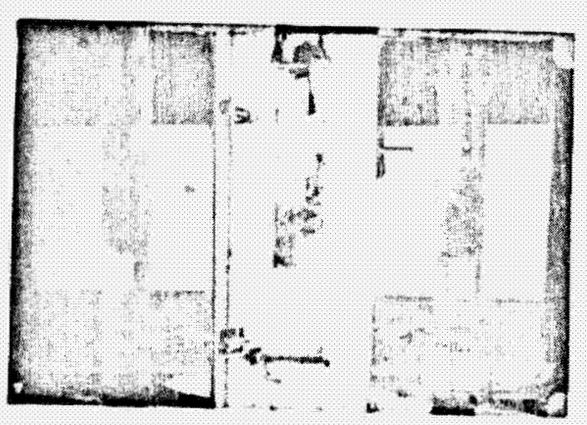

0.30

Figure 31 Typical Film Frames Used in Film Analysis

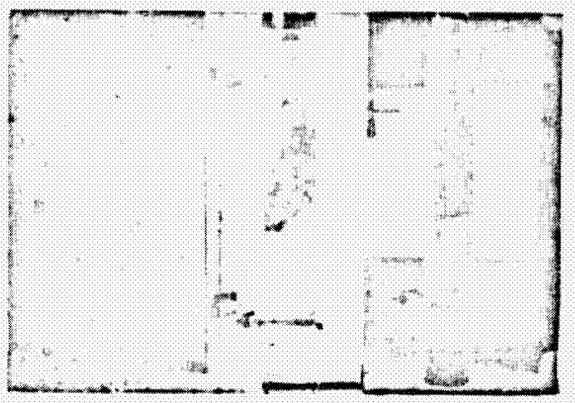

0.38 sec

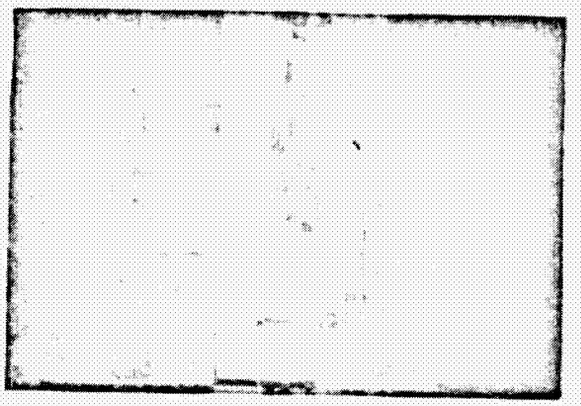

0.45 sec.

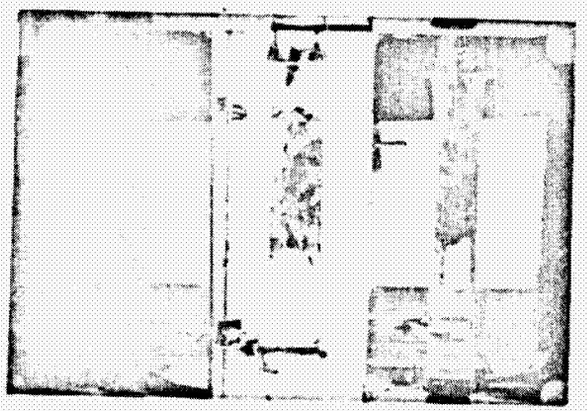

0.53 sec

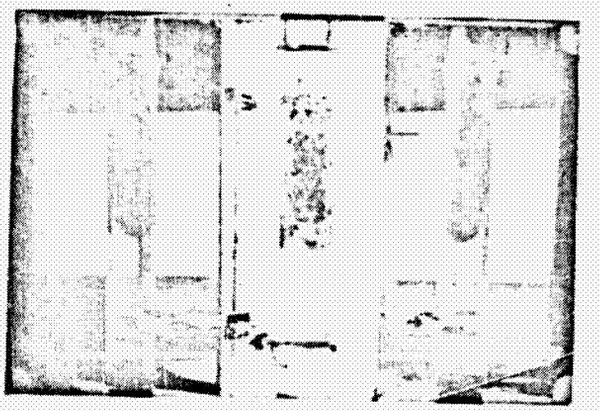

0.61 sec.

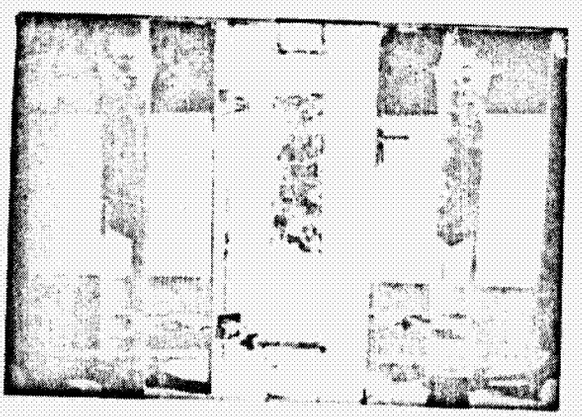

0.69 sec.

Figure 31 (Continued)

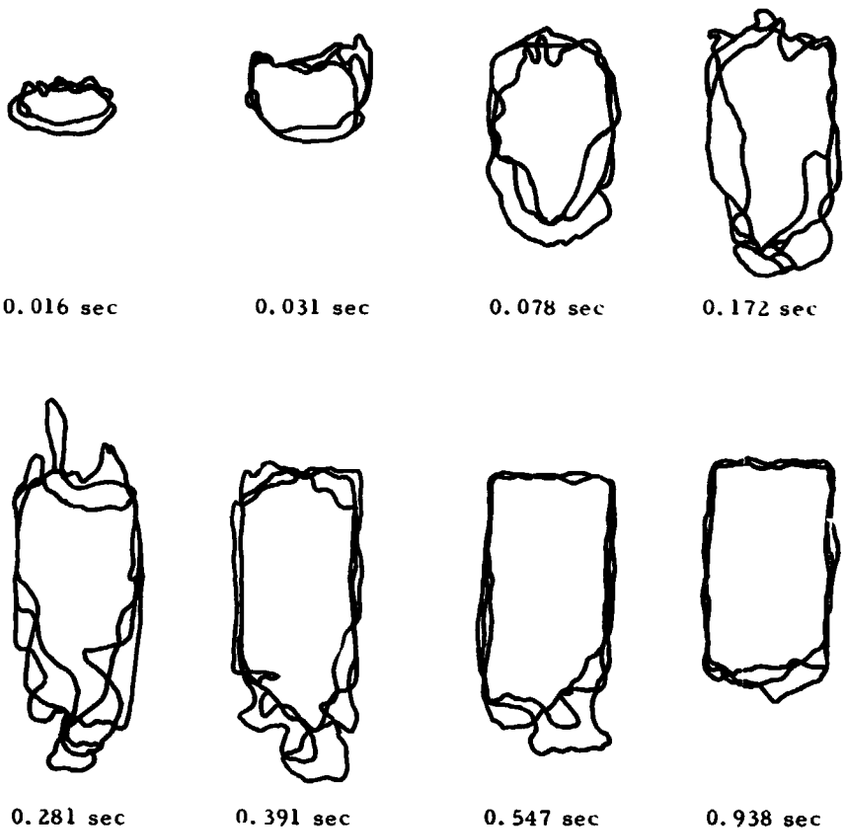

Figure 32 Superimposed Profile Traces of the Mixing Experiments

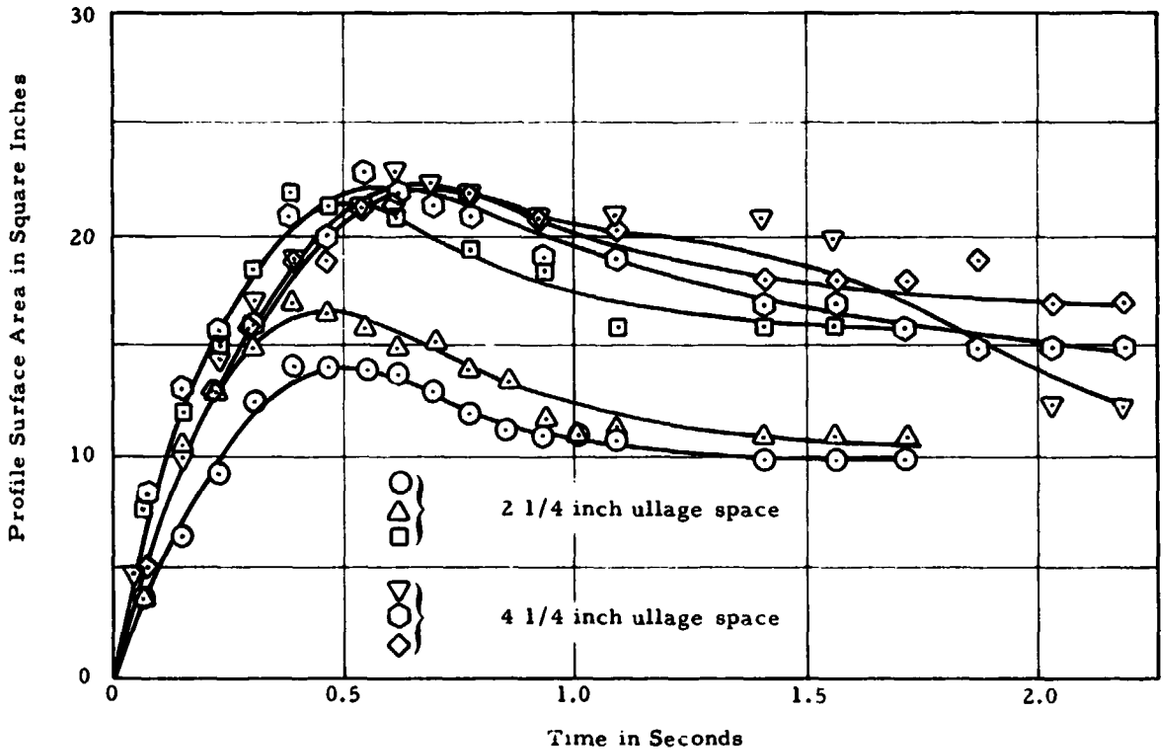

Figure 33 Profile Surface Area versus Time (Film Analysis)

this frame. This slow process of determining the total areas or [illegible]ct areas was shortened considerably later by the very satisfactory approximate method of comparing frames for different runs with standard frames for which the "Turbulence Factors" had been determined carefully, and ascribing the same "Turbulence Factor" to other similarly appearing frames.

Figure 34 presents the "Turbulence Factor" for the runs presented in Figure 33 .

Using Figure 33 and Figure 34, and combining them, gives the total area or an area directly proportional to the true contact area between the liquids. The result is seen in Figure 35.

The "Turbulence Factor" has been further substantiated by the Wax Cast Analysis which will be described below.

Figure 35 , in addition to giving the total area, shows the remarkable reproducibility of these experiments. Furthermore, this figure demonstrates the effect of mixing energy. It shows three runs with a 2 1/4 in. ullage space and three runs with a 4 1/4 in. ullage space. Considerably more area is obtained for the 4 1/4 in. ullage space since the upper liquid obtained greater kinetic energy before mixing. In these, as well as all other experiments, it was observed that the reproducibility of mixing increases with the increase in mixing energy.

The Film Analysis as described above proved to be an invaluable aid in the study of the mixing phenomena of liquids. The results, however, were not taken as correct unless they checked with the results

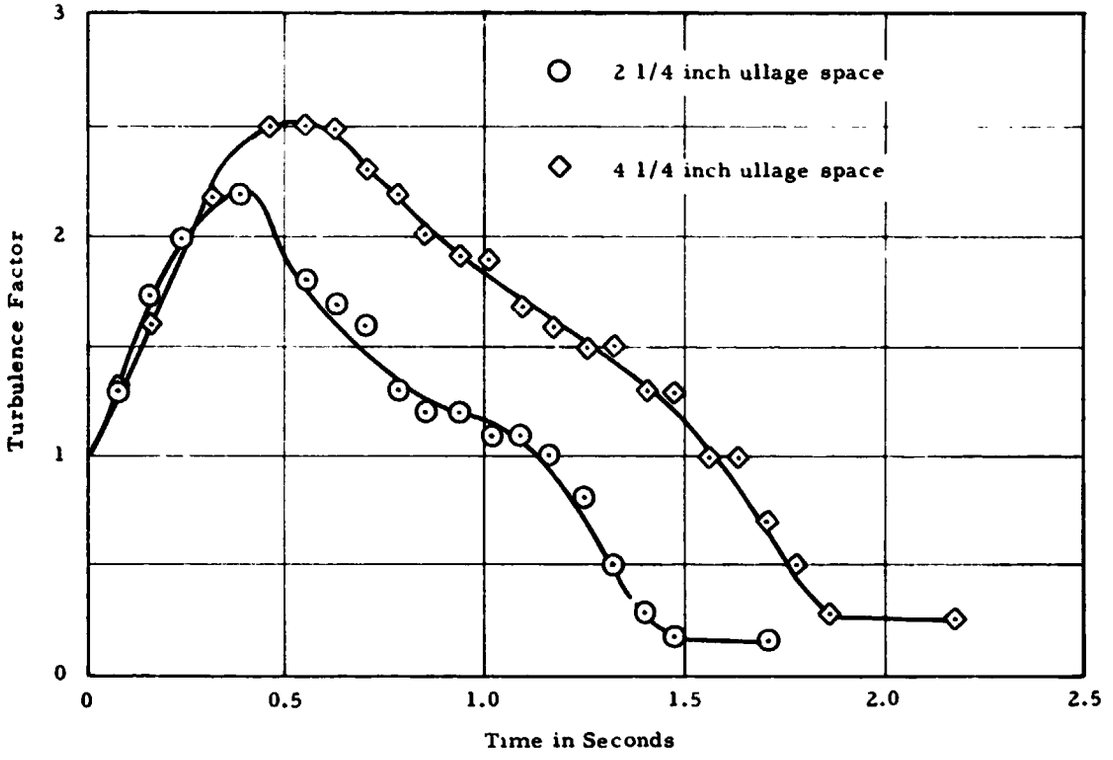

Figure 34 Turbulence Factor versus Time (Film Analysis)

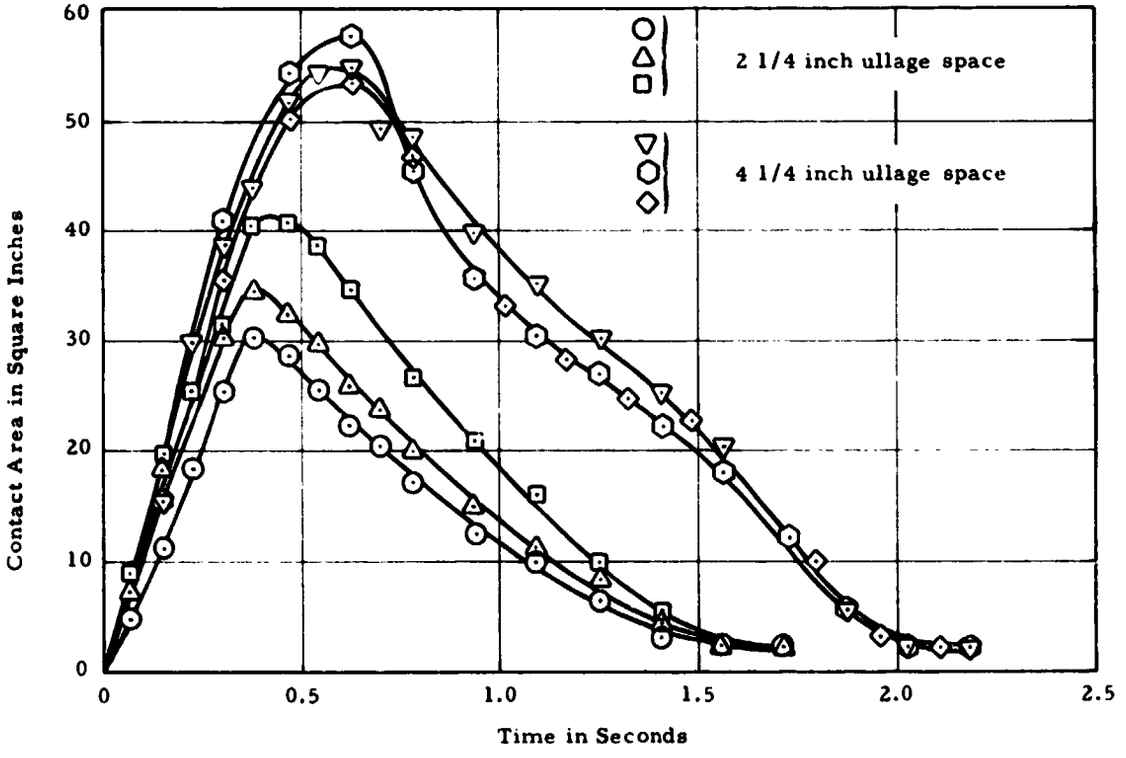

Figure 35 Contact Area versus Time (Film Analysis)

of another of the methods described below, simultaneously applied to the same experiment.

In the case of the mixing of hot and cold liquids with temperature differences great enough to produce boiling of one of the liquids, another factor - the "Boiling Factor" - was introduced which accounted for the surface produced by the vapor bubbles of one of the constituents.

A number of different diameter Pyrex glass tubes were used in the mixing studies ranging from 3/4 in. I.D. to 6 3/4 in. I.D. to give a relationship for size. In these experiments the effect of surface tension could be observed since it altered some of the phenomena in the smallest sizes.

B. Wax Cast Analysis

The Film Analysis as described previously was a dynamic method of analysis and the results had to be obtained by interpreting recordings of the actual mixing phenomena through the profile area and utilizing the turbulence, boiling, and freezing factors to obtain the total area or contact area.

The Wax Cast Analysis allowed the "freezing" of the actual mixing process at various stages of the mixing by mixing hot wax with cold water. By varying the temperatures slightly the wax would solidify earlier or later in the mixing process and the wax casts obtained in this manner could be analyzed at leisure at any time thereafter.

The experimental apparatus and setup for the Wax Cast Analysis is identical with the one for the Film Analysis, and so for many

experiments both methods of analysis were used simultaneously and checked against each other.

Figure 3 6 shows a series of such wax casts representing a complete experiment. Excellent reproducibility indicated by the Film Analysis allowed the experiments to be carried out identically except for slight variations in temperature. The wax casts indicate the progress of the mixing process. The profile area was determined from these wax casts by two methods: A small grid was laid out on the surface and then the area determined by counting squares. This procedure was checked by dipping these samples into paint and letting them dry. By determining the thickness of the paint film and its density and by weighing the sample before coating and after coating, the profile area could be determined. Essentially the same answers were obtained by both methods.

The serially sectioned samples or wax casts in Figure 37 allowed the total area to be determined by the same method used for the profile area again represented the "Turbulence Factor".

Curves of the profile area versus time (Figure 38), the total or contact area versus time (Figure 39), and the "Turbulence Factor" versus time (Figure 40) were plotted.

The Wax Cast Analysis was primarily used to check the results from the Film Analysis and, after it was found that the results from both analyses were in essential agreement, it was not used further.

C. Vibration Mixing Analysis

Another method by which the mixing processes and phenomena were

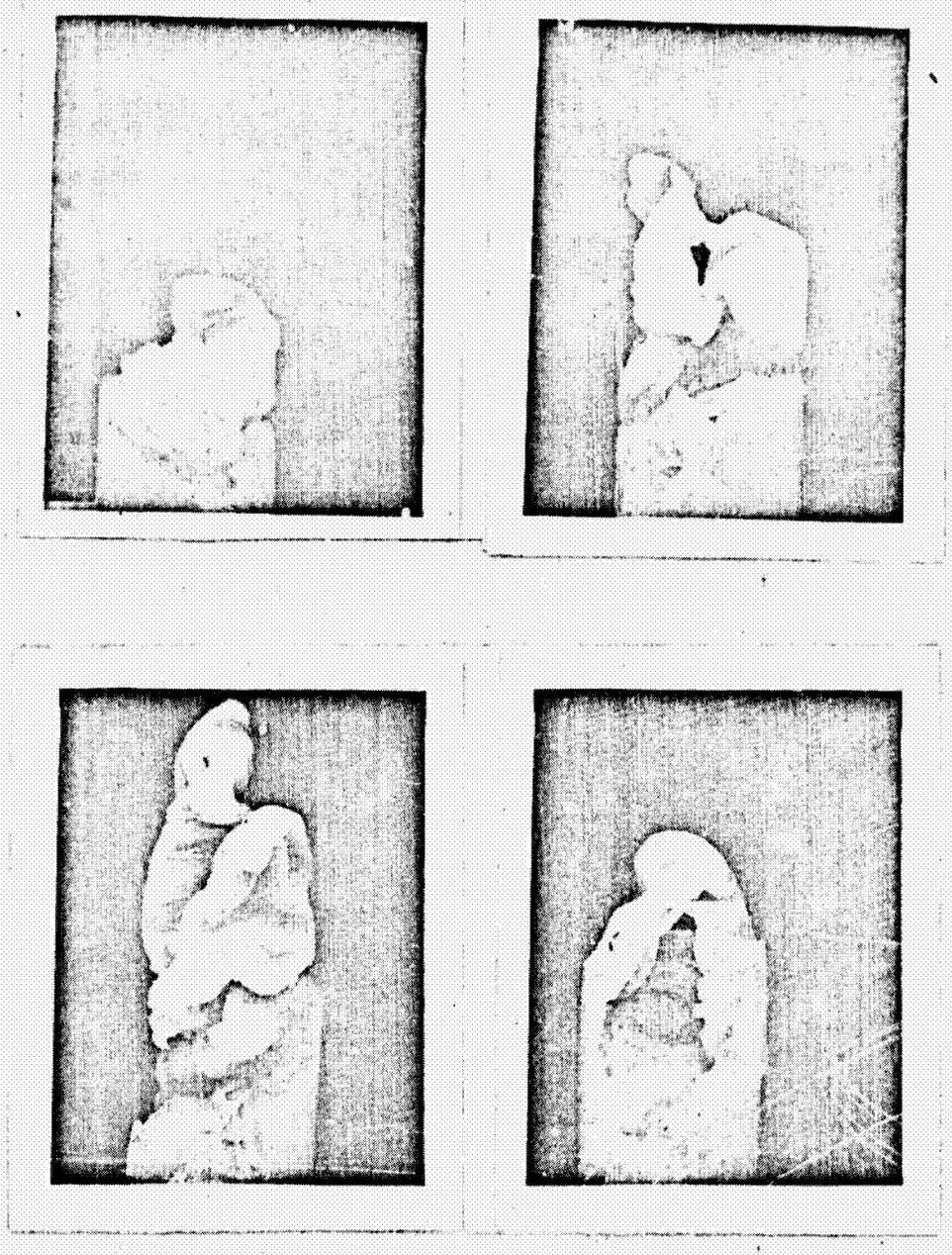

Figure 36 Typical Wax Casts

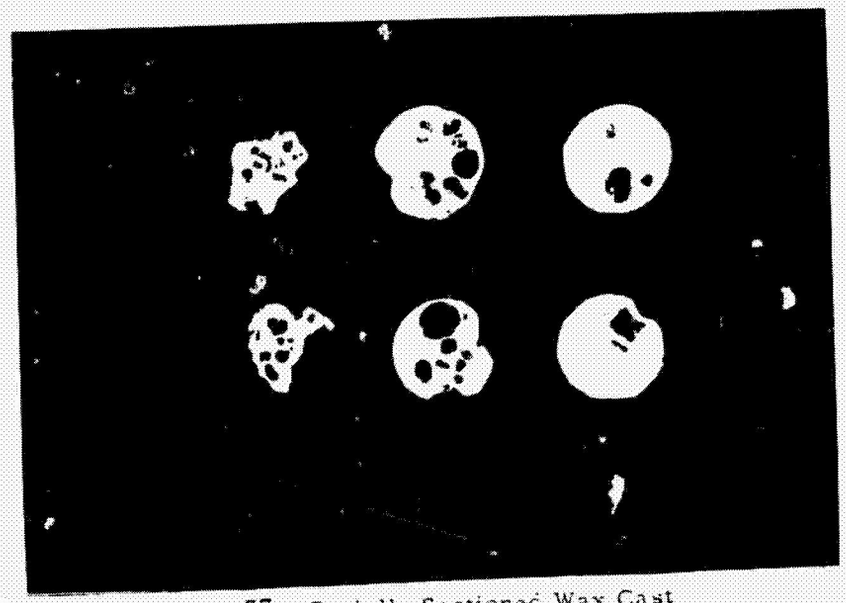

Figure 37 Serially Sectioned Wax Cast

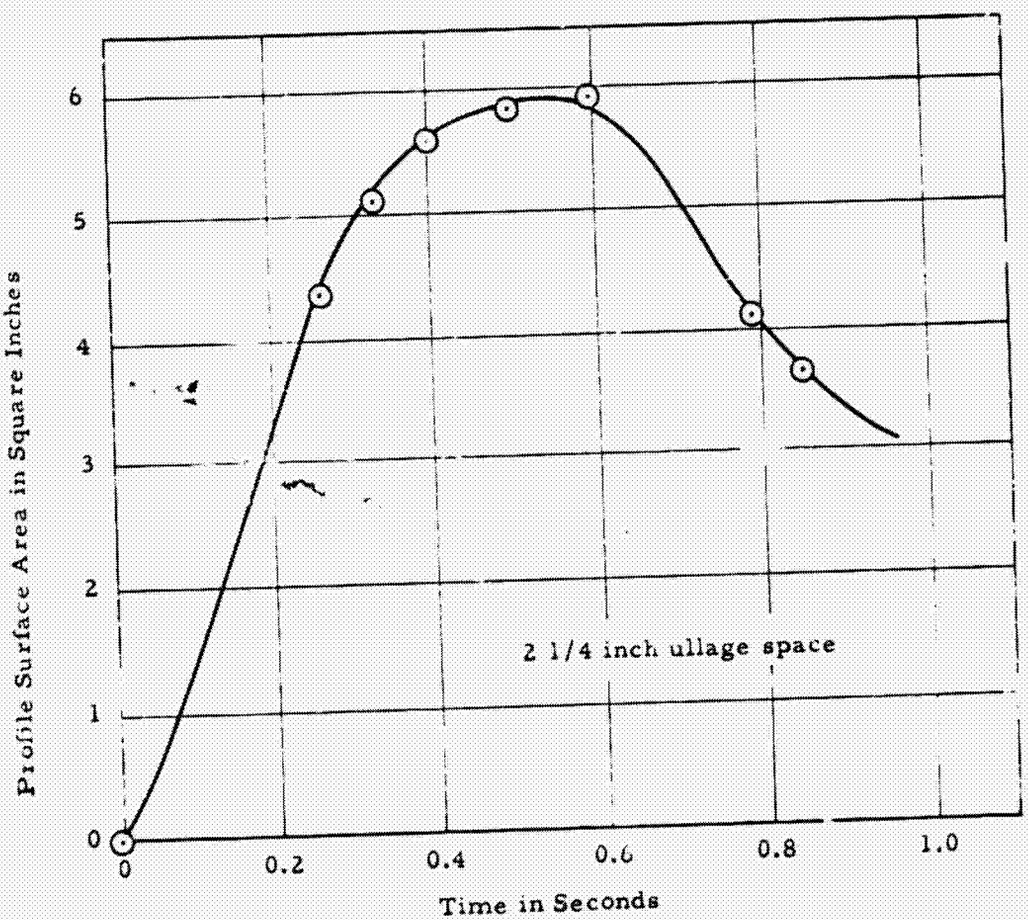

Figure 38 Profile Surface Area versus Time
(Wax Cast Analysis

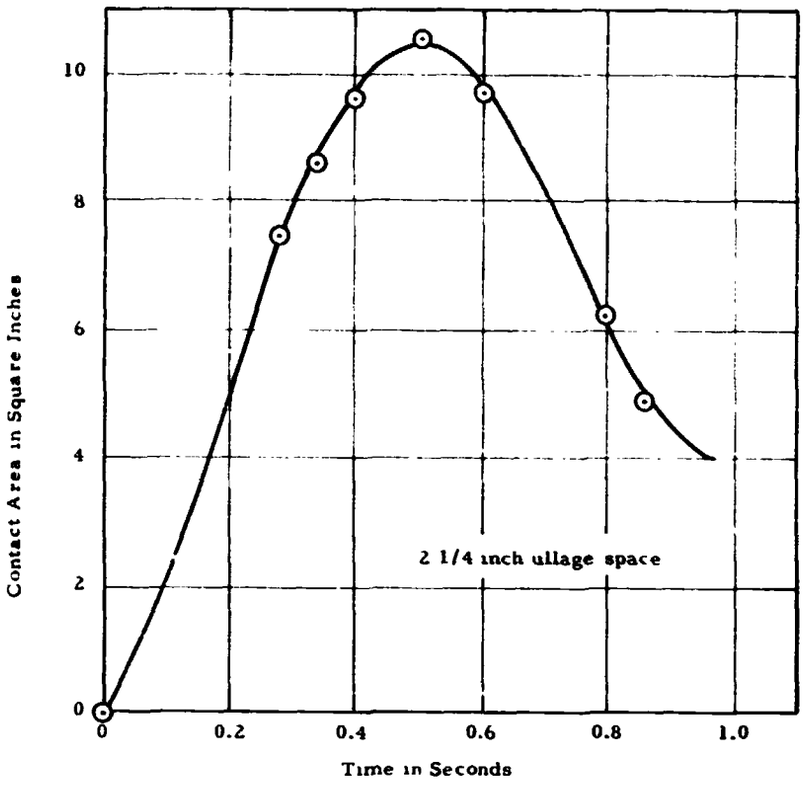

Figure 39 Contact Area versus Time
(Wax Cast Analysis)

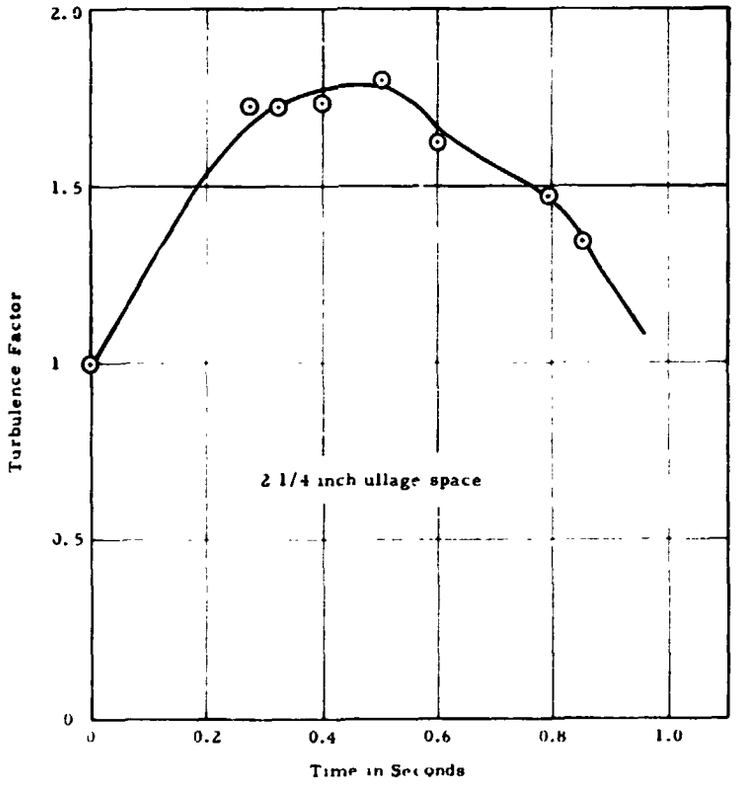

Figure 40 Turbulence Factor versus Time
(Wax Cast Analysis)

studied is the Vibration Mixing Analysis. In this method, the fluid particles are simulated by solid particles of various sizes, shapes, colors, densities, etc. These solid particles used in various proportions and configurations are mounted on a vibration table and shaken for certain lengths of time. Figure 41 shows the experimental arrangement simulating spill mixing configuration. Three liquids are represented by different color marbles and are arranged in a desired configuration. Shaking the configuration for predetermined times, the marbles will diffuse into each other. Thus in this manner the mixing process simulated here can be studied in steps.

Figure 42 presents a number of the views representing these steps. Any particular region can be studied in this manner by removing this volume and counting the particles of each of the constituents present. This gives the percentages of each one of these constituents, thus the degree of mixing in this region.

Removal of some of the particles from certain regions as programmed and governed by the fundamental relationships of heat transfer can further account for evaporation losses. This takes into account boil-off as part of the mixing process.

In this manner a curve can be plotted for the fraction mixed as a function of time. The time scale is arbitrary since the amplitude and frequency of the shaking table have a pronounced effect on the speed with which the mixing progresses. To find the absolute mixing time either an experiment with liquids or theoretical calculations will give the time scale needed. This absolute time superimposed upon the curve gives the true mixing function - time relationship.

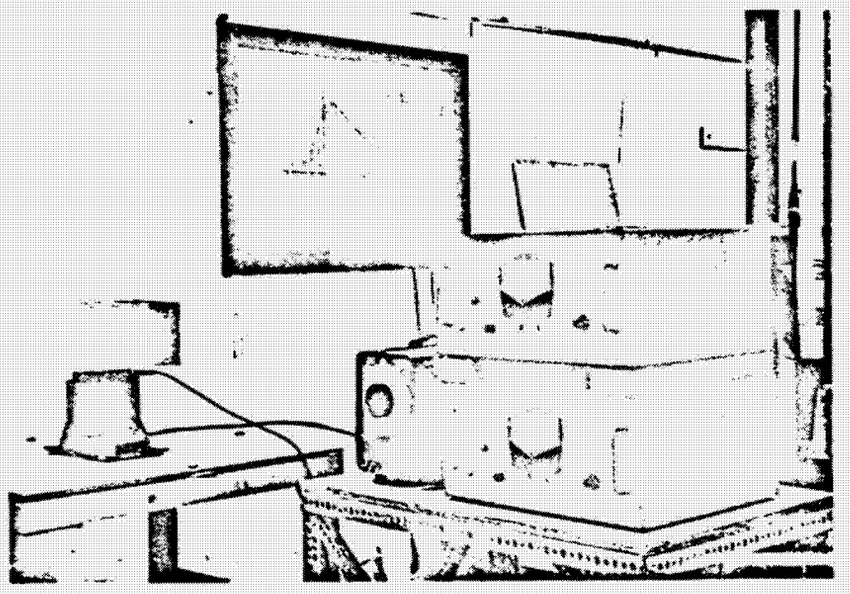

Figure 41 Experimental Arrangement for Vibration Mixing Analysis

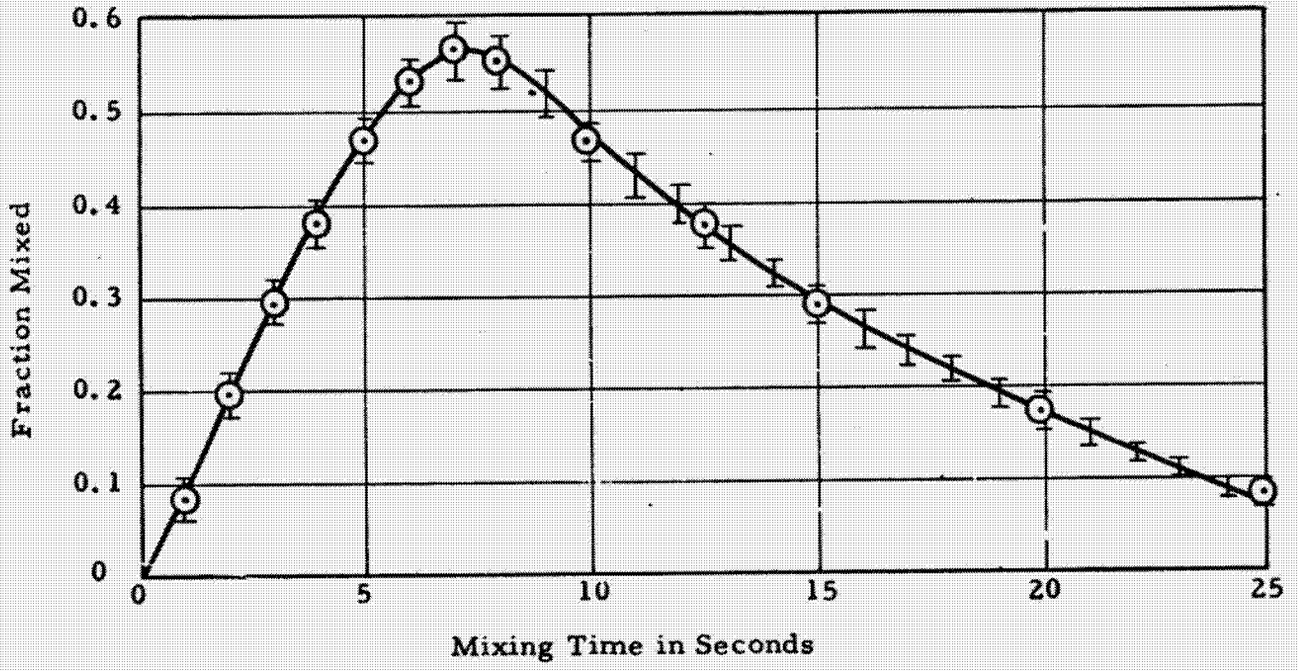

Figure 43 Mixing Function of Spill Function for Simulated Three Component Liquid Propellant Spill Tests (Vibration Mixing Analysis)

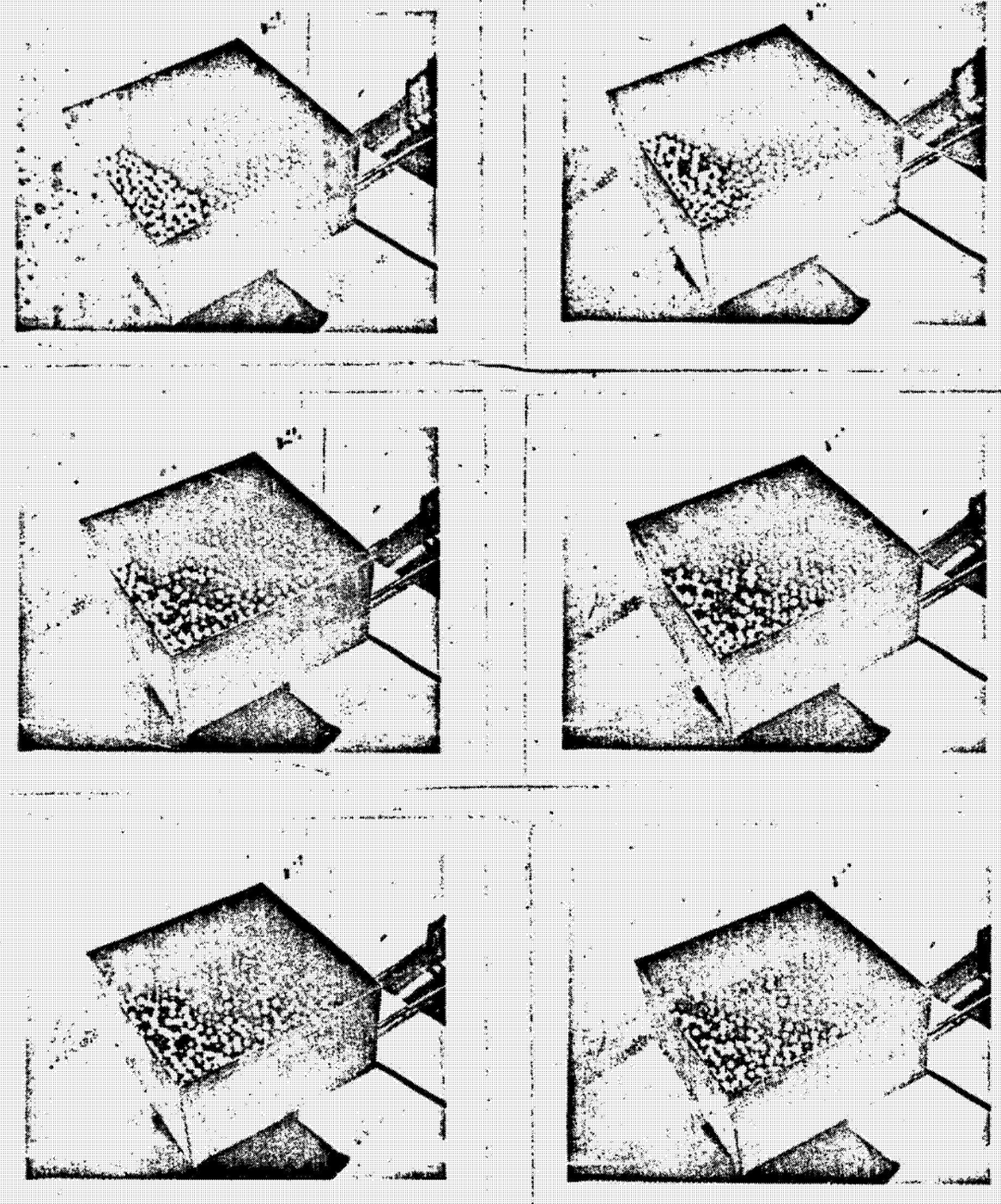

Figure 42 Successive Stages of Mixing Processes

Figure 43 presents a mixing function curve representing the J-test series of the Arthur D. Little Spill Test Program[6].

It is interesting to note that all mixing experiments produced the same characteristic shape of the mixing function curve, only the actual values and speed with which the process occurred were different.

D. Thermocouple Grid Analysis

The three methods for studying the mixing process, the Film Analysis, the Wax Cast Analysis, and the Vibration Mixing Analysis are excellent methods for obtaining insight into the phenomena taking place when different liquids mix. They are, however, simulation methods and are not readily applicable to actual explosive mixtures where detonation and explosion would, in most cases, destroy the records.

The Thermocouple Grid Analysis overcomes this difficulty and can, therefore, be considered the most powerful and best of the methods discussed in this paper. It is the best but also the most elaborate, most expensive (and the data reduction the most tedious) of the four methods. For explosive tests, it is, however, the only method which will give information from time zero of the failure up to and beyond the time of ignition.

The heart of this method is a grid of thermocouple junctions spaced throughout the region under study. These can be placed inside the tanks of a missile and extend around it if fireball data are desired. A continuous time record of the signals from the individual junctions is kept for the complete period of the processes under investigation. This method, through its three-dimensional records of the complete

time history, can provide a great amount of information with respect to:

1. The three-dimensional mixing front of a particular constituent
2. The degree of mixing at a particular point
3. The degree of turbulence at a particular point

and, in explosive tests, in addition to the above:

4. The location of the point or points of ignition
5. The time delay from initiation to mixing to ignition
6. The propagation of the reaction front
7. The propagation of the shock front
8. The separation of shock front and reaction front, etc.
9. Other phenomena and events obtainable by detail data analysis

The experimental arrangement and equipment for the Thermocouple Grid Analysis is the same as that for the Film Analysis and can readily be incorporated into static explosive test series. The only addition necessary is a three-dimensional grid of fine thermocouple junctions giving good response characteristics. Full response times of less than 10 micro-seconds have been obtained in our laboratory.

The signals from these thermocouple junctions can be fed to the recording equipment, which may be close by, in inert tests, or at some distance in explosive tests.

The overall experimental arrangement for the work reported here is shown in Figure 44. The experimental apparatus and the recording equipment are shown. All the control experiments using this arrangement, in addition, made use of high-speed camera recordings of the mixing phenomena so as to have a check and comparison between the Film Analysis and the Thermocouple Grid Analysis.

Figure 45 pictures thermocouple grids which were used in some of

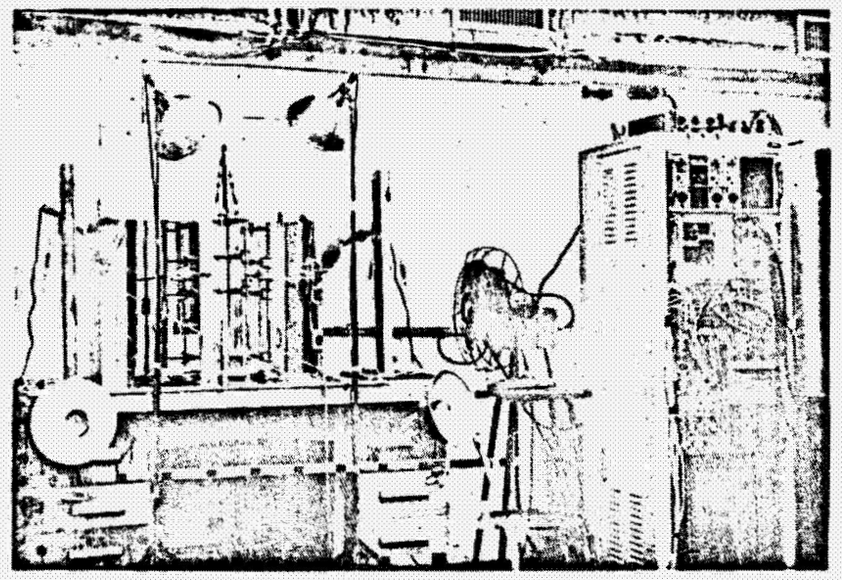

Figure 44 Experimental Arrangement for Thermocouple Grid Analysis

a

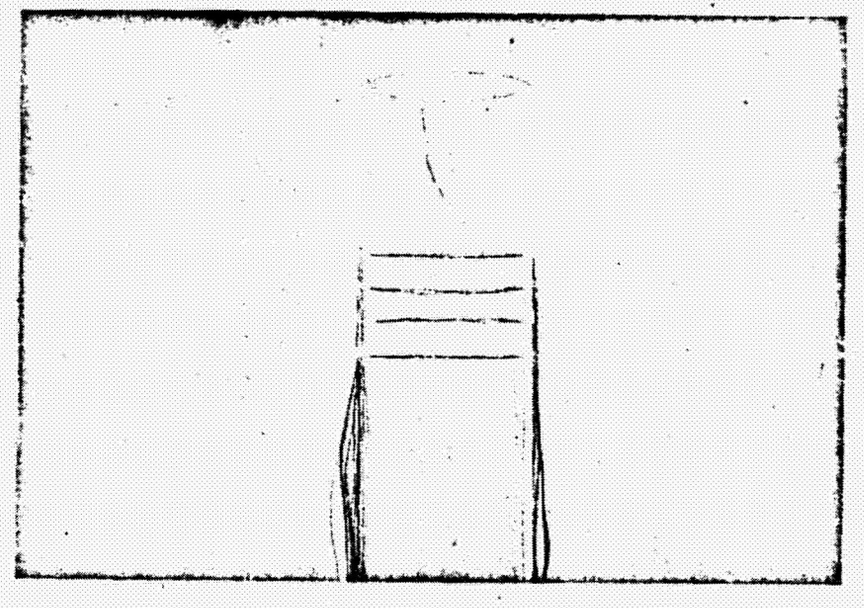

b

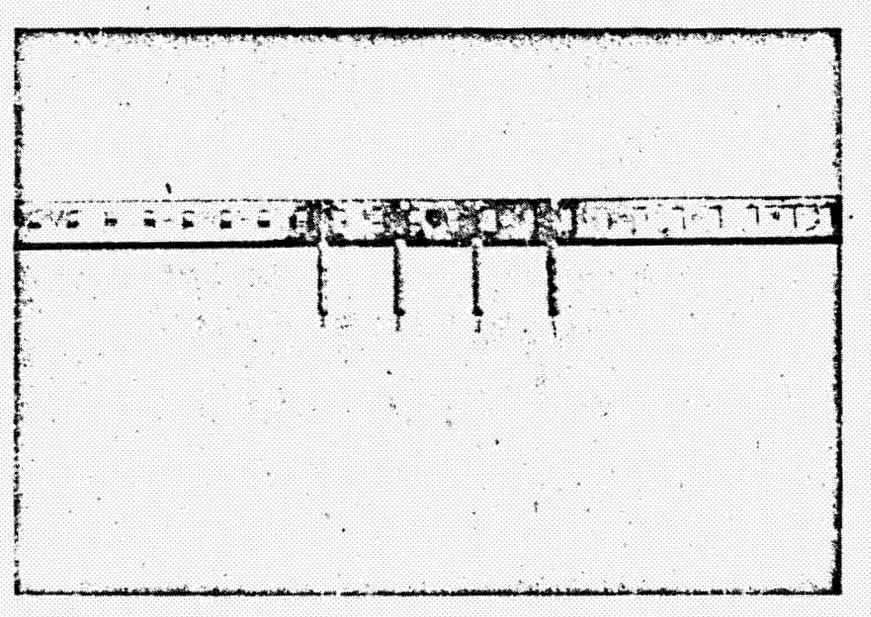

Figure 45 Typical Sections of Thermocouple Grids

these investigations. Our laboratory has the capability of monitoring over 40 individual junctions at present which can be extended to 65 if needed. By high-speed periodic sampling through commutation this capacity can be increased manyfold, but the time continuity of the records has to be sacrificed.

Figure 46 presents traces obtained from a mixing experiment. All twelve traces in this case correspond to junctions in a vertical plane at three different elevations with four junctions equally spaced in each one of these elevations and arranged in straight lines.

Figure 46-A presents traces of the mixing of hot oil and water. Figure 46-B presents traces of the mixing of LN_2 and kerosene.

Figure 47a presents the resulting mixing profile as determined by interpolation between the junctions of the thermocouple grid at time τ .

Figure 47b also presents the resulting mixing profile of the same hot oil and water experiments as determined by the Film Analysis at the same time τ .

It can be seen that the results from both methods of analysis are essentially the same. More and closer spaced thermocouple junctions would give more points for drawing the mixing profile and would fix this surface with greater reliability.

The degree of mixing at any time, τ , around a particular junction can be determined from the time history at this junction by writing the relationship for mass and energy balance at this junction incorporating the laws of thermodynamics, fluid flow, and heat transfer. A Computer program to do this is of great help if a considerable number of junctions are involved.

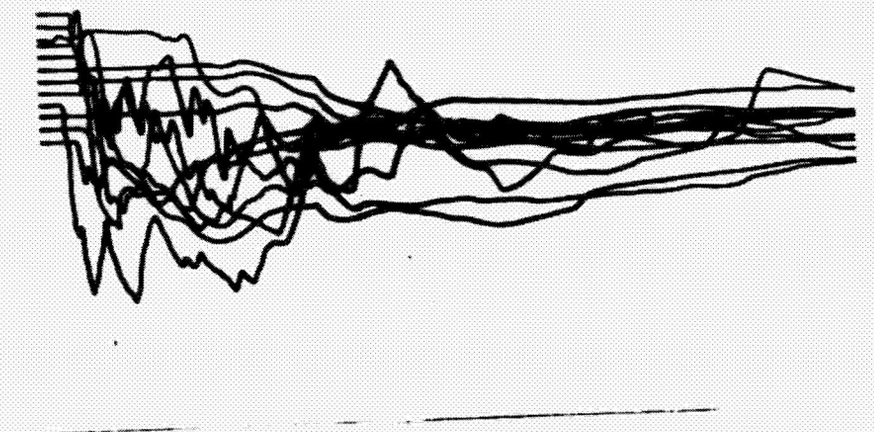

a. Hot Oil and Water

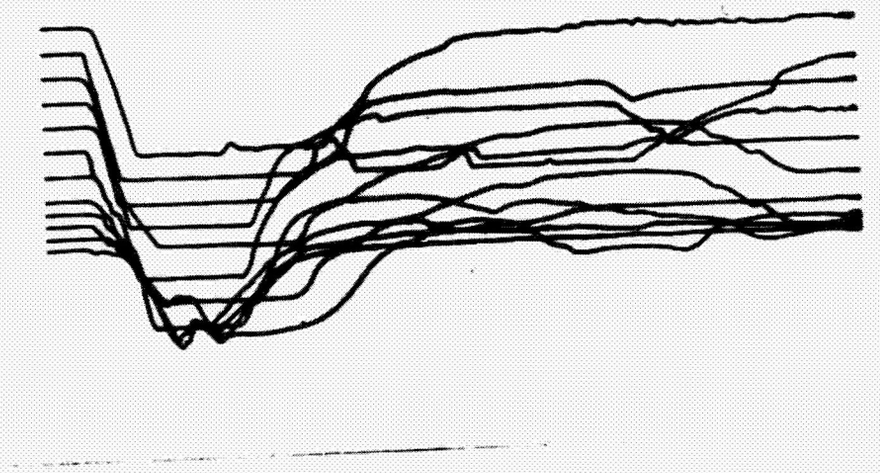

b. Liquid Nitrogen and Kerosene

Figure 46 Thermocouple Grid Time Traces

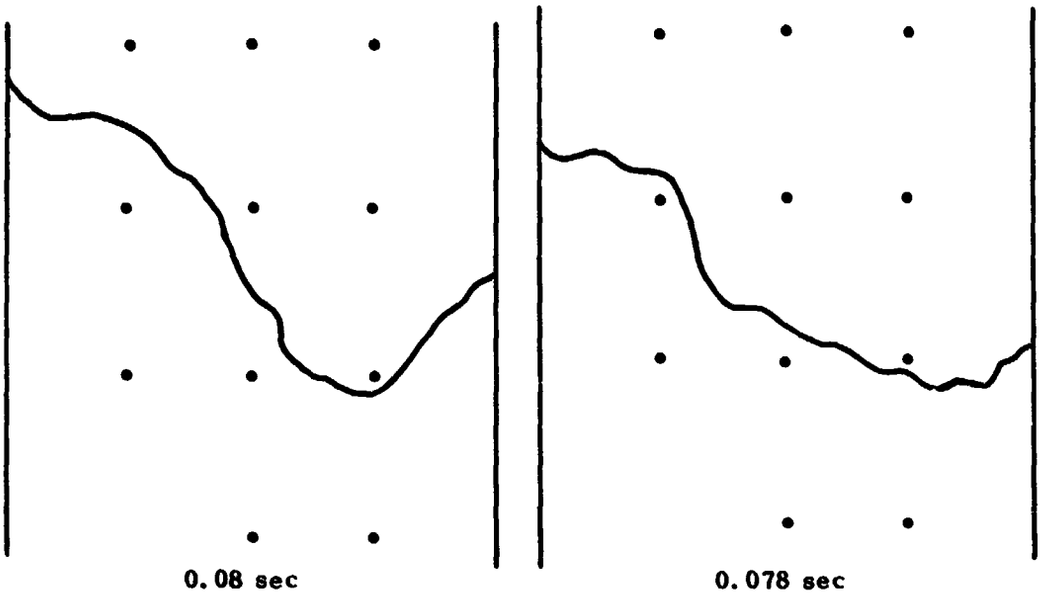

a. Thermocouple Grid Analysis b. Film Analysis

Figure 47 Comparison of Mixing Profiles Obtained Simultaneously by Thermocouple Grid Analysis and Film Analysis

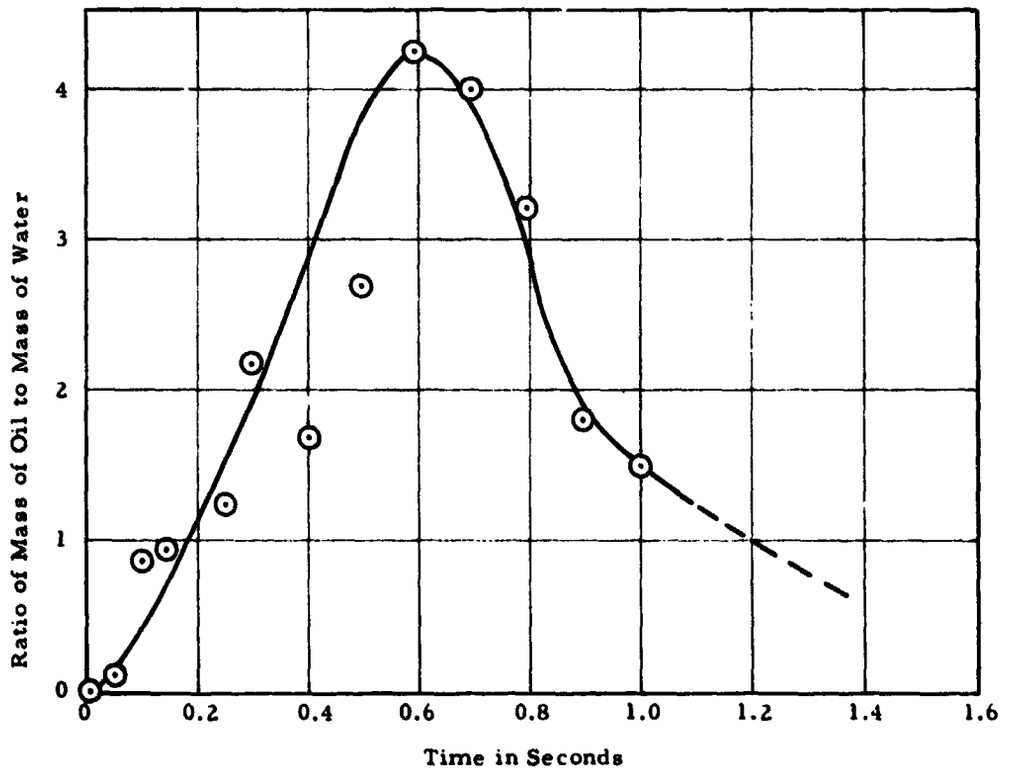

Figure 48 Mixing Function or Spill Function for Simulated Two Component Liquid Propellant Mixing Test (Thermocouple Grid Analysis)

Averaging the conditions around each of the individual junctions can then give the mixing function, the fraction mixed at any time τ, Figure 48.

SUMMARY

The preceding discussion of the four methods which can be employed in investigating the mixing phenomena of liquids to establish a mixing function-time relationship shows the value of these methods, their relative merits, and singular advantages to do the job.

The Film Analysis is relatively simple and easily carried out, but in its simplest form, the use of light requires transparent containers and rather transparent constituents. In its more sophisticated forms - using shorter wavelength radiation, such as X-ray, Gamma-ray or tracer methods - the equipment necessary becomes much more complex.

The Wax Cast Analysis allows the checking of the results obtained by the Film Analysis by independently establishing the mixing profile, total or contact area, and turbulence factors.

The Vibration Mixing Analysis provides a method by which, again as in the Wax Cast Analysis, the mixing process can be stopped at any point in its development and studied at leisure.

The Thermocouple Grid Analysis, the most powerful of the four methods, can provide all the information of the above methods (except for stopping the mixing process at any point in its development) and, in addition, can be used in actual missile configuration explosive experiments.

In the manner described above these methods can provide information which is not available at the present time and, through this information, can give better insight into, and understanding of, the actual happenings during the mixing process and leading up to the explosion of liquid propellant mixtures - information which is needed if we ever hope to control and guide these processes.

Electrostatic Charge and Voltage Generation (2)

Much of this method was described in the section on Critical Mass and some of the supporting results were given at that time.

Basically it was theoretically predicted when fluids mix that electrostatic charges and voltages are generated and these were then verified by actual measurements in the laboratory.

To verify the results obtained by use of the Fluid Plug Model a simple experiment was set up. Figure 49 schematically describes it. A glass cylinder was used and filled to a desired level with RP-1. Above the RP-1 was a partition with a hole in the center which could be opened by sliding out two plastic sheets. The hole diameter was 1/2 that of the glass cylinder. The space above the partition was filled with the desired quantity of LN_2 and when the hole was quickly opened the LN_2 dropped into the RP-1 through the hole, simulating a fluid plug.

In the RP-1 space were mounted two screen electrodes, one just above the RP-1 liquid surface and the other in this case 1.25 inches below the upper one. Leads from the two screen electrodes were led

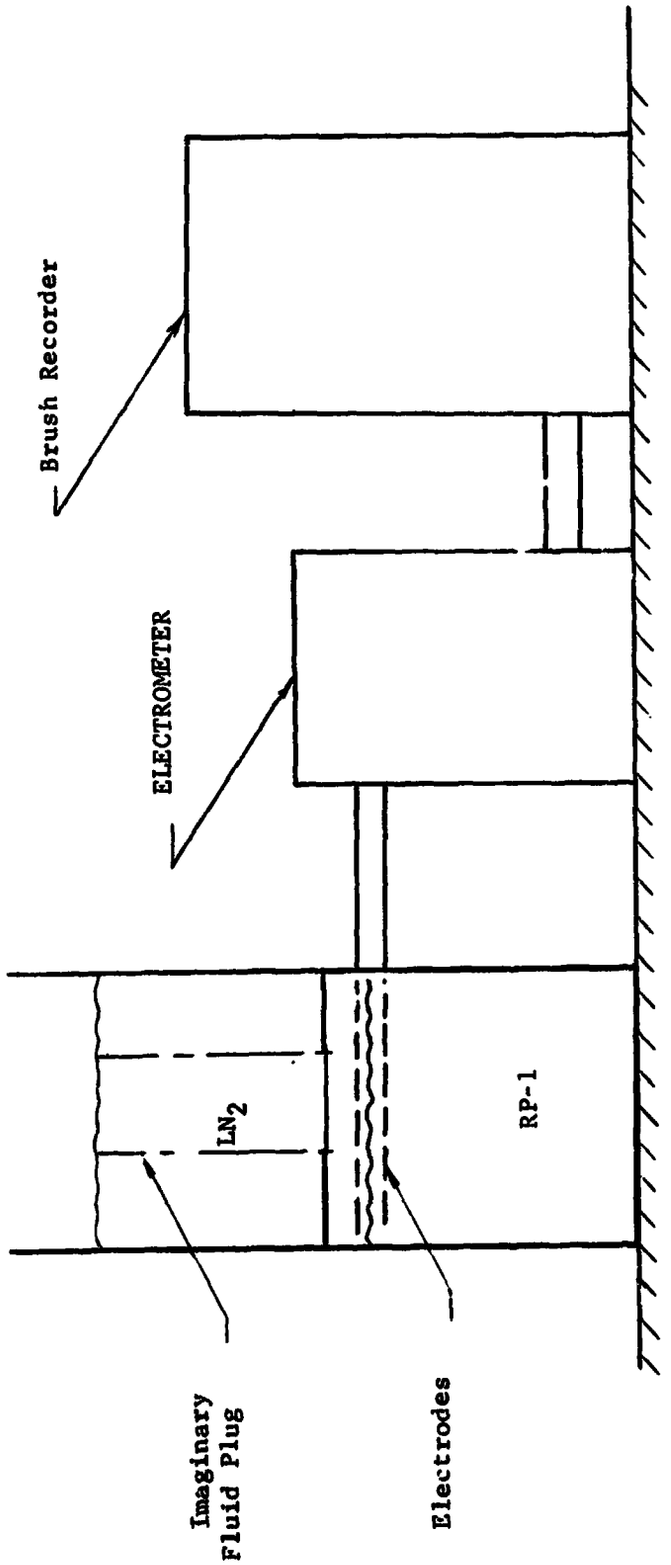

Fig. 49 Experimental Set-up for Electrostatic Charge and Voltage Generation Measurements

to an Electrometer and its output to a Brush strip chart recorder.

In this manner, the charge and voltage build-up as a function of time could be determined for different combinations of liquids and for different quantities.

The actual traces obtained look very much like the theoretical traces of Figure 11. Again it does not seem to make any difference whether the whole quantity is used all at once or in steps, providing in the latter case leakage is prevented.

First single probes were used and only on occasion were charges and voltages observed, then double probes were used with similar results. The more probes were used the more often were readings obtained and finally with the use of screens which are really just multi-junction probles, readings were obtained every single time. It was observed that the screens had an averaging effect. It could be established at least that the charge and voltage generation is an integral part of the mixing process of liquids and occurs whenever there is mixing of dielectric fluids.

When the large quantities were allowed to come together it seemed that the mixing takes place in very rapidly repeated jumps so that the same voltage was reached as if the same quantities were mixed in discrete steps. Since the mixing occurs in such small steps over and over again, the average value takes on much more meaning especially when applied to large quantities.

The manner of mixing did not seem too critical since just pouring one component into the other produced essentially the same results.

The reason for this seems to be that the boiling action which provides considerable violence to the mixing process is the over-riding phenomenon. If, however, considerably more mixing energy is used, such as the pouring from a height of 10 feet, the mixing and the charge generation and voltage generation occur much more rapidly.

It seemed, however, that the mixing occurred relatively more rapidly than the charge and voltage build-up when compared with the more gentle method of bringing the components together. Figure 50 shows an actual trace of voltage versus time for 200 ml incremental LN_2 additions.

Due to the small quantity of RP-1 and the rapid addition of LN_2 the temperature difference between the components decreased during this test showing the effect of less vapor generation in the later additions, resulting in deeper penetration of the fluid plug and therefore more voltage generation.

The high speed film analysis indicated that the bulk of the bubbles was very uniform in size and very close to 1/4 in. in diameter. There were larger and smaller ones but they were very few in number.

Sometimes voltages of opposite polarity are recorded since with the turbulence in the mixing region the charged layers can come in contact with either electrode, and each one can become positive or negative with respect to the other. The actual amounts of voltage generated and recorded did not in general vary too much but on occasion a large jump was observed.

The average voltage generated was four volts with electrode spacing optimum based upon many observations for 200 ml of LN_2 . This voltage

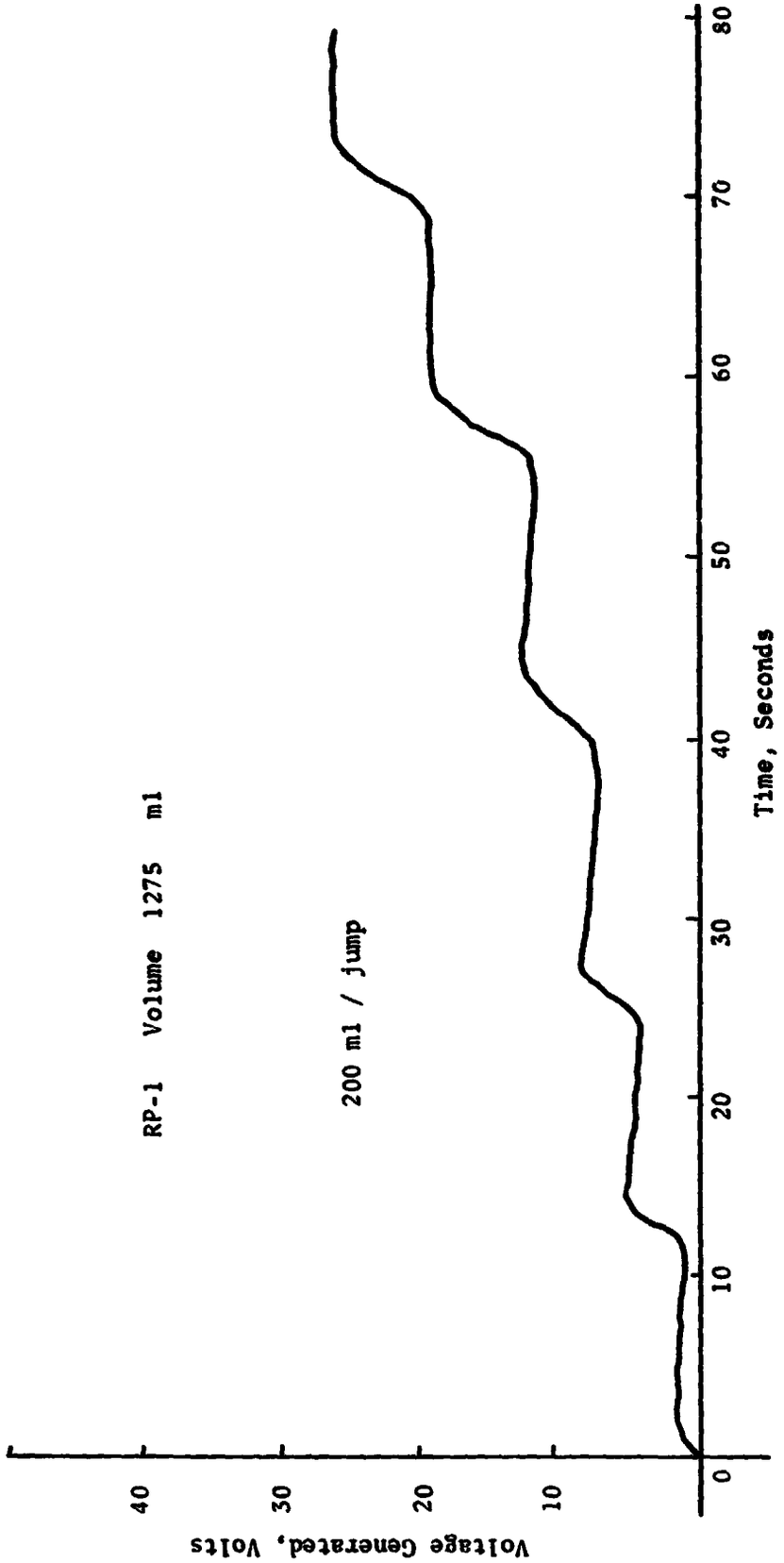

Fig. 50 Typical Voltage-Time Trace for Successive Mixing of LN_2 and RP-1 Using Small Quantities of LN_2

was built up through the use of large quantities or small quantities in succession to several hundred volts during these experiments. Sometimes, but not very often, a single jump of several hundred volts was observed with as little as 200 ml of LN_2.

The actual values of charges and voltages generated increased with the quantity of propellants mixed.

The theory and the laboratory verification resulted in the formulation and prediction of the existence of the critical mass which was several years later further substantiated in actual field tests.

Another important observation in these experiments was that the amount of charge and voltage generated depended upon the energy which was used in mixing the components, the results of this were presented earlier.

B. Explosive Field Experiments

To determine how mixing of liquid rocket propellants compares with the laboratory studies which have substantiated the theories, a number of different experiments have been conducted bring out this comparison.

1. PYRO Project

25,000 lb. LO_2/RP-1 Explosion Experiments

To show and demonstrate how the theory can predict the explosive yield for liquid rocket propellant explosions, two 25,000 lb. LO_2/RP-1 experiments were completely instrumented by the University of Florida Group with thermocouple grids. The thermocouples were installed inside the tank assemblies of the liquid propellant explosion test series, planned and conducted with project PYRO at the Air Force Rocket

Propulsion Laboratory at Edwards Air Force Base, California. This instrumentation was to measure the phenomena following the initiation of failure.

Because of the mode of failure selected by project PYRO, the region swept through by the star cutter had to be excluded from detailed analysis since the instrumentation in that region would have been destroyed by the cutter (see Figure 51) before the events which were to be measured occurred.

The overall purpose of this instrumentation was to:

1. Correlate the mixing phenomena of the true propellants with laboratory mixing experiments using inert fluids for simulation.
2. To substantiate experimentally parts or all of the "Fireball Hypothesis"[16] proposed earlier in these studies.

Specifically it was hoped to be able to determine by this experimental procedure part or all of the following:

After failure but before ignition:

1. The three-dimensional mixing front, or boundary of the mixing region
2. The degree of mixing at a particular point
3. The degree of turbulence at a particular point
4. The time delays from initiation of failure to start of mixing, and to ignition
5. The location of the point or points of ignition
6. The propagation of the reaction front
7. The propagation of the shock front

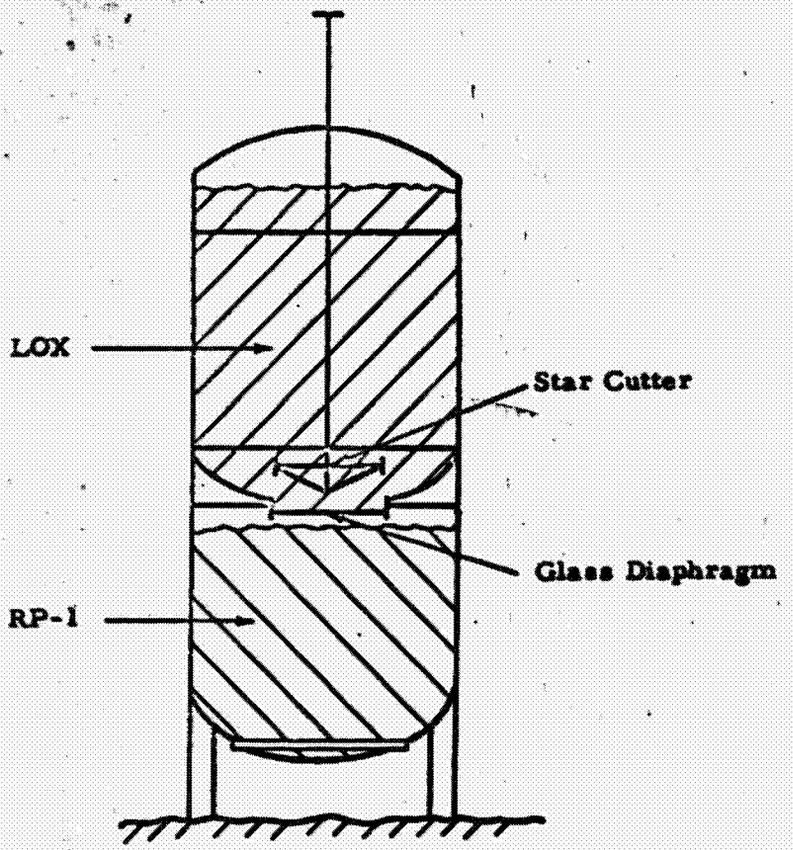

Fig. 51
Schematic Sketch of 25,000-Lb LOX/RP Tank

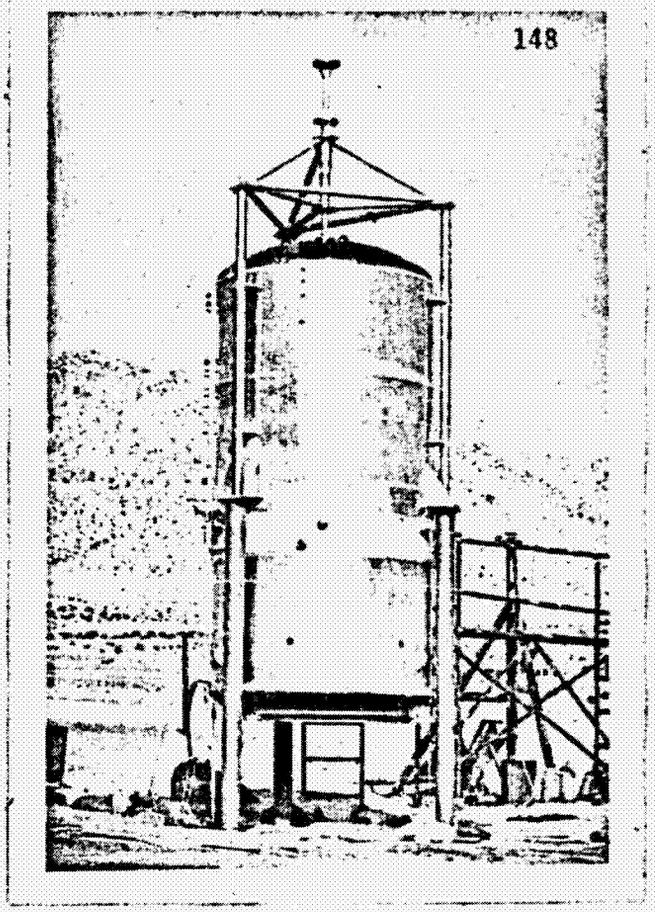

Fig. 52
25,000-Lb LOX/RP Tank Assembly.
Experiment No. 282

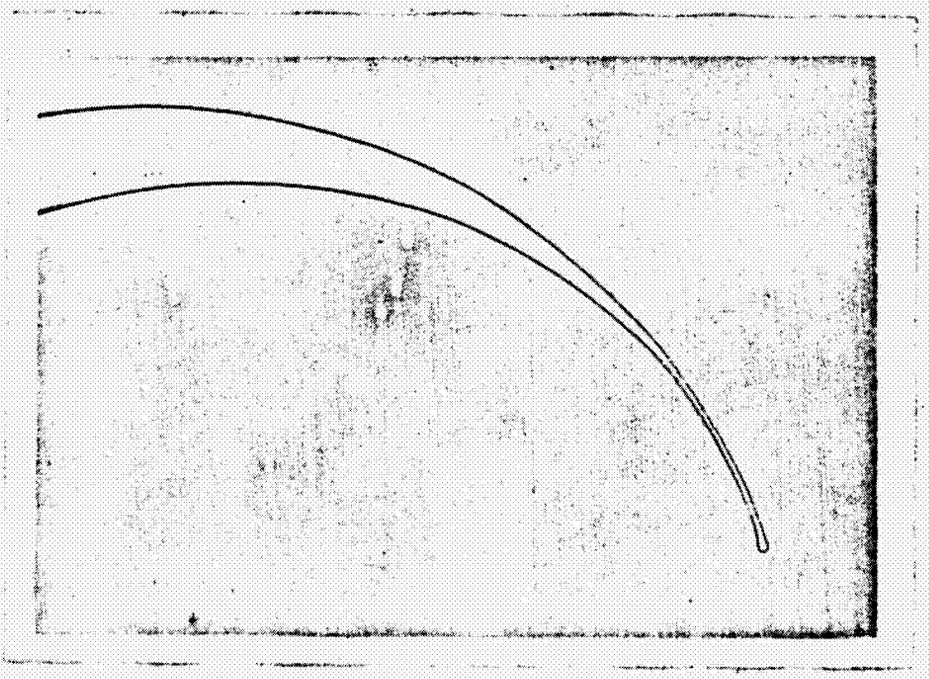

Fig. 53
No. 36 Gage Copper Constenten Thermocouple Sensor

8. The separation of the shock front and the reaction front
9. Other phenomena and events obtainable by detailed data analysis

Only in (2) and (3) above do the thermocouple response characteristics have to be considered since in all other cases only relative time differences are needed.

Excellent data were obtained in both experiments. Advantage was, however, taken of knowledge obtained from the data analysis of the first experiment, No. 278, to obtain the best results possible from the second experiment, No. 282. The main improvements were the moving up of some of the thermocouples higher in the tank and closer to the star cutter, or into the mixing region, since it was found that the star cutter did not travel as far as was previously expected. The chart speed of the recording oscillographs was, in the second experiment, operated at four times the speed of the first experiment to increase the resolution capabilities.

The instrumentation to accomplish the above consisted of:

1. Very fine thermocouples inside the tank
2. A reference junction box in an underground steel box near ground zero
3. High speed recording oscillographs

The sensing elements inside the tank (Figure 52) consisted of 37 copper-constantan thermocouples, No. 36 gage, shellacked and Teflon-coated. These thermocouples were made so that no excess material was present at the junction and the whole thermocouple looked like a continuous wire with no visible variation at the junction (Figure 53).

A small plastic tube was slipped over the wires to about 1/4 inch behind the junction and filled with epoxy, both to support the junction preventing relative motion between the wires, and to provide a means for attaching the thermocouple to the support wires inside the tank.

The thermocouples were located in the tank (Figure 54) so as to give an optimum pattern of the data. They indicated the arrival of events at their location and changes occurring at or in their region.

The leads of the 37 thermocouples (74 individual wires) were guided along the support wires and loosely tied to them about every 8 inches (Figure 55). This gave the needed support to the fine wires and at the same time allowed them to give, in case they were hit by some small fragments from the shattered glass diaphragm.

The leads were then fed by means of two Cannon plugs through the tank wall, and on the outside by copper-constantan thermocouple cables to the hot reference junctions, located in an underground steel box. From there the signals produced by the thermocouples were carried by copper cables to three CEC recording oscillographs. These recorders were operating at a chart speed of 40 in./sec for experiment 278 and at 160 in./sec for experiment 282.

The data obtained by the above instrumentation and methods are shown in Figure 56 for a few thermocouples; Figure 56A giving traces from initiation of failure to some time after detonation; Figure 56B showing only the time increment during which mixing starts and indicating the passage of the reaction and shock fronts.

Analysis of the data from these two liquid propellant explosion

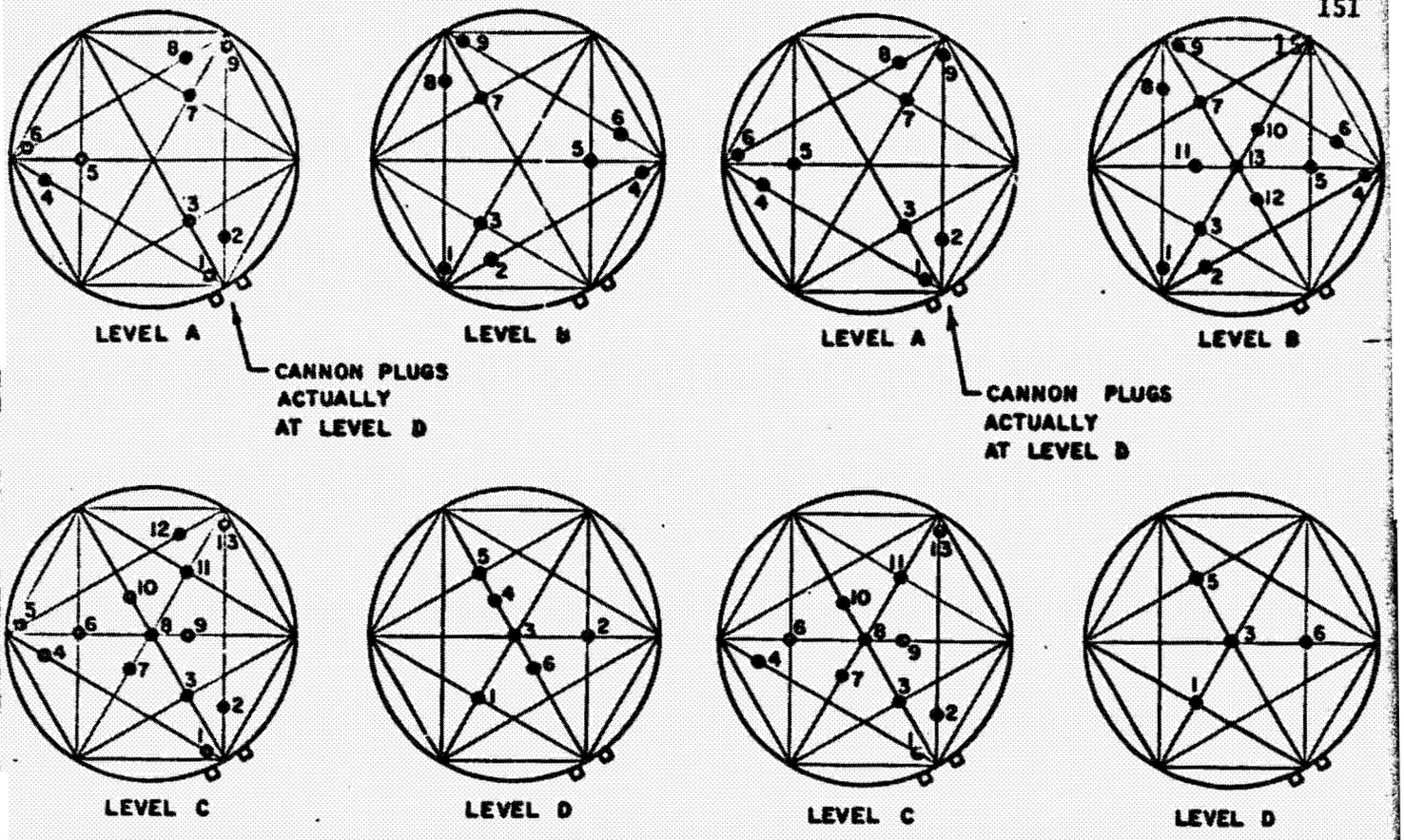

Fig. 54A
Thermocouple Locations. Experiment No. 278.

Fig. 54B
Thermocouple Locations. Experiment No. 282.

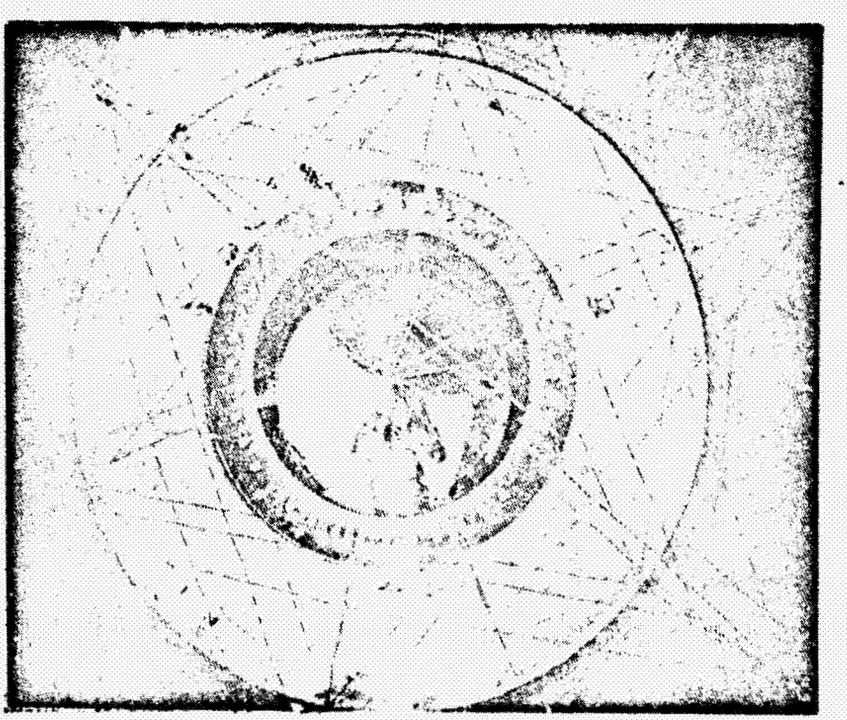

Fig. 55
Thermocouple Grid in Tank

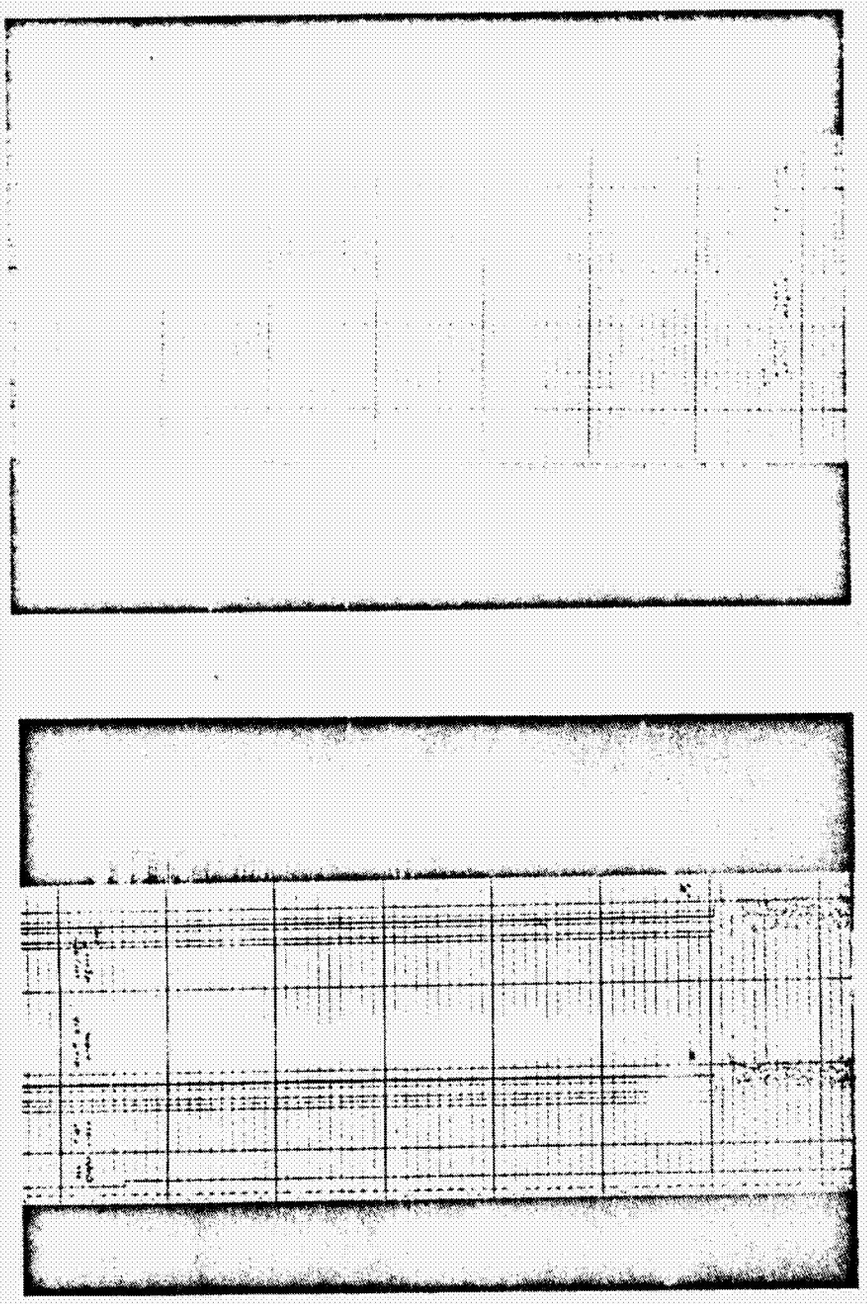

Fig. 56A
Oscillograph Traces. Experiment No. 278.
Complete Interval from Initiation of Failure to Detonation.

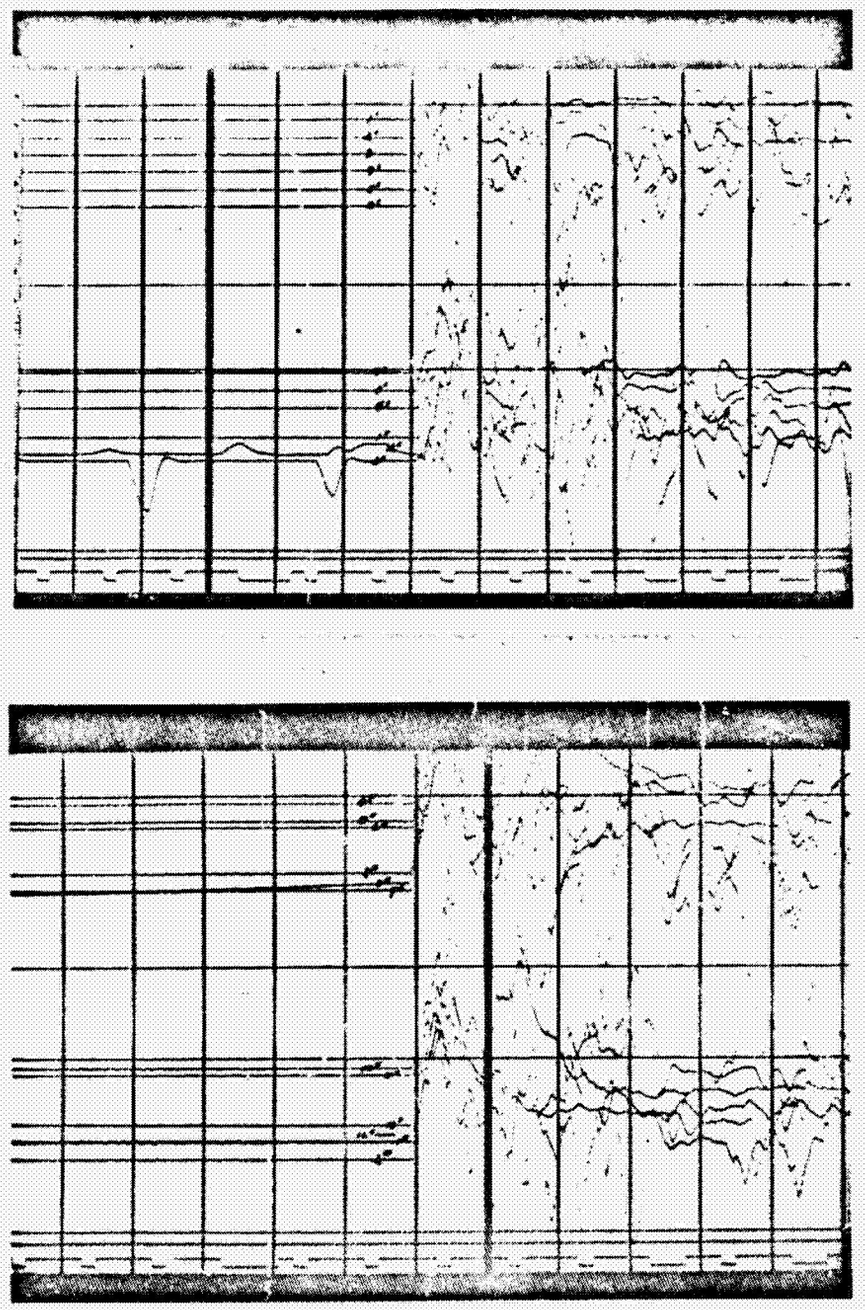

Fig. 56B
Oscillograph Traces. Experiment No. 282.
Ignition and Events Following.

experiments allow the following statements to be made:

1. Experiments No. 278 and 282 were amazingly similar in propellant mixing, ignition and explosion characteristics.
2. Practically all the mixing up to the time of ignition was confined to the volume swept through by the star cutter. This volume as determined from the data was about 12 percent of the total, based upon the RP, giving an upper yield estimate of about 12 percent of the theoretical maximum or somewhat less than 15 percent TNT equivalent.
3. The actual temperatures as recorded by the traces allow the calculation of the degree of mixing by means of a number of simultaneous equations which can most conveniently be solved by computer.
4. The degree of turbulence at a particular point (the points where the thermocouple junctions were located) can be determined from the fluctuations and fine structure of the traces in terms of frequency and amplitude.
5. There was only one point of ignition in each of the experiments and this point was located in each case (Figure 57A and 57B).
6. The time delays between various events can be determined from the traces. If projected on a screen these times can be read to a 1/1000 of a millisecond. The time delay from failure or firing of of the ram to ignition in experiment 278 was 543 milliseconds and in experiment 282 it was 580 milliseconds (read to the closest millisecond. Greater accuracy is available if desired).

The accurate reading of these delay times also allows the exact

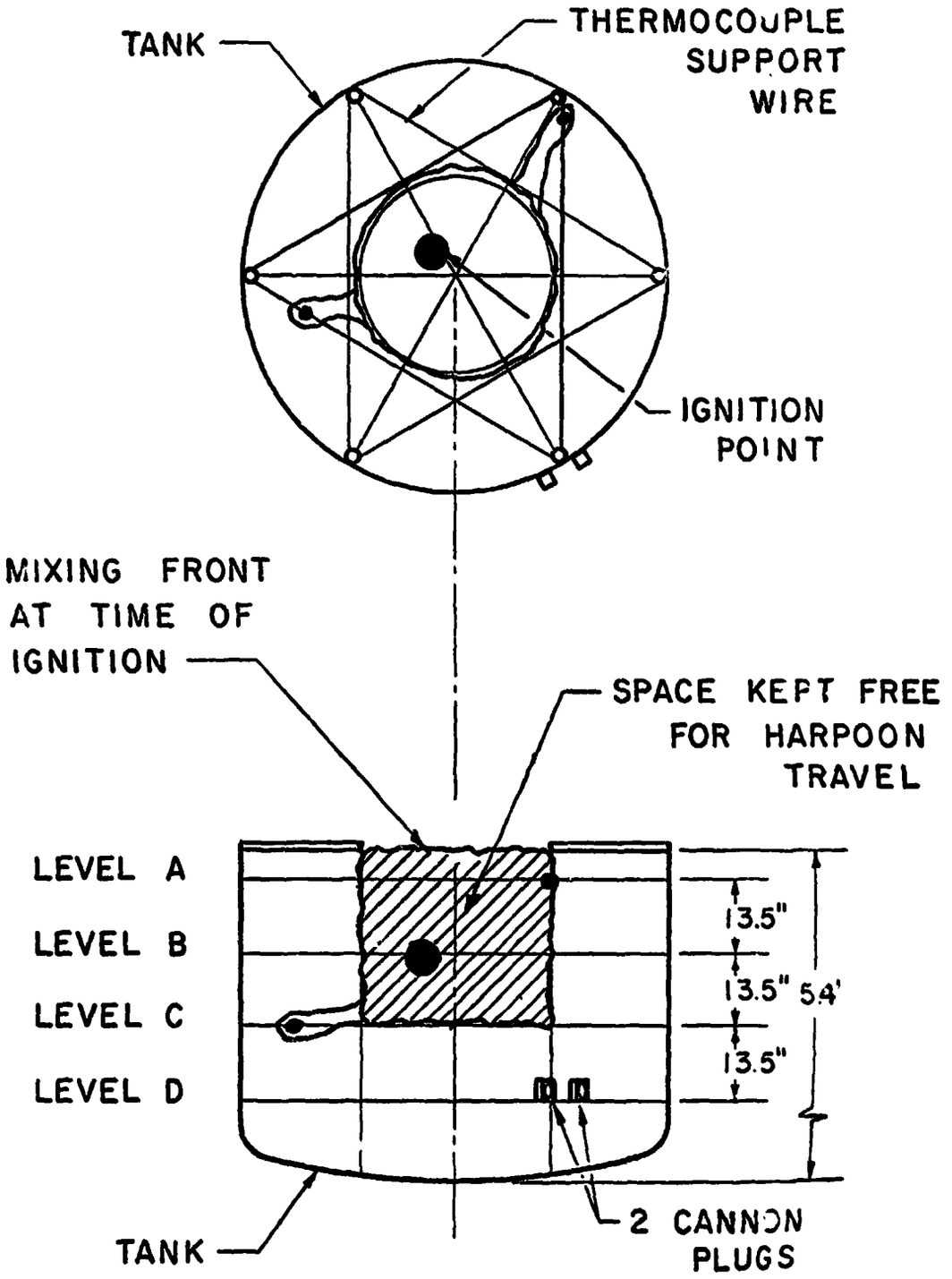

Fig. 57A
Mixing Front and Ignition Point. Experiment 278.

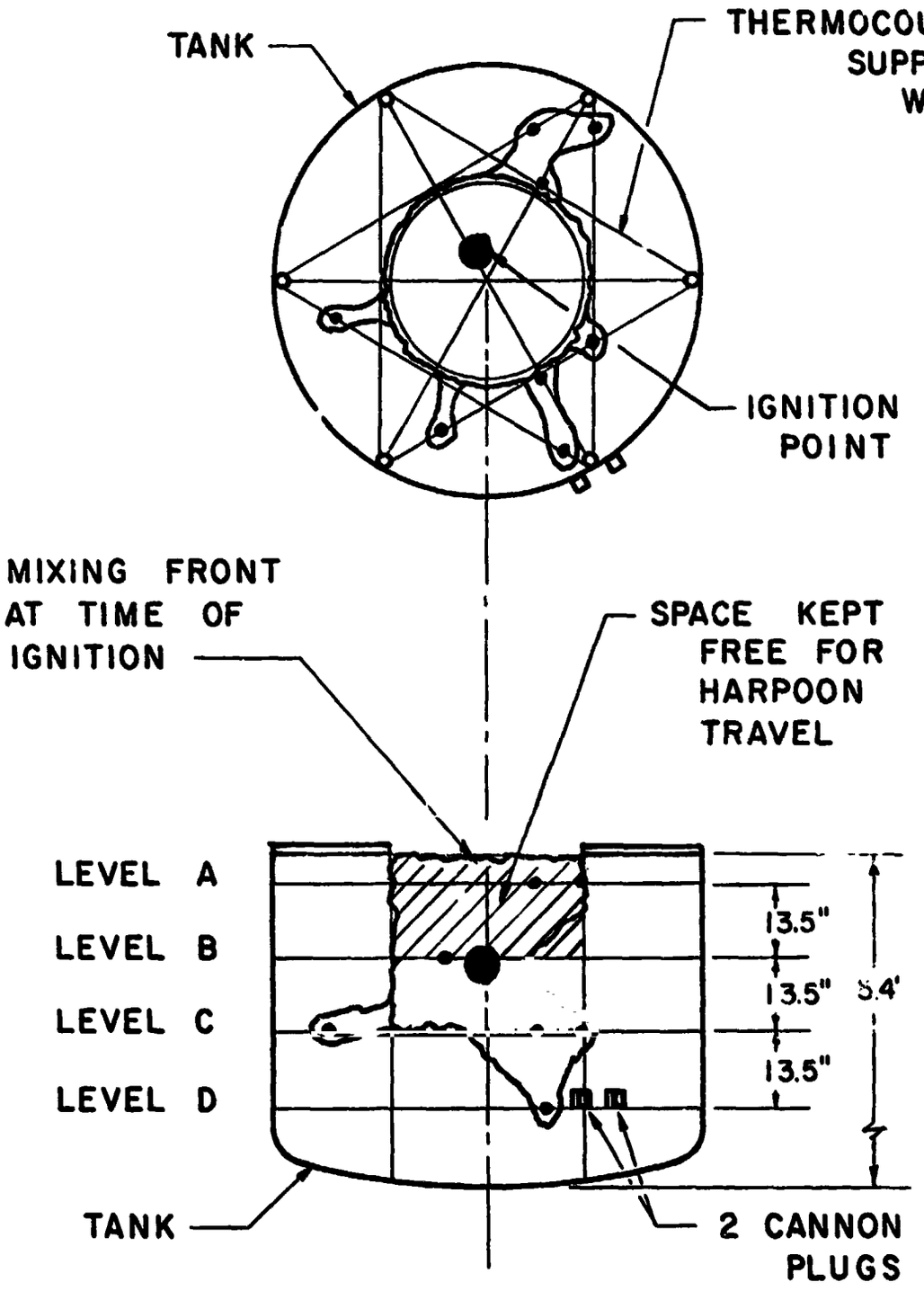

Fig. 57B
Mixing Front and Ignition Point. Experiment 282.

determination of the film speeds of the various cameras used. The importance of this is brought out, since none of the cameras operate at their nominal speeds and vary from one time to the next. For instance, the two 4000 fps cameras during experiment 282 were operating actually at 2620 fps and 3750 fps respectively.

7. The propagation velocities of the reaction front and shock front could be determined and the analysis gives the results shown in Figure 58.
8. By careful study of the fine structure of the traces the shock front propagation characteristics can be determined.
9. From (7) (8) above it can be determined where the two fronts travel together and where and when the shock front leaves the reaction front behind.
10. With the delay times exactly determined and the film speeds known, then the volume-time or volume-distance characteristics of reac- and shock fronts can be determined (Figure 59).
11. The fine structure of the traces reveals that some of the glass fragments from the shattered diaphragm hit some of the thermocouples in the uppermost of the four layers but did not damage them, so they recorded this and later events. The glass fragments did not penetrate during their high energy state to the lower layers since the attenuation in the liquid was too great.
12. From the fine structure of the traces, at least three typical shapes are observed, Figure 60. The first is caused by the arrival of the LC followed by the reaction and shock fronts; the second is caused

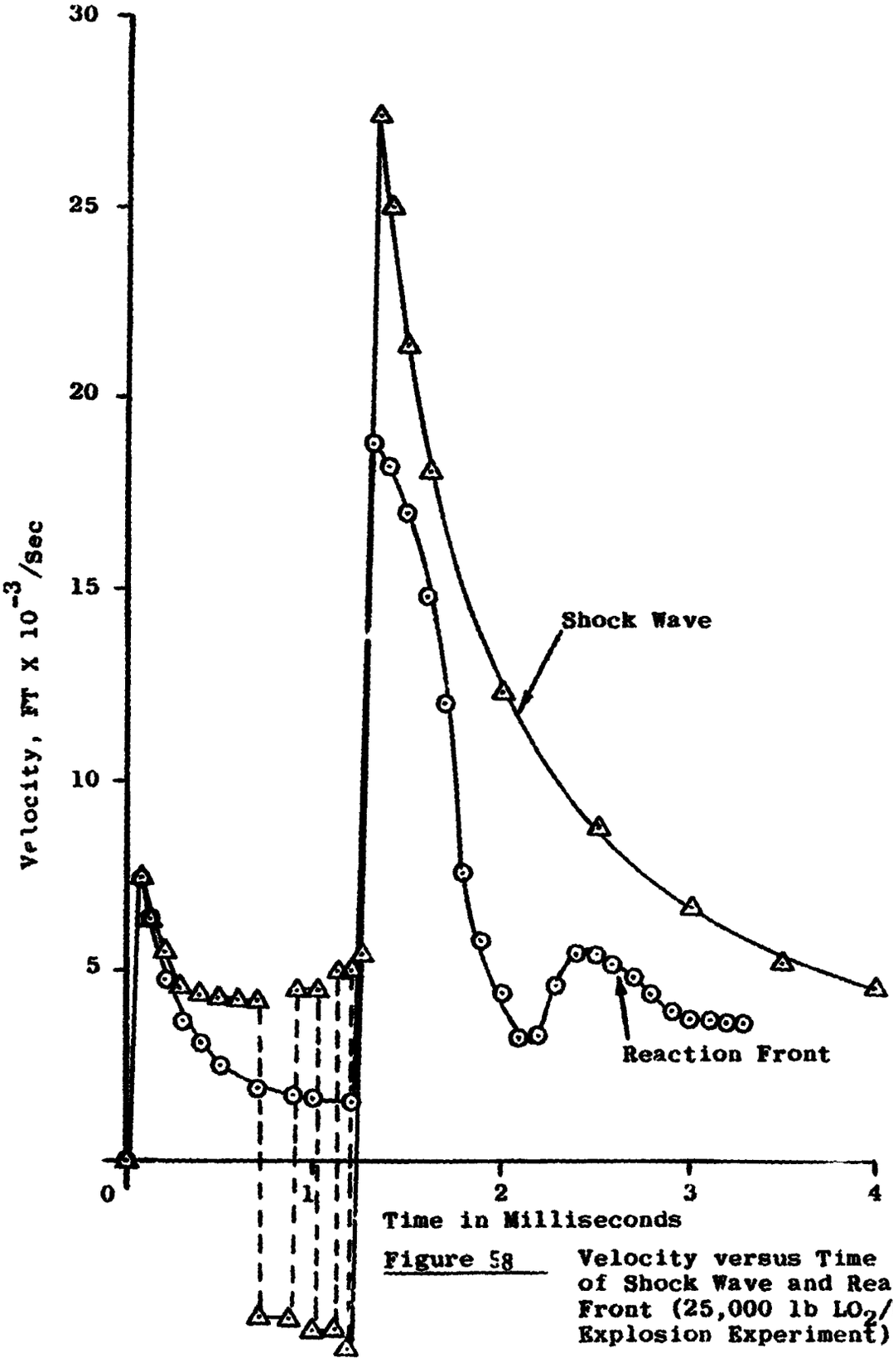

Figure 58 Velocity versus Time of Shock Wave and Reaction Front (25,000 lb LO_2/RP-1 Explosion Experiment)

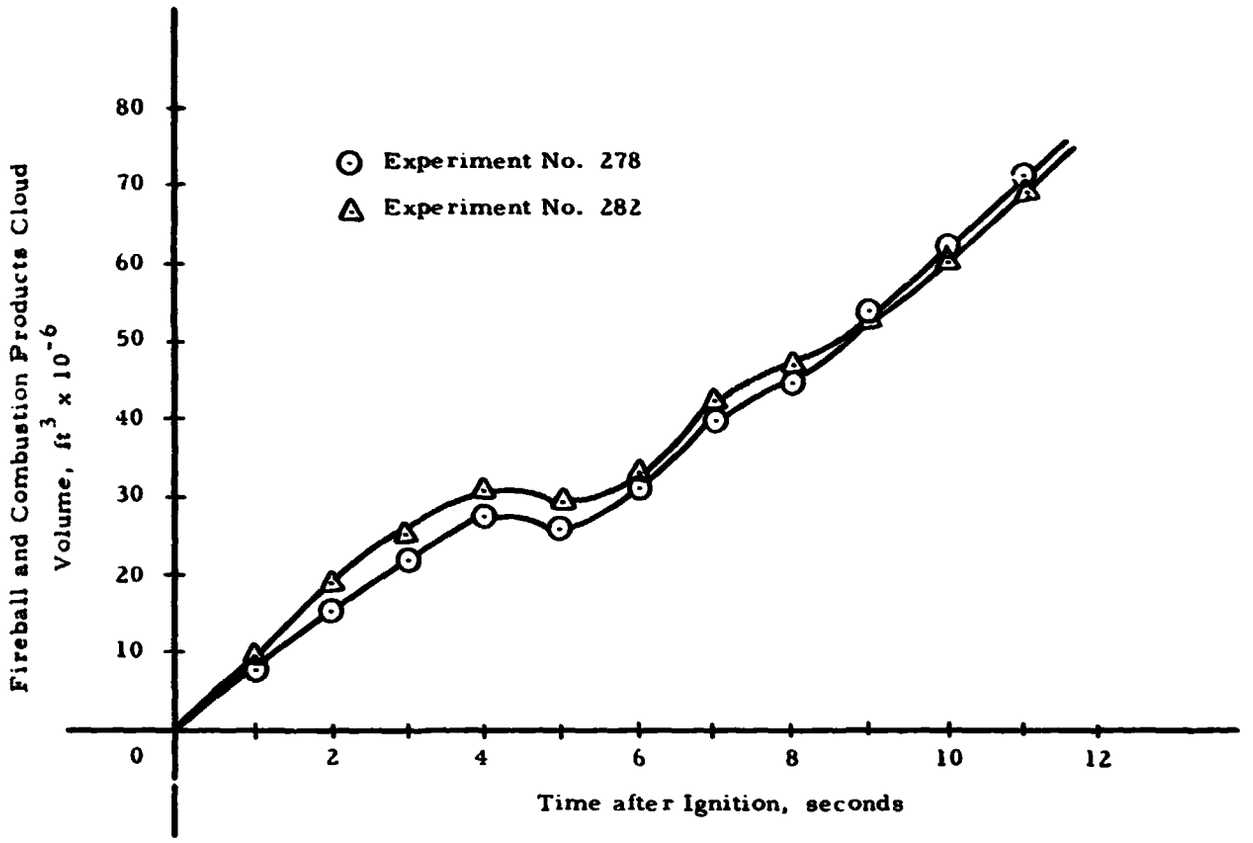

Fig. 59
Fireball and Combustion Products Cloud Volume as a Function of Time.

Sketches of Typical Thermocouple Traces
(Temperature versus Time)

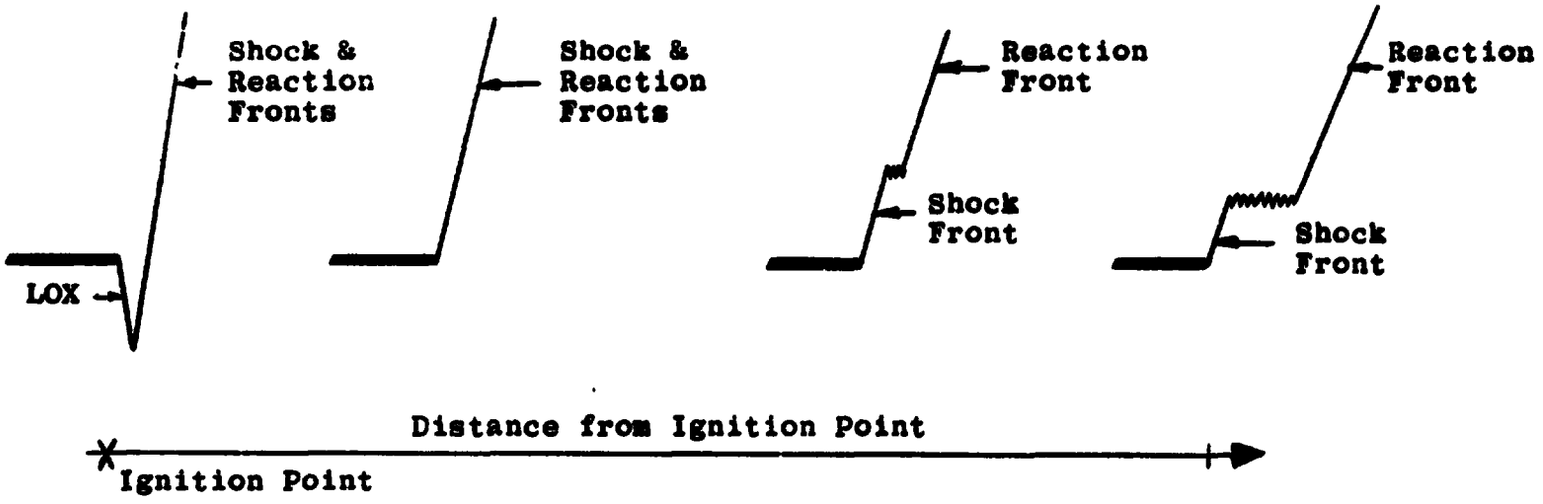

Figure 60 Typical High Speed Thermocouple Traces

by the reaction and shock fronts arriving simultaneously at the thermocouple, and the third is caused by the shock front arriving first closely followed by the reaction front.

The above statements are only a few of the many which could be made in extracting information from these experiments.

Simulating the configuration and the mode of failure of the 25,000 lb. LO_2/RP experiments in the laboratory produced the curve shown in Figure 61. It again shows the typical quick rise and then the two typical humps for this type of failure. Naturally in the actual case the curve after the ignition point did not exist.

The ignition point was determined by the critical mass technique which indicated that when 2900 lb. of the propellants are mixed, ignition is a certainty. Thus both the quantity and the ignition time were pinpointed and then plotted on the mixing curve. Again perfect agreement is found between the experiments in the laboratory and the results obtained in the actual explosive field tests.

Taking 2900 lb. and dividing it by 25,000 lb. or the total quantity of propellants present gives an indication or prediction of explosive yield of 11.6%. This value can be compared to the value which was measured, namely 12%.

200 lb. Cold Flow Experiment

To actually compare the mixing characteristics of the inert fluids used in the laboratory for simulation and the explosive liquid rocket propellants a 200 lb. LO_2/RP experiment was completely instrumented in

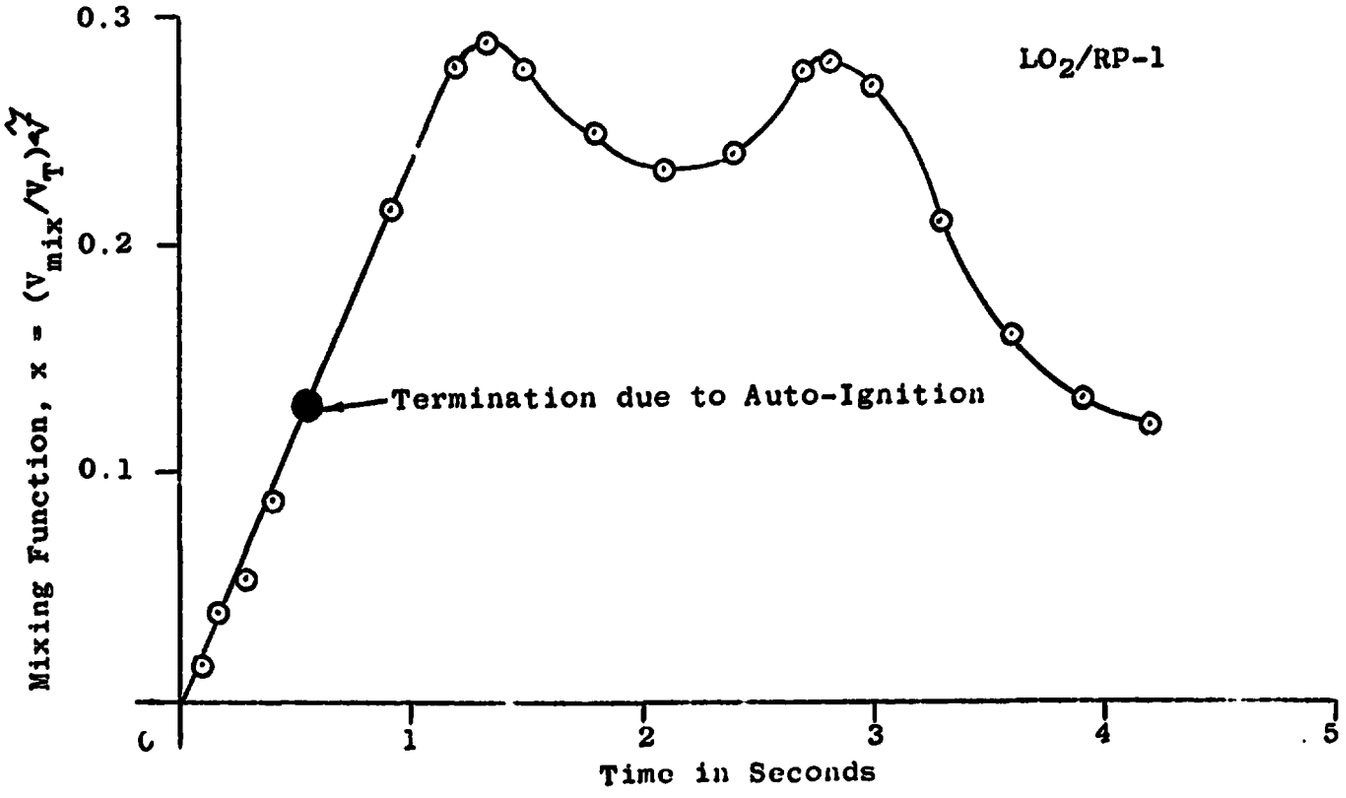

Figure 61 Mixing Function, 25,000 lb Explosion Experiment (Based Upon 3" Diameter Simulated Experiment)

the same manner as the 25,000 lb. experiments.

An explosion was not expected in this case and so the mixing process could be followed for a much longer period, as a matter of fact until the mixing actually stopped due to sludge formation.

Again the cutter volume had to be excluded from the analysis but the results were in excellent agreement with the curves obtained for the simulation, Figure 62.

The mixture was then set off by an explosive bolt and the yield actually measured was the same as predicted.

The S-IV B LO_2/LH_2 Explosion Experiment

To see how a prediction based on the simulation of the S-IV B explosion experiment would compare with the actual measurements, the mixing function was determined for the above configuration and the corresponding mode of failure, Figure 63.

The ignition time was determined again as in the previous predictions by the critical mass method and thus was plotted on the mixing function curve which is the yield curve in the early stages.

From the simulation it was shown that the mixing occurred with two distinct larger humps but which even at their peak values are relatively low and then stabilizes to an almost constant value. This is due to the evaporation occurring essentially at the same rate as new propellants are added to the mixture.

The explosion occurred again very early thus not allowing large values of yield to be obtained.

This self-limiting phenomenon is fortunate since large explosions with liquid rocket propellants are almost impossible to obtain.

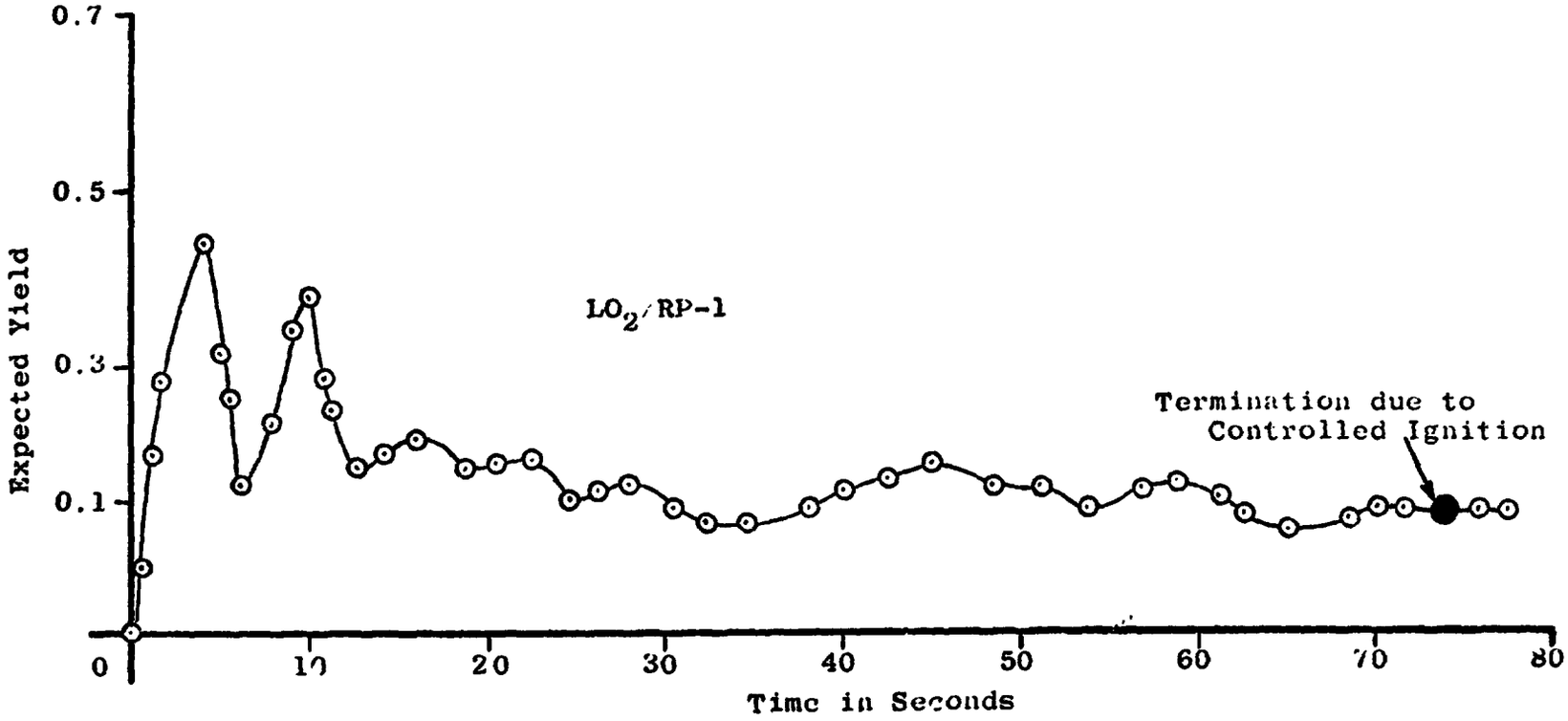

Figure 62 Expected Yield as a Time Function
(200 lb Cold Flow and Explosion Experiment)

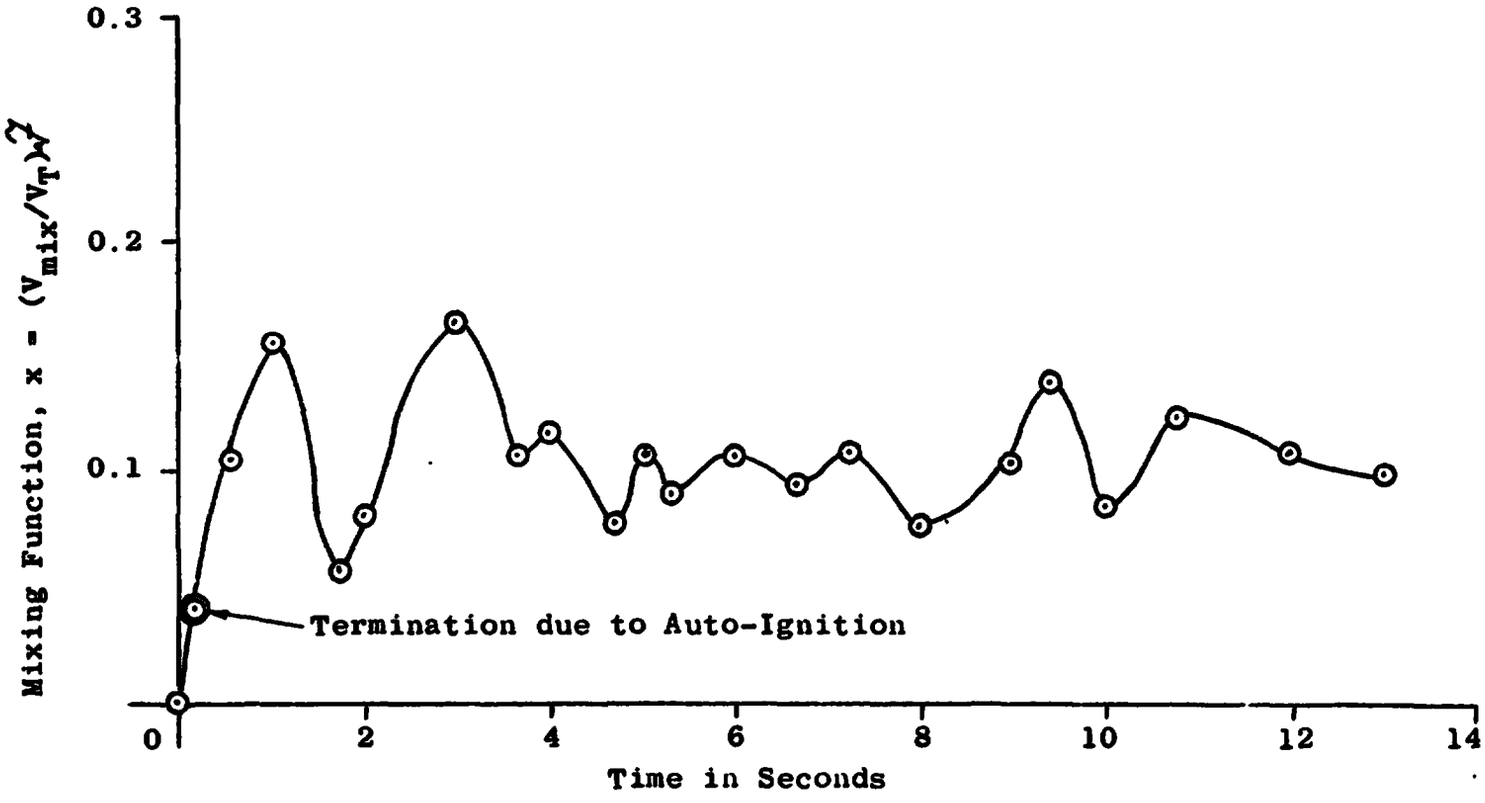

Figure 63 Mixing Function, S-IV LO_2/LH_2 (Based upon 3" Diameter Simulated Experiment)

The ADL Spill Explosion Experiments

The work done with liquid rocket propellants by Arthur D. Little, Inc.[6] was to determine the explosive yield obtainable with liquid rocket propellants. The experiments were designed to give very good and rapid mixing so as to obtain large yields.

When small quantities of propellants were used the ignition time could be controlled and was varied. It was observed that early ignition produced small explosive yields, and late ignition produced small explosive yields. In between a maximum value was observed.

When large quantities were used in the experiments early ignition always occurred due to self-ignition and the yields obtained could not be controlled.

Again the mixing function was obtained in our laboratory and with the critical mass method, considering the higher mixing energy available, and the ignition time was determined. This time could also be checked against the measured value, Figure 64.

Again excellent agreement between the predictions and the actually measured values could be observed.

Electrostatic Charge Generation and Auto-Ignition Results of Liquid Rocket Propellant Experiments

It has been observed that when large quantities of liquid fuels and oxidizers are brought together, either during experiments or accidentally, liquid propellant explosions result.

Many different phenomena can trigger these explosions such as flames, sparks produced by striking or breaking metal, hot materials or

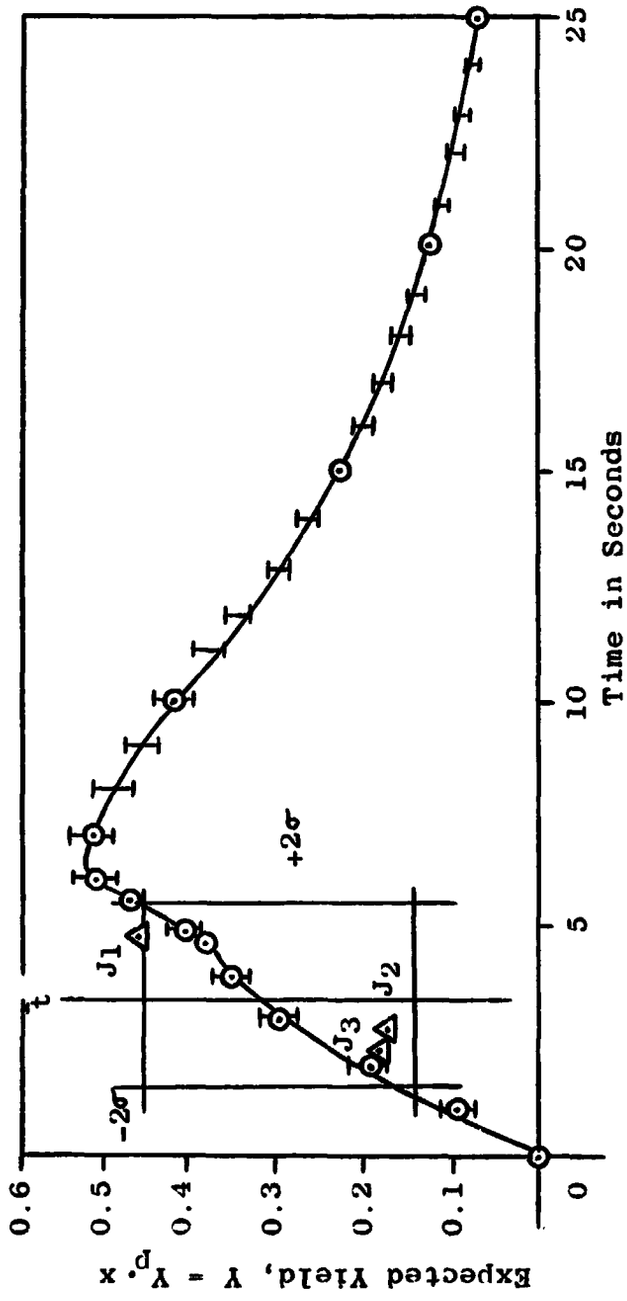

Figure 64 Actual Yield for Random Ignition and Detonation Showing the Upper and Lower Limits of the Statistical Confidence Regions for Liquid Propellant Spill Tests

hot spots produced by slow chemical reactions of fuel and oxidizer, the breaking of crystals which are formed when one of the liquid components freezes the other and which are broken mechanically or by thermal stresses, or by static electricity which is the result of internal friction and which may produce a spark discharge.

Many more possibilities could be cited but these additional sources do not change the basic picture.

Thus if there is contact or mixing of a liquid fuel with a liquid oxidizer, ignition is possible if an ignition source is available. If not, the mixing process may proceed with more and more of the fuel and oxidizer mixing until an ignition source appears either through external or internal action.

The Critical Mass concept was developed earlier[75,104,116,118] as also shown in detail in section I-C. Figure 65.

2. KSC Auto-Ignition Experiments

The following presents verification of the theory and predictions which were made earlier[1,2,3,4,24,75,79,104,116,118] through experimentation and measurement of the critical parameters involved in the real explosive Liquid Rocket Propellant combinations.

For the actual explosive experiments which were planned and then carried out at the Kennedy Space Center, the experimental procedure had to be modified as well as the equipment. Since the experiments had the potential of an explosion (although none or only a very few were expected with this quantity) precautions requiring remote operation had to be taken.

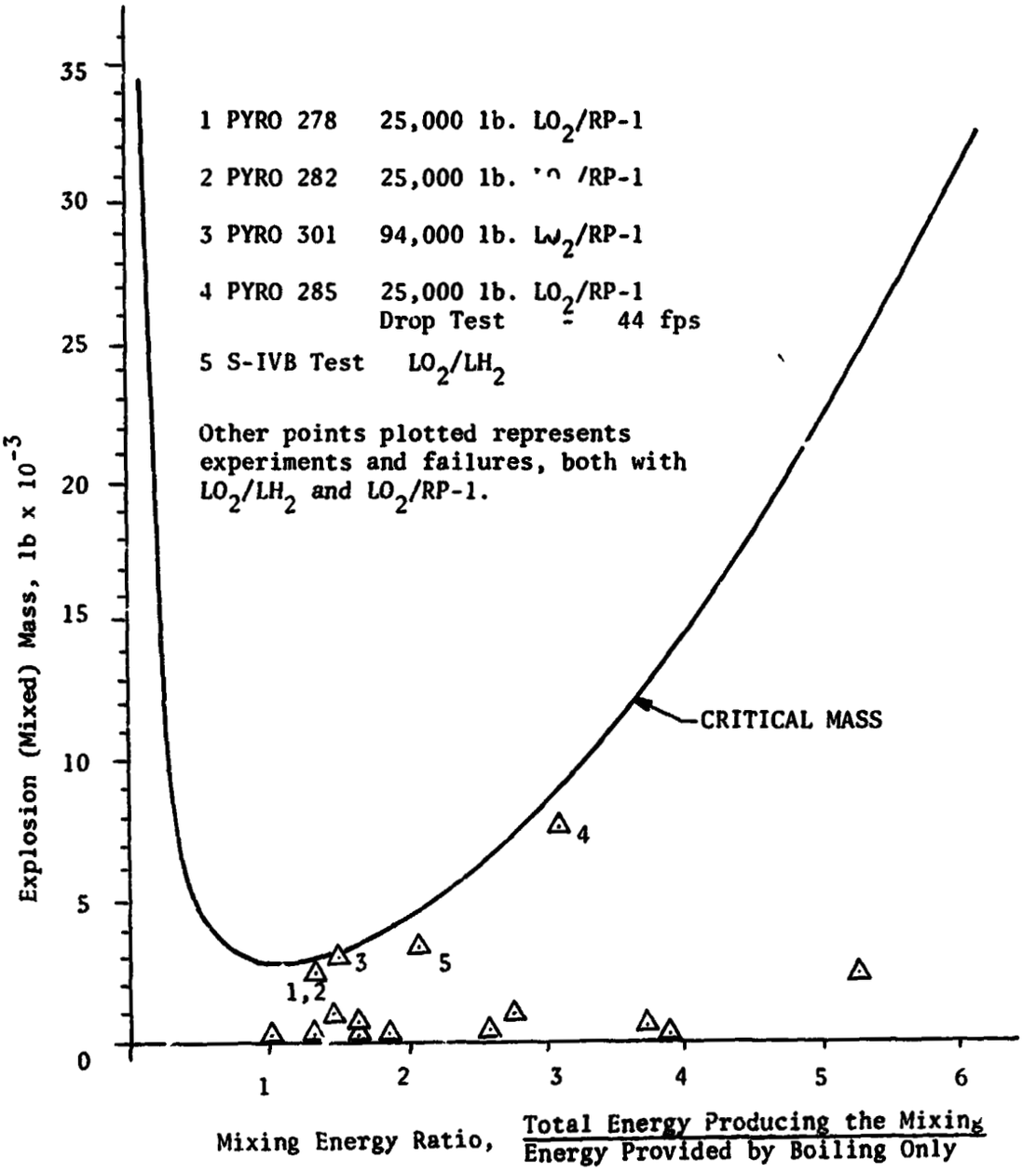

Fig. 65 Explosion Mass - Mixing Energy Relationship

A test set-up was designed, consisting essentially of two cylindrical containers, a larger one on the bottom and a smaller one on top. The exact dimensions were, Lower Tank: 12 3/4" O.D.X. 12 3/4" high, Upper Tank: 8 3/4" O.D.X. 8 3/4" high.

The top tank was hinged so it could tip and pour its contents into the lower tank. See Figure 66. Both tanks had lids and were thermally insulated so as to reduce the evaporation losses of the cryogenic liquids used as fuels and oxidizers.

Temperature probes, consisting of stainless steel sheathed thermocouples, two in each of the tanks, were used; these monitored the liquid levels in the tanks so that proper quantities were in each tank at the time an experiment was started.

The lower tank was fitted with two copper screens, approximately one inch apart, spaced so that they would be surrounded by the mixing region during the experiment. These screens formed the electrodes to measure the charges and voltages generated due to the mixing processes. The signals from the probes and screens were transmitted through amplifiers to the instrumentation van where they were recorded on strip charts and tape. Figure 67 shows the screens installed in the lower tank.

The test set-up allowed experimentation with any one of the propellants in either tank.

The experimental procedure, described in greater detail in the appropriate section, was to fill each tank to the desired level, then by remote operation:

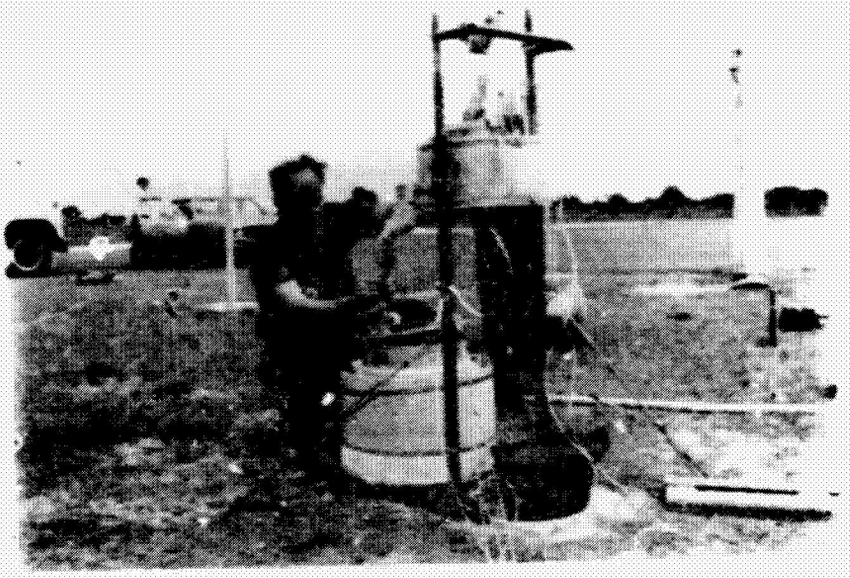

(a)

(b)

Fig. 66 The Six Pound Experiment

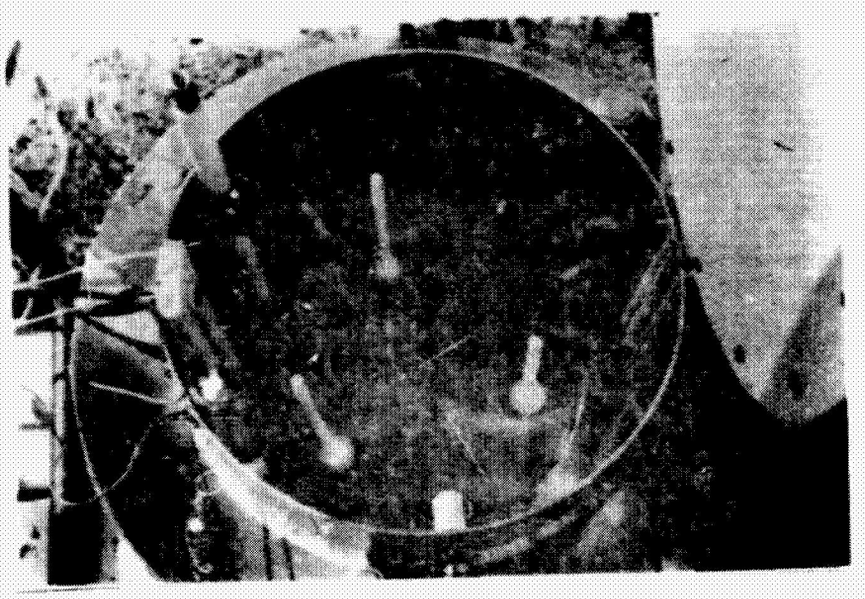

Figure 67 Screen Installation in Lower Tank

6 lb Experiment

1. Lift the lid of the lower tank
2. Pull the safety pin on the upper tank
3. Dump the upper tank

Records of the probe temperatures and screen voltages were made during the above procedure.

The 60 Pound Explosive Experiments

The test set-up for the sixty pound experiments was essentially the same as for the six pound experiments except that the tanks needed were considerably larger. The dimensions were, Lower Tank: 27 1/4" O.D. x 27 1/4" high, Upper Tank: 18 1/2" O.D. x 18 1/2" high.

Figure 68 gives the experimental arrangement for this series of experiments with the instrumentation part being the same as for the smaller tests except that the stainless steel probes which had proved to be erratic and slow in response were replaced with exposed small thermocouples and the screens were larger in diameter.

The actual operation and running of the experiments was slower since larger quantities of cryogenic fuels and oxidizers were involved requiring longer chill-down and filling times as well as longer warm-up times after the experiments were conducted.

The 240 Pound Explosive Experiments

While no actual explosions were expected with the six pound experiments, maybe one or two with the 60 pound experiments (although none occurred for the number of experiments carried out), about one out of ten experiments with the 240 pound quantities was expected to produce an explosion.

Fig. 68 The 60 Pound Experiment

Fig. 69 The 240 Pound Experiment

The experimental set-up was essentially the same. See Figure 69. The tank sizes were, Lower Tank: 43 1/4" O.D. x 43 1/4" high, Upper Tank: 30 1/4" O.D. x 30 1/4" high. The exposed thermocouple type probes used in the 60 lb. test had not always been able to distinguish between the vapor and the liquid; therefore, these were replaced with heated thermocouples. These would remain cool in the liquid but would heat up rapidly in vapor where the heat gain was considerably larger than heat loss. Also the times for chilling-down, filling, stabilizing, dumping, and then warm-up after each experiment were considerably longer.

Fluidic Oscillator Gas Sensors

As an additional experiment not directly connected with the measurement of the electrostatic charge and voltage generation, fluidic oscillators, developed under a separate phase of this contract were used to monitor the H_2 cloud produced by the experiments.

Figure 70 shows one of the earlier designs of this very simple device which can instantaneously detect a change in the density of a gas going through it, indicating the concentration of another gas.

The device is simple, easy to make, and inexpensive. A transistor radio earphone can be used as the transducer to change the frequency impulses from the oscillator into an electrical signal which can be heard, displayed on an oscilloscope and/or recorded on tape.

The oscillator frequency produced by the gas flowing through the device by applying a vacuum indicates the gas mixture and its concentration. A separate report is being written on this part of the work.

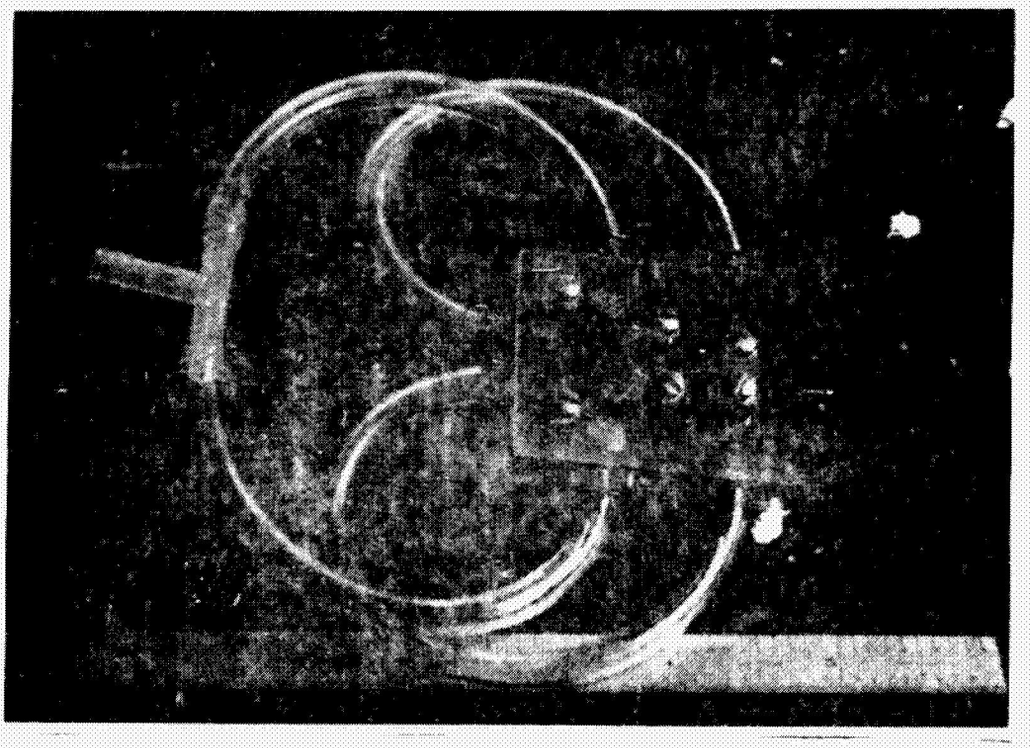

Figure 70 The F-1 Fluidic Oscillator

Experimental Procedure

General: The experimental procedure was designed to allow the filling of the two tanks of the experimental set-up to the required liquid levels and then allow the dumping of one of the components into the other with the resulting voltage and charge generation being measured.

To accomplish this a test procedure had to be written since many people from different support groups were involved at Kennedy Space Center; this procedure had to be agreed upon and approved by everyone concerned.

Evaporation or Boil-Off Experiments

The first step in the procedure was to determine the heat losses from the two tanks so that the filling and holding procedure and timing could be worked out.

Theoretical calculations were made on the evaporation rates of the cryogenic components and they were experimentally verified. The probes, two in each tank were set a certain distance apart and then the tanks were filled to the upper probe and the time determined for the liquid level to drop to the lower probe.

This was done for LN_2, LO_2, and LH_2 for each of the tanks in the 6, 60, and 240 pound experimental configurations.

Actually these boil-off experiments were carried out at the beginning of each of the series involving different quantities.

Charge Generation and Auto-Ignition Experiments

On the morning of each test day the calibration of the instrumentation was verified and the equipment was checked to see that it was recording properly.

1. to open the lower tank lid
2. to pull the safety pin of the upper tank
3. to dump the upper tank

The high speed camera and the documentary camera were started during the countdown. The recording instrumentation which was running all through the filling operation at low speed was switched to high speed during the countdown to produce maximum resolution for the data taken during the actual experiments. Figure 71.

After completion of the test it was necessary to wait until the cryogenics vaporized before one could safely approach the test equipment, check it over, and ready it for the next experiment.

This procedure was followed in each case for all the charge and voltage generation auto-ignition experiments.

In all cases the LO_2/LH_2 experiments were carried out first since both the LO_2 and the LH_2 vaporized without leaving traces of their presence and no cleaning operation was necessary. When RP-1 was used some of it froze and the waiting period until a-l the LO_2 vaporized and RP-1 gel melted was considerably longer. It also was necessary to remove any RP-1 which splashed into the upper tank which was to be filled with LO_2 for the next test.

Data and Results

In this section the data and the results of the various experiments will be briefly reported and the significance and deeper meaning of these results will be discussed in the next section.

Figure 71 The Instrumentation Van

The documentary and high speed remote controlled cameras were loaded and readied for the experiments.

With these tasks completed the chill-down of the tanks was started. LN_2 was used first to conserve LO_2 and LH_2. The tanks were both partially filled with LN_2 and this LN_2 then allowed to vaporize; this pre-cooled the equipment for the experiments.

Regardless of whether the LH_2 was to be in the upper or lower tank for the particular experiment the LH_2 flow was started and the liquid level monitored. It took considerable time before the probes showed liquid levels. The lower probe was set at the level required for the experiment and the upper probe at the level to which the tank had to be filled to offset evaporation losses and have the correct quantity of liquid in the tank at the time of dumping.

When the liquid level reached the upper probe the signal was given to terminate flow; then the LH_2 tanker truck was shut off, disconnected and driven away. This operation took from two to three minutes.

When the LH_2 tanker had cleared the hazard zone the signal was given by the safety director to start the LO_2 flow into the second tank. Again the liquid levels were monitored and this tank was filled to the upper probe and held at this level until the relative timing between the two tank levels was right so that with the proper count-down the liquid levels in both tanks were at the correct level at the moment of dump.

At the command "dump", three control cables were pulled in sequence:

Evaporation and Boil-off Experiments were necessary to predict the proper timing of the experiments. Evaporation losses occurred in both tanks when filled with cryogenics; safety considerations required these tanks to be filled sequentially. For this reason, theoretical calculations were made as to the rate at which the liquid levels dropped in the tanks and were then verified by experiment.

The results obtained were as follows:

	Calculated Rates	
Six Pound Experiments	Upper Tank	Lower Tank
LN_2	0.131 in/min	0.11 in/min
LO_2	0.08	0.067
LH_2	1.05	1.00
60 Pound Experiments		
LN_2	0.113	0.089
LO_2	0.07	0.055
LH_2	.86	0.72
240 Pound Experiments		
LN_2	0.084	0.08
LO_2	0.053	0.05
LH_2	0.67	0.06

Three different types of probes were used during the experiments. Each successive type was an improvement. Excellent agreement was shown between the experimentation and calculated values reported here.

Charge Generation and Auto-Ignition Experiments

The objective of this series of tests was to determine if electrostatic charges are generated and if so to find their functional relationship to other parameters. An important parameter involved in these experiments is the weight or mass of the propellants involved.

Six Pound Experiments

Figure 72 shows the actual traces from a typical experiment. Recorded on the graph are the upper and lower probe readings in each of the tanks and the generated voltage. Table II lists all the LO_2/LH_2 experiments. It should be noted that the actual voltage generated exceeded the range of the instrumentation in the first five experiments. In the first test the range was $\pm$ 100 volts, for the next four $\pm$ 1000 volts and for the remaining experiments $\pm$ 10,000 volts.

For the LO_2/RP-1 experiments the range was set at $\pm$ 10,000 and after the first eight experiments changed to $\pm$ 1,000 volts to obtain better resolution. Table III presents the LO_2/RP-1 results.

60 Pound Experiments

Figure 73 presents the actual traces of a typical experiment, again showing the temperature traces of the liquid level probes in both the upper and the lower tanks and the voltage generation trace indicating the "spike" voltage due to the mixing. Table IV presents the results for the LO_2/LH_2 experiments in which the LO_2 was poured into the LH_2. The voltage range was set at $\pm$ 20,000 volts. Table V presents the results for the LO_2/RP-1 experiments with the voltage range set at $\pm$ 1000 volts. The voltage range was then changed to $\pm$ 10,000 volts

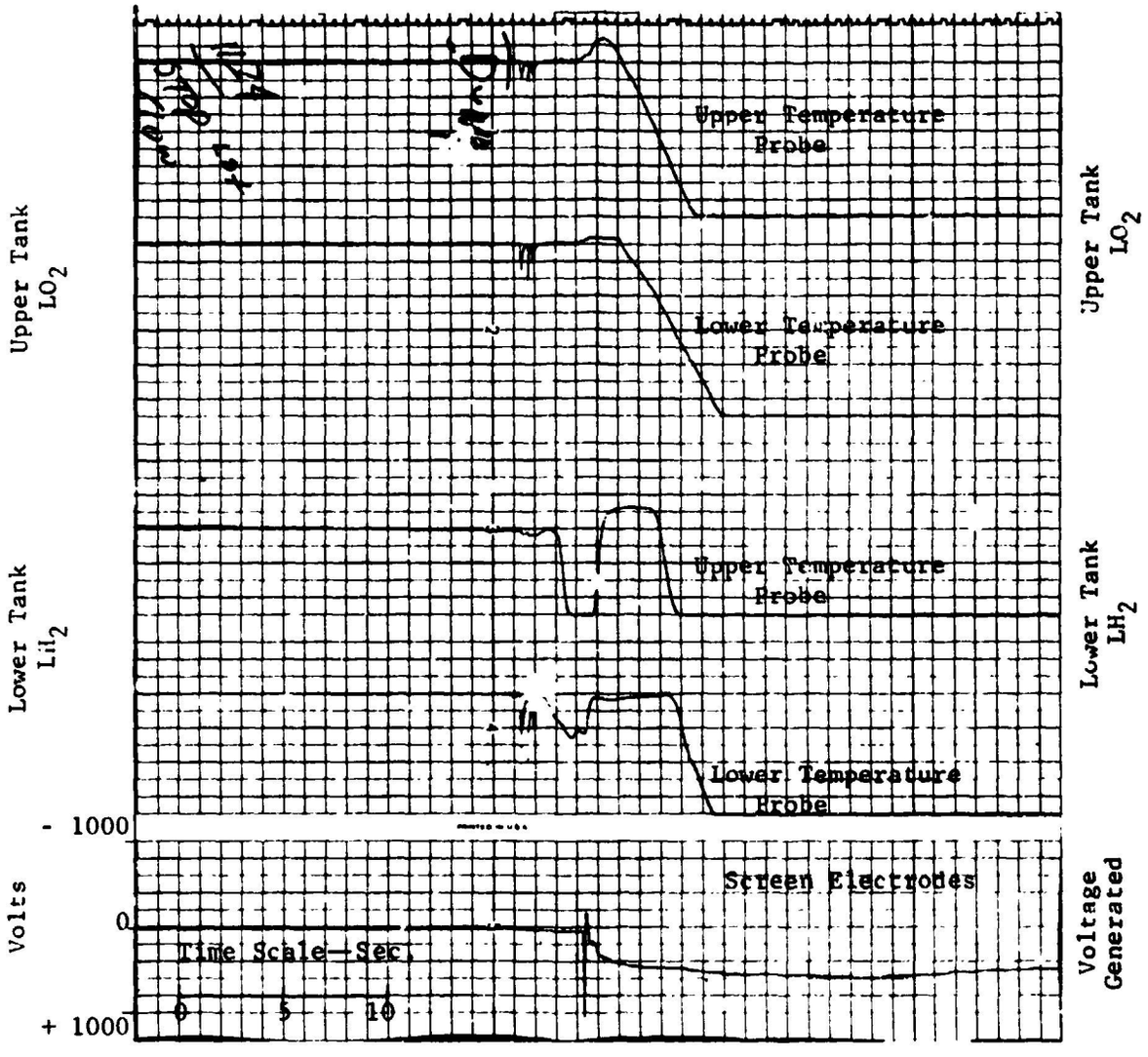

Fig. 72 Chart Traces from the Six Pound Experiment

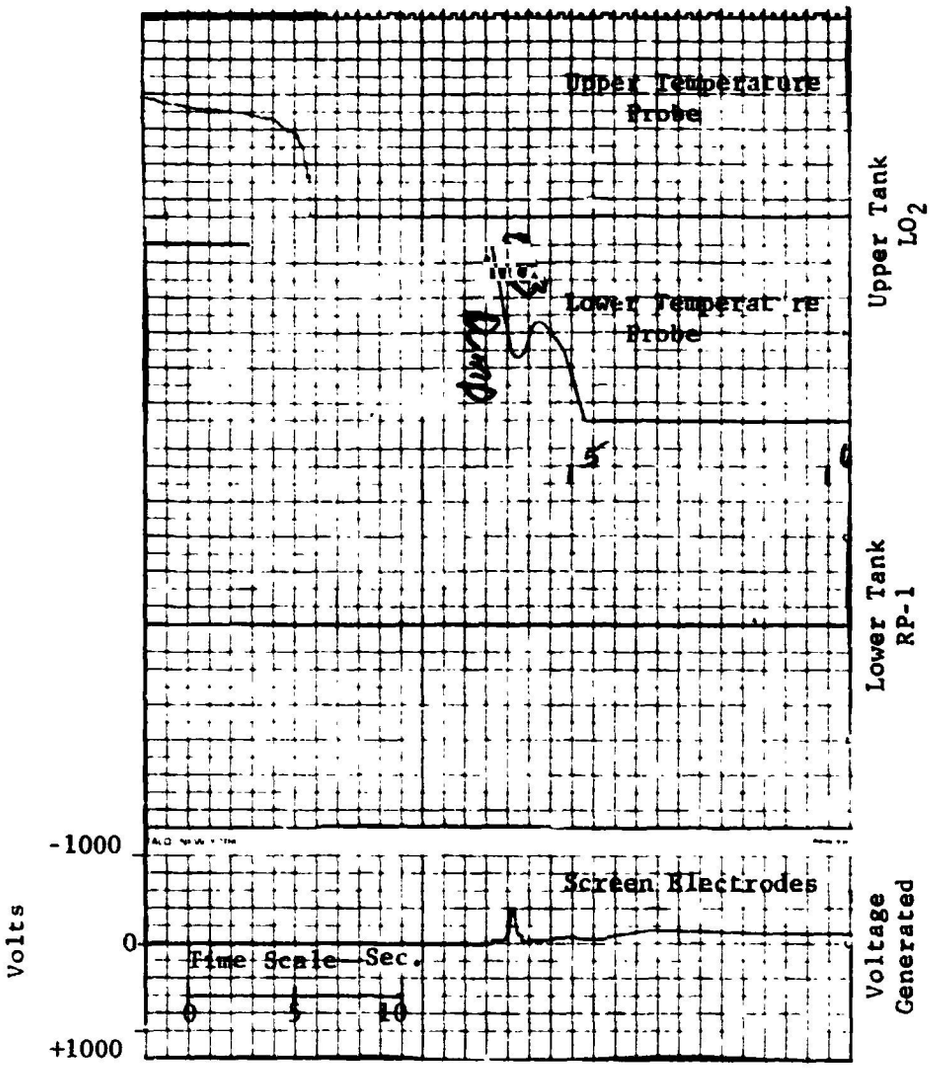

Fig. 73 Chart Traces for the 60 Pound Experiment.

TABLE II

Voltage Data from Six Pound LO_2/LH_2 Experiments
(LO_2 is Poured into LH_2)

No.	Date	Screen Diameter-In.	Voltage - Volts
1	1/12/72	11	+ 40
2			> +100
3	1/13/72		> +1000
4			> +1000
5			+ 350
6			> +1000
7	1/14/72		+4800
8			+2800
9			+1600
10			+6400
11			+2000

TABLE III

Voltage Data from 6 lb. LO_2 -- RP-1 Experiments

(LO_2 is poured into RP-1)

No.	Date	Screen Diameter-In.	Voltage - Volts
1	1/14/72	11	+400
2			+ 80
3			+800
4	1/17/72		+ 80
5			-350
6			-140
7			-350
8			-300
9	1/18/72		-240
10			-500
11			-720
12			-760
13			-120
14			-400
15			- 40
16			-200
17			-700
18			-680

TABLE IV

Voltage Data from 60 Lb. LO_2/LH_2 Experiments
(LO_2 is poured into LH_2)

No	Date	Screen Dia. - in.	Voltage--volts
1	1/27	25	+1200
2	1/28		+3200
3			+ 800
4	2/1		+ 800
5			+1600
6			+1600
7			+ 80
8	2/2		+ 400
9			+1600
10			+1100
11			+2800
12	2/3		+1620
13			+ 200
14	2/4		+1300
15			- 500
16			+1000
17			- 600

TABLE V

Voltage Data from 60 lb. LO_2/RP-1 Experiments
(LO_2 is poured into RP-1)

No.	Date	Screen Dia.--in.	Voltage--volts
1	2/11/72	25	-80
2			-400
3			-200
4			- 80
5			-160
6			-390
7			-380
8			-255

TABLE VI

Voltage data from 60 lb. LH_2/LO_2 Experiments
(LH_2 is poured into LO_2)

No.	Date	Screen Dia.--in.	Voltage--volts
1	2/15/72	25	-1000
2			-1000
3			-1000
4			- 500
5			- 500

for the LH_2/LO_2 experiments, Table VI. In this last set of experiments the LH_2 was poured into the LO_2 in contrast to the first series of experiments with 60 pounds of propellants where the LO_2 was poured into the LH_2.

The 240 Pound Experiments

In these experiments, the ones with the largest quantities of propellants used, the LH_2 was poured into the LO_2 in all but the last two tests. While in those two the LO_2 was poured into the LH_2.

Figure 74 presents the traces of a typical experiment and Figure 75 the traces of the last experiment in this series, carried out the morning of March 2, 1972, which resulted in auto-ignition and the predicted explosion.

Table VII and Table VIII give all the data for the 240 pound experiments with the voltage range set at $\pm$ 10,000 volts for the first day and at $\pm$ 5,000 volts for the remainder of the experiments. Since this series terminated with the explosion, no further runs could be made at this time and the LO_2/RP-1 experiments were postponed.

Discussion

The purpose of the LO_2/LH_2 and LO_2/RP-1 experiments was to verify the Critical Mass Hypothesis which is based upon an ignition source inherent in the mixing process or, in other words, one which will always be present whenever liquid propellants are mixed.

Among the many possible ignition sources, electrostatic charge generation with attendant measurable voltages is always present. This was shown in the laboratory with inert components such as LN_2 and RP-1

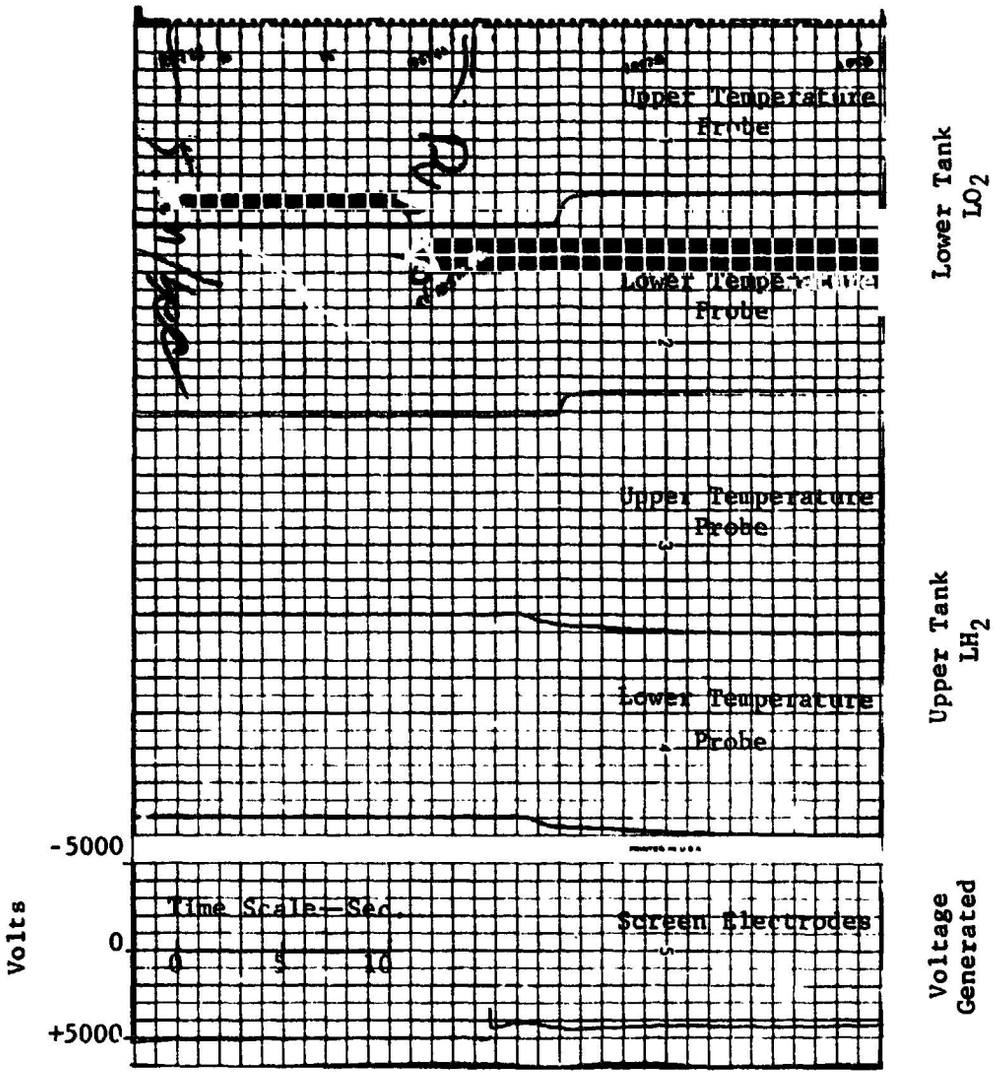

Fig. 74 Typical Chart Traces for a 240 Pound Test

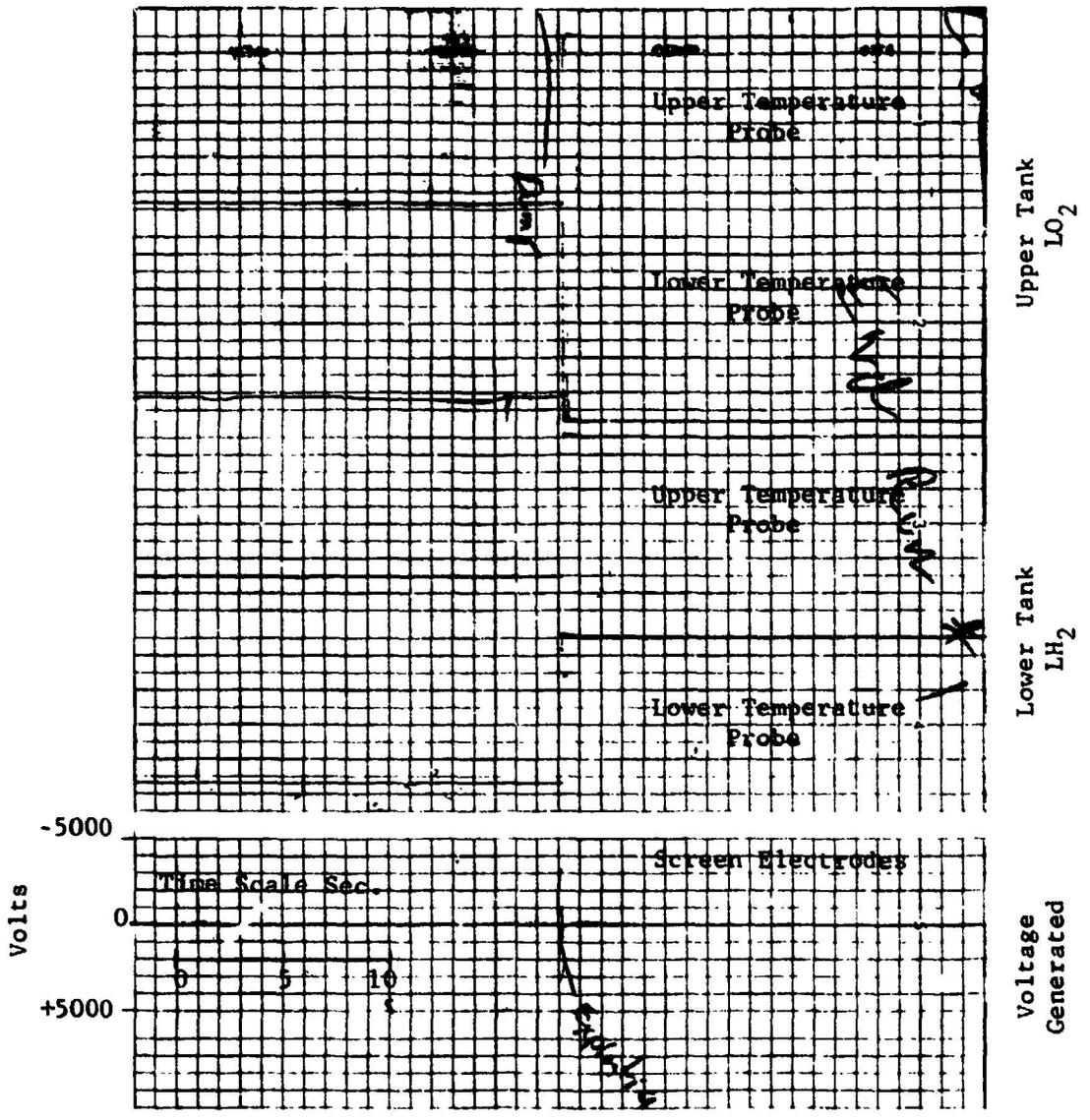

Fig. 75 Chart Traces for the 240 Pound Test Explosion

TABLE VII

Voltage Data from 240 lb. LH_2/LO_2 Experiment
(LH_2 is poured into LO_2)

No.	Date	Screen Dia. - in.	Voltage--volts
1	2/25/72	40	+ 400
2	2/28/72		+ 250
3			+ 600
4			- 200
5	2/29		- 300
6			- 300
7	3/1		$>$ -1700
8			$>$ -1300

TABLE VIII

Voltage Data from 240 lb. LO_2/LH_2 Experiment
(LO_2 is poured into LH_2)

No.	Date	Screen Dia. - in.	Voltage--volts
1	3/1	40	+1000
2	3/2		-3300
3	10/12		$\pm$ 300
4	10/13		$\pm$ 300
5			+2500 (Spike)
6	10/16		$>$ -5000 (Spike)
7	10/18		+2250
8	10/19		$>$ +5000 (Spike)
9	10/31		$>$ -5000 (Spike)
10			-3300 (Spike)
11	11/1		- 500
12			- 700
13	11/2		-2100

and others. The question, however, remained whether this would be true with the actual propellants used in these tests. All theory indicated that there should be the same basic behavior. The voltage and charge generated were predicted from the physical constants of the constituents and the formulation of a physical model, the "Fluid Plug Model", which lends itself to mathematical treatment[4,30,44,83,104,116].

Basically this is the concept that one fluid falls into the other like a plug and the heat transfer between them will vaporize the other proportional to the contact surface area. The vapor formed makes the fluid plug bob or oscillate giving it a motion similar to that observed in the laboratory with inert systems.

Then electrical analogy was used to transform the mechanical system into an electrical system. This allowed the determination of electrical properties such as voltages, charges, etc. The mathematical treatment involves basic heat transfer equations and vibration relationships coupled with the mechanical to electrical analogy.

The motion of one fluid layer across the other produced electric double layers of rather high voltages and since the constituents were good dielectrics these voltages built up until discharge occurred across one of the many bubbles formed in the mixing and boiling.

High speed photography of glass contained inert systems showed the size of the great majority of bubbles to be about 1/4 inch in diameter; from this the necessary charge to produce discharge and consequent ignition was determined.

The theoretical work and the inert laboratory experiments were

in excellent agreement and were reported in part in the "Prediction of Explosive Yield and Other Characteristics of Liquid Rocket Propellants"[75,104] by Farber, et. al. and in more detail in "Critical Mass (Hypothesis and Verification) of Liquid Rocket Propellants"[116] by E. A. Farber.

The tests described in this report were planned, coordinated, and executed at the Kennedy Space Center to determine how closely the previous theoretical and laboratory work predicted the actual behavior of the real potentially explosive rocket propellants.

The most important relationship predicted both by theory and laboratory experiment was that there exists a limit to the amounts of liquid propellants which might be mixed without an explosion. Thus there is an upper limit to the size of explosion which can be produced regardless of the actual quantities of propellants present. The propellants not taking part in the explosion may contribute to the subsequent fire.

To show this relationship between charge generation and mass, tests were planned with quantities of 6, 60, and 240 pounds of propellants and if necessary with 5,000 and 25,000 pounds.

The Six Pound Experiments

These tests were the first ones in the series. Because of the small size they were easiest to handle, and the explosion probability was less. None or possibly only one explosion was expected for the number of experiments planned.

The voltage instrumentation range was set at $\pm$ 100 volts since

enough sensitivity was desired to measure any voltage and charge generated even though it was expected that if all parameters were properly controlled the generated charge and voltage would by far exceed this value.

The first two experiments showed that in both cases the pen of the brush recorder rather violently reached the end of its travel and stayed there.

The range was then changed by one order of magnitude and the following day the next three experiments again each produced enough voltage to "peg the pen", indicating that more than $\pm$ 1,000 volts were generated in each case.

The range was again increased by one order of magnitude and this time the actual readings were obtained with the maximum reaching 6,400 volts. From the size of the screens and their spacings the charges which were generated could be calculated.

After these experiments with LO_2/LH_2 which produced rather high voltages in every test (thus showing that voltages and charges are produced in every case of mixing of these fluids) the experiments were repeated with LO_2/RP-1.

Again voltages and charges were generated in each case. The actual values were smaller than in the LO_2/LH_2 case since the energy available for the mixing process was smaller.

Tables II and III give the data for the six pound series of experiments.

It was felt that the results from these experiments verified the

predictions and thus no more tests were required and the program moved on to the 60 pound experiments.

The 60 Pound Experiments

With the experience gained from the first series of experiments the 60 pound test equipment was set up and the test procedure repeated with LO_2 being poured into LH_2. New values were worked out for evaporation rates and the corresponding liquid level drop rates. New filling times and proper probe settings were determined.

The explosive likelihood in these experiments also was higher with the expectation of possibility of one or two of the experiments auto-igniting.

The probes were set at levels which allowed proper timing to carry out the necessary change-overs in between the filling of LH_2 and LO_2 tanks. The voltage range was left at $\pm$ 20,000 volts to save time and not require recalibration, and the change to a smaller range postponed.

A few preliminary experiments were necessary until the timing had been worked out satisfactorily and then the experiments were carried out just as were the smaller ones with the voltages recorded and the charges calculated for the larger screens. Since the screen areas in these experiments were 5.2 times as large, equal voltage generation indicates a charge 5.2 times as large. As shown by equations (90), (91), (92), and (93).

Given $$Q = CV, \tag{90}$$

Where,

Q = charge-coulombs

C = capacitance-farads

V = voltage-volts

then for the same voltage generated V, we have by division:

$$\frac{Q_{60}}{Q_6} = \frac{C_{60}V}{C_6V} = \frac{C_{60}}{C_6} \quad \text{or} \quad Q_{60} = \frac{C_{60}}{C_6}\ Q_6 \tag{91}$$

Where,

Q_{60} = Charge developed in 60 pound Experiment.

Q_6 = Charge developed in 6 pound Experiment.

C_{60} = Screen capacitance in 60 pound Experiment

C_6 = Screen capacitance in 6 pound Experiment.

Also $$c = 0.224\ \frac{KA}{d}\ (n\text{-}1) \tag{92}$$

Where,

A = screen area - in^2

D = screen separation - in (constant)

n = number of screens (constant)

K = dielectric constant (3.3)

C = capacitance - $\mu\mu$ farads

then substitute into (91) and simplify; (due to experimental similarity the K, d, and n values are equal and cancel)

$$\frac{C_{60}}{C_6} = \frac{A_{60}}{A_6} \text{ or } \frac{C_{60}}{C_6} = 5.2 \quad (93)$$

therefore $Q_{60} = 5.2\, Q_6$ (for the same generated voltage).

A series of these experiments was carried out. Voltage and charges were again generated in each case with the larger screen having more of an averaging effect.

When it was considered that enough of these tests had been conducted the next set of experiments involving LO_2 being dumped into RP-1 were started. The probes were changed to respond to the proper propellant temperatures and the voltage instrumentation range was set at $\pm$ 1,000 volts. The voltages generated and the corresponding charges were again smaller than those produced with LO_2 and LH_2. This was in perfect agreement with the predictions and after it had been established that the voltage and charge generation was present in each of the cases the last set of experiments was initiated.

These experiments involved again LO_2 and LH_2 but this time the LH_2 was poured into the LO_2. The voltage range was set at $\pm$ 10,000 volts. No significant difference was found in the behavior of the first and last series except that the voltages and charges generated with LO_2 dumped into the LH_2 might have generated slightly higher voltages on the average. This can be explained by the greater energy supplied to the mixing process by dumping the heavier LO_2 into the lighter LH_2.

No explosion occurred in this series of experiments, although some of the experiments, based upon the theory, came close to auto-ignition.

The actual results are reported for these experiments in

Tables IV, V, and VI .

The 240 Pound Experiments

Since the screen area of the 240 pound test is 13.2 times the six pound screen area, equal voltage generation indicates a charge 13.2 times as large.

This may be shown as in the 60 Pound Experiment by substituting into equation (90), and obtaining by division:

$$\frac{Q_{240}}{Q_6} = \frac{C_{240}V}{C_6V} \quad \text{or} \quad Q_{240} = \frac{C_{240}}{C_6} Q_6 \tag{94}$$

Where,

Q_{240} = Charge developed in the 240 Pound Experiment

Q_6 = Charge developed in the 6 Pound Experiment

C_{240} = Screen Capacitance in the 240 Pound Experiment

C_6 = Screen Capacitance in the 6 Pound Experiment

Combining Equations (92) and (94) yields

$$\frac{C_{240}}{C_6} = \frac{A_{240}}{A_6} = \frac{C_{240}}{C_6} = 13.2 \tag{95}$$

Therefore

$$Q_{240} = 13.2\, Q_6 \quad \text{(for the same generated voltage)}$$

In these experiments it was expected that an explosion would occur; from experimental history it was predicted that one out of ten

experiments with LO_2/LH_2 should auto-ignite.

Because of the chill down times and then the filling times it was decided to start with the LH_2 in the upper tank and the LO_2 in the lower tank.

Again the experiments were carried out in the same manner as the earlier ones. The timing improved with the number of experiments carried out and the last three experiments of the first day of this series turned out to be the best ones. It is believed that the first of these came very close to auto-ignition.

The last experiment of that day was carried out be reversing the propellants, having the LO_2 in the top tank and the LH_2 in the lower tank.

The first experiment of the next day, carried out in exactly the same manner as the others, actually produced auto-ignition and the consequent explosion. These data are shown in Tables VII and VIII.

The 240 Pound Auto-Ignition

The tenth experiment of the 240 pound series was carried out the same way as all the others. Since it was the first experiment of the day, the tanks were first chilled down with LN_2 to conserve LO_2 and LH_2. Then the lower tank was filled with LH_2 to the desired level and the LH_2 tanker truck was disconnected and driven away.

The upper tank was filled with LO_2 to the required level. Then a short waiting period reduced both tank levels to the exact levels desired. At this time the LO_2 from the upper tank was dumped into the lower one containing the LH_2.

The experiment looked just like all the others with a vapor cloud appearing from the mixing process. It grew as the others and up to this point the test proceeded just the same as before.

Then Dr. Farber observed a small red glow looking like a reflection appearing near the opening of the lower tank and changing to yellow and then white as it grew. It then rapidly developed into the detonation and explosion with shock wave, fireball, etc. of a typical liquid rocket propellant explosion.

Figure 76 shows six frames taken during this test by the high speed movie camera which was running at 1600 frames/sec. Frames 2 through 6 were taken sequentially prior to and during the explosion. The development of the vapor cloud and the explosion can be seen clearly.

The prediction of an auto-ignition with these quantities or propellants was satisfied and the prediction that one of ten would produce an explosion (a rough estimate) was exactly met, probably more by coincidence than by design. This again indicates that much can be predicted from theory.

Figure 77 shows a plot of the generated charge ratio (to bring all measurements to the same basis) versus the quantity of propellants involved.

In this plot the lower bound of all the charges generated can be extrapolated to produce auto-ignition with a mass of about 2300 pounds, a value predicted about four years earlier[4,83,104]. When that value of charge producing auto-ignition is reached by a smaller mass it will explode.

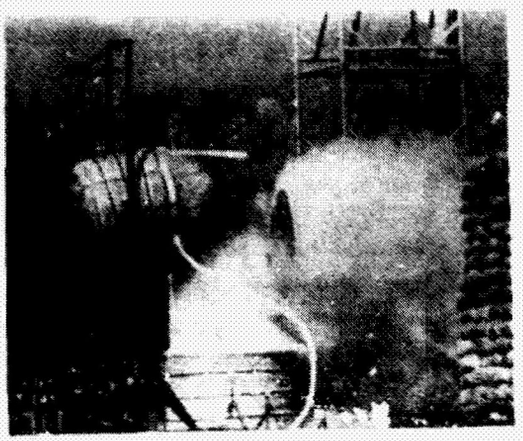

(1)

(2)

(3)

(4)

(5)

(6)

Fig. 76 The 240 Pound Test Explosion Sequence

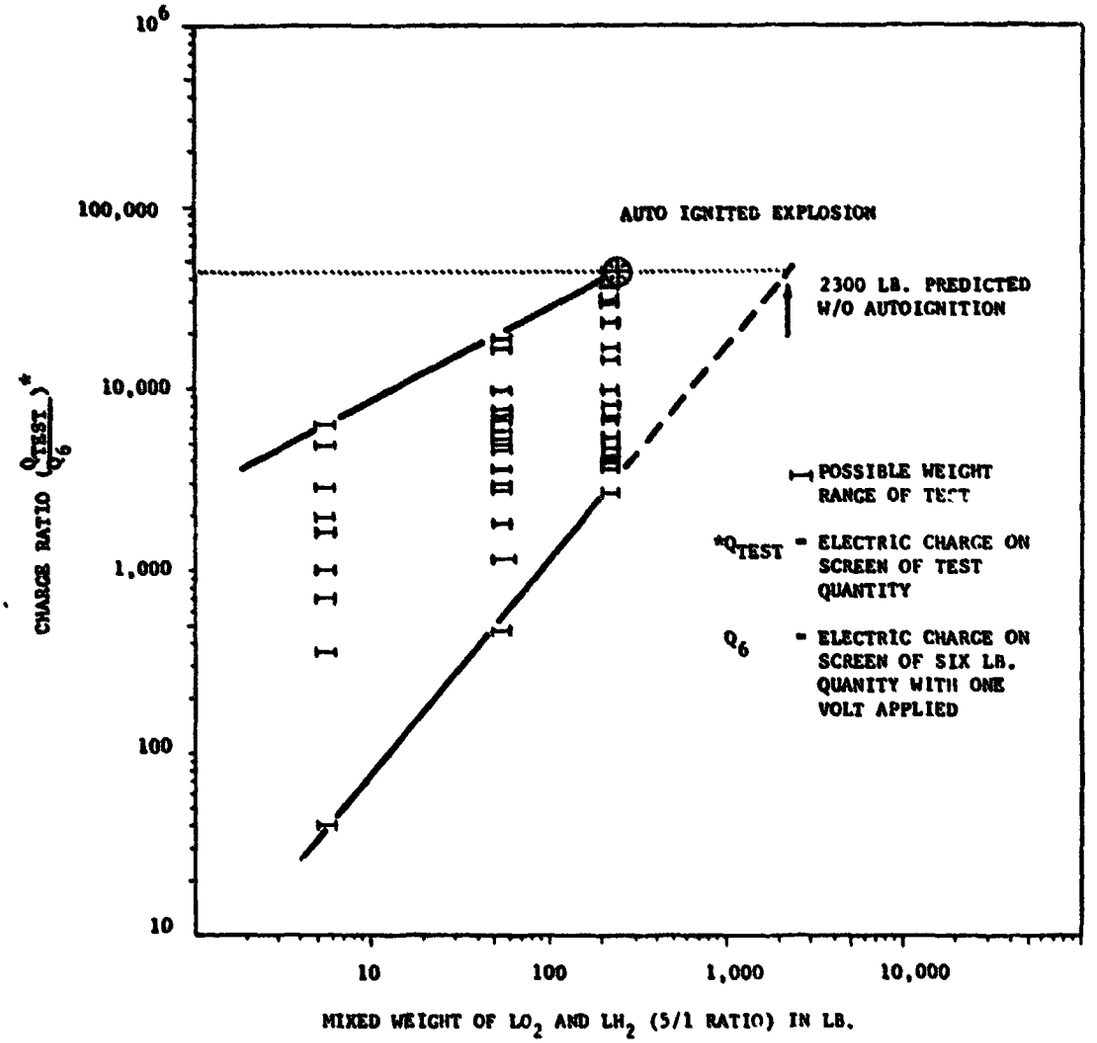

Fig. 77 Charge Ratio as a Function of Propellent Weight (LO_2/LH_2 Mixtures)

Again it should be emphasized that the theory and its verification by these experiments predicts that auto-ignition becomes a certainty when the masses become large enough reaching the Critical Mass. Below the critical mass quantities the probability of an explosion due to auto-ignition should decrease with decreasing mass, or in other words the smaller the mass the less likely is an auto-ignition. Since the probability of auto-ignition is not zero, however, for masses smaller than the critical mass, explosions with these quantities can and do actually occur.

In these experiments there were no auto-ignitions with the six or 60 pound masses but one out of ten with the 240 pound masses.

This explosion in the 240 lb. series verified the hypothesis of auto-ignition from self generated charges and voltages in the mixing of liquid propellants. The voltage spike measured was more than ample to produce the electric discharge which triggered the explosion, and it exceeded the predicted value needed for auto-ignition. Since the explosion was considered the successful conclusion to this test series, these experiments were terminated.

240 lb. LO_2/RP Auto-Ignition Experiments

Some time had to be taken to rebuild the experimental set-up and also ground zero was moved further from the control center where it was to be set up originally but was changed because of lack of cryogenic lines.

Also because some of the shrapnel action during the 240 lb. LO_2/LH_2 explosion more barricades were erected for protection of

equipment and personnel. TV monitors were provided so that the experimental procedures and phenomena could be observed closely.

Since more elaborate testing procedures and also more complicated data acquisition was used, involving more personnel requiring closer coordination, a more formal test procedure was established to the satisfaction of all concerned.

After all this was done, the experimentation was started exactly like the one for the 240 lb. LO_2/LH_2 experiments.

The results obtained from these experiments were again recorded and the important data is given in Table IX.

The charges and voltages produced by the mixing of the LO_2 and the RP were again characteristic of these experiments producing spikes, but none were large enough to actually produce ignition and consequent explosion.

Figure 78 is a plot of the normalized charge versus the mass of propellants used and again gives the same curves as the one for LO_2 and LH_2 but the value predicted for ignition several years ago and indicated on the graph was never reached. It is again seen that the lower bound of the measured values merges with the predicted value needed. As a further check also the average value at each mass quantity produces a line which also merges at that value. The charge and voltage which is needed to set off the 240 lb. mixture is the minimum and also the average value.

Non-Instrumented Experiments

The question was raised as to what effect the instrumentation may

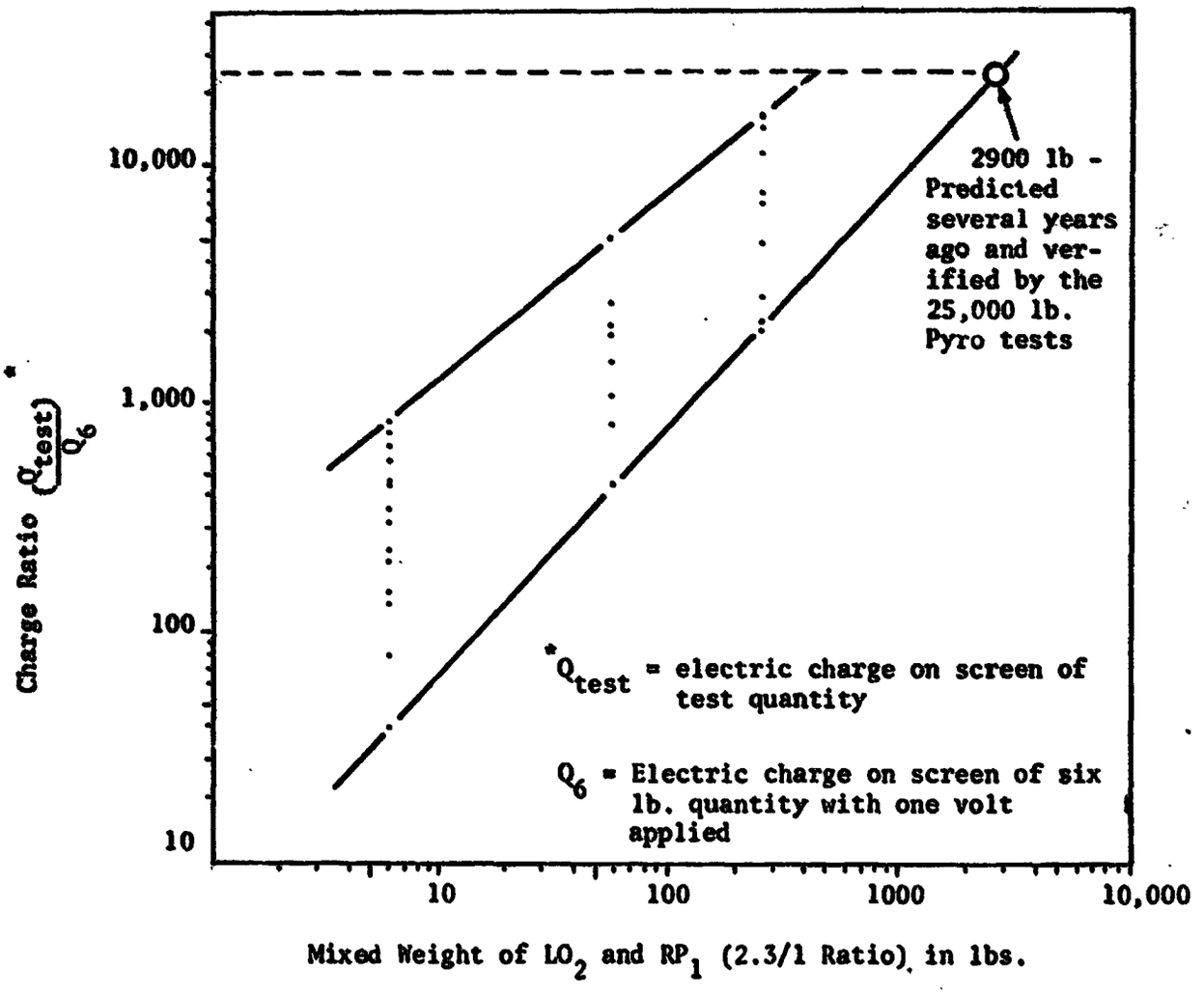

Fig. 78 Charge Ratio as a Function of Propellant Weight (LO_2/RP_1 Mixtures)

Table IX

Voltage Data from 240 Pound LO_2/RP-1 Experiments

(LO_2 is Poured into RP-1)

No.	Date	Screen Diameter - In.	Voltage - Volts x 13.2
1	9/14/72	40	1,850
2			12,400
3			1,850
4	9/15/72		12,500
5			9,120
6			2,510
7			16,300
8	9/18/72		7,900
9	9/25/72		4,750
10			1,580
11	9/26/72		1,580
12	9/27/72		1,580

have on the auto-ignition phenomena. From analysis it was deduced that the screens have if anything an averaging effect since they spread the produced charges over a larger region and do not allow the concentration which otherwise may occur.

When the equipment was rebuilt and set-up no internal instrumentation was used in connection with the experiments, nothing was put into the tanks which may effect the charge and voltage generation or any other phenomena.

Since no instrumentation was used in the tanks, the liquid levels in the tanks had to be estimated by timing. This procedure was checked out earlier and produced accurate predictions as to liquid levels. The chill time, the filling time and the evaporation time were closely monitored.

With what was estimated to be the correct quantities of propellants in the tank, the second test produced the expected explosion indicating that the phenomena without instrumentation if anything allows the ignition conditions to occur more easily. This is exactly what was predicted and expected.

Fully Instrumented Auto-Ignition Experiments

Again the equipment was rebuilt and set-up at ground zero and this time the objective was to measure and determine as many parameters as possible. In addition to the probes to determine the liquid levels in the tanks and the screens which measured the charge and voltage generation, three high speed cameras were used to record the phenomena, a thermocouple grid was put into the lower tank consisting of 36 couples

in four layers, a photomultiplier tube to sense any light from the ignition and explosion before it was destroyed by the explosion, and two antennas, one looking immediately over the lower tank, the other a little farther away.

The thermocouple grids were to measure the shock front and the reaction front velocities as well as mixing, etc. as in the tests described earlier which were carried out at the Air Force Rocket Propulsion Laboratory and Edwards Air Force Base. They were made of #36 gauge teflon coated copper-constantan wires manufactured into a single cable. The thermocouples were carefully welded under a small 20 power microscope with a minimum of mass at the junction.

As in the previous instrumented experiments, they were then fastened to thin support wires and passed from the tank through a conduit and to a junction box located at ground level.

A series of blast gauges were set at ground level in three lines 120 degrees apart radiating out from the lower tank.

The two antennas were to pick up signals from the discharges as a result of the fields generated by the mixing processes.

All the signals from all this instrumentation were transmitted back to several instrumentation vans where much of the information was put on tape and strip charts.

Again the tests were conducted as previously and all the data recorded. The mixing was monitored with the thermocouples and the voltage generated measured with the screens. The eleventh auto-ignition experiment produced ignition and a subsequent explosion.

All the data was recorded from this explosion and the information which was on tape was later reporduced on strip charts for analysis.

Again the expected number of experiments necessary to produce an explosion with a certain mass was verified and the yield as determined by comparing the blast gauge data to published literature was as expected.

Some time had to be taken to pull all the information off the tapes and to put it on strip charts so that the various traces could be stabilized. Unfortunately the paper used by NASA was of the non-permanent type and the records darkened as they were used and a second set had to be obtained to complete the analysis.

The analyses of the traces were simpler in this case than on the earlier experiments since the traces had more separation between them and it was easier to follow all the variations.

A. Velocity Vector Analysis

This method was based on the average velocity components obtained from the ratio of the distance, Δs, between two thermocouples to their difference in response time ΔT as the reaction front passes over them.

Case I The reaction front (assumed spher.) is oriented perpendicular to a line between two thermocouples and moves as shown in Figure 79A. This would give an average velocity of the reaction front directly equal to $\frac{\Delta s}{\Delta T}$ and would be located as a good approximation on the midpoint of the line between the two thermocouples. If the reaction front moves in any other direction the ratio becomes a component of the front velocity only.

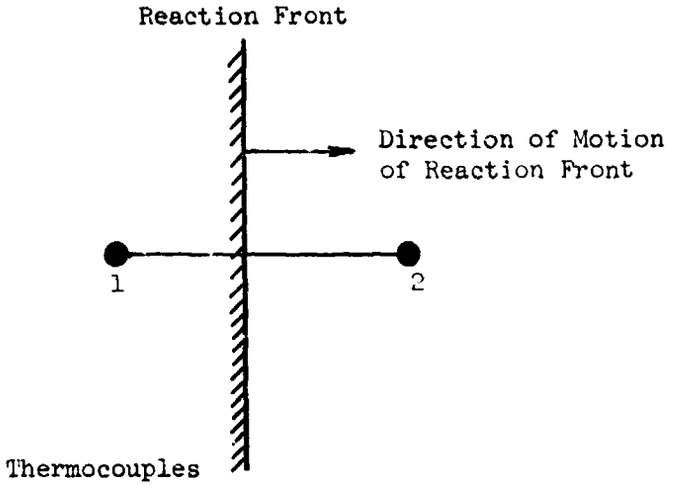

Fig. 79A Case I Reaction Front Normal to Line Between Thermocouples

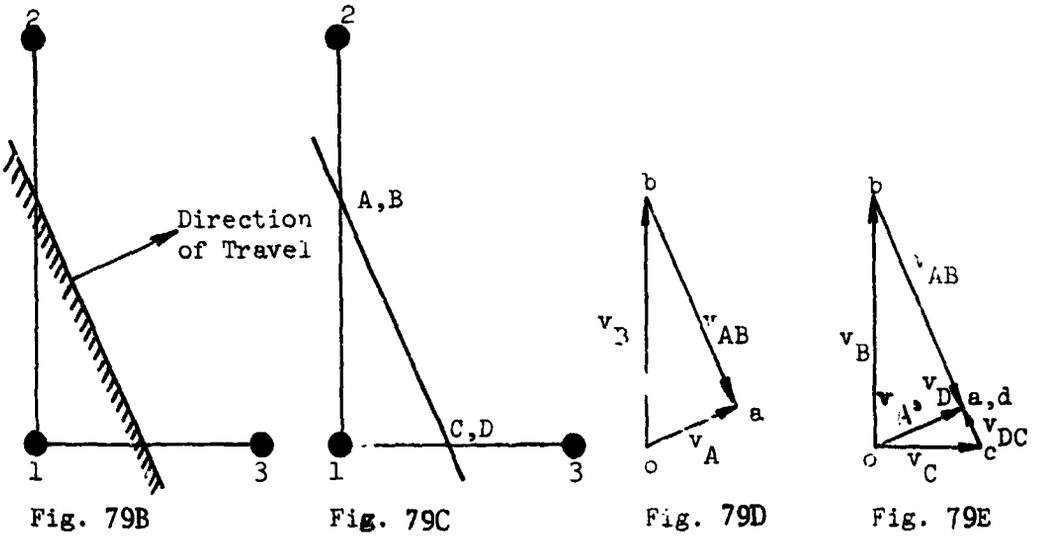

Fig. 79B,C,D,E Case II Reaction Front Normal to Plane of Thermocouples 1,2 and 3

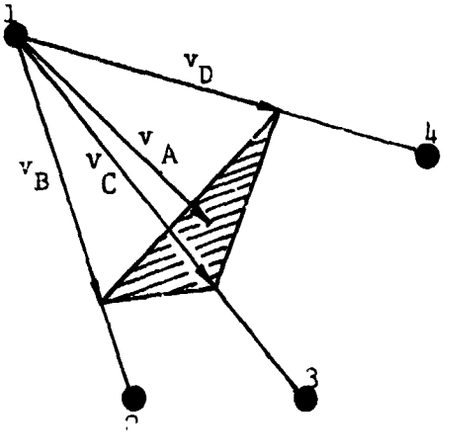

Fig. 79F Case III Reaction Front Oblique in Space Passing Through Thermocouples 1, 2, 3 and 4

Case II The reaction front (assumed planar) is oriented perpendicular to a plane containing three thermocouples and moves as shown in Figure 79B. This is essentially a two dimensional case with the edge of the front appearing as a straight line.

We can see in Figure 79C the relation between the velocities of a point A on the reaction front and a coincident point B moving along the line connecting the Thermocouples 1 and 2 can be found from the relative velocity equation

$$\tilde{v}_A = \tilde{v}_B + \tilde{v}_{A/B} \tag{96}$$

The direction of $\tilde{v}_A$ is perpendicular to the reaction front and $\tilde{v}_{A/B}$ is parallel to the front (Figure 79D). Similarly, if a pair of coincident points C and D be taken with point C in the front and point D moving along line 1-3, we have the relation

$$\tilde{v}_D = \tilde{v}_C + \tilde{v}_{D/c} \tag{97}$$

Again the direction $\tilde{v}_D$ is perpendicular to the front and $\tilde{v}_{D/C}$ is parallel to it. Since the front is assumed to be planar and translating $\tilde{v}_D = \tilde{v}_A$ then we can see from the figure that the line terminating the known vectors $\tilde{v}_B$ and $\tilde{v}_C$ is also parallel to the reaction front and from the vector polygon Figure 79E, the velocity of the reaction front is seen to be a vector perpendicular to this line and is also terminated by it.

Thus in this case if two average velocity components $\tilde{v}_B = \frac{\Delta \tilde{s}_{1-2}}{\Delta \tau_{1-2}}$ and $\tilde{v}_C = \frac{\Delta \tilde{s}_{1-3}}{\Delta \tau_{1-3}}$ are known, $\tilde{v}_A$ the average front velocity can be found from the velocity polygon. This average velocity is located as a good

approximation at the centroid of the triangle formed by the three thermocouples.

Case III The last case is the most general in which reaction front (assumed planar) passes obliquely in space through 4 thermocouples not all on the same plane. By an analogous development it can be shown that in space the reaction front velocity $\tilde{v}_A$ will be perpendicular to a plane terminus of three component average velocity vectors - and will also be terminated by it. (Figure 79).

Thus if $\tilde{v}_B = \frac{\Delta\tilde{s}_{1-2}}{\Delta\tau_{1-2}}$ and $\tilde{v}_C = \frac{\Delta\tilde{s}_{1-3}}{\Delta\tau_{1-3}}$ and $\tilde{v}_D = \frac{\Delta\tilde{s}_{1-4}}{\Delta\tau_{1-4}}$

are known $\tilde{v}_A$ can be found.

Again $\tilde{v}_A$ is located as a best approximation at the centroid of the tetrahedron formed by the four thermocouples. This method could be carried out using three different techniques:

1. Graphically using projections of the space vectors and descriptive geometry.
2. By vector analysis using the equations
   a. Equation of the reaction front plane:

$$\tilde{\phi} \cdot (\tilde{r} - \tilde{v}_B) = 0 \quad \text{where} \quad \tilde{\phi} = (\tilde{v}_B \times \tilde{v}_C + \tilde{v}_C \times \tilde{v}_D + \tilde{v}_D \times \tilde{v}_B) \tag{98}$$

   b. Equation of the reaction front velocity:

$$\tilde{v}_A = \frac{\tilde{\phi}}{\tilde{\phi} \cdot \tilde{\phi}} \; (\tilde{\phi} \cdot \tilde{v}_B) \tag{99}$$

3. By analytic geometry using the equations

a. Equation of the reaction front plane

$$Ax + By + Cz + D = 0$$

where

$$A = \begin{vmatrix} v_{By} & v_{Bz} & 1 \\ v_{Cy} & v_{Cz} & 1 \\ v_{Dy} & v_{Dz} & \end{vmatrix}, \quad B = - \begin{vmatrix} v_{Bx} & v_{Bz} & 1 \\ v_{Cx} & v_{Cz} & 1 \\ v_{Dx} & v_{Dz} & 1 \end{vmatrix}$$

$$C = \begin{vmatrix} v_{Bx} & v_{By} & 1 \\ v_{Cx} & v_{CY} & 1 \\ v_{Dx} & v_{Dy} & 1 \end{vmatrix}, \text{ and } D = \begin{vmatrix} v_{BX} & v_{By} & v_{Bz} \\ v_{Cx} & v_{Cy} & v_{Cz} \\ v_{Dx} & v_{Dy} & v_{Dz} \end{vmatrix}$$

b. Equation of the reaction front velocity

$$v_A = - \frac{D}{\sqrt{A^2 + B^2 + C^2}}, \text{ with direction numbers } (A,B,C) \quad (101)$$

These methods gave a first approximation of the location of the ignition source in a region 6 to 8 inches above the top level of the thermocouple grid and near thermocouples 3 and 4. This allowed the use of a second method of analysis shown in part B.

(B) Reaction from Displacement versus Time Analysis

After the ignition source had been approximately located, several plots of front displacement versus time were made from points in this region. Theoretically the proper location should give a plot forming a smooth curve. Actually scattering was observed in the plots. This was attributed to the differences in reaction times of the individual

thermocouples due to different bead sizes. The best plot showed a clearly defined group of thermocouples on a smooth curve (practically a straight line). This group would represent those thermocouples of the same size and the same reaction time. Method A was iterated with the select group of thermocouples as in the following example.

Example: Using the analytic geometry equations Part A Method B

Given Thermocouple group 1,31,28,11

Number	Location in ft. (from #1)			Time in sec	in sec	Velocity Comp. ft/sec		
	x	y	z			v_x	v_y	v_z
1	0	0	0	3.65787	0	0	0	0
31	1.63	1.53	.582	3.65803	.00016	10,187	9,562	3,637
28	.822	.083	.582	3.65797	.00010	8,220	831	5,820
11	.822	.083	.166	3.65795	.00007	11,743	1,187	2,371

Substituting in equation (100) we have

A = 29.332

B = .9036

C = 30.058

D = -416.82

then

$$v_A = \frac{D}{\sqrt{A^2 + B^2 + C^2}} = 9{,}921.8 \text{ ft/sec}$$

with direction numbers (29.33, .903, 30.06).

In a similar manner other groups of thermocouples gave the following data:

Group	Velocity ft/sec	Direction Numbers
1,4,9,6	10,601.1	29.33, .903, 30.089
9,10,19,16	8,897.3	21.23, 54.597, 37.647
11,28,10,19	13,111.7	53.91, -53.54, -61.53
9,19,6,8	7,563.9	88.54, 281.3, 182.4

This allowed a refinement of the center location to a point 8" about the top level of the thermocouple grid and 2.6" from #4 thermocouple horizontally and 8" from #12 horizontally (about 1.7" from tank wall). See Figure 80.

Part B was iterated again from this new center and gave a smoother plot with less scatter (Figure 81). Applying the least squares method to the data to obtain the slope of the plot gave a front velocity of 10,600 ft/sec as the best value of the reaction front velocity in the tank.

Separation between the shock front and the reaction front was not observed as in previous experiments since due to the design of the experiment the whole container was filled with the mixing region.

Also the fireball was not observed since no over-all fast cameras were set up and all of them were monitoring close in data.

Time Relationship Between the Various Instrumentation Systems

In the instrumentation set-up each individual part had its characteristic time constant and also the transmission lines between

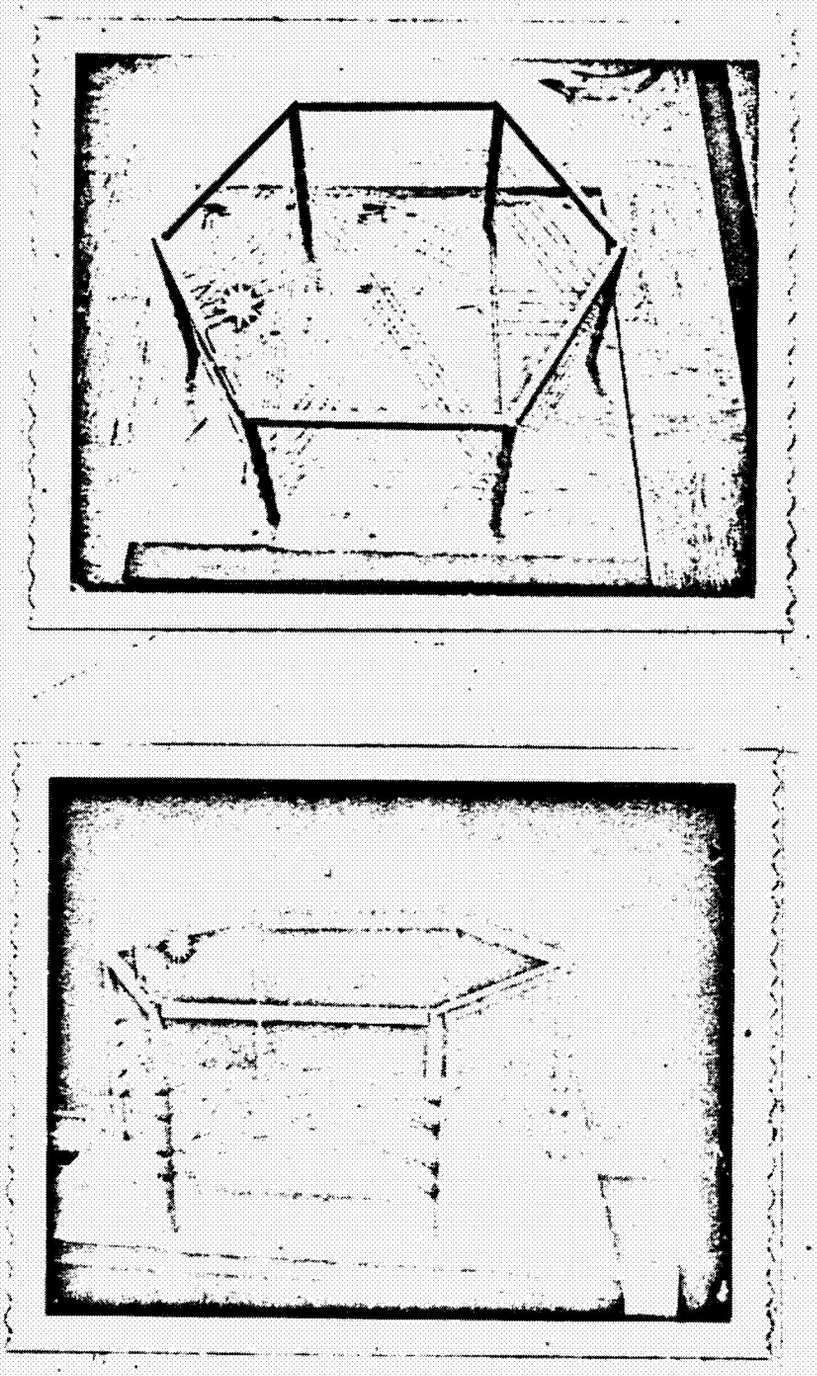

Fig. 80 Views of Model of Thermocouple Network Showing Location of Thermocouples (White Dots) and Location of Ignition Source.

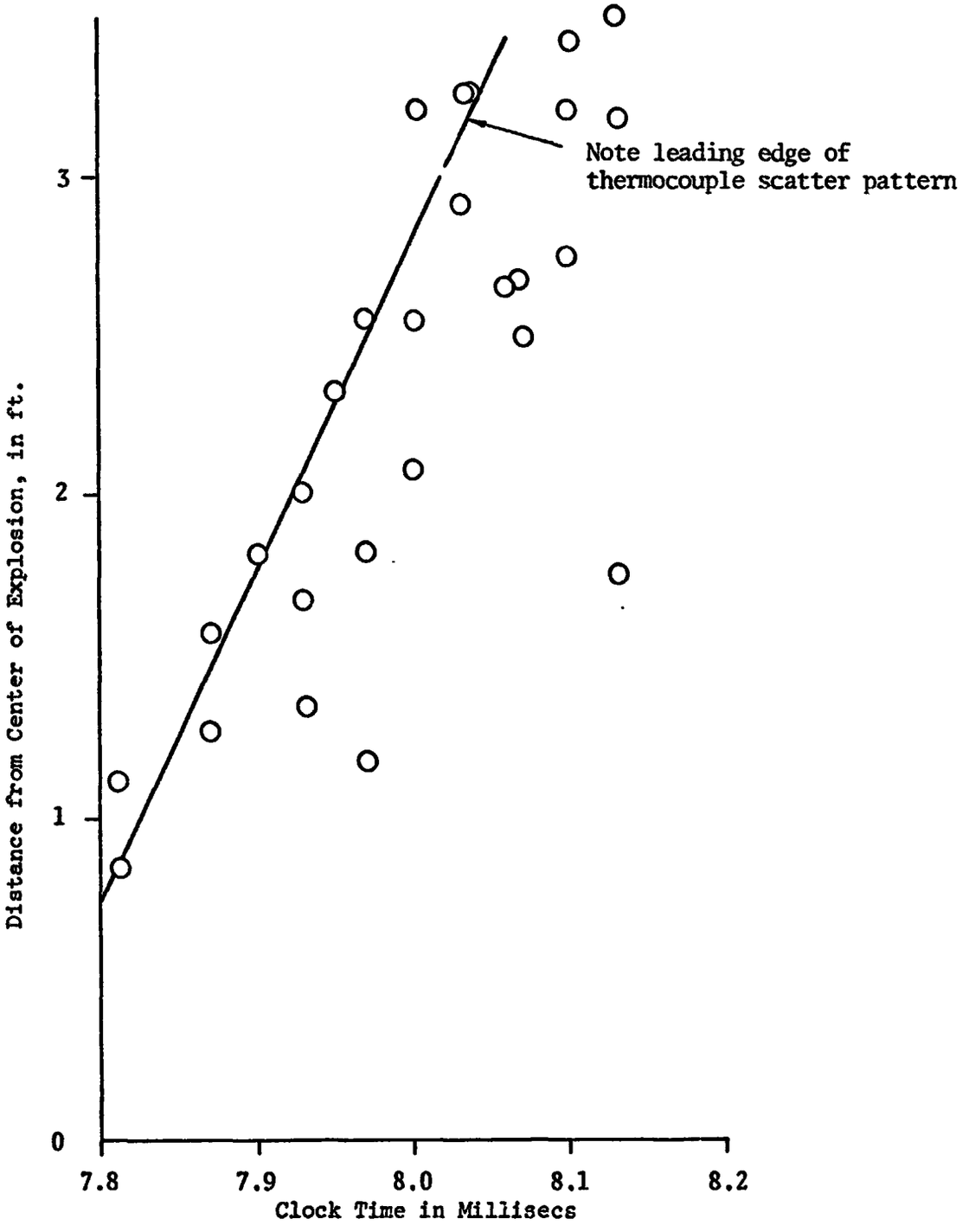

Figure 81 Reaction Front Displacement Versus Clock Time, Determined from the Thermocouple Response Times Shown

components effected the response to the signal input.

The cameras were operating at different speeds and the timing lights were located at different points with respect to the shutter so that the physical event recorded was in a different spot on the film with regard to the universal timing code. Also since the physical event could have occurred while the shutter was closed, a certain amount of uncertainty as to absolute time for a specific event exists.

The thermocouples had a certain amount of delay in response, but since they are made very similar the variation between them is not too great. Each will respond somewhat late to a signal but the differences in time between measurements are not great. They exist however, and therefore the leading edge of the plot was taken as the wave front since the data both bunched up and indicated the most accurate timing.

Taking the data and allowing it to be shifted in time within the interval of uncertainty then allowed the lining up of the physical events as shown in Figure 82. Obviously all instrumentation recorded only one and the same physical event, the explosion, and so the event must have occurred only at one time and each instrument recorded it at the same time although taking the uncorrected records just as they were put on tape or film it seems that the same event was recorded at different times.

Figure 82 shows how the different instrumentation systems line up. The thermocouples sensed the explosion first, naturally they were located closest to the point of ignition. Then the cameras recorded the first flash of light as the explosion emerged from the mixing tank.

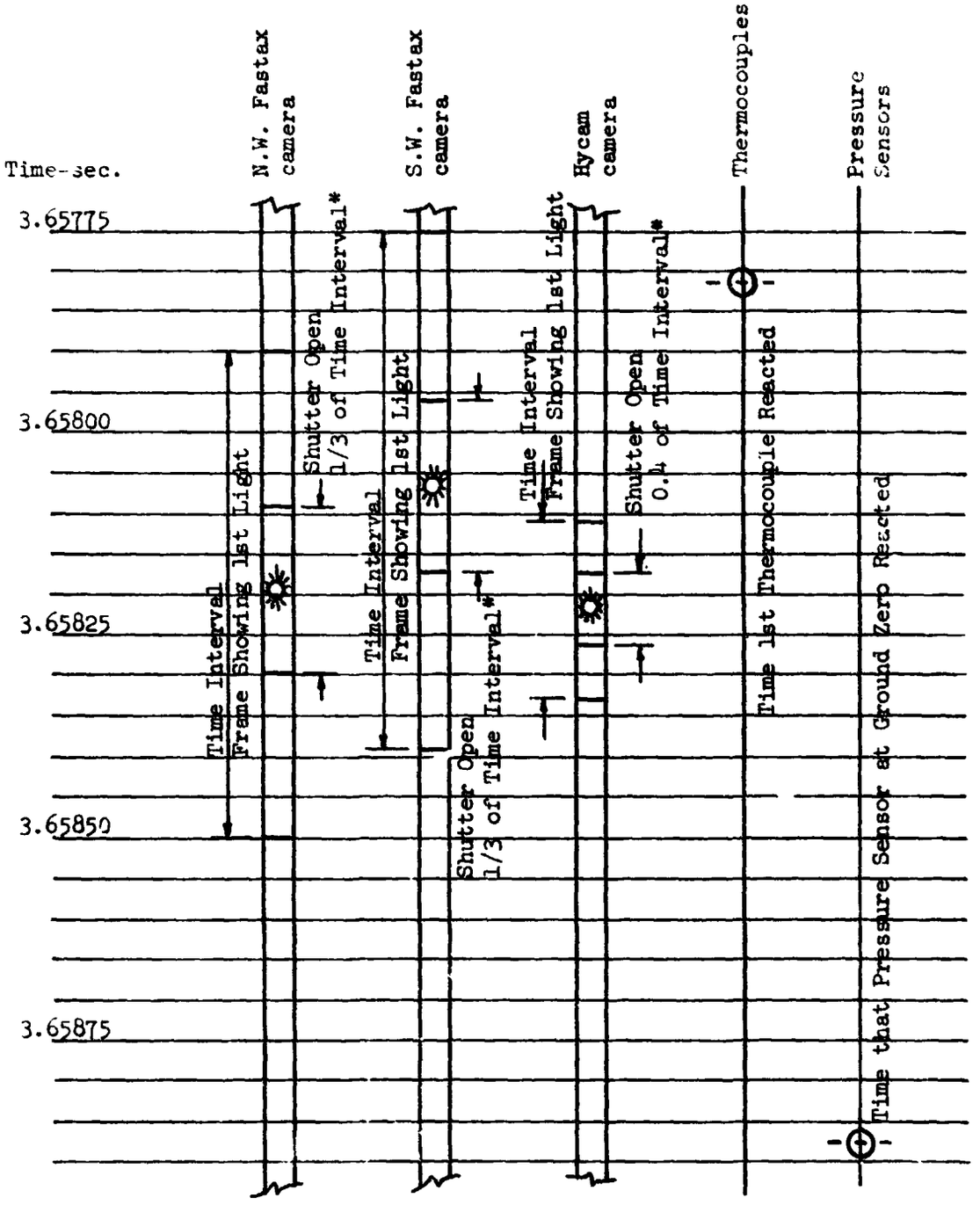

* Position of Shutter "Open time" increment may vary within total time interval.

Note - No meaningful data was obtained from the photomultiplier, or the antennas.

Fig. 82 Time relationship of instrumentation during last 240 lb. test explosion

Last in time the pressure sensor at ground zero picked up the explosion and recorded it.

It must be realized that the time intervals between these recordings are very small but nevertheless existent and must be taken into account for exact analyses and interpretation of events.

All the time constants and delay times and camera dark times, etc. evolved through numerous discussions with the KSC personnel responsible for the particular instrumentation and circuitry of each measurement.

PART III

SATURN V DESTRUCT SYSTEM ANALYSIS*

Having developed methods for analyzing and predicting, both theoretically and experimentally through modeling, the behavior of liquid rocket propellant mixtures and their explosive yield as described in the previous parts, this section will be concerned with the application of these methods to actual systems.

Since the more certain prediction of explosive yield is a function of the mode of failure, which in many cases is difficult to predict, it was suggested by the principal investigator to analyze the Saturn V destruct system. Since, if it should give a low explosive yield, it could be used to control the mode of failure of the Saturn V in case a catastrophic failure is imminent. Rather than letting a failure occur at random and not knowing what to expect it is better to have the rocket fail in a certain predetermined manner and have the knowledge of what to expect under these conditions.

With this in mind the analysis of the Saturn V destruct system was undertaken, and the analysis discovered a number of interesting facts.

A. Theoretical Analysis

For the purpose of the theoretical analysis several models were selected, and since the results were amazingly similar, the simplest ones were believed to be the best, or at least most useful.

The first step in the analysis required a knowledge of the mode of failure and to this end it was necessary to obtain information as to the effect of the destruct system upon the Saturn V. This proved to be much more difficult than anticipated. Since this information was to be

*Footnote at end of Part III, p. 345.

furnished by NASA a number of knowledgeable individuals were consulted. Much disagreement was found among the groups in NASA.

Finally we received a letter from Marshall Space Flight Center[120] which spelled out the effect of the destruct system upon the Saturn V vehicle, and since this was the only information which we received in writing it was used as the basis of this analysis.

If better information should become available at a later date the analysis as presented here could be repeated using the identical relationships but different numbers.

Figure 83 shows the effect of the destruct system upon the Saturn V vehicle as given to us by NASA.

The destruct system was to cut slots into the various tanks and let the fuel disperse out one side and the oxidizer out the other. This seems to be fulfilled except for the third stage and this problem will be treated later and in greater detail since it seemed to hold a potentially dangerous situation.

Thus the analysis then, except for the above mentioned problem, consists of the determination of the following:

1. Outflow for each stage with respect to time for the slot encountered.
2. Determination of the quantities of liquids on the ground at any time.
3. Determination of the spill ellipses, including hydraulic jump, etc. which determines the puddle depths at different points or regions.

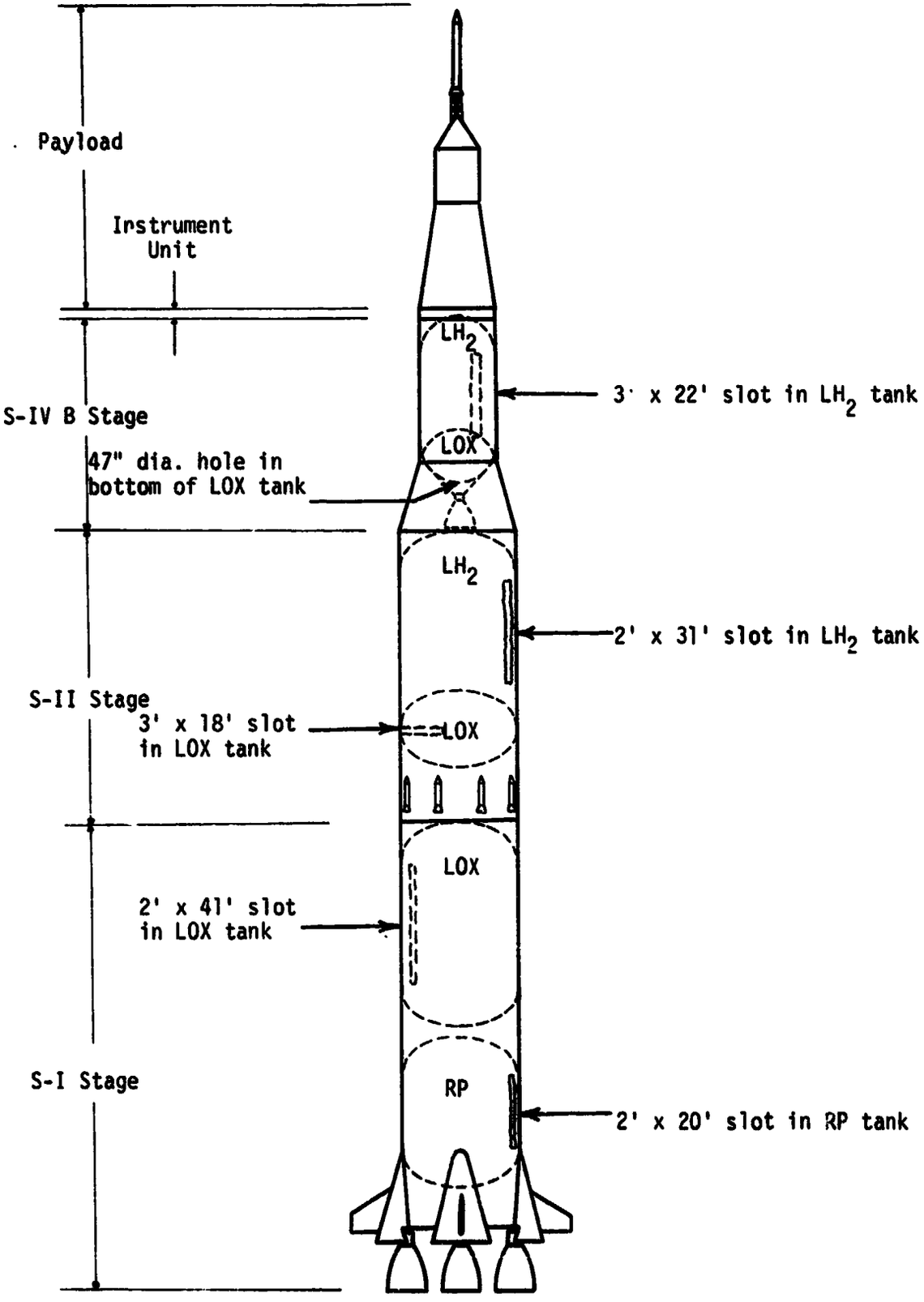

Figure 83 Schematic Diagram of Saturn V, with Effects of Destruct Initiation Indicated--NASA Information.

4. Determination of the puddle size and the spreading velocity at any time.

5. Determination of the liquid stream impact point at any time.

6. The plotting of the spill areas at sequential times.

7. Determination of the amounts of liquid vaporized both due to ground action (small) and due to the mixing of the various components.

8. Determination of the mixing characteristics in the overlapping puddles of both fuels and oxidizers.

9. Determination of the mixed areas and volumes for LO_2/RP-1, and LO_2/LH_2.

10. Determination of gas volumes - the gas cloud forming a hemisphere proportional to the areas (assuming no wind).

To determine the above the following procedures were used.

Having accepted the mode of failure or the effect of the destruct system as given to us by NASA, computer programs were set up to determine the outflow of the liquids from the slots in the tanks.

The next few pages show the theoretical treatment of the tank outflow.

Liquid release rate from the tank

Efflux velocity through the slot.

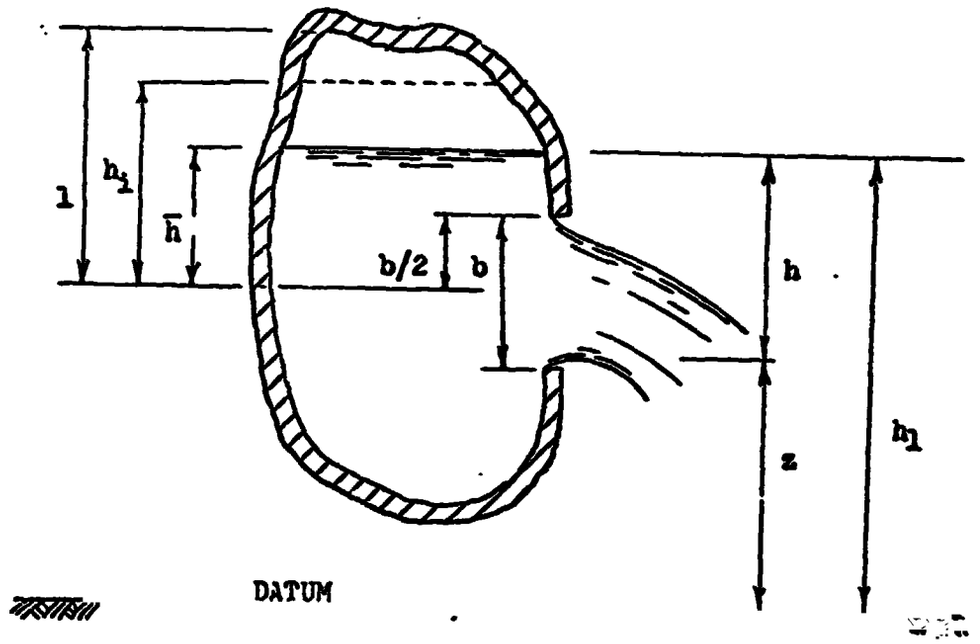

z - any point in the fully contracted jet

h_l - liquid level

$\bar{h}$ - mean head in jet

h_i - initial level in tank

Figure 84 Liquid Outflow (Slot)

Figure 84 gives a schematic sketch used in the following analysis.

At the instant when the liquid is at h_i , the velocity V,

at any point z in the jet is given by

$$V^2 = V_1^2 + \frac{2}{\rho}(p_1 - p) + 2gh \qquad (102)$$

where,

$h = h_1 - z$

ρ = density of fluid

p_1 = pressure in tank at liquid level h_1

From continuity

$$A_1 V_1 = A \bar{V}_s \qquad (103)$$

where,

$\bar{V}_s$ = average velocity in slot

A = area of slot

The average velocity in the slot can be found by integrating equation (102) for V between $h = \bar{h} - b/2$ and $h = \bar{h} + b/2$

$$\bar{V}_s = \frac{1}{b} \int_{\bar{h}-b/2}^{\bar{h}+b/2} V \, dh \qquad (104)$$

Substituting for V from (102) into (104) gives:

$$\bar{V}s = \frac{2}{3}(2gb)^{\frac{1}{2}} c_v \left[\left(\frac{V_1^2}{2gb} + \frac{p_1 - p}{\rho gb} + \frac{\bar{h}}{b} + \frac{1}{2}\right)^{\frac{3}{2}} - \left(\frac{V_1}{2gb} + \frac{p_1 - p}{\rho gb} + \frac{\bar{h}}{b} - \frac{1}{2}\right)^{\frac{3}{2}}\right] \qquad (105)$$

where c_v is the velocity coefficient and V_1 is given by equation (103).

An iterative scheme, eg. Newton-Rhapson, can be used to solve for $\bar{V}s$, knowing p_1.

Equation (105) gives the average instantaneous velocity in the slot when the liquid level is exactly at h_1. The equation is valid for $\bar{h} \geq b/2$.

When $\bar{h} < b/2$, the slot becomes a weir.

Efflux Velocity Through a Weir

The velocity at any point z at the instant when the liquid level is at h_1, is given by

$$V^2 = V_1^2 + 2gh \qquad (106)$$

where $h = h_1 - z$

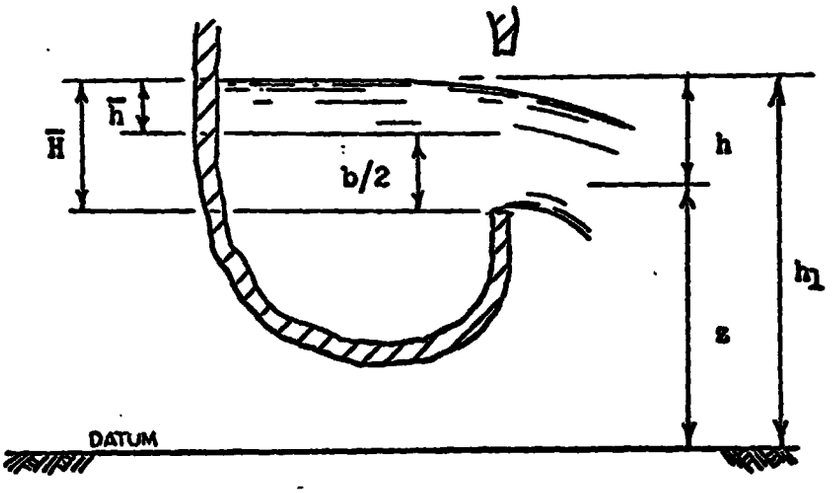

Figure 85 Liquid Outflow (Weir)

The average velocity is given by

$$\bar{V}_w = \frac{1}{\bar{H}} \int_0^{\bar{H}} V \, dh \tag{107}$$

Substituting for V into equation (107) gives

$$\bar{V}_w = \frac{2}{3}(2g\bar{H})^{\frac{1}{2}} c_v \left[\left(1 + \frac{V_1^2}{2g\bar{H}}\right)^{\frac{3}{2}} - \left(\frac{V_1^2}{2g\bar{H}}\right)^{\frac{3}{2}}\right] \tag{108}$$

Equation (108) gives the average instantaneous velocity in the weir when the liquid level is exactly at h_1. The equation is valid for $\bar{H} \leq b$, or for $\bar{h} \leq b/2$.

The areas of the slot and weir are ab and $a\bar{H}$ respectively where a = width of slot. Hence, the average flow rates are given by

$$Q_s = ab\,\bar{V}_s \tag{109}$$

$$Q_w = a\bar{H}\,\bar{V}_w \tag{110}$$

Tank Pressure, p_1

Assuming a polytropic process, then

$$p_1 = p_i(\alpha_i/\alpha_1)^k \tag{111}$$

where p_i = initial pressure at level h_i

k = 1, isothermal expansion

k = c_p/c_α, reversible isentropic expansion

$\mathcal{L}_i$ = initial volume above level h_i

$\mathcal{L}_1$ = volume above level h_i

For uniform area tank with flat top, equation (111) becomes

$$p_1 = p_i\left(\frac{\mathcal{L} - h_i}{\mathcal{L} - \bar{h}}\right)^k \tag{112}$$

Equation (111) may be written

$$p_1 = p_i f_h \tag{113}$$

where $f_h = (\mathcal{L}_i/\mathcal{L}_1)^k$ (114)

Time to Lower Liquid Level in Tank, t

$$t = \int_0^t dt = -\int_{h_i}^{\bar{h}} \frac{A}{Q}\,dh = \int_{\bar{h}}^{h_i} \frac{1}{V}\,dh$$

for the slot then

$$t_s = \frac{1}{\frac{2}{3}(2gb)^{\frac{1}{2}} c_v} \int_{\bar{h}}^{h_i} \left[\left(\frac{V_1^2}{2gb} + \frac{p_i f_h^{-1}}{p\rho gb} + \frac{\bar{h}}{b} + \frac{1}{2}\right)^{\frac{3}{2}} - \left(\frac{V_1^2}{2gb} + \frac{p_i f_h^{-1}}{p\rho gb} + \frac{\bar{h}}{b} - \frac{1}{2}\right)^{\frac{3}{2}}\right]^{-1} dh \tag{115}$$

where f_h = function of $\bar{h}$

V_1 = function of $\bar{h}$

for the weir then

$$t_w = \frac{1}{\frac{2}{3} C_v} \int_{\bar{H}}^{b} (2g\bar{H})^{-\frac{1}{2}} \left[\left(1 + \frac{V_1^2}{2g\bar{H}}\right)^{\frac{3}{2}} - \left(\frac{V_1^2}{2g\bar{H}}\right)^{\frac{3}{2}} \right]^{-1} dH \qquad (116)$$

where V_1 = function of $\bar{H}$

Jet Velocity at Datum and Jet Trajectory

The velocity at the ground is given by the vector sum of the horizontal velocity leaving the slot, equations (105) and (108), and the fall velocity of a particle of water falling a distance $d + b/2$ for the slot and $d + H/2$ for the weir. Calling this distance D, then

$$V_g = (\bar{V}^2 + 2gD)^{\frac{1}{2}} \qquad (117)$$

and the cross-sectional area of the jet at the ground is

$$A_g = \frac{Q}{V_g} = A\,\bar{V}/V_g \qquad (118)$$

Letting D be the mean vertical distance from the datum to the slot or weir, the time t_f, for a fluid particle to fall distance D,

is given by

$$t_f = \left(\frac{2D}{g}\right)^{\frac{1}{2}} \tag{119}$$

The horizontal distance x, that the fluid particle travels before reaching datum is

$$x = \bar{V}\, t_f \tag{120}$$

Procedure

1. Equations (105) and (108) can be solved numerically for $\bar{V}_s$ and $\bar{V}_w$ with given values $\bar{h}$ and $\bar{H}$ and the corresponding values of f_h.

2. From continuity and (1) above, V_1 as a function of $\bar{h}$ and $\bar{H}$ can be determined.

3. Equations (115) and (116) can be integrated numerically to determine t_s and t_w the time required to lower the liquid level to the specified values of $\bar{h}$ and $\bar{H}$.

4. From (1) or (2) and (3) above, the flow rate Q, as a function of time can be determined.

5. The curve of the flowrate Q, as a function of time can then be displaced by time t_f so that the velocity at the ground, V_g and the flow rate, Q, at the ground can be determined as a function of time.

6. The horizontal displacement of the jet, x, as a function of time is readily determined from equation (120).

7. The area of the jet at the ground can be determined as a function of time or distance. See figure 86.

Time required for jet stabilization

After the destruct system is initiated and the slots opened in the tanks it will take a short but finite time to establish the stabilized flow. The following will give a short analysis of this phenomenon.

Using the momentum equation

$$whA - \frac{wAc^2V^2}{2g} = \frac{wA}{g} c^2V \frac{dV}{dt} \tag{121}$$

$$h - \frac{2V^2}{2g} = \frac{c^2}{g} V \frac{dV}{dt}$$

$$h \left(1 - \frac{c^2V^2}{2gh}\right) = \frac{c^2}{g} V \frac{dV}{dt}$$

$$\int_0^t dt = \int_0^V \frac{\frac{c^2}{g} V \, dV}{h \left(1 - \frac{c^2V^2}{2gh}\right)} = \int_0^V - \frac{\frac{c^2}{gh} V \, dV}{\left(1 - \frac{c^2V^2}{2gh}\right)} \tag{122}$$

from the above

$$t = - \ln \left(1 - \frac{c^2V^2}{2gh} \right)$$

and

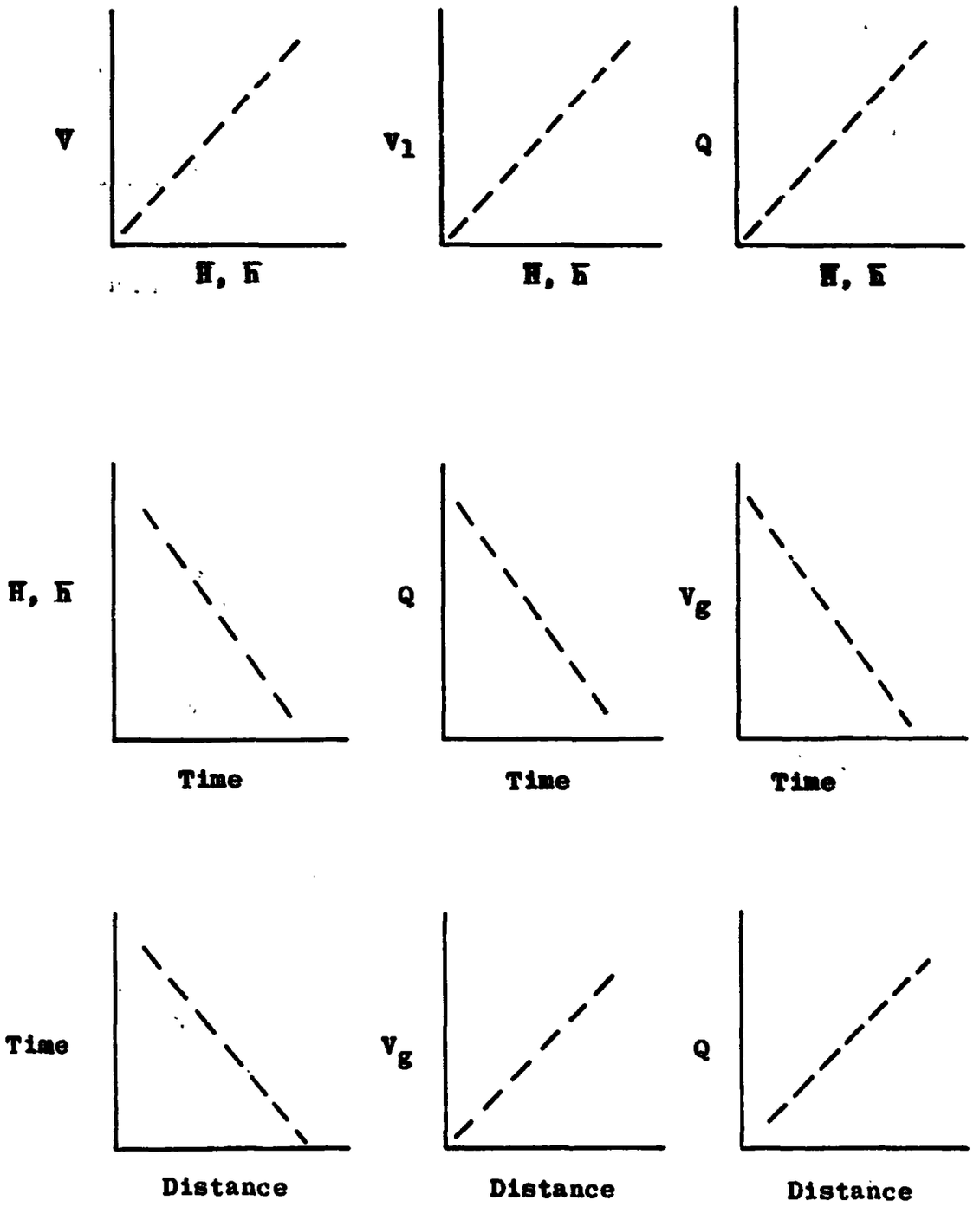
V
H, h
V_1
H, h
Q
H, h
H, h
Time
Q
Time
V_g
Time
Time
Distance
V_g
Distance
Q
Distance

Figure 86

$$e^{-t} = \left(1 - \frac{c^2V^2}{2gh}\right)$$

$$V^2 = \frac{1}{c^2}\, 2gh\, \left(1 - e^{-t}\right)$$

$$V = \frac{1}{c}\left[2gh\left(1 - e^{-t}\right)\right]^{\frac{1}{2}} \qquad (123)$$

The above equation is the outflow jet velocity at any time t after the opening of the slot. A quick analysis gives the following results.

Table X

$1 - e^{0}$	=	0	
$1 - e^{-1}$	=	1 - 0.368	= 0.632
$1 - e^{-2}$	=	1 - 0.135	= 0.865
$1 - e^{-3}$	=	1 - 0.05	= 0.95
$1 - e^{-4}$	=	1 - 0.018	= 0.982
$1 - e^{-5}$	=	1 - 0.007	= 0.993

Table XI

$V_o = 0$

$V_1 = 0.795\ V_{max}$

$V_2 = 0.925\ V_{max}$

$V_3 = 0.975\ V_{max}$

$V_4 = 0.991\ V_{max}$

$V_5 = 0.997\ V_{max}$

Shape of the Liquid Pool

Next it was necessary to establish or estimate the shape of the liquid splash pool with the liquid jets impinging upon the surface.

The derivation on the next pages indicates that the pool is essentially circular and the eccentricity of the splash ellipse is too small to warrant its consideration in the further treatment of this problem.

Below, the method for estimating the shape of the liquid pool is outlined and its variation with time given.

Basic Assumptions

1. The pool is elliptical with the stream impact center coinciding with the focal point nearest the rocket.

2. The pool has constant depth as long as fluid continues to be added.

3. The fluid stream is circular with uniform velocity

as it hits the ground.

Figure 87 is a schematic sketch of the physical configuration used in this analysis.

Figure 88 gives some of the nomenclature used in the analysis of the splash puddle configuration.

Derivation

$$V_{vert.} = a\,t = g\,t$$

$$t = \left(\frac{2z}{g}\right)^{\frac{1}{2}}$$

$$V_{vert} = (2gz)^{\frac{1}{2}} \tag{124}$$

z – distance from the bottom of the slot to ground

Letting V_A and V_B be relative velocities with respect to the velocity of the focal point of the ellipse V_{f_1}

At time t

$$\frac{\overline{Af_1}}{\overline{Bf_1}} = \frac{\overline{V}_A\,t}{\overline{V}_B\,t} \tag{125}$$

and

$$\begin{aligned} \overline{V}_A &= \overline{V}_{SP} - \overline{V}_H \\ \overline{V}_B &= \overline{V}_{SP} + \overline{V}_H \end{aligned} \tag{126}$$

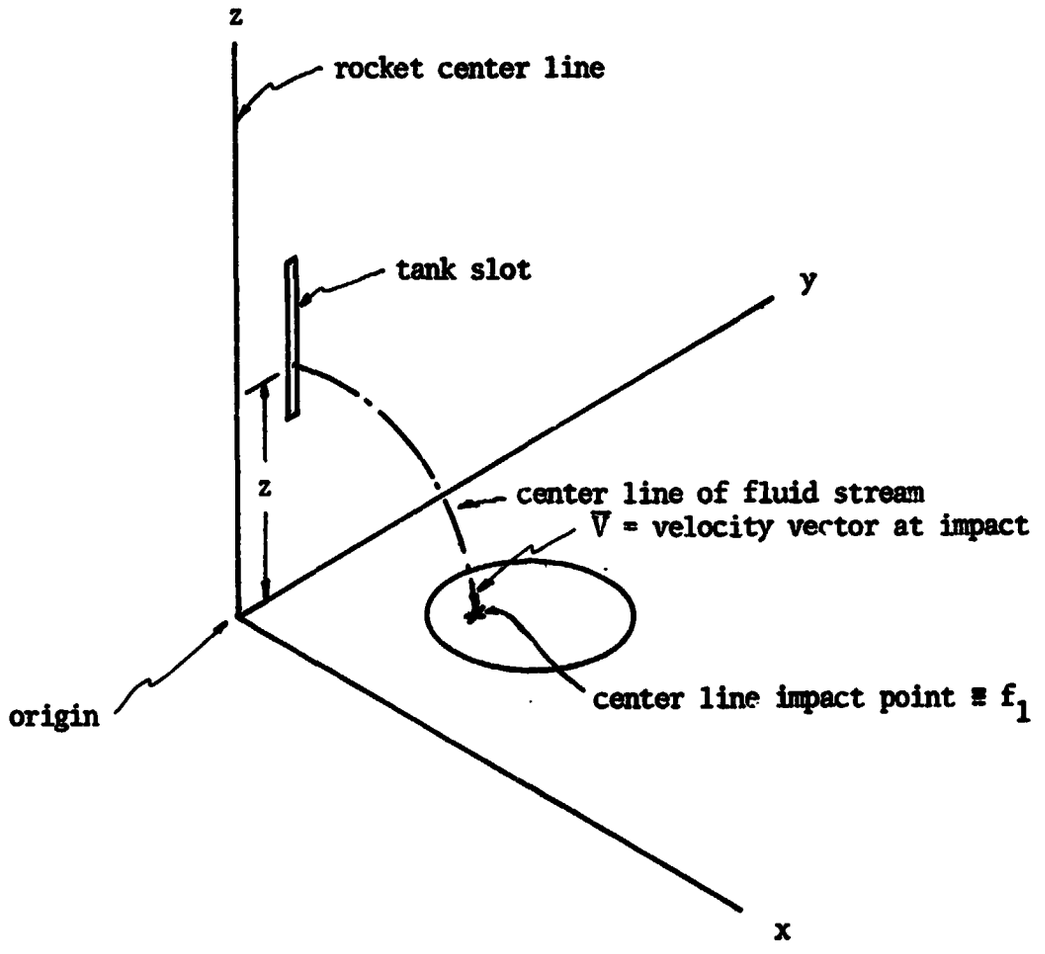

Figure 87 Schematic Sketch of Slot, Fluid Stream and Splash Puddle

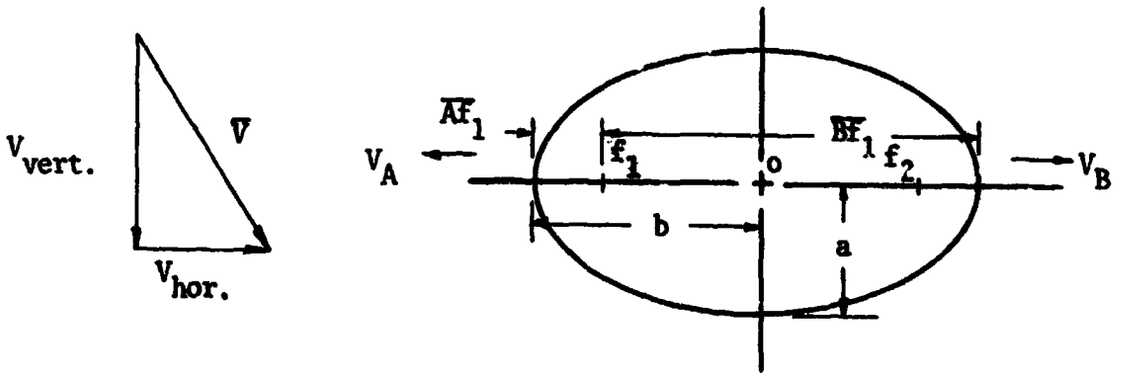

Figure 88 Nomenclature

where in equation (126) $\overline{V}_{SP}$ is the spreading velocity due to the vertical component of the mass flow. $\overline{V}_H$ is the velocity caused by the horozontal momentum.

To determine the distances $\overline{Af}_1$ and $\overline{Bf}_1$, from the definition of the ellipse

$$Of = (b^2 - a^2)^{\frac{1}{2}} \tag{127}$$

and

$$\left.\begin{aligned} \overline{Af}_1 &= b - (b^2 - a^2)^{\frac{1}{2}} \\ \overline{Bf}_1 &= b + (b^2 - a^2)^{\frac{1}{2}} \end{aligned}\right\} \tag{128}$$

From (125) and (128)

$$\frac{\bar{V}_A}{\bar{V}_B} = \frac{b - (b^2 - a^2)^{\frac{1}{2}}}{b + (b^2 - a^2)^{\frac{1}{2}}} \tag{129}$$

multiplying out

$$\bar{V}_A \left[b + (b^2 - a^2)^{\frac{1}{2}}\right] = \bar{V}_B \left[b - (b^2 - a^2)^{\frac{1}{2}}\right]$$

and collecting terms

$$b\,(\bar{V}_A - \bar{V}_B) + (\bar{V}_A + \bar{V}_B)\,(b^2 - a^2)^{\frac{1}{2}} = 0 \tag{130}$$

also from (126)

$$\left.\begin{aligned} (\bar{V}_A - \bar{V}_B) &= -2\,\bar{V}_H \\ (\bar{V}_A + \bar{V}_B) &= 2\,\bar{V}_{SP} \end{aligned}\right\} \tag{131}$$

Substituting (131) into (130)

$$b\,\bar{V}_H - \bar{V}_{SP}\,(b^2 - a^2)^{\frac{1}{2}} = 0 \tag{132}$$

and

$$\bar{V}_H^2 = \bar{V}_{SP}^2\,(b^2 - a^2) \tag{133}$$

If Q is the total volume on the ground and

d is the puddle depth

$$Q = \pi\, a\, b\, d \tag{134}$$

and

$$a = \frac{Q}{\pi\, b\, d} \tag{135}$$

Substituting (135) into (133)

$$b^2 V_H^2 = V_{SP}^2 \left(b^2 - \frac{Q^2}{\pi^2 b^2 d^2}\right)$$

and

$$V_H^2 = V_{SP}^2 \left(1 - \frac{Q^2}{\pi^2 d^2 b^4}\right)$$

$$V_{SP}^2 - V_H^2 = \frac{V_{SP}^2 Q^2}{\pi^2 d^2 b^4} \tag{136}$$

and

$$b = \left[\frac{V_{SP}^2 Q^2}{\pi^2 d^2 (V_{SP}^2 - V_H^2)}\right]^{\frac{1}{4}} \tag{137}$$

Determination of V_{SP} and V_H

For the first step assume that the puddle is circular with Q cubic feet on the ground and $\dot{Q}$ being the volume flow rate into the puddle. Figure 89.

$Q = \pi\, r^2\, d$, $\dot{Q} = 2\pi\, r\, d\, \frac{dr}{dt}$, but since $dr/dt = V_{SP}$,

$r = (Q/\pi\, d)^{\frac{1}{2}}$

$$Q = 2\ d\ (Q/\ d)^{\frac{1}{2}} \tag{138}$$

$$\bar{V}_{SP} = \dot{Q} / 2\ (Q\ \ d)^{\frac{1}{2}} \tag{139}$$

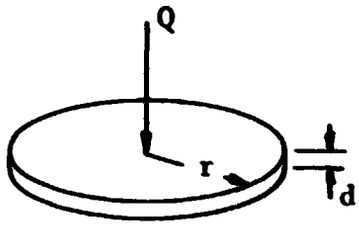

Figure 89 Splash Puddle

Let $\bar{V}_{hor}$ Horizontal component of velocity as the stream leaves the rocket (vertical component = 0)

A_o Cross-sectional area of the stream leaving the rocket

A_1 Cross-sectional area of stream as it hits the ground

$\bar{V}_{vert}$ Vertical component of velocity as stream hits ground [$\bar{V}_{vert} = (2gz)^{\frac{1}{2}}$]

From Continuity

$$A_0\ \bar{V}_{hor} = A_1\ \bar{V}_{vert} \tag{140}$$

and

$$A_1 = \frac{A_o\ \bar{V}_{hor}}{\bar{V}_{vert}}\ , \qquad r_1 = (\ A_1/\ \pi\ )^{\frac{1}{2}} \tag{141}$$

Since $$\dot{Q} = A_o \bar{V}_{hor} \quad (142)$$

$$\bar{V}_{SP_1} = \frac{\dot{Q}}{2\pi r_1 d}$$

and using (141)

$$\bar{V}_{SP_1} = \frac{\dot{Q}}{2d\,(\pi A_o \bar{V}_{hor} / \bar{V}_{vert})^{\frac{1}{2}}}$$

and from (142)

$$= \frac{1}{2d} \left(A_o \bar{V}_{hor} \bar{V}_{vert} / \pi \right)^{\frac{1}{2}} \quad (143)$$

Assuming that

$$\frac{\bar{V}_{SP_1}}{\bar{V}_{hor}} = \frac{\bar{V}_{SP}}{\bar{V}_H} \quad (144)$$

$$\bar{V}_H = \frac{\bar{V}_{SP} \bar{V}_{hor}}{\bar{V}_{SP_1}} \quad (145)$$

using (139) and (143) and substituting it to (145)

$$\bar{V}_H = \left(\bar{V}_{hor}^3 A_o d / Q \bar{V}_{vert} \right)^{\frac{1}{2}} \quad (146)$$

Solving for a and b

from (135)

$$a = \frac{C}{\pi\ b\ d}$$

from (137)

$$b = \left[\frac{\bar{V}_{SP}^2\ Q^2}{\pi^2\ d^2\ (\bar{V}_{SP}^2 - \bar{V}_H^2)} \right]^{\frac{1}{4}}$$

$$= \left[\left(\frac{Q}{\pi\ d}\right)^2 \left(\frac{1}{1 - \left(\frac{\bar{V}_H}{\bar{V}_{SP}}\right)^2}\right) \right]^{\frac{1}{4}} \qquad (147)$$

since from (144), (146) and (139)

$$\left(\frac{\bar{V}_H}{\bar{V}_{SP}}\right)^2 = \left(\frac{\bar{V}_{SP}}{\bar{V}_{hor}}\right)^2$$

$$= \left(\frac{\bar{V}_{hor}^3\ A_o\ d}{Q\ \bar{V}_{vert}}\right) \left(\frac{4\ \pi\ Q\ d}{Q}\right) \qquad (148)$$

with (142)

$$\left(\frac{\bar{V}_H}{\bar{V}_{SP}}\right)^2 = \left(\frac{\bar{V}_{hor}^3\ A_o\ d\ 4\ Q\ \pi\ d}{Q\ \bar{V}_{vert}\ \bar{V}_{hor}^2\ A_o^2}\right)$$

$$= \frac{4\ \pi\ d\ \bar{V}_{hor}}{\bar{V}_{vert}\ A_o} \qquad (149)$$

and substituting (149) into (147)

$$b = \left(\frac{Q}{\pi d}\right)^{\frac{1}{2}} \left[\frac{1}{1 - \left(\frac{4\pi d^2 \bar{V}_{hor}}{\bar{V}_{vert} A_o}\right)}\right]^{\frac{1}{4}} \qquad (150)$$

From the computer programs Q, $\bar{V}_{hor}$, A_o, d, and f_1 can be determined at any time t, and with this information a and b can be calculated giving the configuration of the splash puddle ellipse.

Taking the first stage of the Saturn V as an example, since it gives the largest impact angle and therefore has the greatest effect upon the results, they are as follows:

LO_2 $\underline{t = 100 \text{ sec}}$

$\bar{V}_{hor} = 6.82$
$Q = 37{,}877$
$A_o = 3.626$
$\bar{V}_{vert} = 74.5$

$b = 158.8$ ft
$a = 152.2$ ft

$\underline{t = 160 \text{ sec}}$

$\bar{V}_{hor} = 4.45$
$Q = 38{,}700$
$A_o = 1.726$
$\bar{V}_{vert} = 74.5$

$b = 161.5$ ft
$a = 152.7$ ft

RP-1

t = 100 sec

$\bar{V}_{hor}$ = 6.30
Q = 18,958
A_0 = 3.142
$\bar{V}_{vert}$ = 51.2

b = 113.8 ft

a = 106.2 ft

t = 160 sec

$\bar{V}_{hor}$ = 4.16
Q = 19,642
A_o = 1.542
$\bar{V}_{vert}$ = 51.2

b = 117 ft

a = 107 ft

From the above it can be seen that the splash puddles are essentially circular and using circles makes the analysis much simpler.

Having shown that the flow pattern on the ground is essentially that of circular splash puddles, another phenomenon of the splash puddles, namely the hydraulic jump was investigated. This last phenomenon produces a variation in thickness of the puddle and this may become important in estimating the quantities mixed by having the puddles flow together and overlap.

The following pages treat this phenomenon and characteristics.

Radial Flow Patterns

The purpose of this part of the study was to provide a method for predicting the depth of flow within a radial flow pattern containing a circular hydraulic jump. The results can be used to aid in predicting mixing rates of the puddles formed by spilling propellant components from a rocket.

Initially a purely analytical approach was tried.

Using the notation as shown in Figure 90, expressions were developed by applying the equations of conservation of mass, momentum, and energy.

I. Conservation of Mass (Continuity), (steady flow and incompressibility are assumed)

a. within impinging jet

$$Q = A_j V_j = \pi r_j^2 V_j \tag{151}$$

b. at toe of jump

$$Q = 2\pi r_o y_o V_o \tag{152}$$

c. at heel of jump

$$Q = 2\pi r_1 y_1 V_1 \tag{153}$$

d. downstream of jump

$$Q = 2\pi r\ y\ V \tag{154}$$

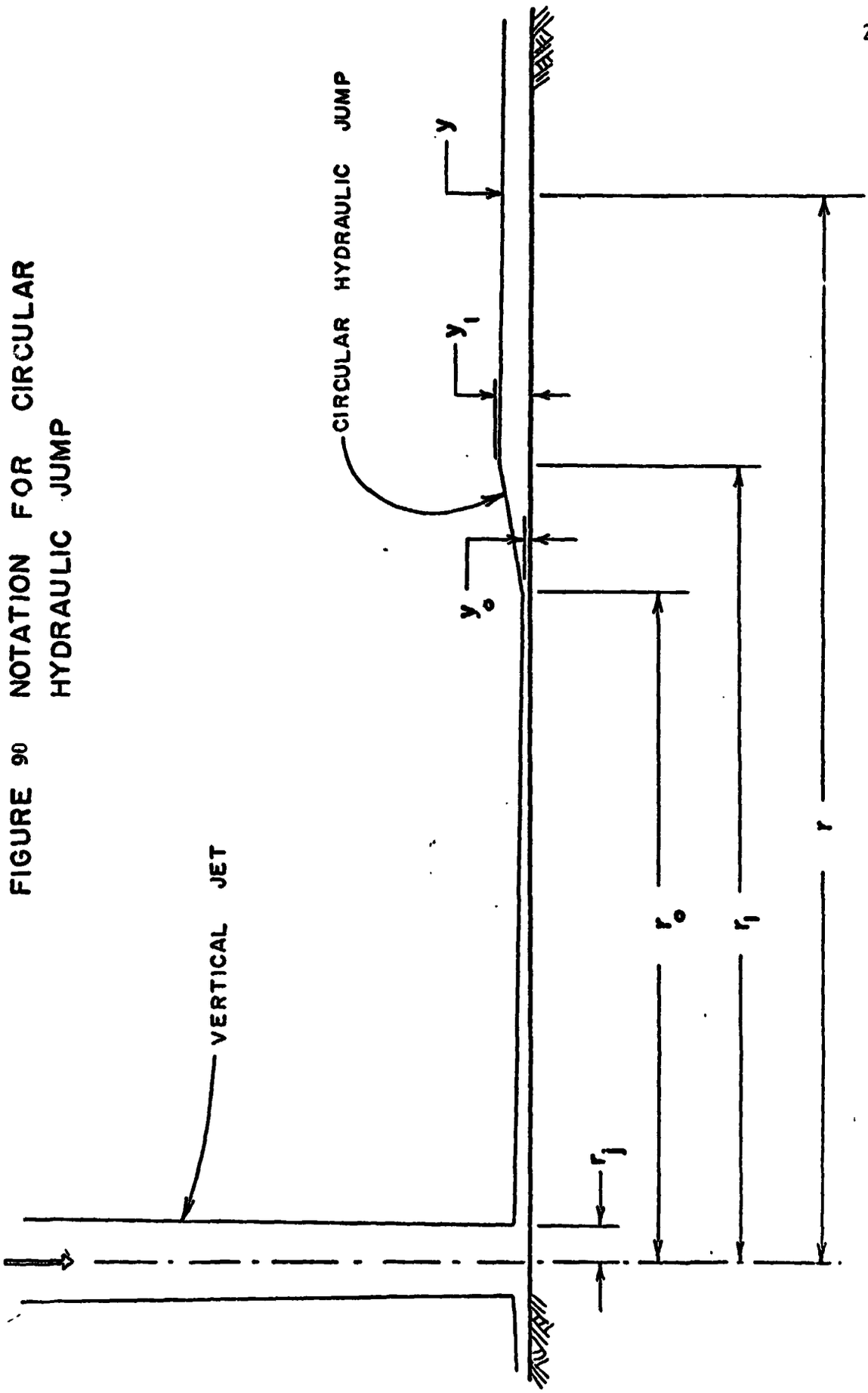

FIGURE 90 NOTATION FOR CIRCULAR HYDRAULIC JUMP

Equations (151), (152), (153), and (154) may be equated assuming no splash before the jump, and no losses due to evaporation or ground seepage.

II. Momentum Across the Jump

It is assumed that the slope of the jump is constant. The forces on an elemental control volume within the jump are as shown in Figure 91, and can be expressed as follows:

$$f_o = p_o A_o = \frac{\gamma}{2} y_o^2 r_o \, d\phi$$

$$f_1 = p_1 A_1 = \frac{\gamma}{2} y_1^2 r_1 \, d\phi$$

$$f_s = p_s A_s = \frac{\gamma}{6} (r_1 - r_o)(y_o^2 + y_1 y_o + y_1^2)$$

The sum of the forces in the horizontal direction, assuming that $\text{SIN} \frac{d\phi}{2} = \frac{d\phi}{2}$, is

$$\sum f = \frac{\gamma}{2} d\phi \; y_o^2 r_o - y_1^2 r_1 + \frac{1}{3} (r_1 - r_o)(y_o^2 + y_1 y_o + y_1^2)$$

The change in momentum in the horizontal direction is

$$\Delta M = \frac{\gamma}{g} Q \Delta V = \frac{\gamma}{g} (V_o y_o r_o d\phi)(V_1 - V_o)$$

The required relationship is (making use of equations (15 2) and (15 3)

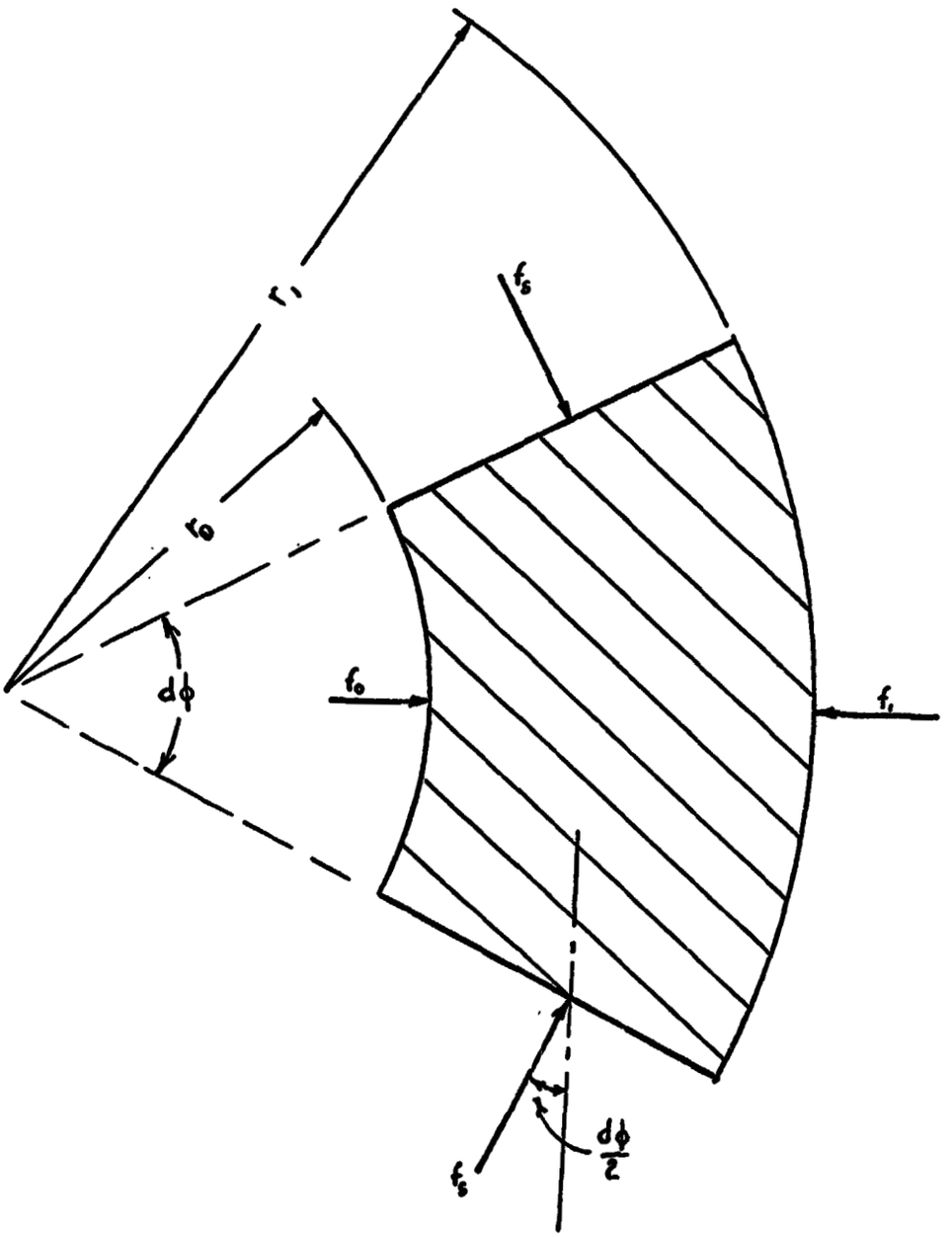

Figure 91 Forces on an Elemental Control Volume within the Jump

$$r_o y_o^2 - r_1^2 + \frac{1}{3}(r_1 - r_o)(y_o^2 + y_1 y_o + y_1^2) = \frac{2 r_o y_o V_o^2}{g}\left(\frac{r_o y_o}{r_1 y_1} - 1\right) \quad (155)$$

Equation (155) can be written as

$$Y^3 - \frac{R-1}{2R+1} Y^2 - \frac{R + 6F_o^2 + 2}{2R+1} + \frac{6F_o^2}{R(2R+1)} = 0 \quad (156)$$

where $Y = \frac{y_1}{y_o}$, $R = \frac{r_1}{r_o}$ and $F_o = \frac{V_o}{(g y_o)^{1/2}}$

III. Energy Balance Between Jet and Flow Field Up to Toe of Jump

The following analysis is made assuming that there are no friction losses and jet impact losses.

The amount of energy passing station 1 (Figure 92 during time interval ΔT, is equal to the amount of energy contained within the region "S", where ΔT is the time interval required to form the region "S" at a given flowrate.

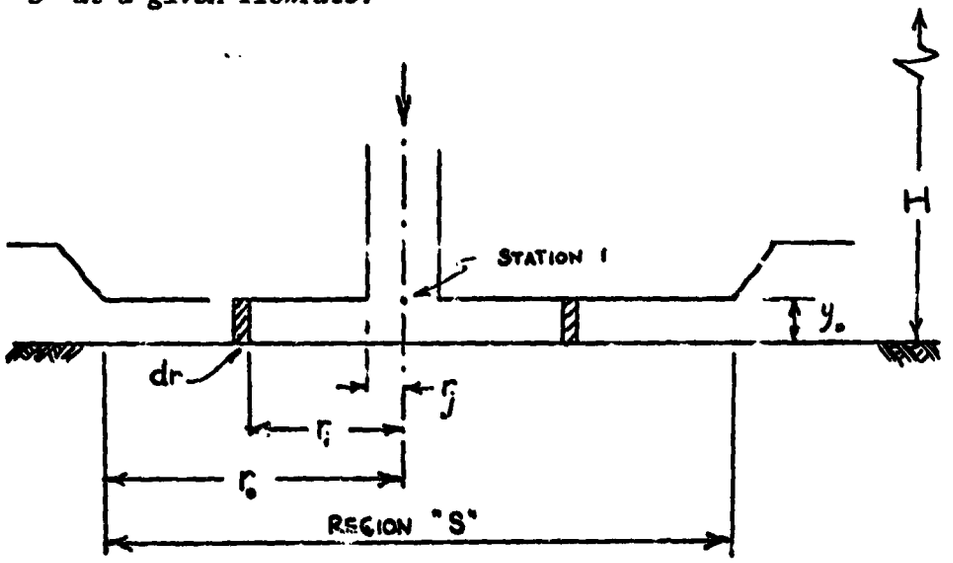

Figure 92 Energy Balance

The energy passing station 1 during time interval ΔT is given by

$$E_1 = \frac{\dot{m}(\Delta T)V_1^2}{2g} \tag{157}$$

The energy contained within the region "S" is

$$E_p = \sum_{i=1}^{\infty} \frac{V_i^2}{2g}\, dm_i \cong \int_1^{\infty} \frac{V_i^2}{2g}\, dm_i \tag{158}$$

Assuming that the depth of flow is constant from r_j to r_o, then

$$dm_i = 2\pi\, r_i \rho y_o dr \tag{159}$$

From continuity,

$$V_i = \frac{\dot{m}}{2\pi\, \rho g y_o}\, \frac{dr}{r} \tag{160}$$

Substituting Equations (159) and (160) into Equation (158) with $r_j \leq r_i \leq r_o$, gives

$$E_p = \int_{r_j}^{r_o} \frac{\dot{m}^2}{4\pi\rho g y_o}\, \frac{dr}{r} = \frac{\dot{m}^2}{4\pi\rho g y_o} \ln \frac{r_o}{r_j}$$

Evaluating the expression within the limits shown, the element of with radius r_j and depth y_o has been omitted, and the energy of the element must be added to Equation (161). This energy is essentially potential energy, and is given by

$$E = \pi r_j^2\, y_o \rho (H - y_o) \tag{162}$$

where $(H - y_o)$ is the height of fall. Since $y_o \ll H$, $H - y_o \cong H$

and Equation (162) can be written

$$E = \pi r_j^2 \, y_o \rho H$$

Adding Equations (161) and (162) gives

$$E_s = E_p + E \frac{\dot{m}^2}{4\pi\rho g y_o} \ln \frac{r_o}{r_j} + \pi r_j^2 \, y_o \rho H \tag{163}$$

Evaluating ΔT in Equation (157)

$$\Delta T = \frac{\pi r_o^2 \, y_o \rho}{\dot{m}} \tag{164}$$

Substituting Equation (164) into Equation (157) gives

$$E_1 = \frac{\pi r_o^2 \, y_o \rho V_1^2}{2g} \tag{165}$$

Equating Equations (165) and (163) by conservation of energy gives

$$\frac{\pi r_o^2 y_o \rho V_1^2}{2g} = \frac{\dot{m}^2}{4\pi\rho g y_o} \ln \frac{r_o}{r_j} + \pi r_j^2 y_o \rho H \tag{166}$$

Since $H = \frac{V_1^2}{2g}$ and $\dot{m}^2 = \pi^2 r_j^4 \rho^2 V_1^2$, Equation (166) can be written

$$\frac{y_o}{r_j} = \left[\frac{\ln \frac{r_o}{r_j}}{2 \frac{r_o^2}{r_j^2} - 1} \right]^{1/2} \tag{167}$$

The description of the flow given by Equations (151), (152), (153), (156), and (167) is incomplete, because the location of the jump, r_o,

is unknown, as is the length of the jump, $r_1 - r_o$. Since analytical methods have been exhausted in the derivation of Equations (151), (152), (153), (156), and (167), an attempt was made to derive empirical expressions containing the unknowns, r_1 and r_o .

Length of Jump

Experimental evidence indicates that for rectangular jumps, the length of the jump varies between 4.3 and 5.2 times the thickness at the heel of the jump. An empirical expression can be given by

$$r_1 - r_o = ny_1 \qquad ; \qquad 3.5 < n < 4.5$$

Letting $n = 4$, and rearranging terms gives

$$\frac{y_1}{r_o} = \frac{1}{4}\left[\frac{r_1}{r_o} - 1\right] \tag{168}$$

Location of Jump

Local experiments were conducted to establish a relationship between the impinging jet's flow characteristics and the radius, r_o , at which the jump begins. It was assumed that the relationship is of the form

$$\frac{r_o}{r_j} = cF_j^b \tag{169}$$

where

$$F_j = \frac{V_j}{(2gr_j)^{1/2}}$$

The results give values for c and b of 0.245 and -0.672 respectively. Substituting these values into Equation (169), gives the following:

$$\frac{r_o}{r_j} = 0.245\ F_j^{-0.672} \tag{170}$$

Experiments Leading to Equation (170)

Procedure

These experiments were conducted on the roof of the Mechanical Engineering Building. The apparatus was set up as shown in Figure 93 and 94. The flow rate was varied giving circular hydraulic jumps ranging in diameter from 2.5 to 11.75 inches. Experiment No. 1 was performed without a nozzle, and Experiment No. 2 was performed with a 3/16 inch I.D. nozzle so as to produce higher jet Froude numbers.

For each flowrate, the Diameter, D_o , was measured, and the flowrate was determined by measuring volumes and elapsed times.

The Froude number of the jet, F_j , is given by

$$F_j = \frac{V_j}{(gD_j)^{1/2}}$$

where V_j = Velocity of the jet and D_j = Diameter of the jet.

Results

A plot of r_j/r_o vs F_j is shown in Figure 95. A curve of the form $r_o/r_j = cF_j^b$ was fitted to the data, where c = 0.245 and b = -0.672.

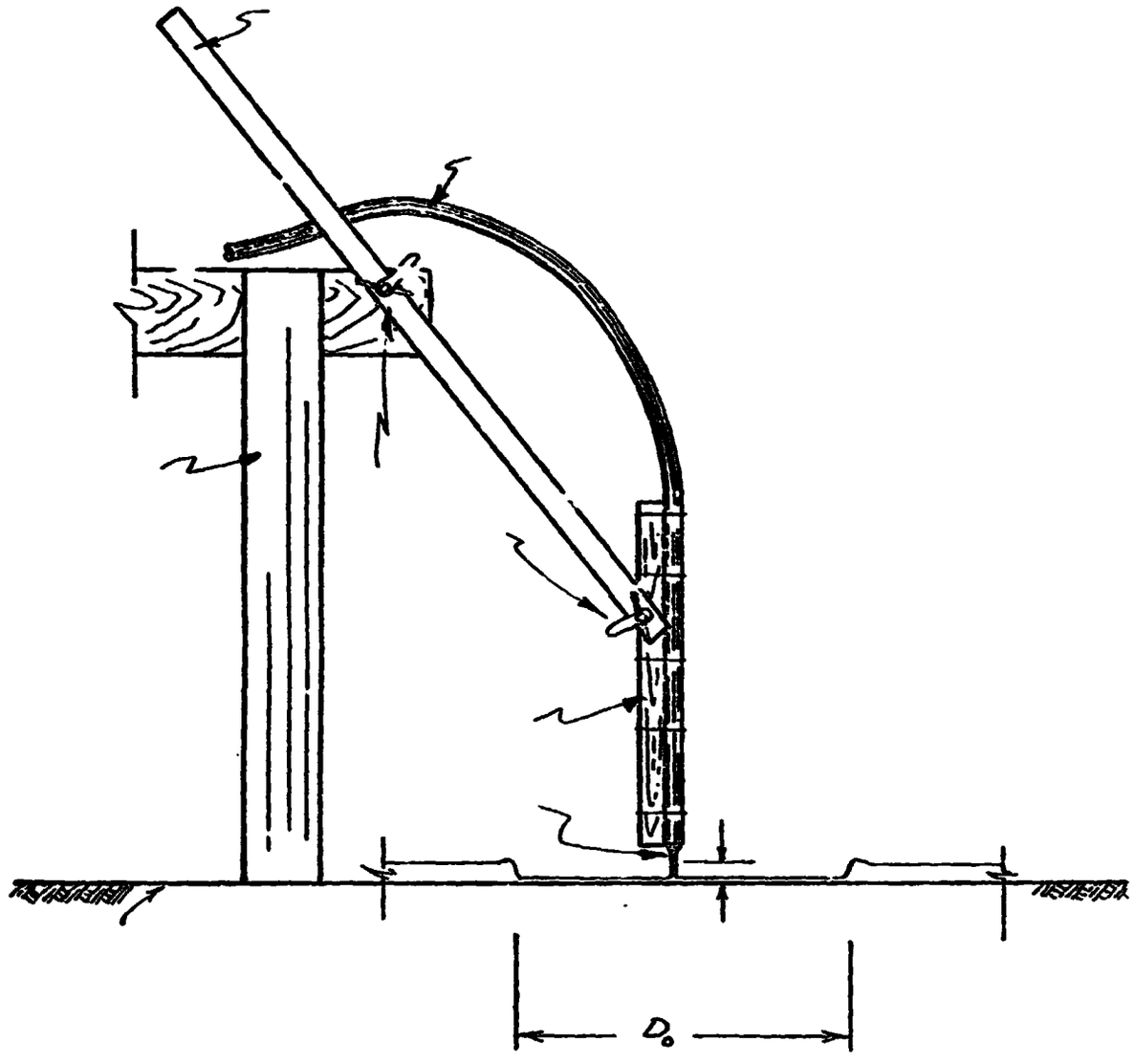

Figure 93 Experimental Apparatus

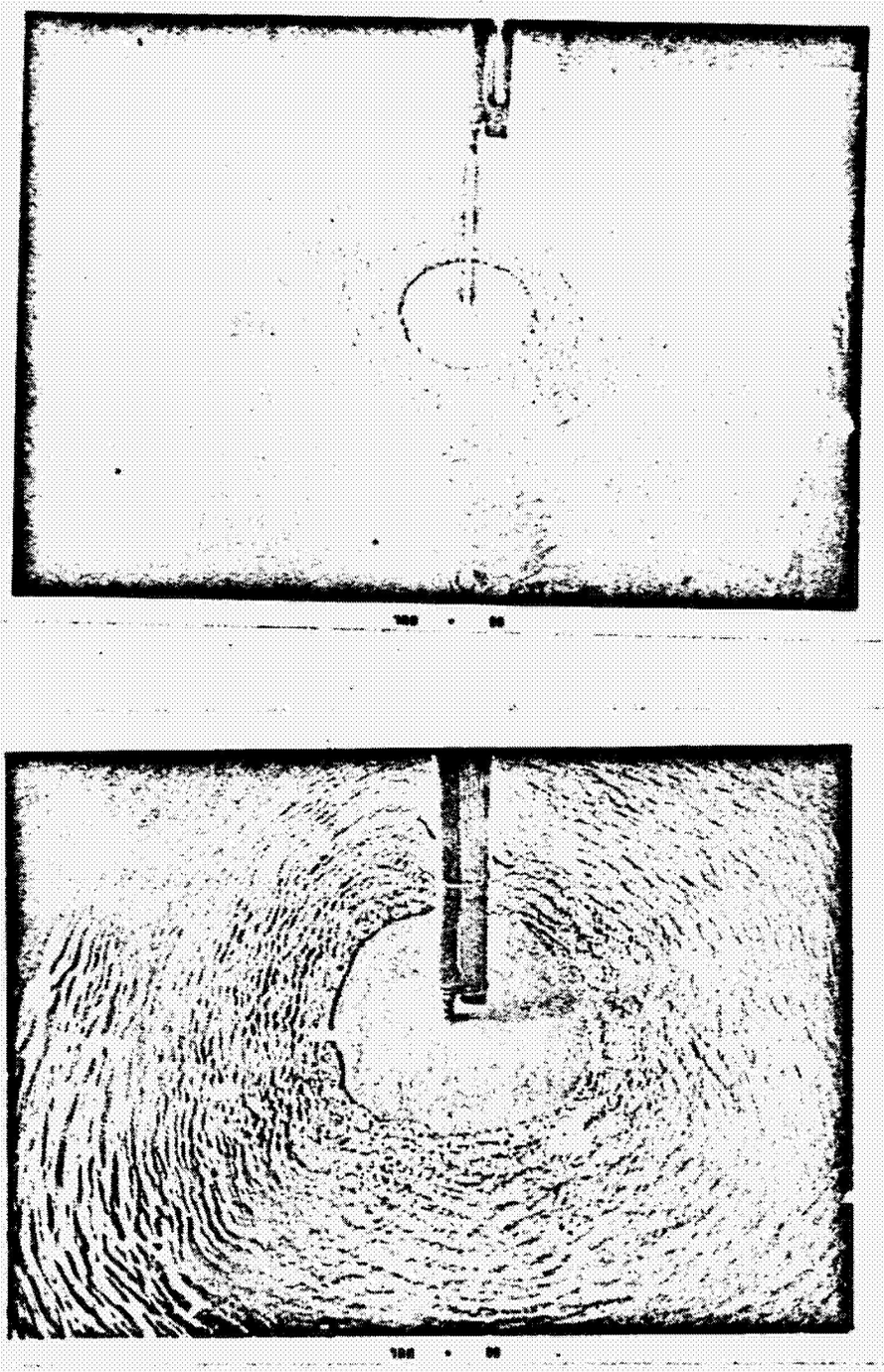

Figure 94 Photographs of Hydraulic Jump Tests

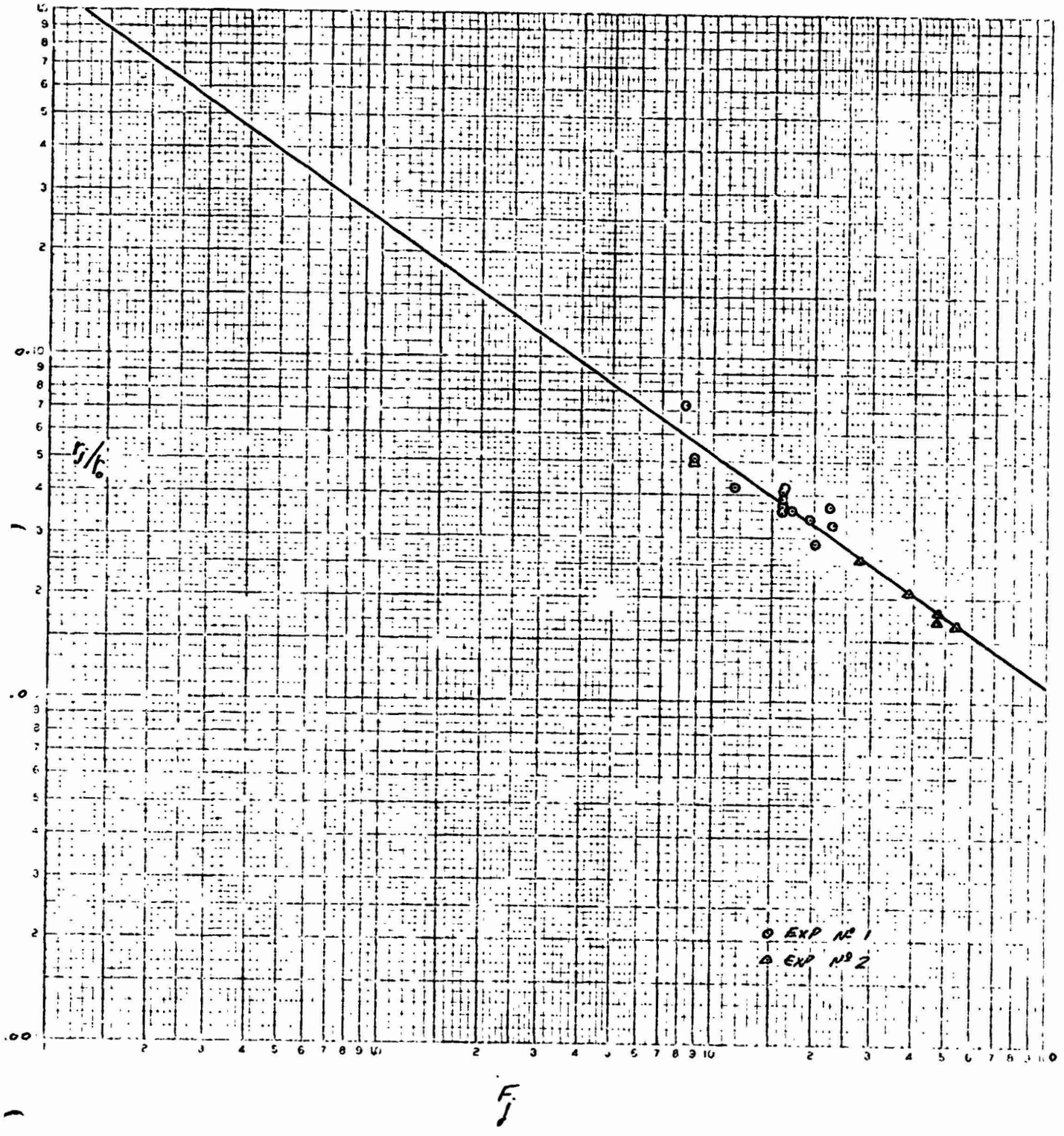

Figure 95 Hydraulic Jump Relationship

Equations (156), (167), (168), and (170) are presented graphically in Figures 96 thru 99 respectively.

A plot of the simultaneous solution of Equations (151), (152), (153), (156), (167), (168), and (170) is shown in Figure 100. After making several sample calculations using Figure 100, it was found that predicted depths at the heel of the jump were approximately twice those observed. Reviewing the assumptions made in the derivation of Equation (167) it was felt that the error involved by neglecting the losses incurred in the abrupt transition from vertical to horizontal flow, by assuming the depth to be constant, and by neglecting frictional losses, accounts for the sizeable departure from observed results experienced when using Figure 100. Unable to account for losses neglected in Equation (167) analytically, Equation (171), using continuity only,

$$\frac{y_o}{r_j} = \frac{1}{2a}\,\frac{r_j}{r_o} \tag{171}$$

where $a = \frac{V_o}{V_j}$

was used to replace Equation (167). A plot of Equation (171), for various values of a, is shown in Figure 101. A value for a of 0.14 to 0.10 gives results which best agree with observed results. A simultaneous solution of Equations (151), (152), (153), (156), (168), (170), and (171), is given by

$$RF_j^b + SF_j^{2b} - TF_j^{3b} - UF_j^{4b} - VF_j^{2+b} + WF_j^{2(1+b)} + X = 0 \tag{172}$$

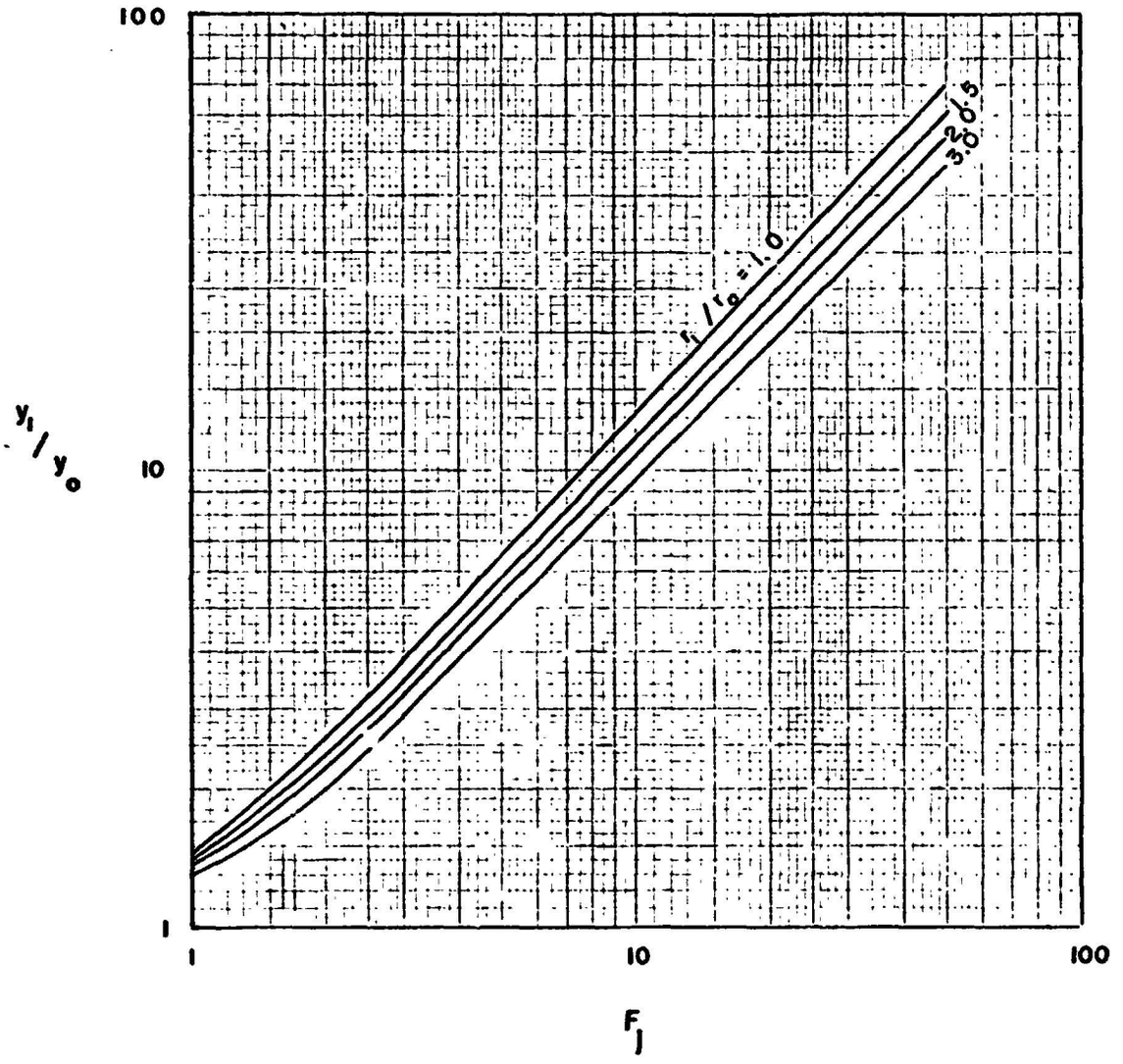

FIGURE 96 CIRCULAR HYDRAULIC JUMP
EQUATION 156

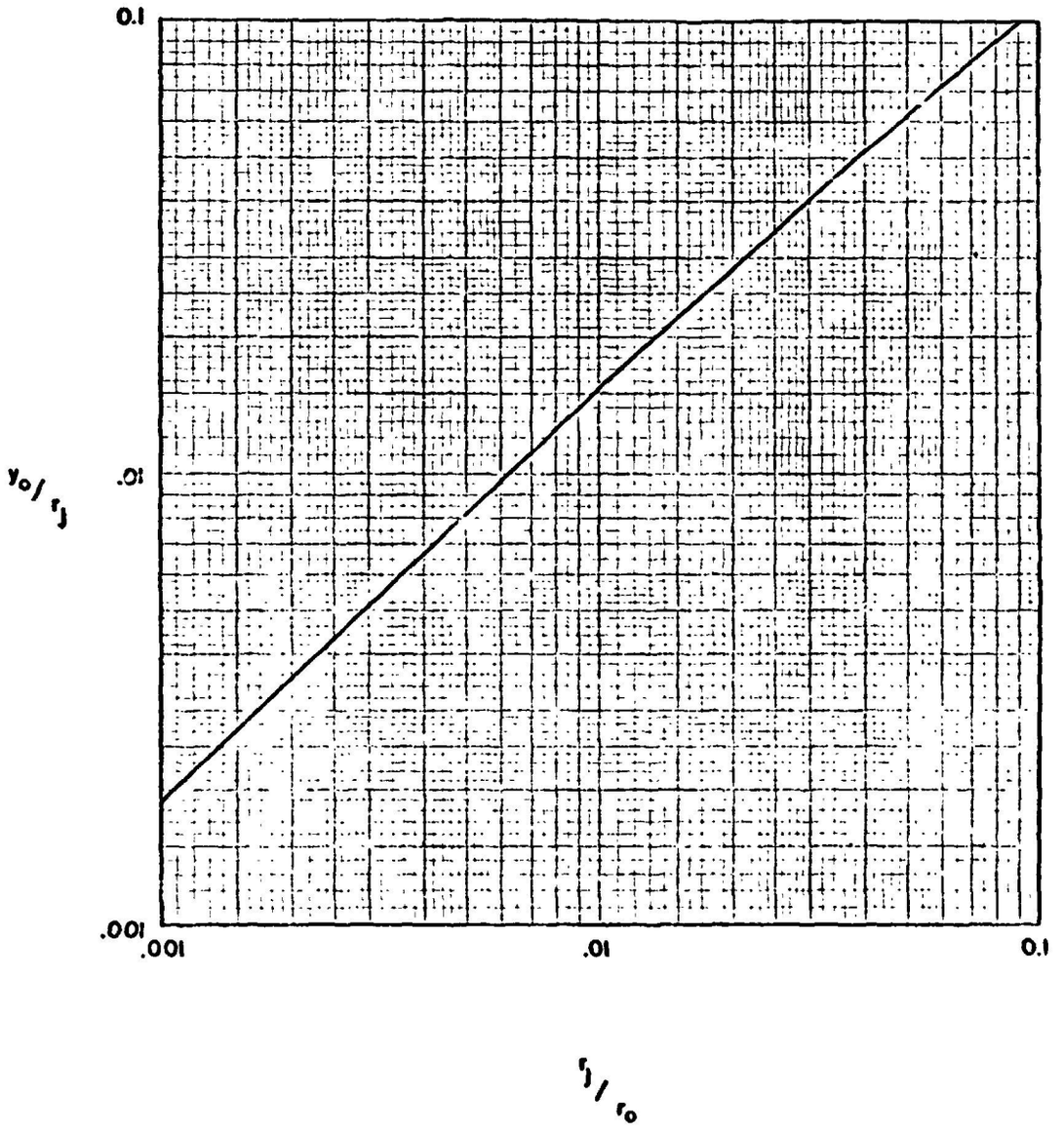

FIGURE 97 CIRCULAR HYDRAULIC JUMP
EQUATION 167

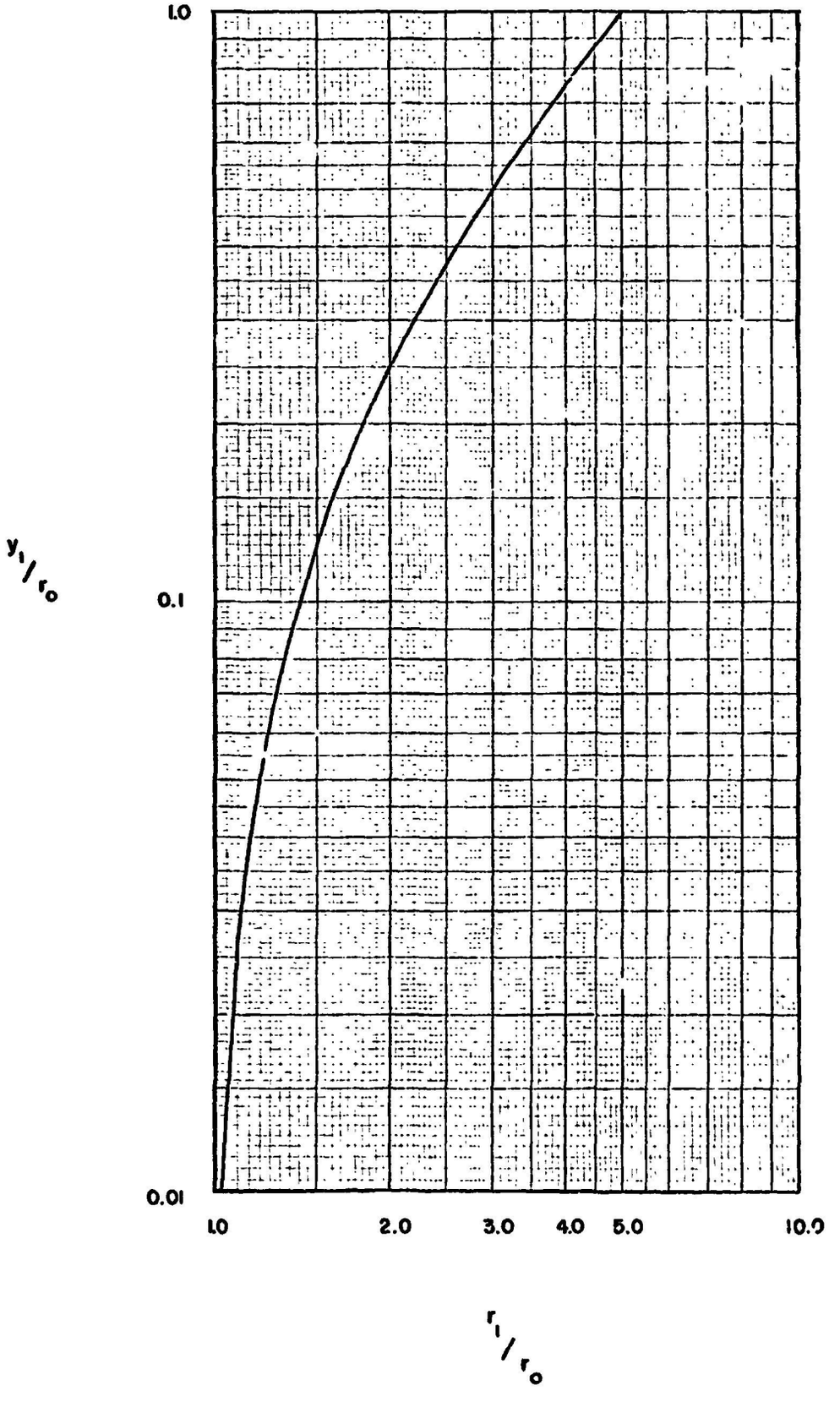

FIGURE 98 CIRCULAR HYDRAULIC JUMP EQUATION 168

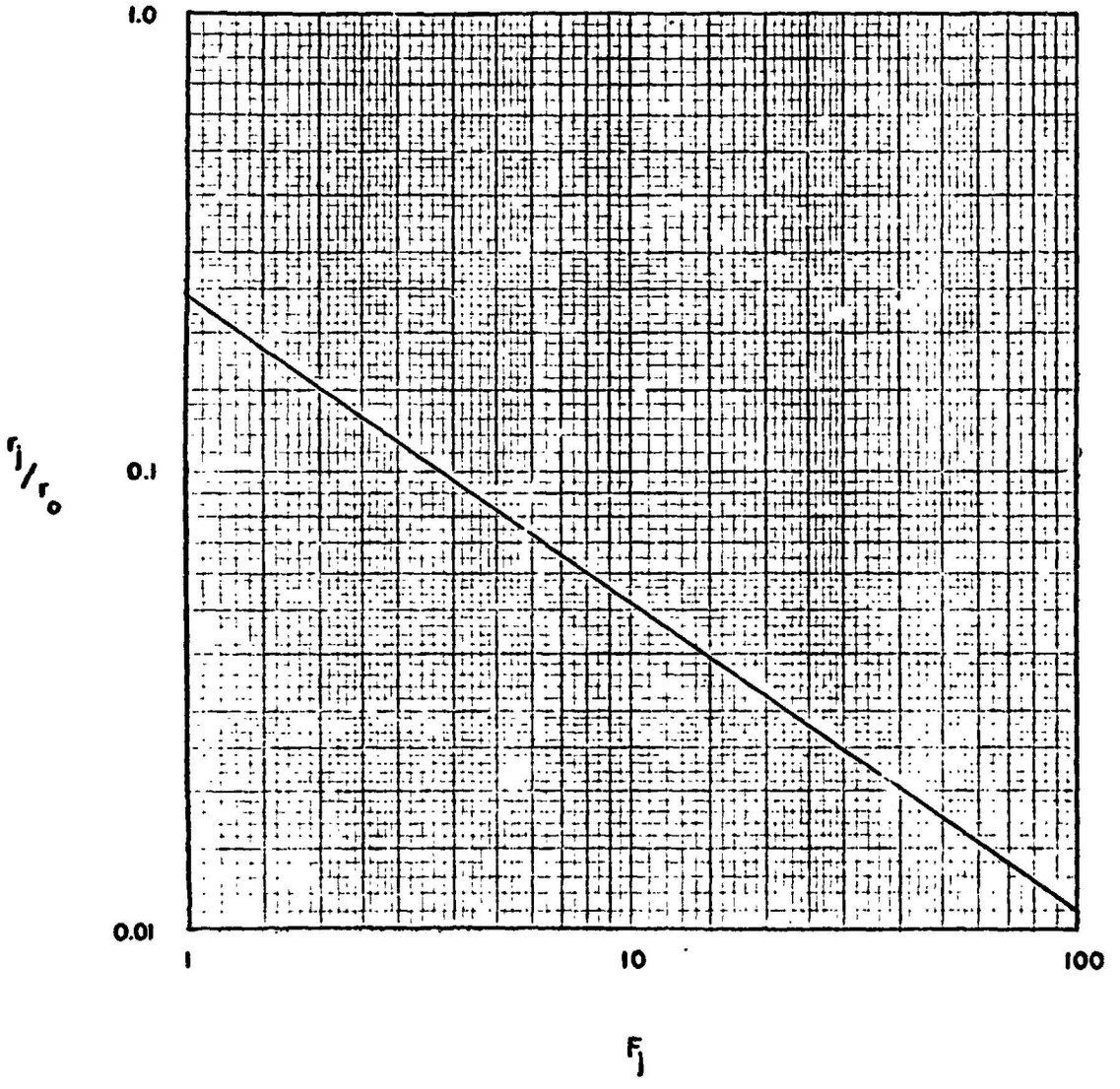

FIGURE 99 CIRCULAR HYDRAULIC JUMP
EQUATION 170 -JUMP LOCATION

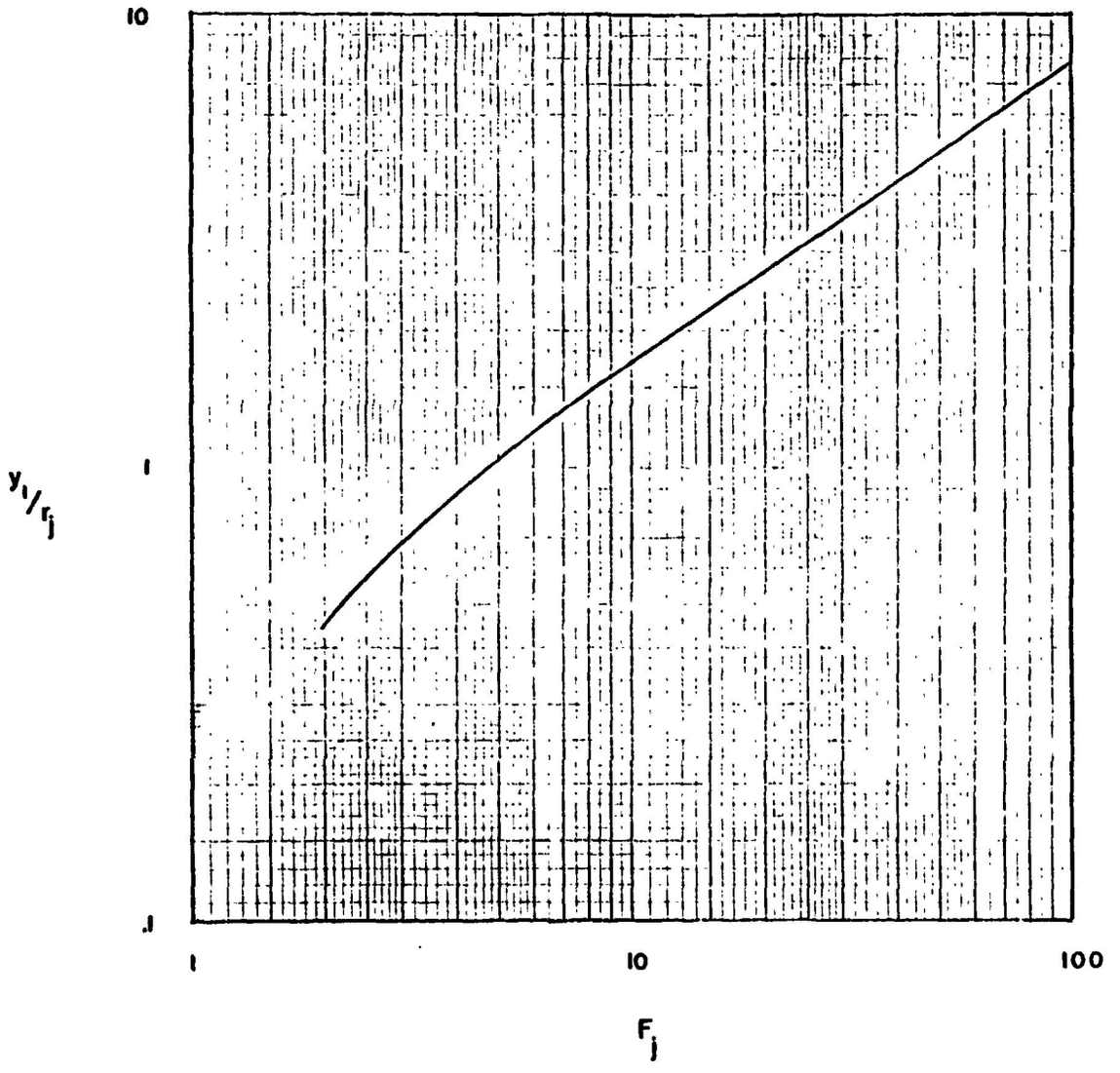

FIGURE 100 CIRCULAR HYDRAULIC JUMP – SIMULTANEOUS SOLUTION TO JUMP EQUATIONS

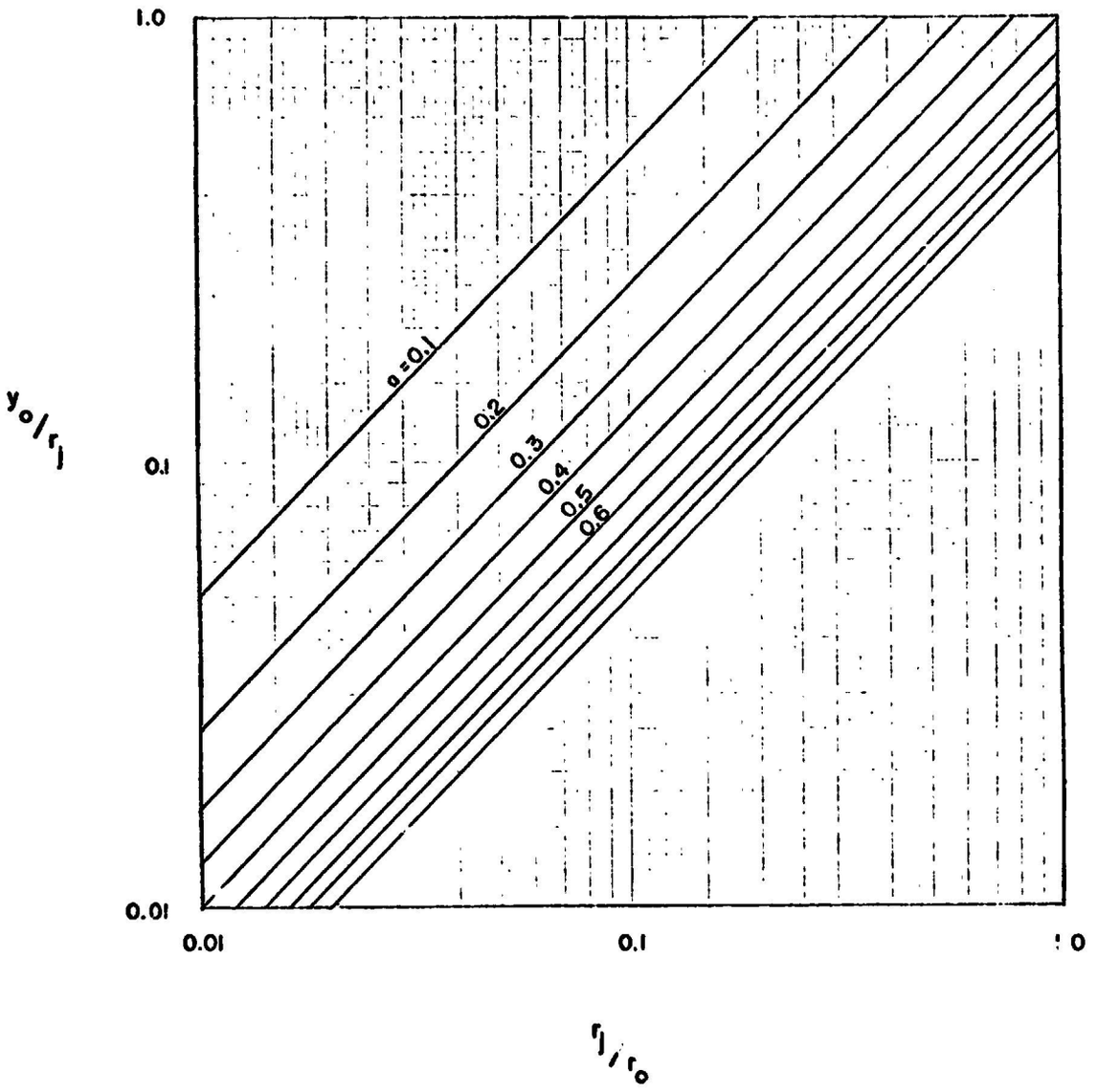

FIGURE 101 CIRCULAR HYDRAULIC JUMP
EQUATION 171

where

$$R = 20A^2a \quad ; \quad S = 32A^2ac - 2Ac - 3c/4Aa$$

$$T = 8A^2c^2 + 4c^2/a \quad ; \quad U = 4Ac^3/a \quad ; \quad V = 6a^2/A$$

$$W = 3ac/A^2 - 24a^2c \quad ; \quad X = 3Aa/c$$

$$A = y_i/r_j \quad ; \quad a = V_o/V_j \quad ; \quad c = 0.245 \quad ; \quad b = -0.672$$

A plot of Equation (172) for vari . values of a is shown in Figure (102).

Computer programs for the solution of Equations (156) and (172) are presented in the Appendix.

Conclusions

An effort was made to apply Equation (156) to the regions downstream of the jump, with the limitation that the Froude number at the heel of the jump be less than one. Computer programs for the solution of the equation, both considering the side forces on the elemental volume and neglecting them, are presented in the Appendix. It was found that a very rapid decrease in thickness was predicted immediately following the jump, and by applying continuity to the predicted dimensions an increase in velocity resulted for an increase in radius. This not only contradicts intuition, but also observed results. Therefore, Equation (156) is only applicable to the situation in which a jump occurs.

From observation, it is felt that the depth downstream of the jump can be considered approximately constant for all practical purposes, its value taken as the depth at the heel of the jump.

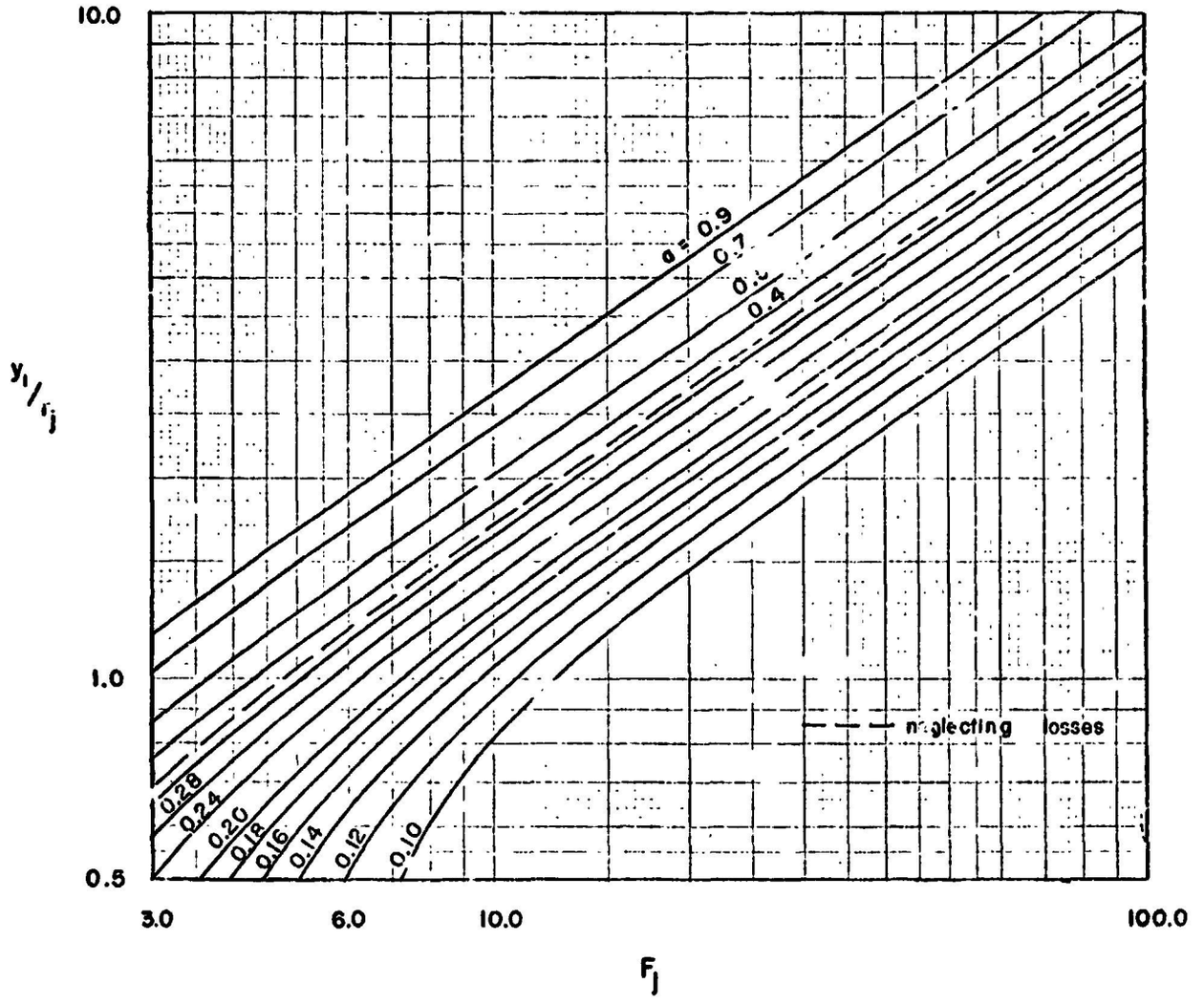

FIGURE 102 CIRCULAR HYDRAULIC JUMP
EQUATION 172

The above analysis showed that the splash puddles can be considered circular for all practical purposes since the eccentricity is very small. This allows for much less laborious treatment of the problem and a much shorter method for determining the mixing function.

From the slot size and basic fluid dynamics the out-flow velocities and flow rates as a function of time can be determined giving the amount of liquid on the ground at any time τ . This was done by computer program and the results are shown in Figure 103, normalized for the Saturn V.

The impact point also can be calculated by the computer program giving the time variation of the impact point on the ground surface. The results of these calculations are shown in Figures 104 through 108.

The depth at any one time τ of the puddles was assumed to be constant as supported by the theoretical investigation, and the variation with time was calculated using the momentum spreading relationships during the early times and the hydraulic head spreading at the later times. Both these curves were plotted and where they crossed the change from one result to the other was made. The complete curves representing the depth of the puddles are also given in Figures 104 through 108.

From the quantity of propellant on the ground and the depth at any one time the radius of the puddle can be calculated and the variations with time are again presented in the same Figures 104 through 108.

Having the impact point for each fuel or oxidizer on the ground and the amount of each component on the ground at any time τ , and the depth, the resulting radii can be plotted to give the splash patterns which allow the determination of the mixing regions and the quantities

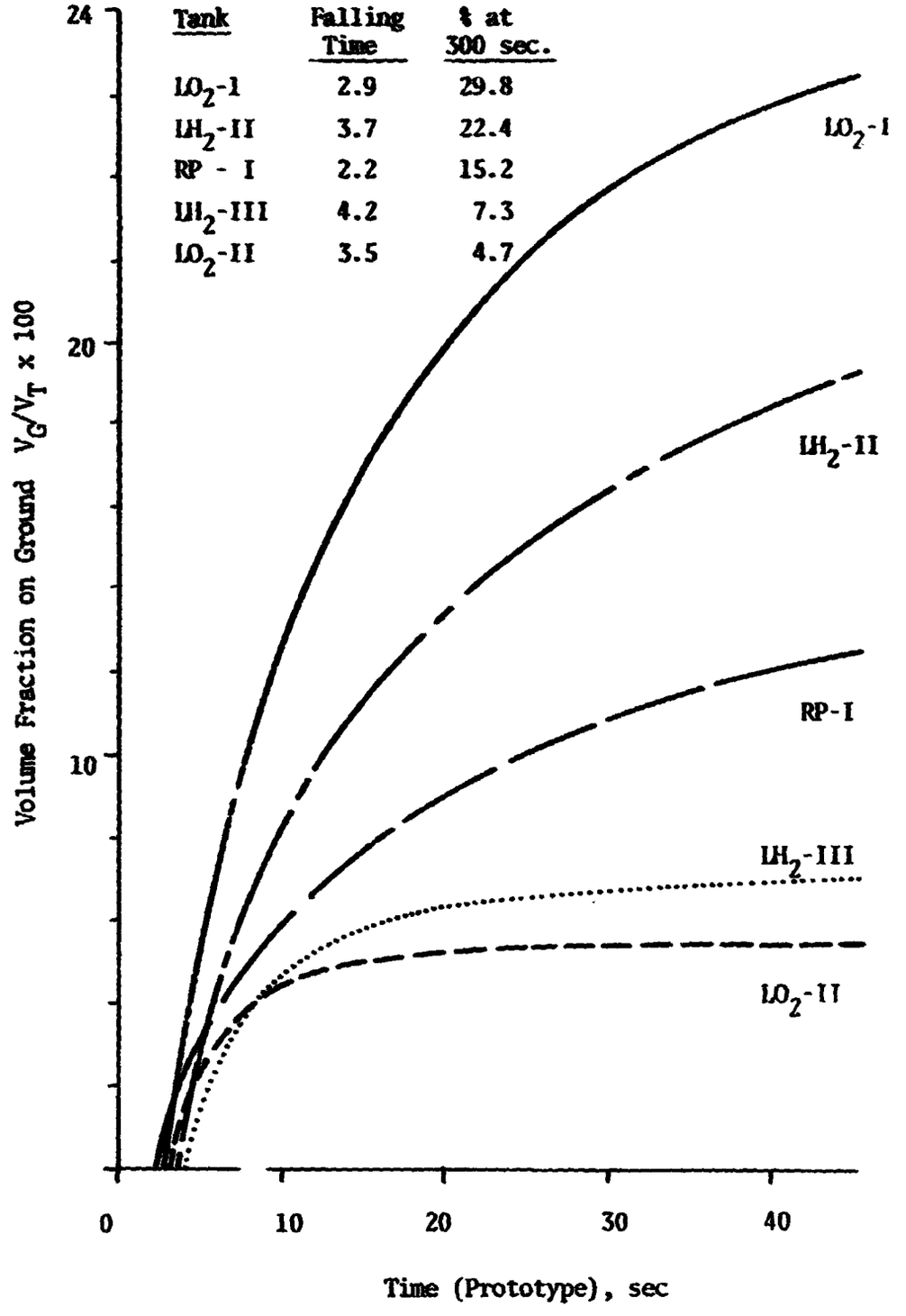

Figure 103 Volume on Ground from Each Tank Based On NASA Slots

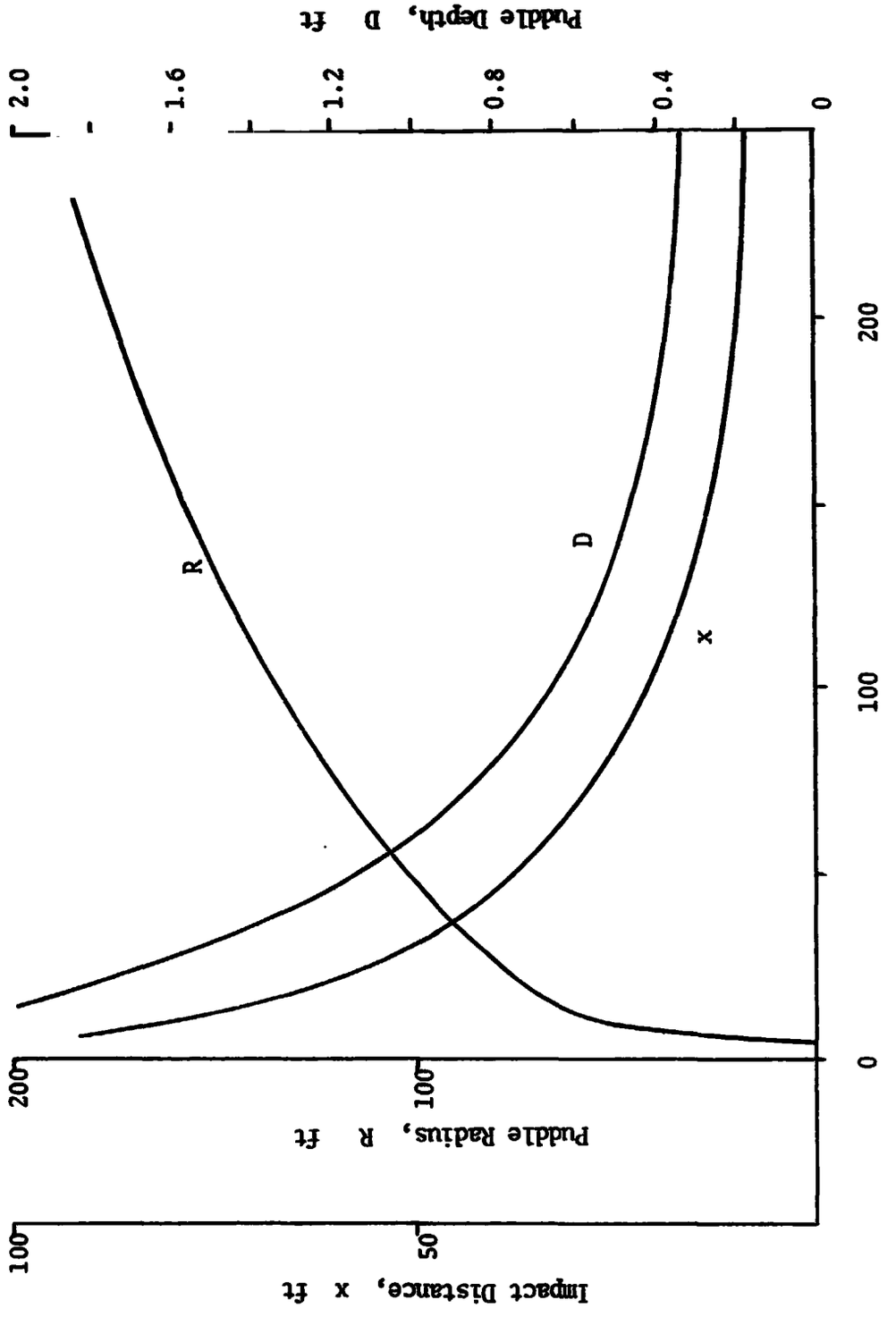

Figure 104 Theoretical Calculations of Impact Distance, Radius, and Depth of Puddle versus Prototype Time for Stage I (LO_2 Tank)

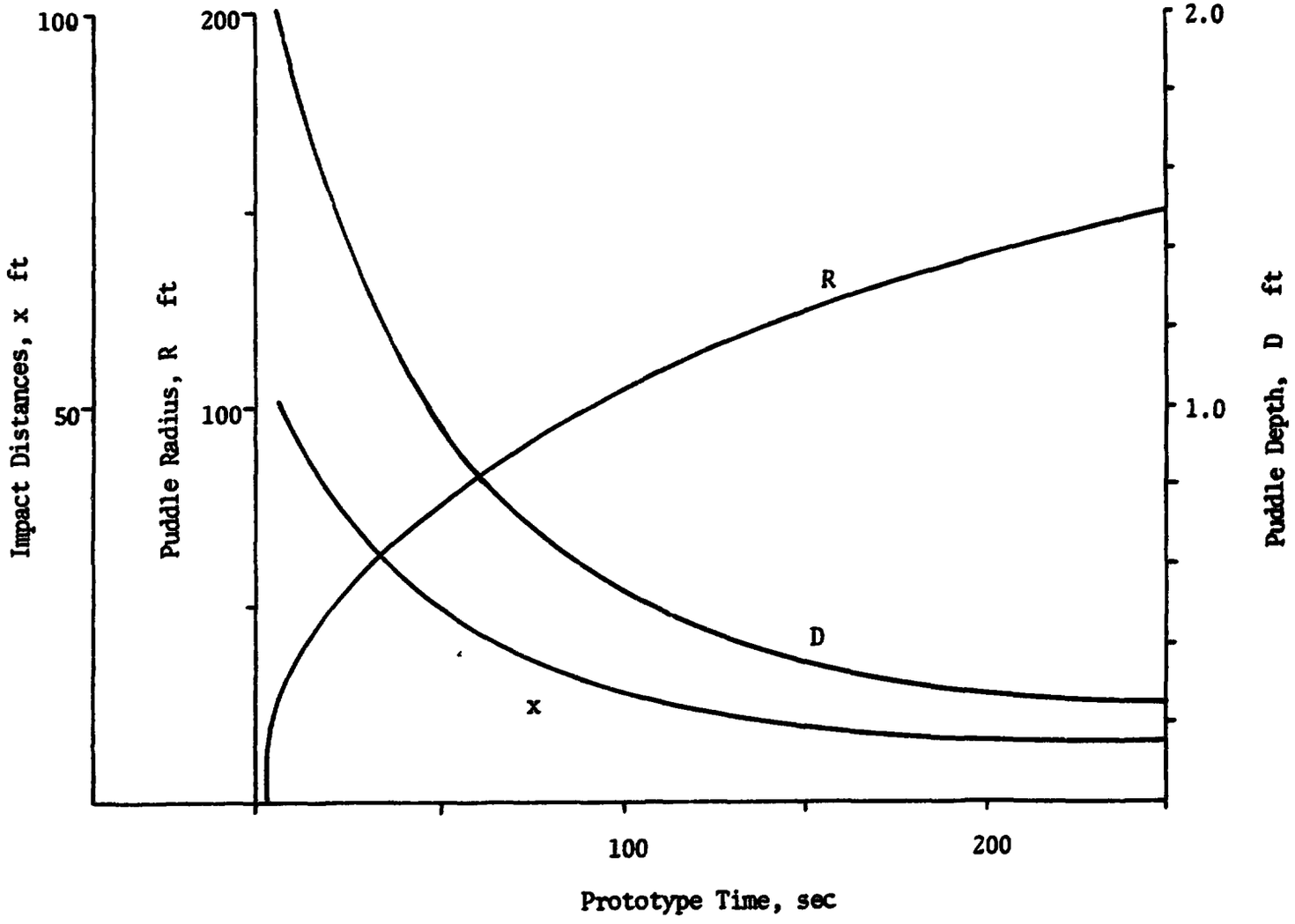

Figure 105 Theretical Calculations of Impact Distance, Radius, and Depth of Puddle Versus Prototype Time for Stage I (RP Tank).

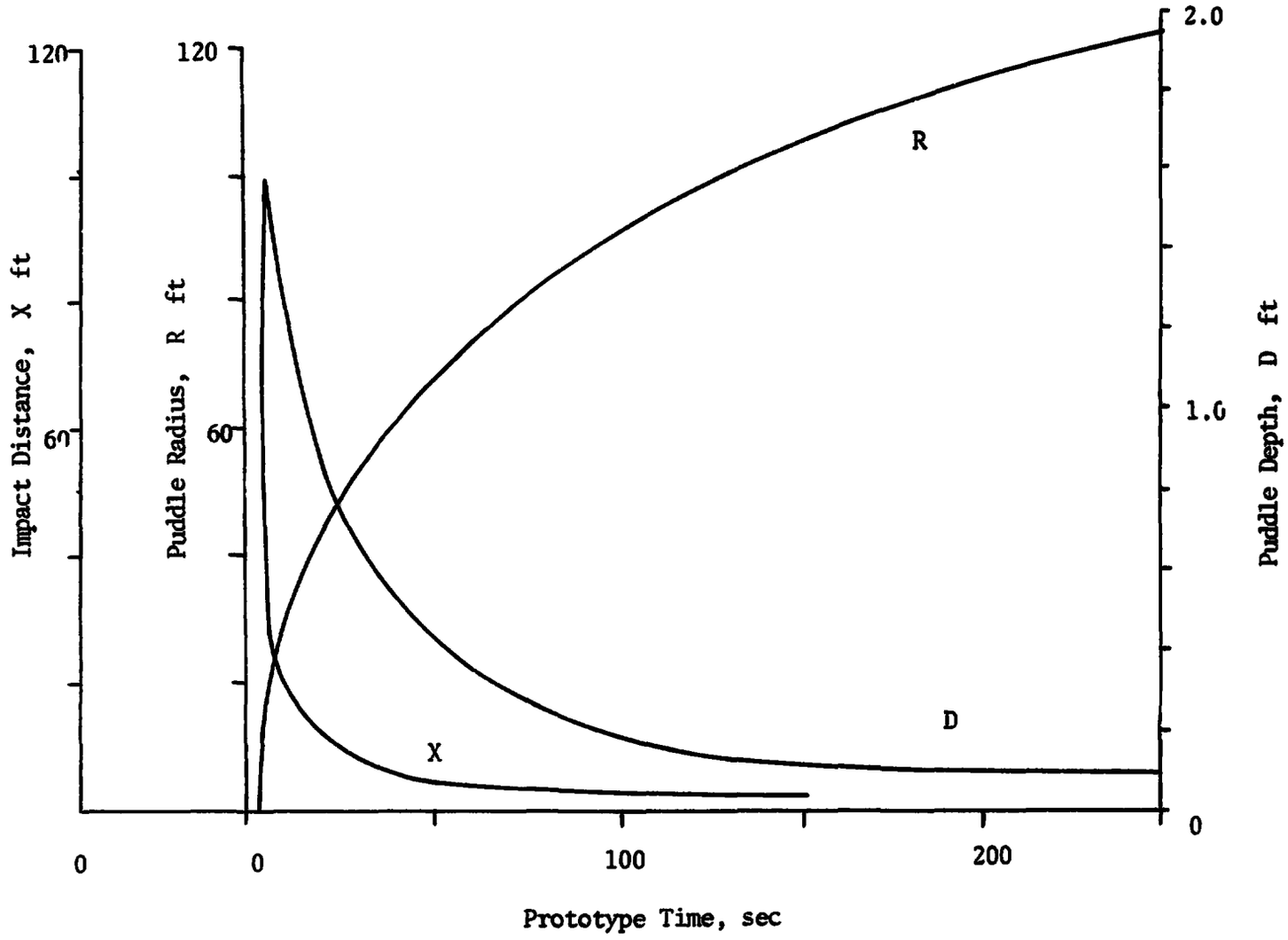

Figure 106 Theoretical Calculations of Impact Distance, Radius, and Depth of Puddle Versus Time for Stage II (LO_2)

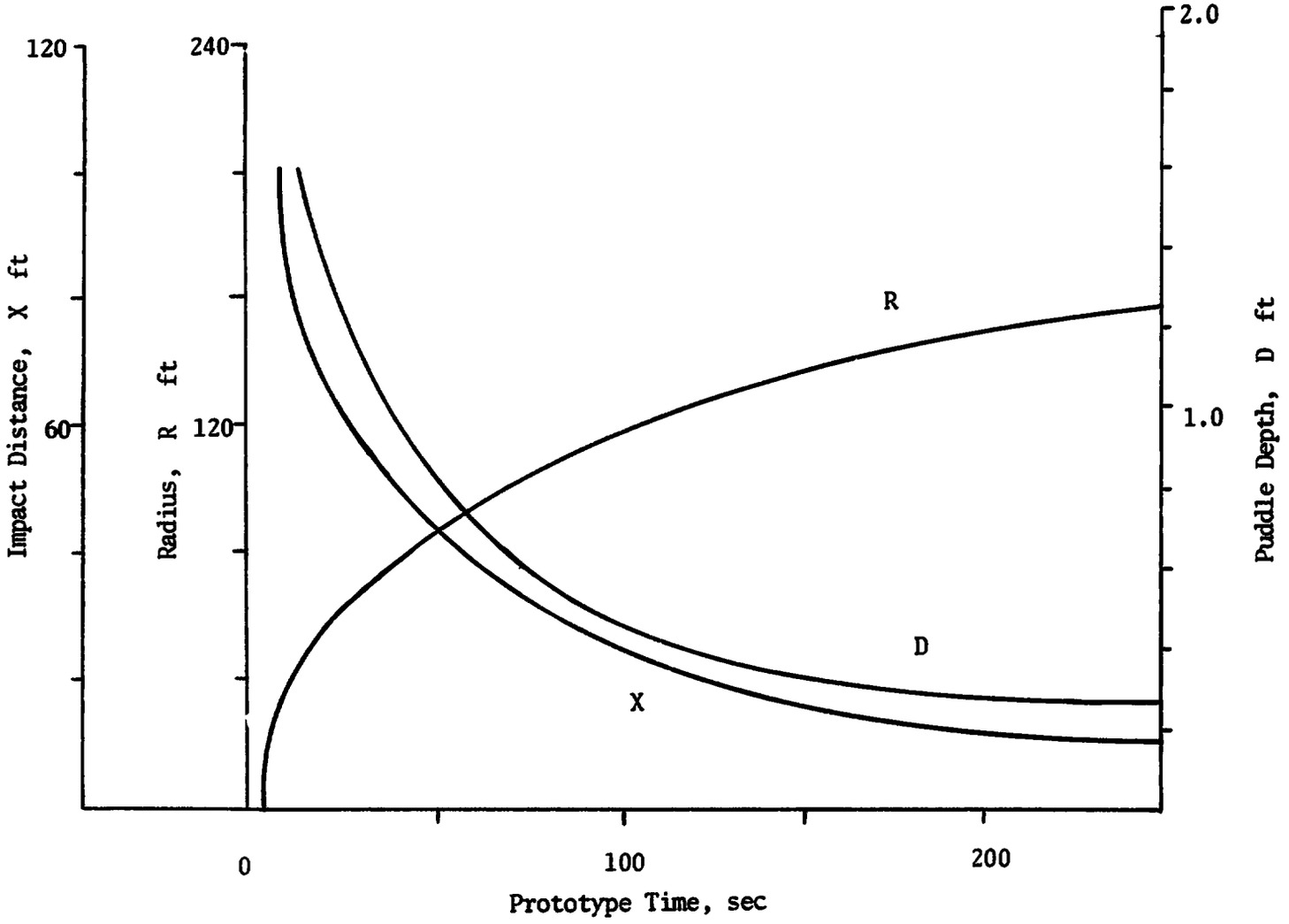

Figure 107 Theoretical Calculations of Impact Distance, Radius, and Depth of Puddle Versus Time for Stage II (LH_2 Tank).

Figure 108 Theoretical Calculations of Impact Distance, Radius and Depth of Puddle Versus Time for Stage III (LH_2 Tank).

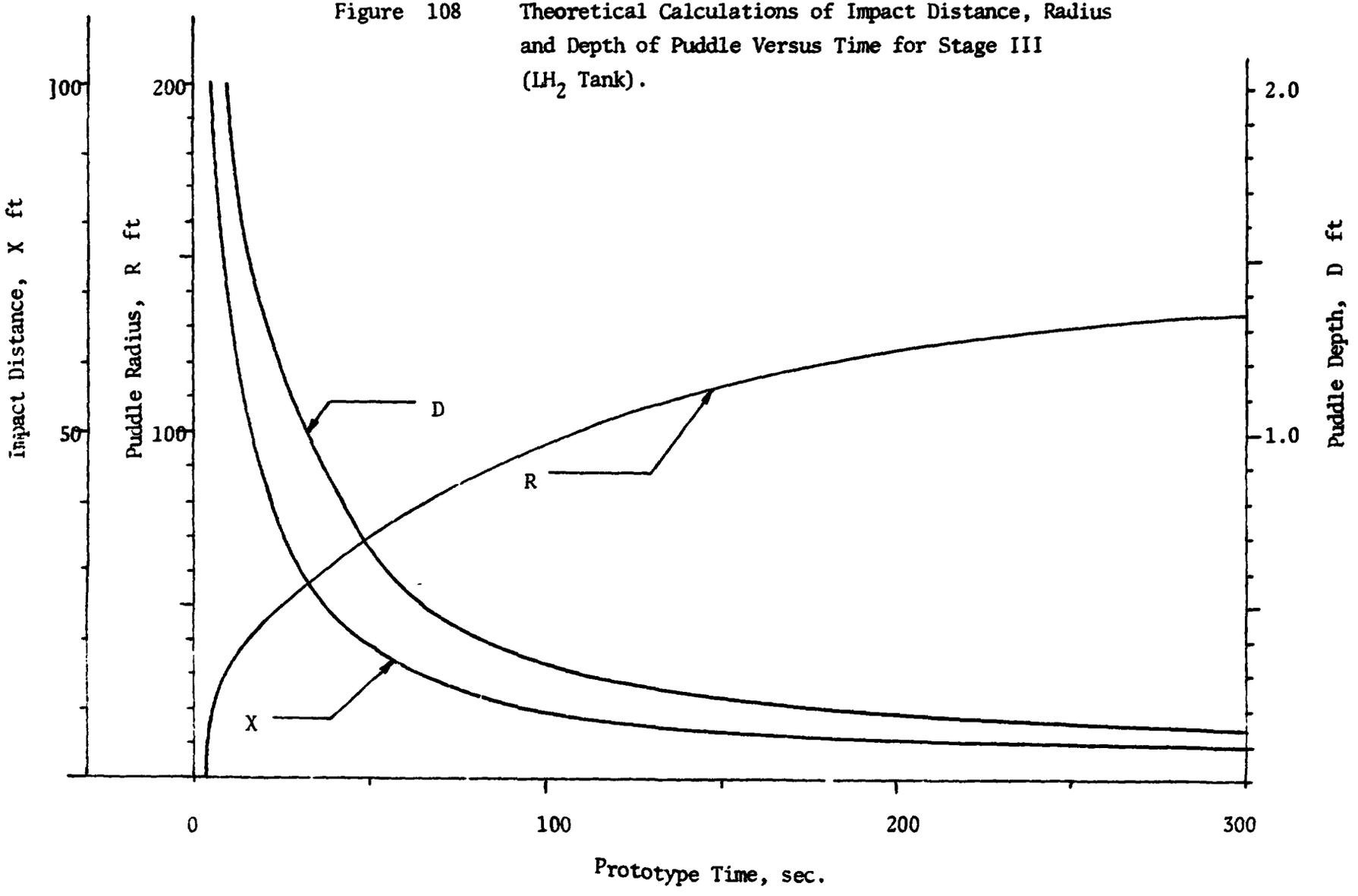

which are actually mixed at any time τ .

Figure 109 gives the splash pattern and the mixing regions around the Saturn V rocket due to the activation of the destruct system and shows the progressive mixing as time goes on. The actual conditions are plotted for 5, 10, 15, 20, 30, 40, and 50 seconds after the initiation of the destruct system.

A scale change was necessitated at this point to be able to present the continuing splash patterns on the same size of paper. So Figure 110 presents the continuing splash patterns for 50, 60, 80, and 120 seconds. The first one was selected to give the overlap with the previous Figure and a comparison can be made.

Another scale change was made for the last part of the splash investigation to again shrink the pattern so as to fit it onto the page. Figure 111 presents the patterns for times of 120, 180, and 240 seconds after the initiation of the destruct system.

From the splash patterns the average depth at any time τ was obtained by dividing the total splash area into the known volume on the ground. The areas of the mixed constituents LO_2/LH_2 , LO_2/RP-1 , and LO_2/LH_2/RP-1 were then multiplied by the average depth at that time to obtain the mixed volumes. The volume of the three way mix was most frequently assumed to be one half LO_2/LH_2 and one half LO_2/RP-1. Other combinations were also investigated such as having all the LH_2 react before any of the RP-1 was allowed to, or the evaporation was such as to produce a certain definite mixing depth. These simplifying assumptions were made to get some approximate answers early in the investigation and after much more detailed work with computers, proved to be

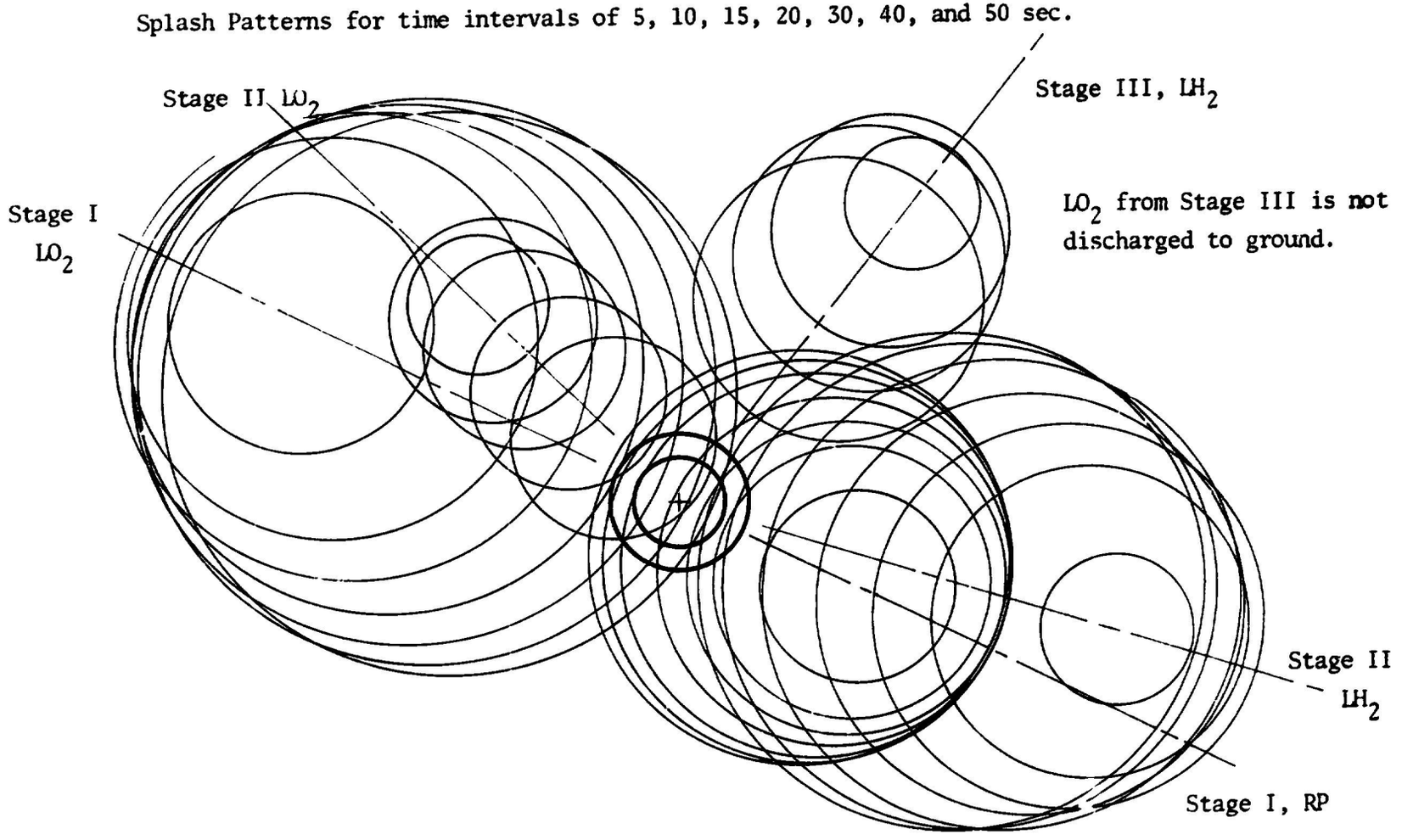

Figure 109 Splash Pattern for Saturn V Destruct System

Splash Patterns for 50, 60, 80, 120 sec.

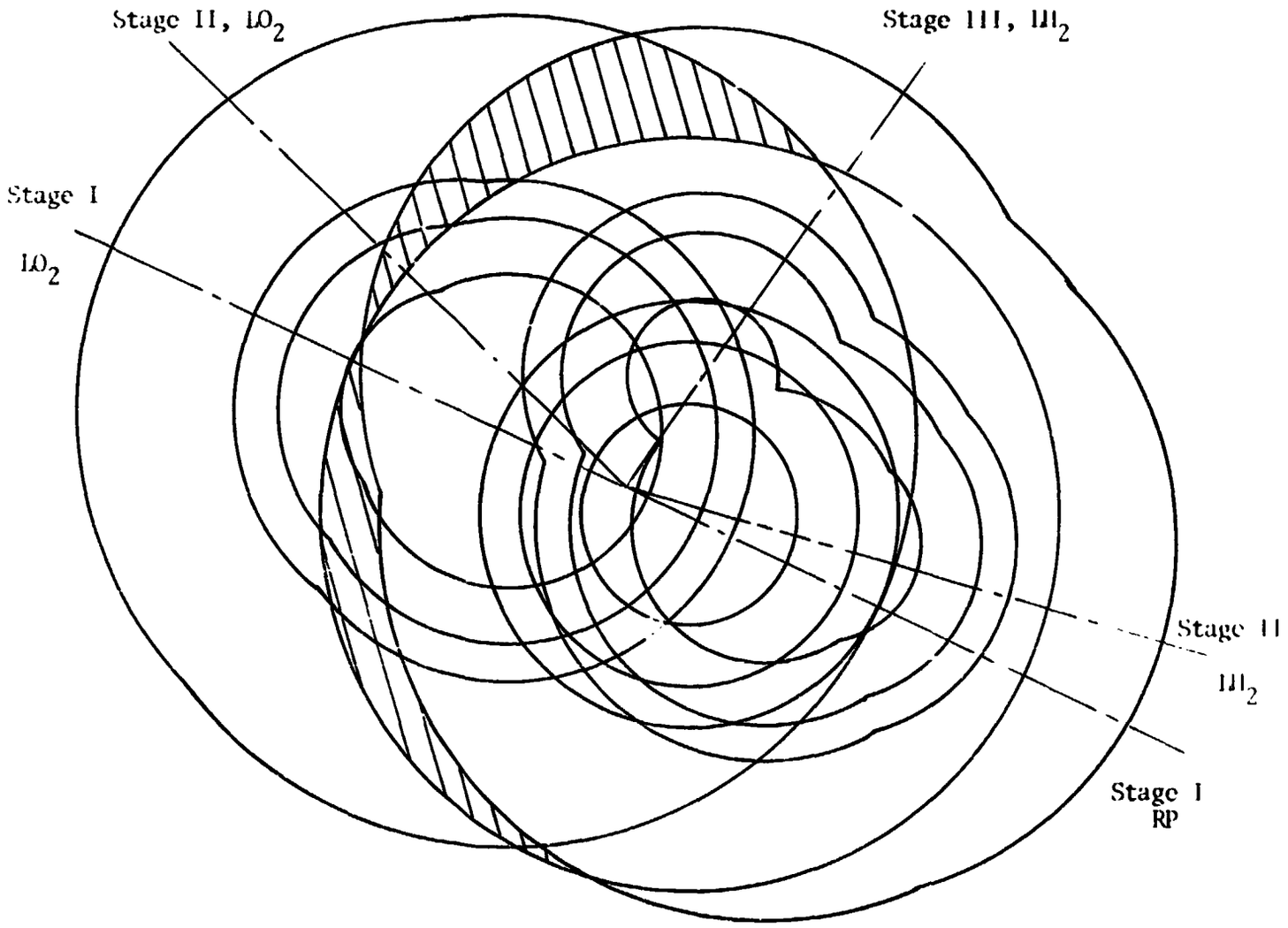

Figure 110 Splash Pattern for Saturn V Destruct System

Splash Patterns for 120, 180, and 240 sec.

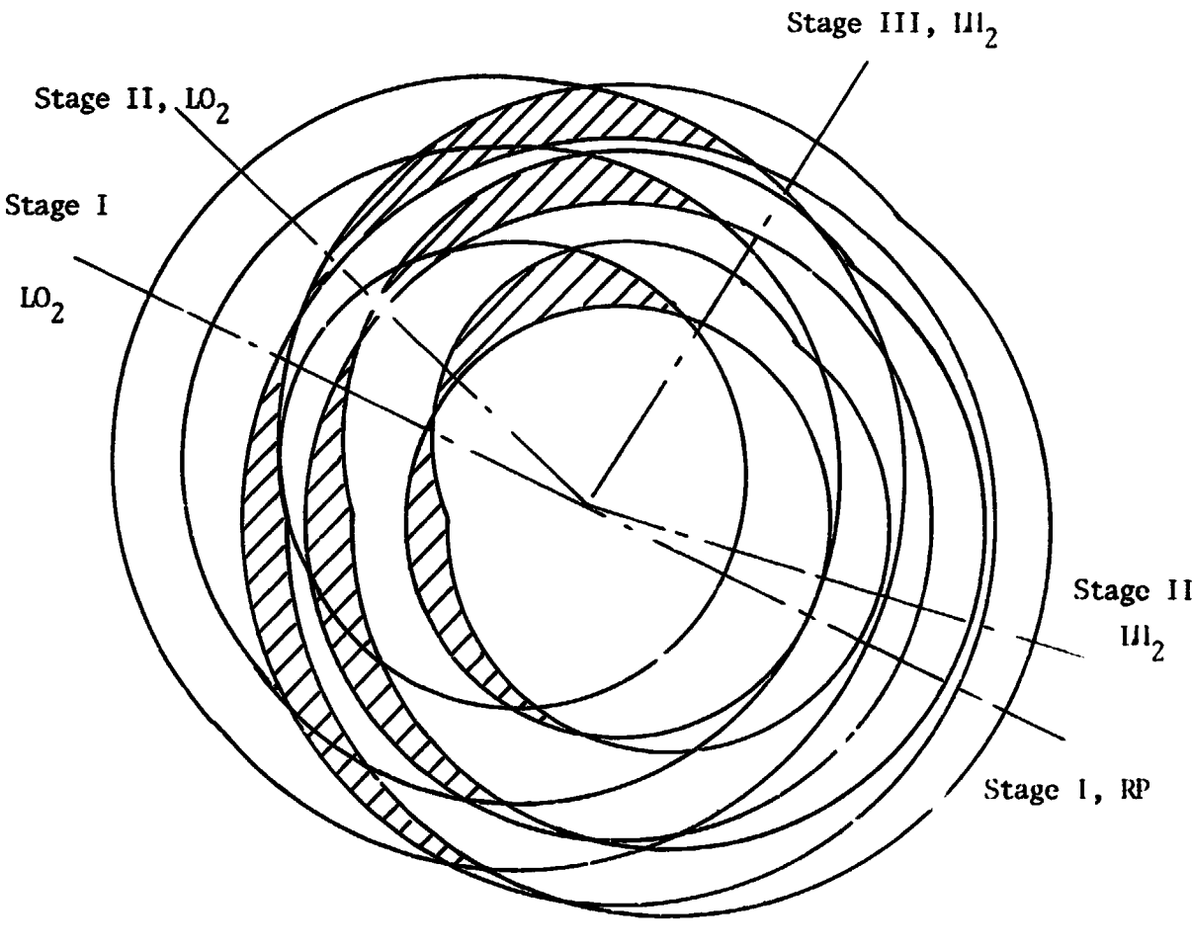

Figure 111 Splash Pattern for Saturn V Destruct System

rather good and in basic agreement with the later much more elaborate methods of analysis.

For the more elaborate work the evaporation losses were theoretically calculated using the methods of Part I. This allowed the determination of the mixture on the ground at any time τ, considering the heat exchange among the propellant components and the propellant components and the ground.

The evaporated material was assumed to form a hemisphere, (no wind) above the puddles. The clouds came together and mixed before the liquids could on the ground and so they show the first potential for producing an explosion and a yield, but the liquids started mixing soon after and they had much more energy which could be released in an explosion. Using the methods as discussed in detail in Part I, for the analysis of the Saturn V destruct system the resulting explosive yield curve can be plotted. Figure 112.

It is well to mention again this curve of Figure 112 is the explosive yield which can be expected at any time τ if ignition should occur at that time. From the previous discussions in Part I and Part II of this report and the many papers and other reports discussing this subject, it has been shown that this curve would actually be terminated rather early in its development either by external or internal ignition sources so that the actual yield values are held to rather small numbers.

The third and second stage, S-IVB/S-II Interstage failure is discussed in detail later in this section.

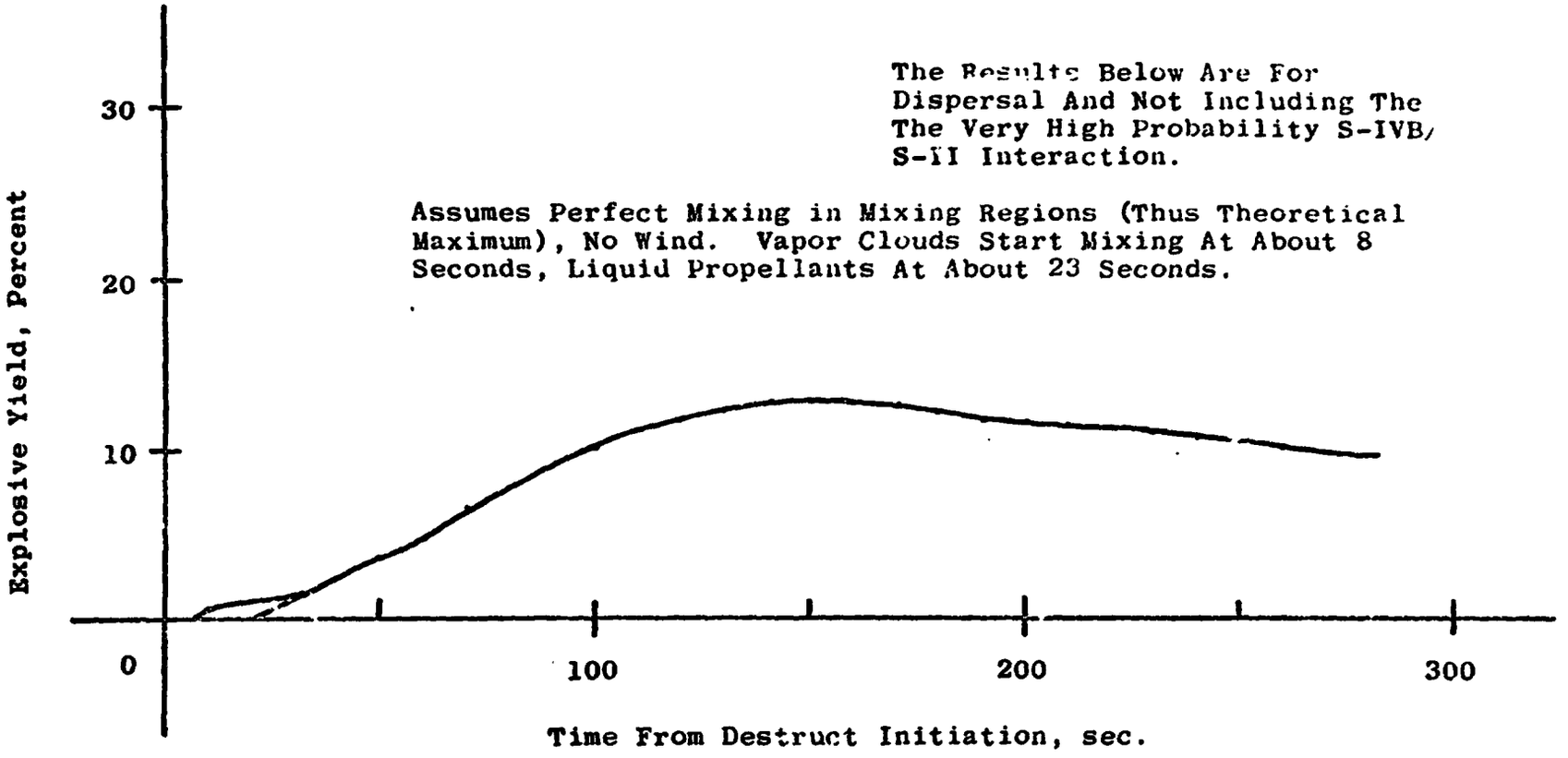

Figure 112 Theoretical Explosive Yield Prediction - Saturn V (Destruct Spill)

B. Experimental Analysis

After having analyzed the Saturn V destruct system theoretically, it was decided to examine the results also from an experimental point of view. For this purpose the destruct system performance was modeled by the methods developed and described in detail earlier. Three modeling methods were used and can be described as

a. 1/373 Scale Sand Model Analysis

b. 1/50 Scale Water Model Analysis

c. 1/28 Scale Water Model Analysis

Basically the procedure was to build models and then use them to determine the mixing function and from it the yield function. This was done by having different colored materials (sand or water) flow from the model tanks and mix. The analysis of these experiments resulted in these functions.

Rather than going through the complete process for each method and thus doing repetitive work, it was decided to obtain the mixing curves for each of the models and methods without consideration of evaporation and then compare the results at that stage. With good agreement of these three experimental procedures, the best resulting curve was processed to finally obtain the modeled yield function.

From the modeling as will be described for each system the percentage mixed as a function of model time is obtained schematically as shown in Figure 113.

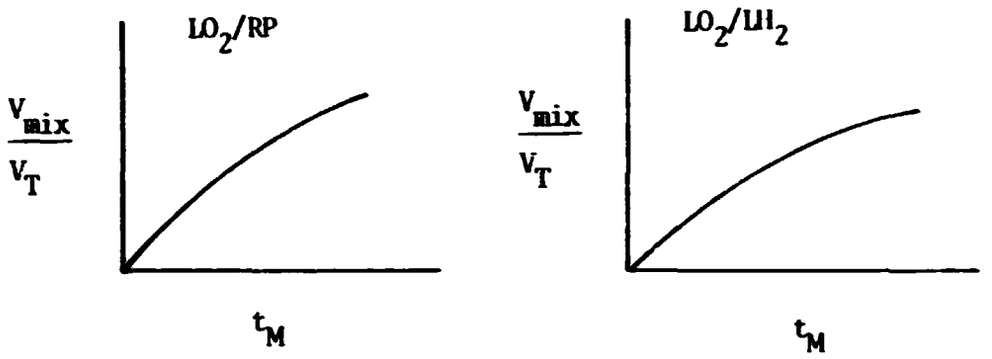

Figure 113 Mixing Ratio Versus Model Time

Two curves must be found, one for LO_2/RP and another for LO_2/LH_2 since they result in different yield values for respective unit volumes. They will have to be added to obtain the total possible yield at any model time.

The mixing areas under analysis will form basically three regions, one where LO_2 and RP mix, the second where LO_2 and LH_2 mix, and the third where all three components mix. A fourth region where LH_2 and RP mix is only of interest for evaporation loss determination or

possibly atmosphere interaction.

In the third region a decision must be made as to the proportion of LO_2 mixing with LH_2 and that mixing with RP.

The next step in the analysis is to expand the model time to the corresponding prototype time. This relationship will be different for each of the systems used, but the method of determination is the same.

Since the outflow for the prototype is calculated by the computer program, while that for the models is determined experimentally, the relationships of prototype time to model times are known while the tanks are emptying. Then with the assumption that the ratios of volumes mixed to volumes on the ground are equal for both model and prototype, step by step construction of the V_{mix}/V_{Total} versus prototype time function is possible during this time. Figure 114. The evaporation losses due to the mixing and the minor effect due to the ground are ignored.

The step by step construction of the prototype mixing curve beyond the emptying time shown in Figure 114 can also be expressed mathematically as follows.

$$\left.\frac{\Delta \frac{V_{mix}}{V_T}}{\Delta\tau}\right)_{M_{i-1}} = C_{i-1} \left.\frac{\Delta \frac{V_{mix}}{V_T}}{\Delta\tau}\right)_{P_{i-1}} \tag{173}$$

The above equation is taken where both the model and the prototype relationships are known so that the next interval can be calculated.

By selecting desirable intervals successively on an overlapping

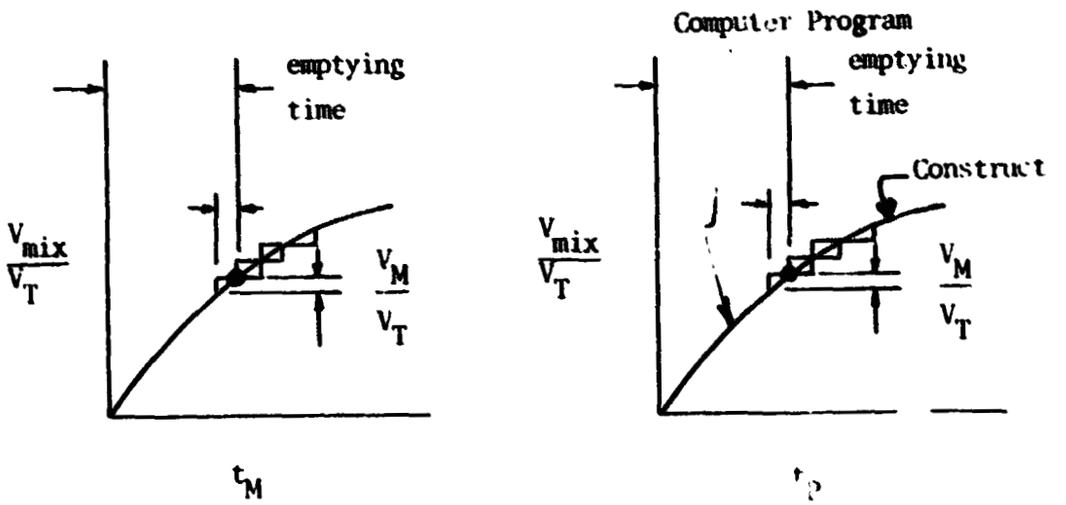

Figure 114 Construction Method for Determining the Prototype Mixing Function from the Model Mixing Function

basis, the complete prototype mixing function can be constructed from the model mixing function.

$$\left.\frac{\Delta \frac{V_{mix}}{V_T}}{\Delta\tau}\right)_{M_i} = C_{i-1} \left.\frac{\Delta \frac{V_{mix}}{V_T}}{\Delta\tau}\right)_{P_i}$$

$$\left.\frac{\frac{V_{mix}}{V_T}}{\Delta\tau}\right)_{M_{i+1}} = C_i \left.\frac{\frac{V_{mix}}{V_T}}{\Delta\tau}\right)_{P_{i+1}} \qquad (174)$$

$$\left.\frac{\Delta \frac{V_{mix}}{V_T}}{\Delta\tau}\right)_{M_{i+2}} = C_{i+1} \left.\frac{\Delta \frac{V_{mix}}{V_T}}{\Delta\tau}\right)_{P_{i+2}}$$

ETC.

Following the above procedure all the curves for each of the models can be constructed, stage by stage or for the total, keeping LO_2/RP separate from LO_2/LH_2.

These curves can then be compared as shown in Figure 115.

Now either any one of the curves or an average from the three models can be selected and an evaporation factor selected, or the actual evaporation calculated at each time from the contact areas of the propellant constituents and the heat transfer characteristics. The characteristic curves are shown in Figure 115 c,d.

Since one unit volume of LO_2/RP-1 has a different amount of energy than one unit volume of LO_2/LH_2, the ordinates of these curves are

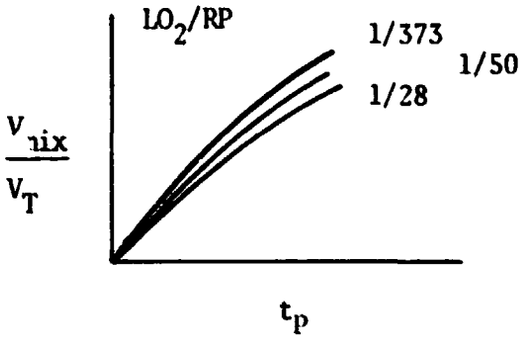

Figure 115 a

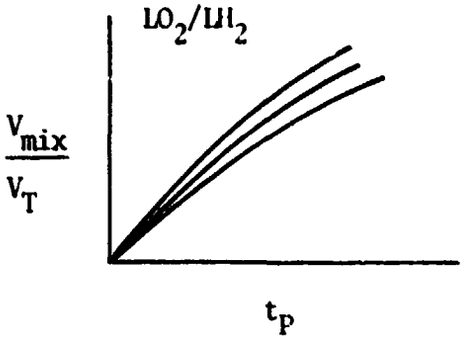

Figure 115 b

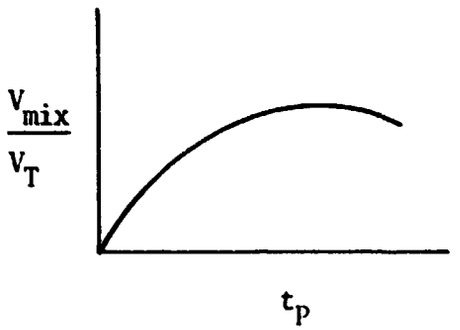

Figure 115 c

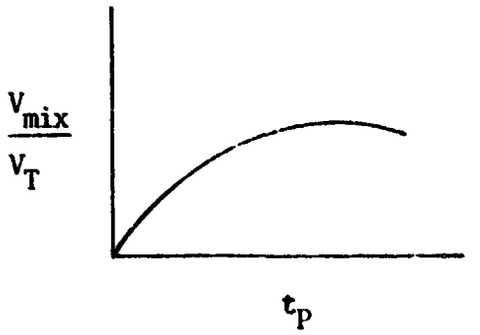

Figure 115 d

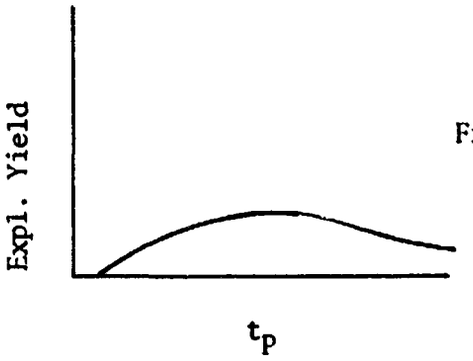

Figure 115 e

Figure 115 Explosive Yield Analysis

multiplied by their respective energy factors and result in the yield which can be produced at any time τ from each of the constituent combinations. The sum of these yield components is then the total yield which can be expected at any time τ . Figure 115 e.

If the cloud is considered in addition to the liquid propellants on the ground, then assumptions have to be made as to the meteorological conditions. These are rather difficult to predict in general and so such conditions as zero wind velocity, etc. can be taken.

With the complete procedure laid out, the detailed modeling methods are now discussed with the

1/373 Scale Sand Model

1/50 Scale Model

1/28 Scale Model

Sand Model Analysis

To determine the mixing function the first modeling method used was to take one of the Saturn V models which were on sale at the KSC Visitor's Center and to subdivide this plastic model into compartments simulating the tanks in the actual Saturn V. The scale of this model is 1/373 of the prototype.

Then slots were cut to scale to simulate the effect the destruct system would have on the prototype as specified by MSFC. These slots were pre-cut after it had veen tried to actually make them by hot wire explosions. None of these worked out as satisfactorially as the pre-cutting.

The various tanks were filled with colored sand, red for RP-1, yellow for LH_2 , and blue for LO_2. A clam shell was put around the model to prevent the sand from flowing from the tanks. Then the sand in the tanks was fluidized by air at 3 inches of Hg to make it behave like a liquid.

The model was set upon a platform which rested on a vibration table which could be controlled in both frequency and amplitude.

This complete system is shown in Figure 116. The sand behaved like a liquid by being fluidized in the tank and then when hitting the vibrating platform kept on flowing just as a liquid would.

With this physical system it was only necessary to start at time zero by opening the clam shell for let us say 1/2 second. With the clam shell closed and the shaking table stopped at that time, the splash pattern on the ground and the mixing could be studied at leisure. The areas and the depth of the various regions could be traced or photographed for later analysis.

This process was repeated as many times as was desirable and thus each record represented a point on the mixing-model time curve. Figure 117 shows photographic records of the mixing process.

By the above method each stage can be analyzed individually or all of them combined giving the mixing function for the desired condition.

By the method discussed in the earlier parts of this section, the prototype mixing function can be determined step by step from the prototype computer program and the complete model mixing curve. The results are shown in Figure 118.

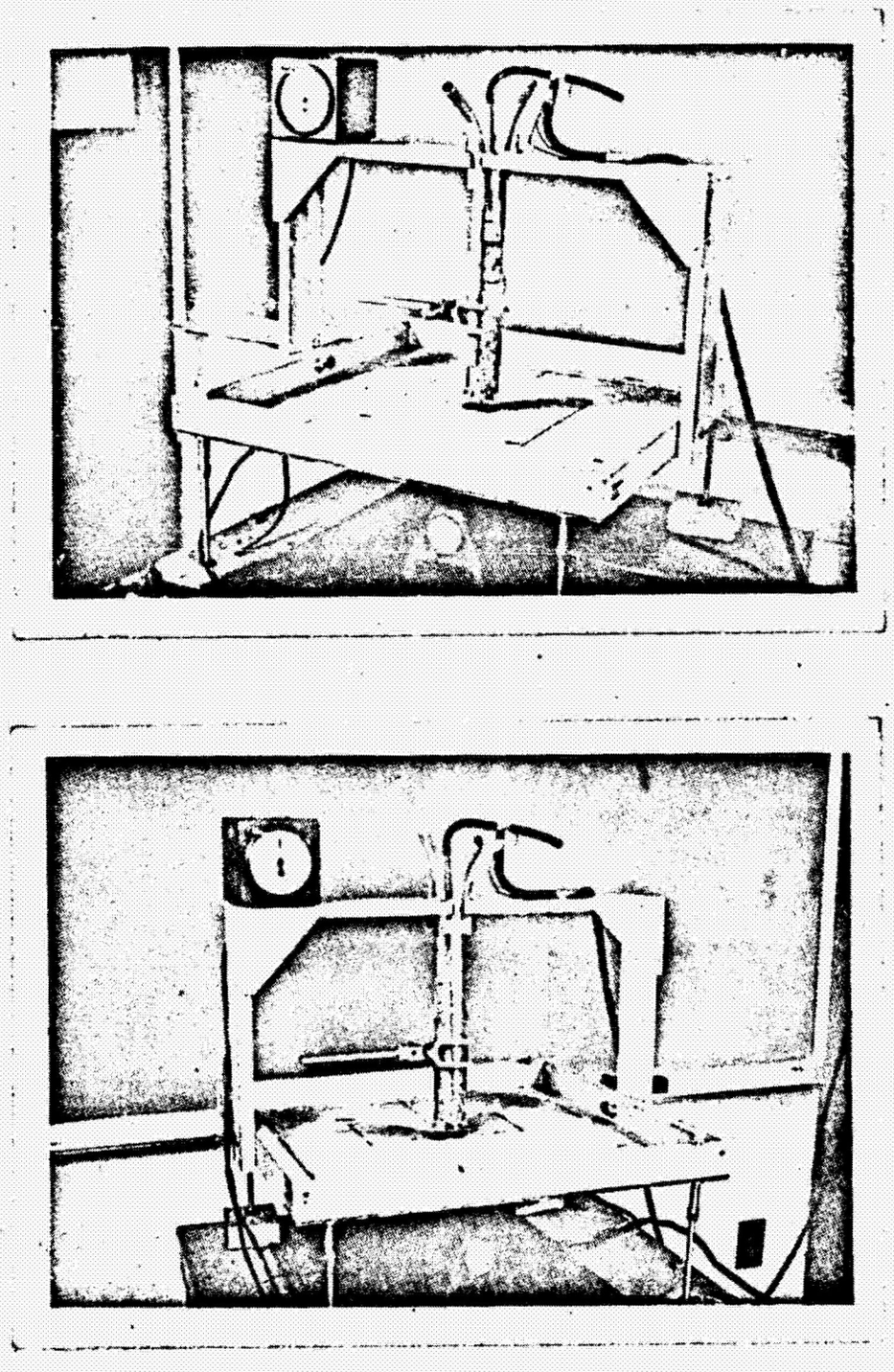

Figure 116 Saturn V Destruct System Vibration Analysis Apparatus

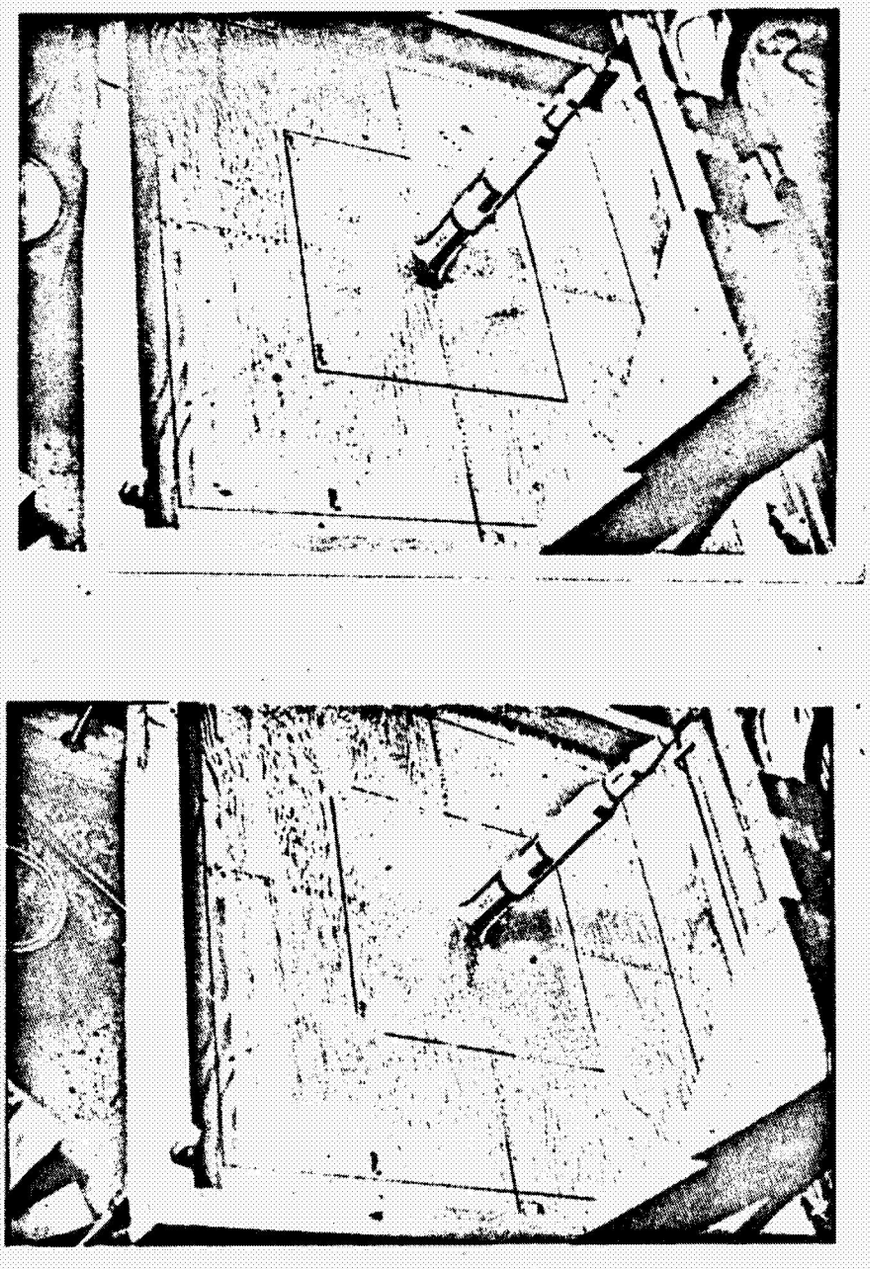

Figure 117 Saturn V Destruct System Experiment in Operation

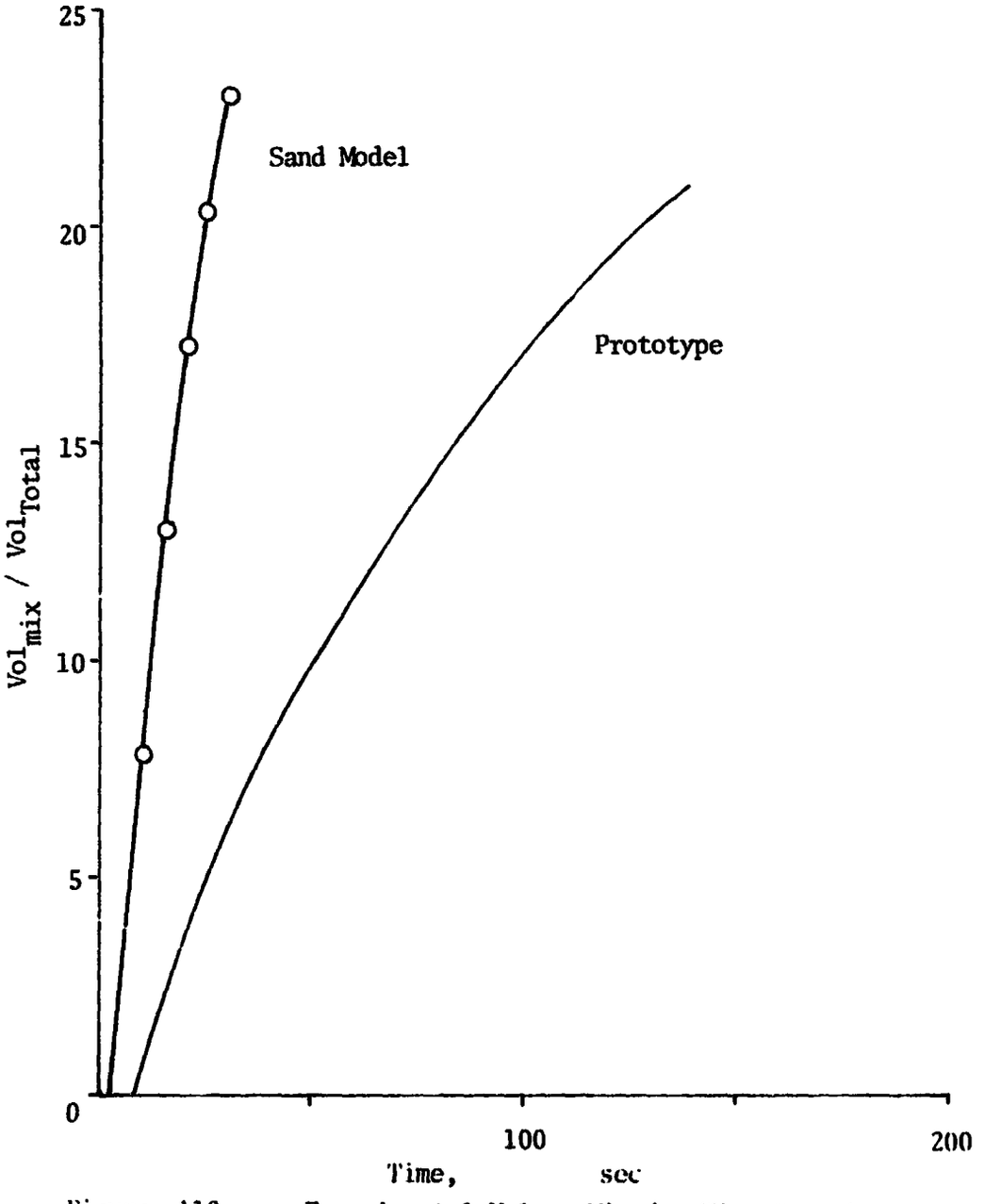

Figure 118 Experimental Volume Mixed - Time Function Normalized for 1/373 Scale Sand Model

If this were the only modeling method used here the evaporation could be calculated point by point and the yield versus time curve obtained, completing the prediction modeling.

Since in this work, however, other modeling methods were used, they will be discussed and the results compared before the mathematical reductions are introduced. In this manner, three modeling methods were compared and used for the predictions.

1/50 Scale Model Analysis

Having carried out modeling with a rather small model and fluidized sand, it was thought to be desirable and probably more accurate to to to a 1/50 scale model of the Saturn V.

The possibility of having this model constructed was investigated by our group and MSFC as well as private industry, and it was found that we could construct this model at a small fraction of the cost it would have taken to have it made.

So for this reason the model was constructed here following the Saturn V configuration. Again the slots were cut into the tankage as specified by MSFC, and after clamping arrangements and other methods of opening the slots quickly were tried, the rip-tape technique developed by our group was found most satisfactory. Duct tape was put over the slots and then fastened to ropes with pullies so it can be ripped off almost instantaneously. Since 5 of these tapes had to be pulled at the same time, it was necessary to have a coordinated system available.

The 1/50 scale model was filled with colored water simulating the

liquid propellants, again yellow for LH_2, red for RP, and blue for LO_2. High speed cameras were set up which recorded the mixing of the propellants as they spilled out onto a marked surface. Figure 119.

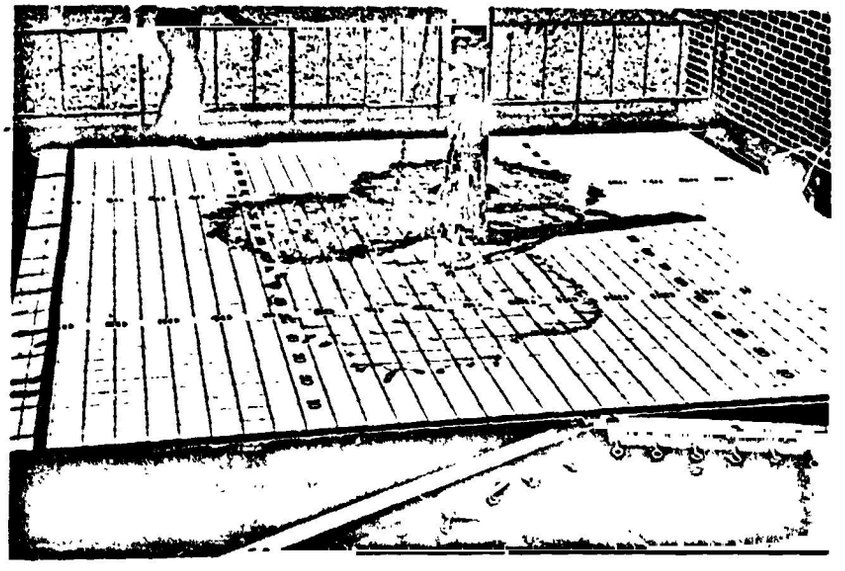

Figure 119 1/50 Scale Model Splash Pattern

Using high-speed films and utilizing the flow out calibration runs, the areas of the spill and mix could be determined frame by frame and the mixing curves determined. These presented the quantity mixed as a percentage of the total propellants present in terms of model time.

The model time was then transformed into the prototype time just as was shown earlier in this report and therefore is not repeated here. The end result is shown in Figure 120.

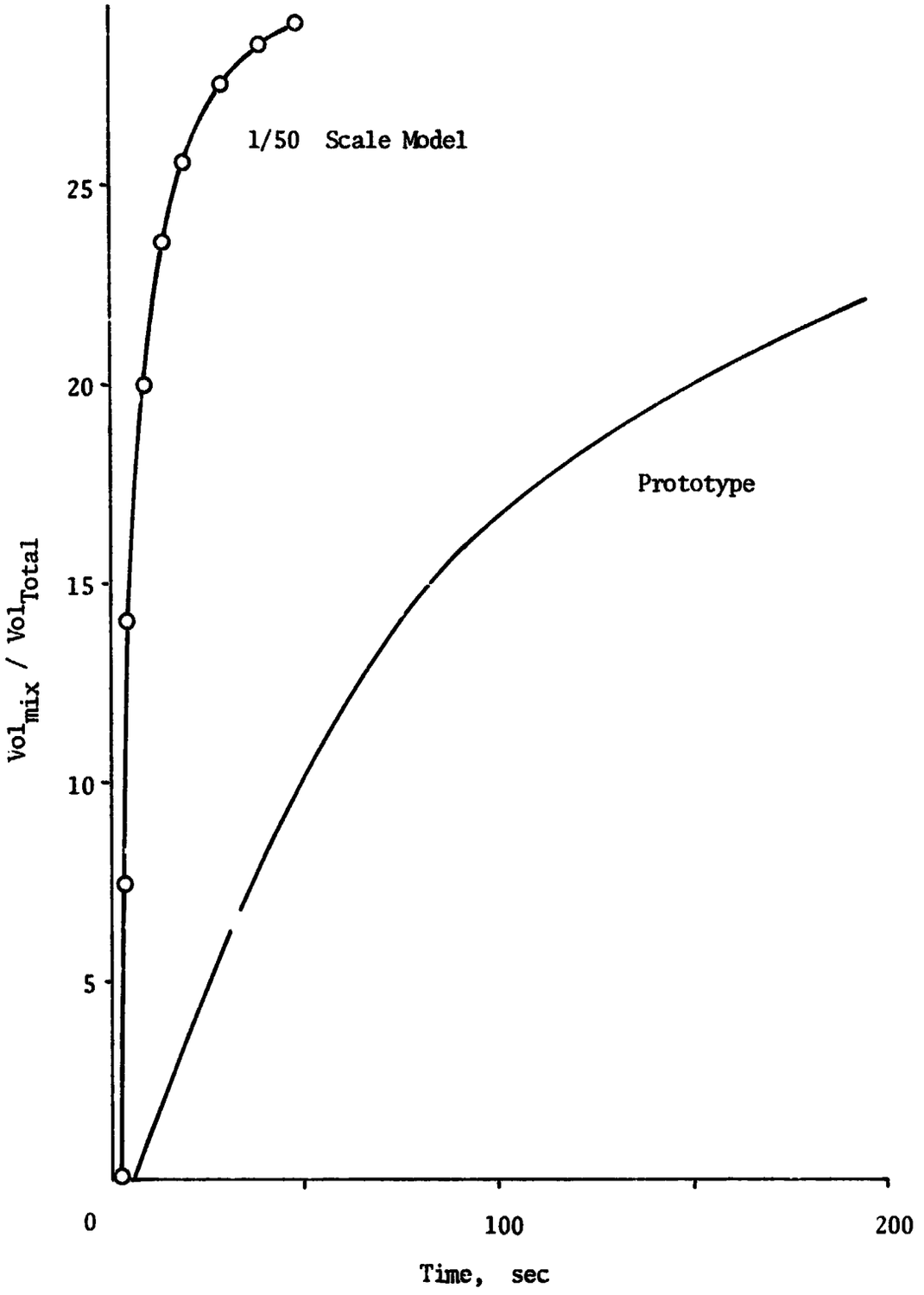

Figure 120 Experimental Volume Mixed - Time Function Normalized for 1/50 Scale Model

1/28 Scale Model Analysis

To have a range of sizes to also get a feeling for the scaling of these methods, it was decided to also carry on the experimentation with a model 1/28 the scale of the actual Saturn V.

Again this model was constructed by our group for a small fraction of the costs involved in having it done elsewhere and also at a tremendous saving in time. Figure 121.

The model was then used exactly as the 1/50 scale model, except that the experimentation had to be carried out at the Solar Energy Laboratory about 12 miles from the campus, since the roof upon which the smaller experiments were carried out was not large enough to give the splash areas room to develop before running off the edges.

Otherwise the experiments were basically the same. Again high-speed cameras recorded the mixing processes for later analysis frame by frame.

The analysis again resulted in a mixing function versus model time, and with the method described earlier could be transformed into the prototype mixing function, again without evaporation. Figure 122.

Having finished the analyses for each of the three models, the Sand Model (1/373), the 1/50 Scale Model, and the 1/28 Scale Model, the results from the modeling can be compared.

Figure 123 shows that mixing curves predicted for the prototype without evaporation are about the same. So the rest of the analysis needs to be carried out only once and will give the same result regardless of which model is taken as the reference.

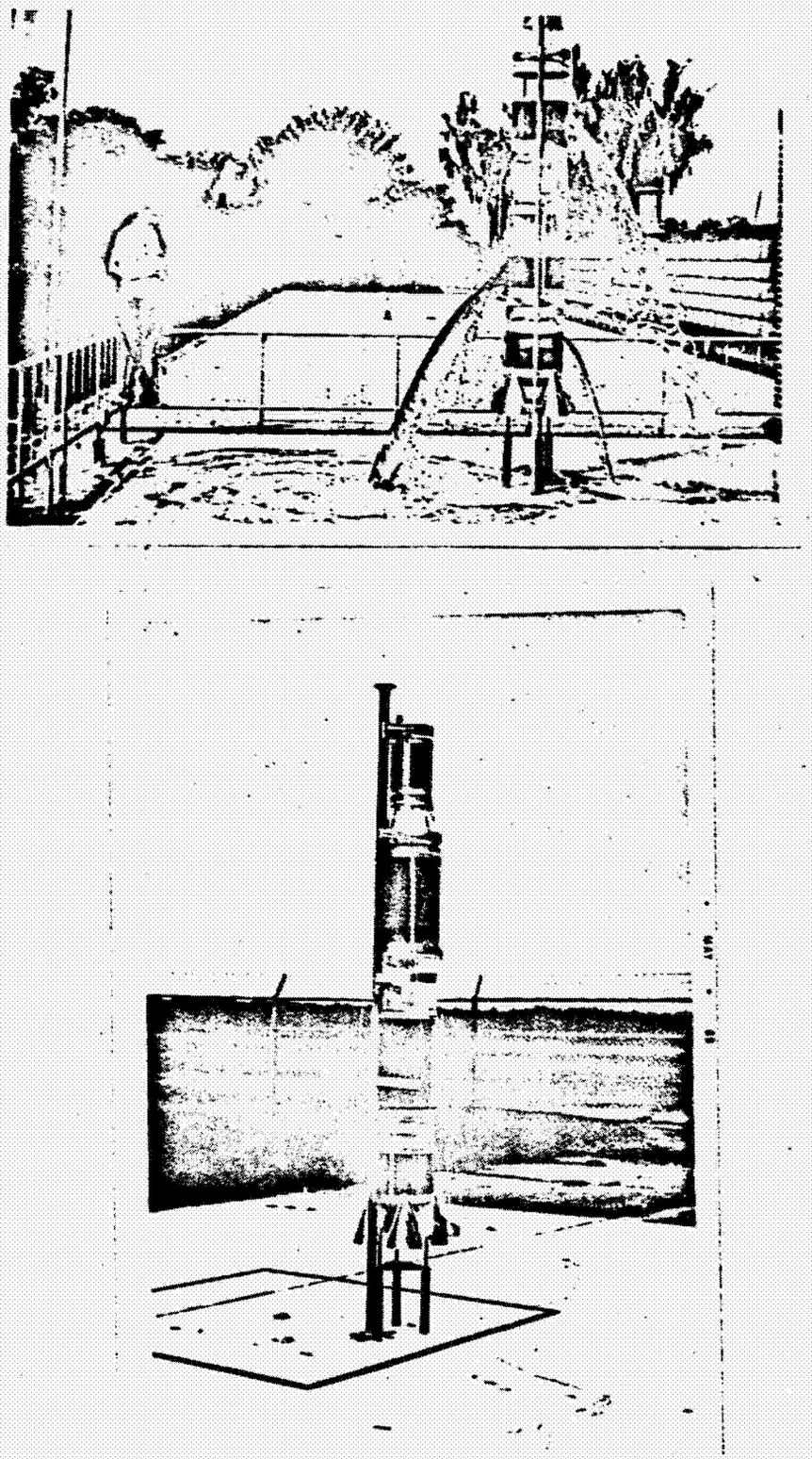

Figure 121 Saturn V, 1/28 Scale Model (Liquid)

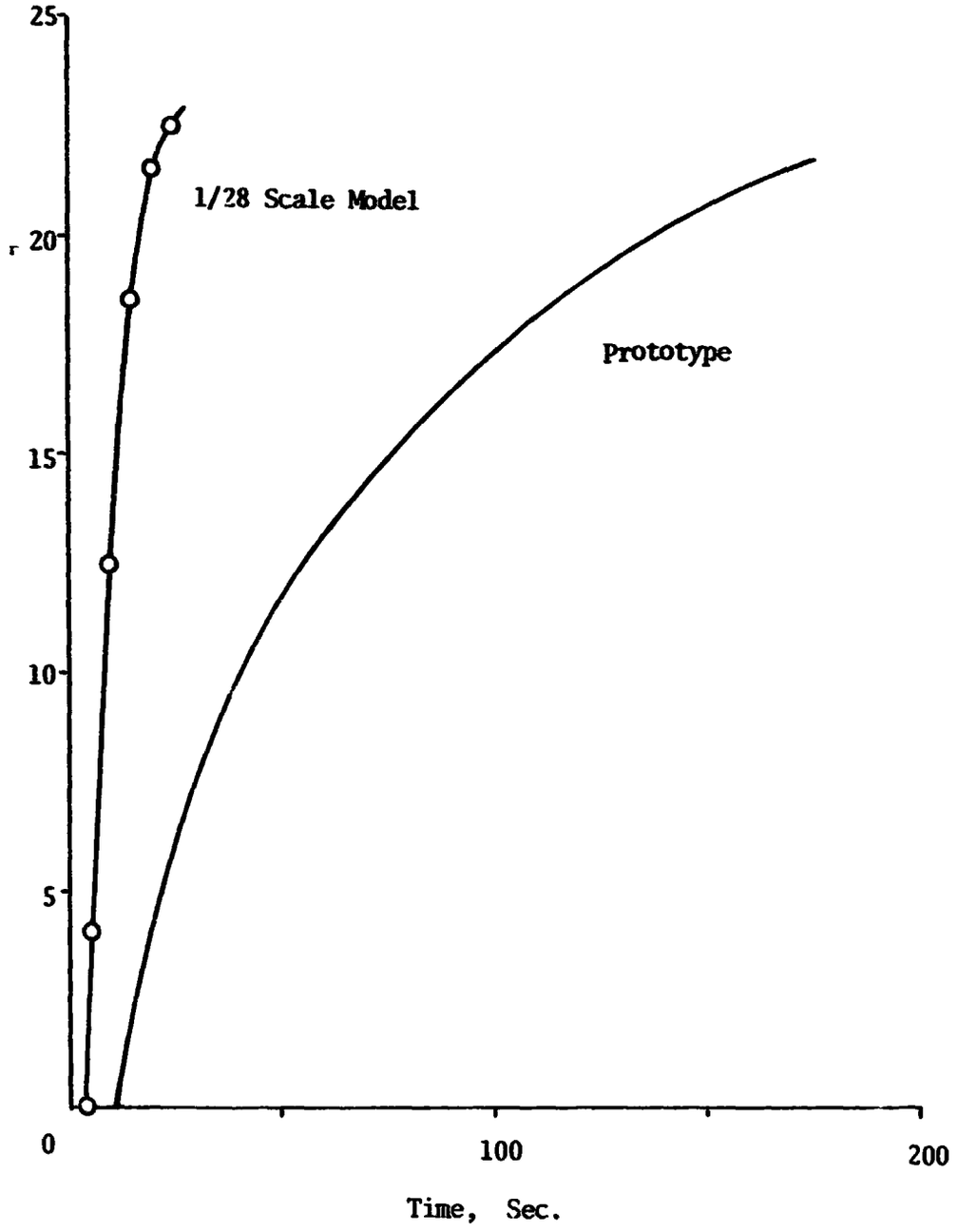

Figure 122 Experimental Volume Mixed - Time Function Normalized for 1/28 Scale Model

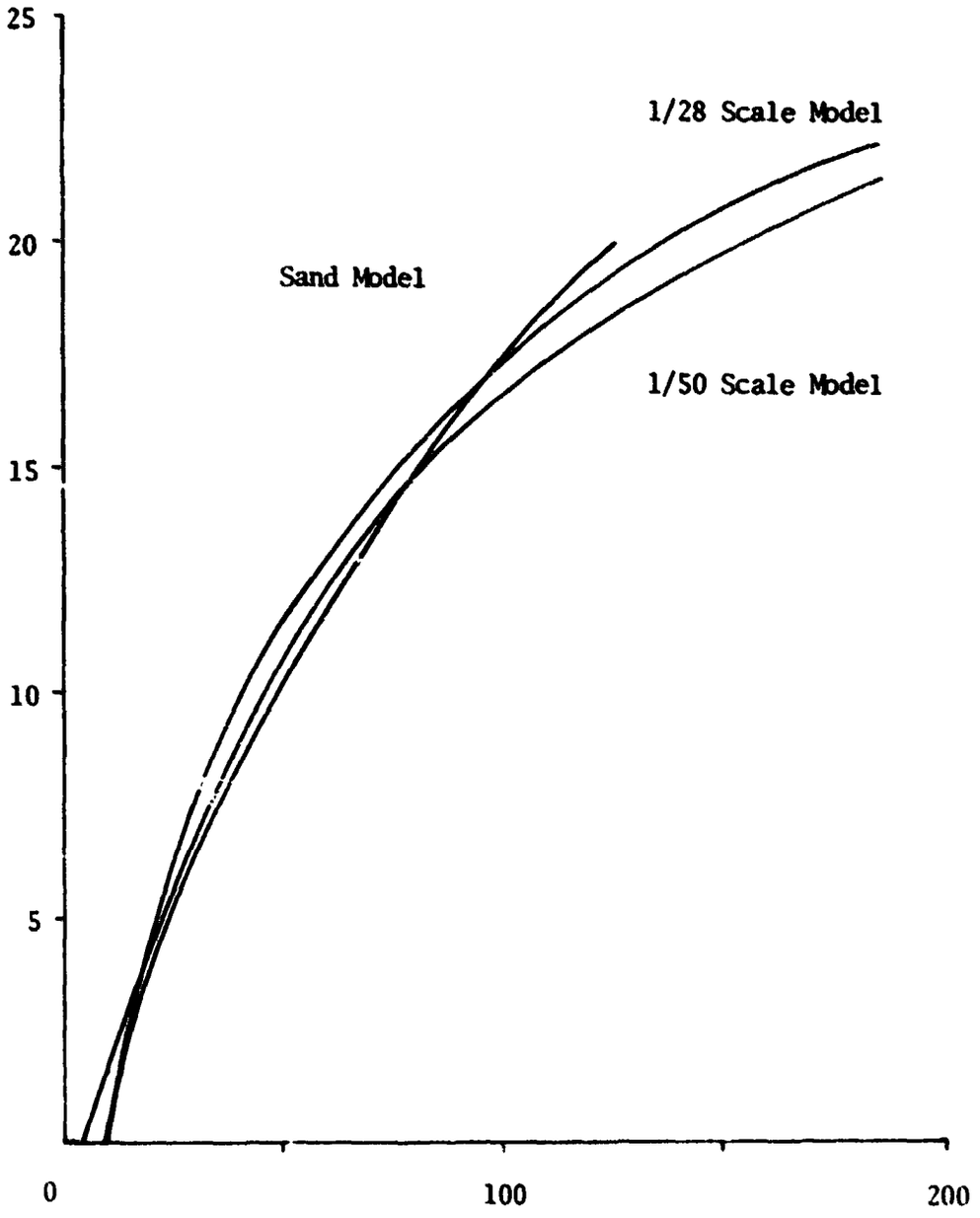

Figure 123 Experimental Volume Mixed - Time Function As Predicted for Saturn V

Evaporation Losses

Since the mixing process of the constituents produces evaporation of the cryogenic components, less and less total quantity of propellants is present and the loss occurs in the mixing region.

If the mixing could be carried out without ignition occurring, which has been shown not to be possible, then eventually all the volatile components would be gone and nothing would be left for any reaction to occur. With this, the explosive yield, which starts at zero when no mixing has taken place, will return to zero. In between these limits in time the explosive yield would reach a maximum when the greatest amount of propellants is mixed and available for reaction.

Since little information is available with regard to evaporation rates, etc., our group carried on some experiments with spilling LN_2 on a sand bed which was resting on a scale.

Weighing the combination of sand and LN_2 at short time intervals, and subtracting out the ice formed from the atmosphere, the evaporation rates and the heat transfer characteristics could be estimated. Figure 124.

Using the heat transfer characteristics obtained and the information that the contact area is essentially proportional to the profile area, the amount evaporated can be determined and the actual amount of mixed propellants present at any time τ is found.

Translated into explosive yield, Figure 125, as described earlier and expressed in percent of the total, it is shown that the explosive yield for the Saturn V through destruct system activation starts to rise in value and reaches a maximum of about 9 percent at about 150

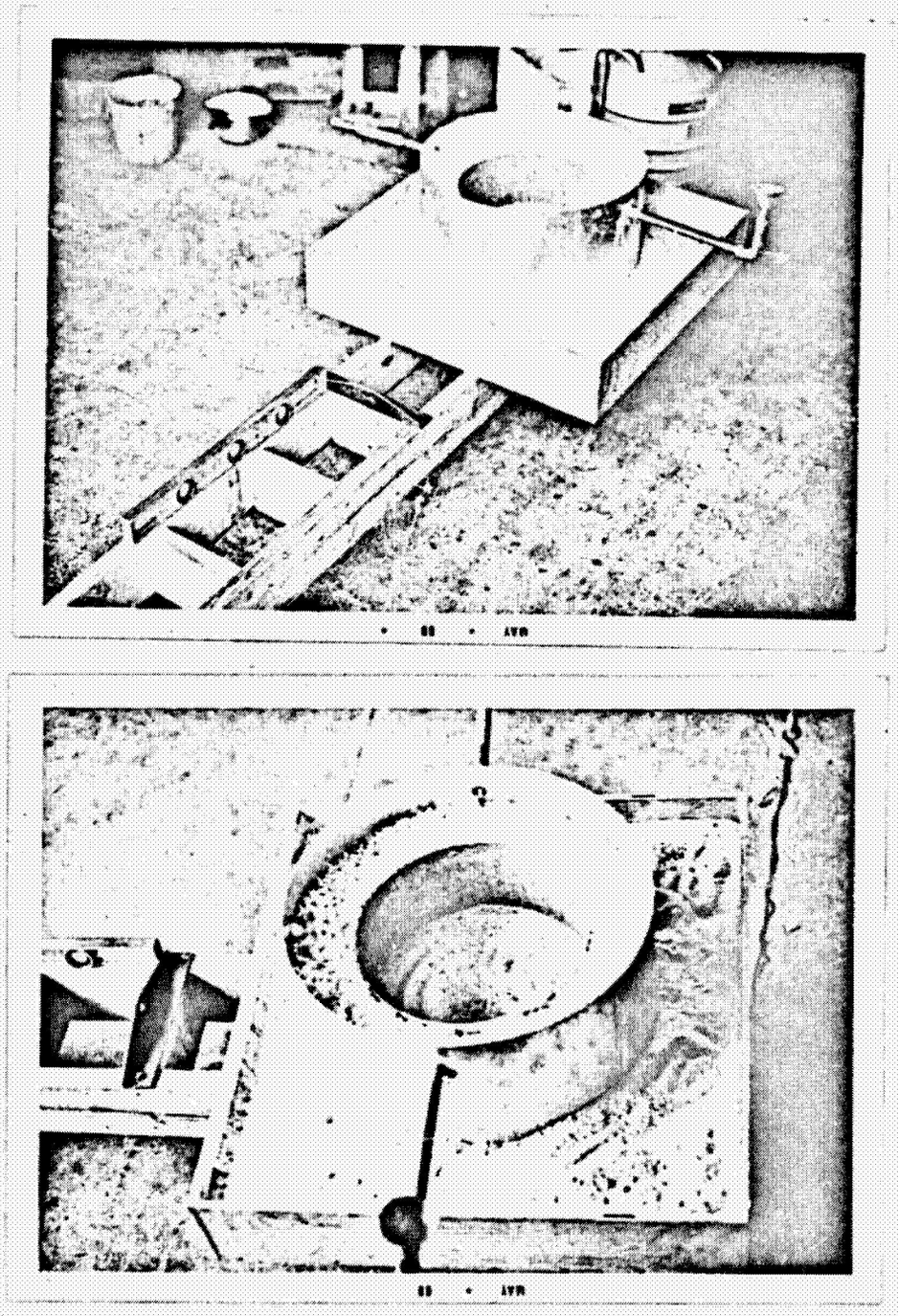

Figure 124 Cryogenic Evaporation Experimental Apparatus

Figure 125 Experimental Expected Yield Function for the Saturn V Destruct System

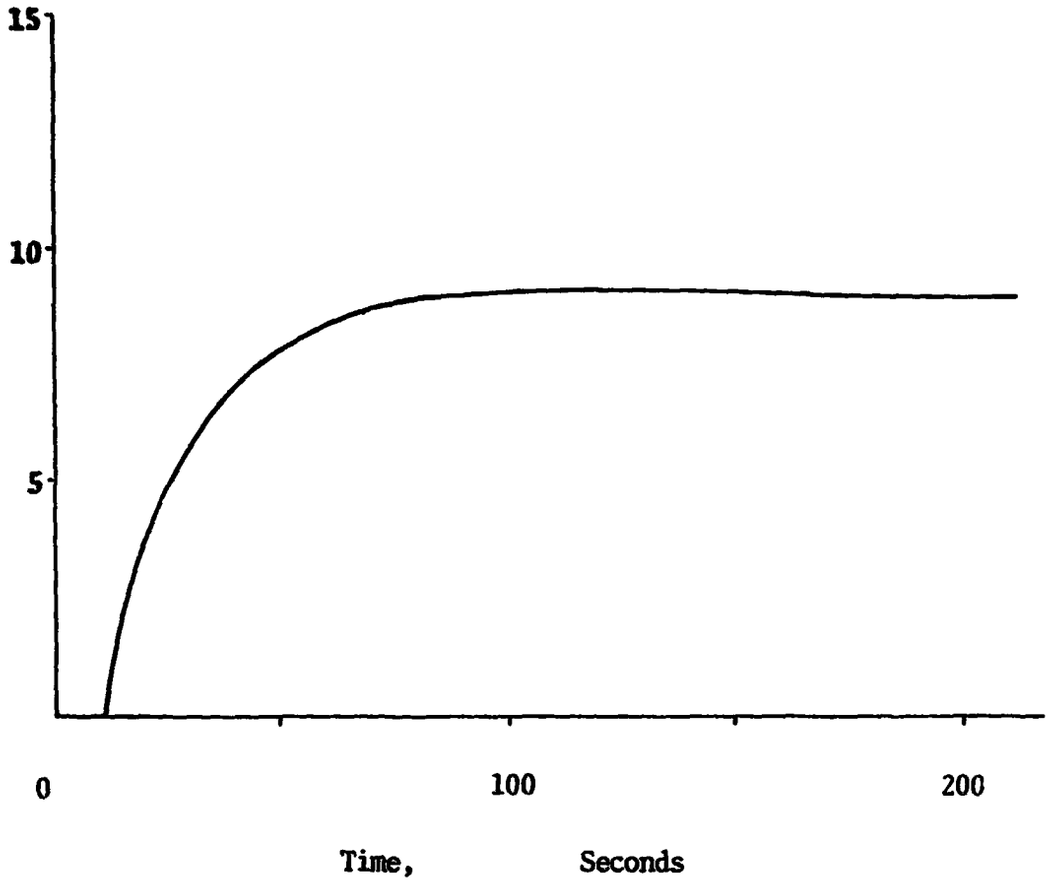

seconds, then slowly falls off.

It is very doubtful that the actual phenomena can follow this curve very long since ignition, either through an external source or through internal action such as charge and voltage generation, will occur leaving us with a rather low explosive yield.

This last fact has been supported a number of times with smaller rockets and liquid propellant quantities which produced rather small explosive yields.

From the above analysis it is seen that the destruct system is essentially doing what it is supposed to do except in the third stage.

There a potentially dangerous condition seems to exist. The activation of the destruct system could lead to an explosion in the second stage which in turn could produce a considerably larger secondary explosion in the third stage. The total explosive yield value is still very low as far as the total Saturn V rocket is concerned, but it occurs near the payload and may through its proximity do considerable damage to vital systems and possibly personnel.

A detailed analysis of this case will be made in the following pages.

S-IVB/S-II Interstage Failure Analysis

During the Saturn V Destruct System Analysis it was found that a serious problem may exist due to the activation of the Saturn V Propellant Dispersal System.

The destruct system is to cut slots into all the fuel and oxidizer tanks except for the S-IVB LOX tank[120,121] where the ring charge will cut a 47 inch diameter hole in the bottom of the tank. The objective of this destruct method was to disperse the propellants and oxidizers, with the propellants pouring out on one side of the rocket configuration and the oxidizers on essentially the opposite side.

The above objective seems to be met in all cases except in the case of the S-IVB stage and its interaction with the S-II stage.

As our analyses, both theoretical and experimental (modeling), indicate, the LOX pouring out the 47 inch hole of the S-IVB LOX tank will, through its weight and momentum, tear loose the thrust cone carrying the rocket engine for this stage. LOX will pour over the engine and through port holes in the thrust cone following some of the supply pipes which go from the tanks to the engine.

The S-IVB engine is only a few inches above the very thin LH_2 tank dome of the S-II stage. The tearing loose of the thrust cone and the resulting downward movement of this engine will cut the LH_2 cone of the S-II stage. This sequence of events will allow LOX to pour directly into the LH_2 - a phenomenon or mode of failure investigated both under Project PYRO[22,119] and the University of Florida program on Liquid Rocket Propellant Explosion Characteristics[1,2,4,5,47,55,56,58,75,79, 122,123,124,125] - resulting in an explosion of as few percent of the

total possible.

This primary explosion will occur essentially under the engine and thrust cone driving them upward or forward with explosive velocities. These velocities may be of the order of several thousand feet per second. Such velocities have been measured for large pieces of metal in liquid propellant explosions through film analyses of the ADL[6] and PYRO experiments.

The forward motion of the thrust cone and engine is very likely to break up the common bulkhead between the LOX and LH_2 in the S-IVB stage, thoroughly mixing the LOX with LH_2 in a very short time increment. This EXPLOSIVE MIXING MODE has not been covered in any of the experiments and test programs carried out such as Project PYRO, the ADL experiments, etc., but was simulated by the modeling techniques at the University of Florida.

The indication is that the EXPLOSIVE MIXING MODE provides much more thorough mixing before ignition than is accomplished by the much more gentle mixing methods of the above cited experimental programs. But even in those programs it was shown that the greater the energy for mixing the greater were the yields which could be obtained. Mr. Fletcher's work[60] also indicated that more thorough mixing before ignition produced larger explosive yields.

Thus our analysis, the only one to the best of our knowledge which covers the EXPLOSIVE MIXING MODE, indicates that this secondary explosion produced by the primary explosion, of the type covered in the ADL and PYRO experiments, can be of much larger magnitude than that produced by the non-explosive mixing modes covered in previous works.

This effect of the destruct system was not originally expected to occur, and even though it does not appreciably effect the over-all explosive yield of the Saturn V, still predicted as low, because of its location near the payload, it may be more critical in nature. It may even trigger further explosions in the LEM, Service Module, etc. with the possible destruction of a radioisotope generator.

This S-IVB/S-II interstage failure or interaction, is man-made, forced upon the Saturn V configuration by the design of the destruct system. It seems that the removal of the ring destruct charge from the S-IVB LOX tank would eliminate the possibility of this particular interstage failure.

Details of the Analysis

Below will be given some of the details and specific results obtained from both theoretical and experimental modeling analyses.

S-II/S-IVB Design Features:

Figure 83 shows schematically the Saturn V configuration with the location of the destruct charges of the present Saturn V destruct system. Figure 126 gives the detail of the important sections of the S-IVB and S-II stages involved in the interstage failure analysis, the subject under discussion here.

Effect of the Destruct Charges Upon the Saturn V Tank Configuration:

Figures 127 and 128 give information as to the amount of LH_2 in the S-II and S-IVB stages respectively as a function of time

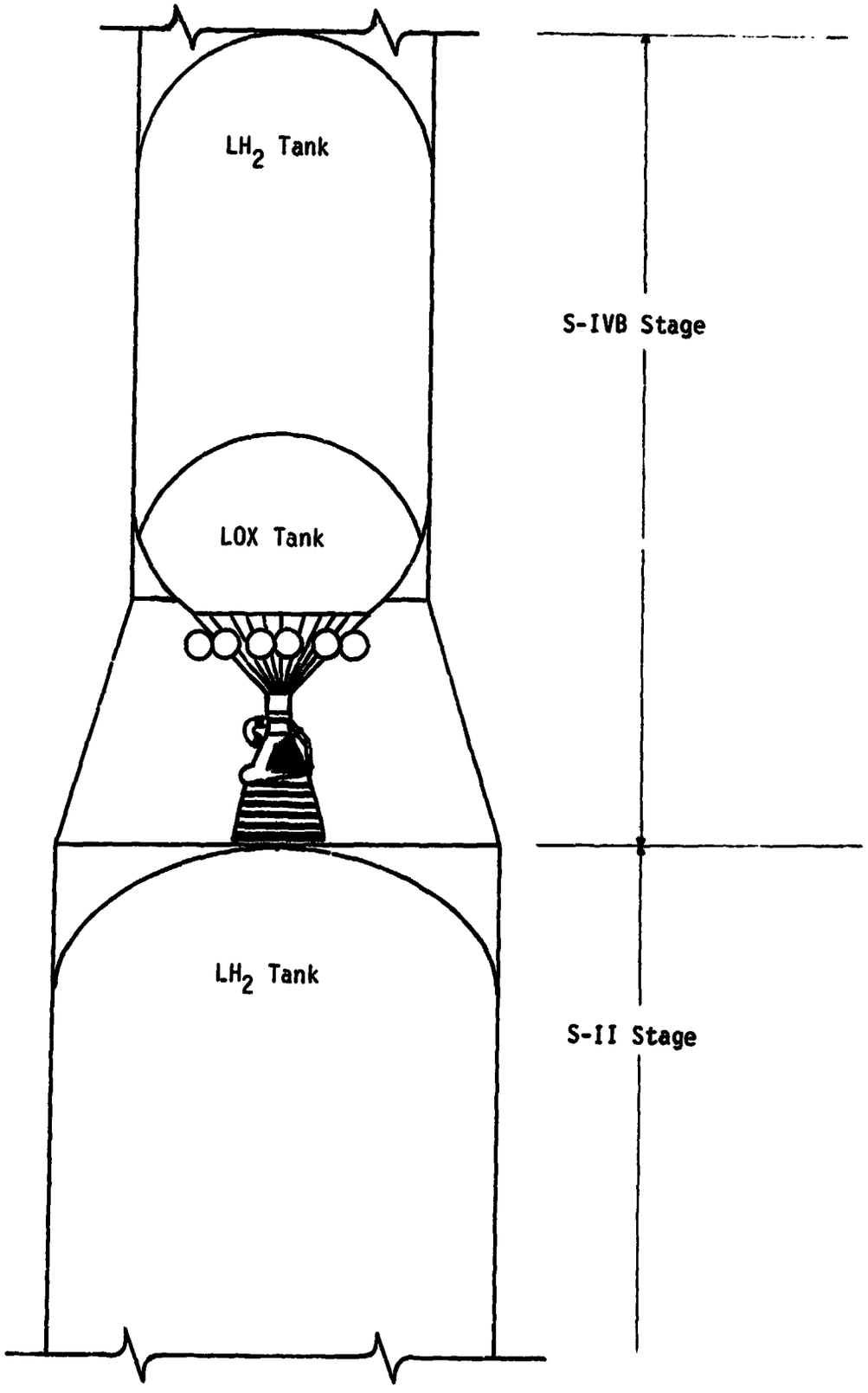

Figure 126 Schematic Diagram, S-II/S-IVB Interstage.

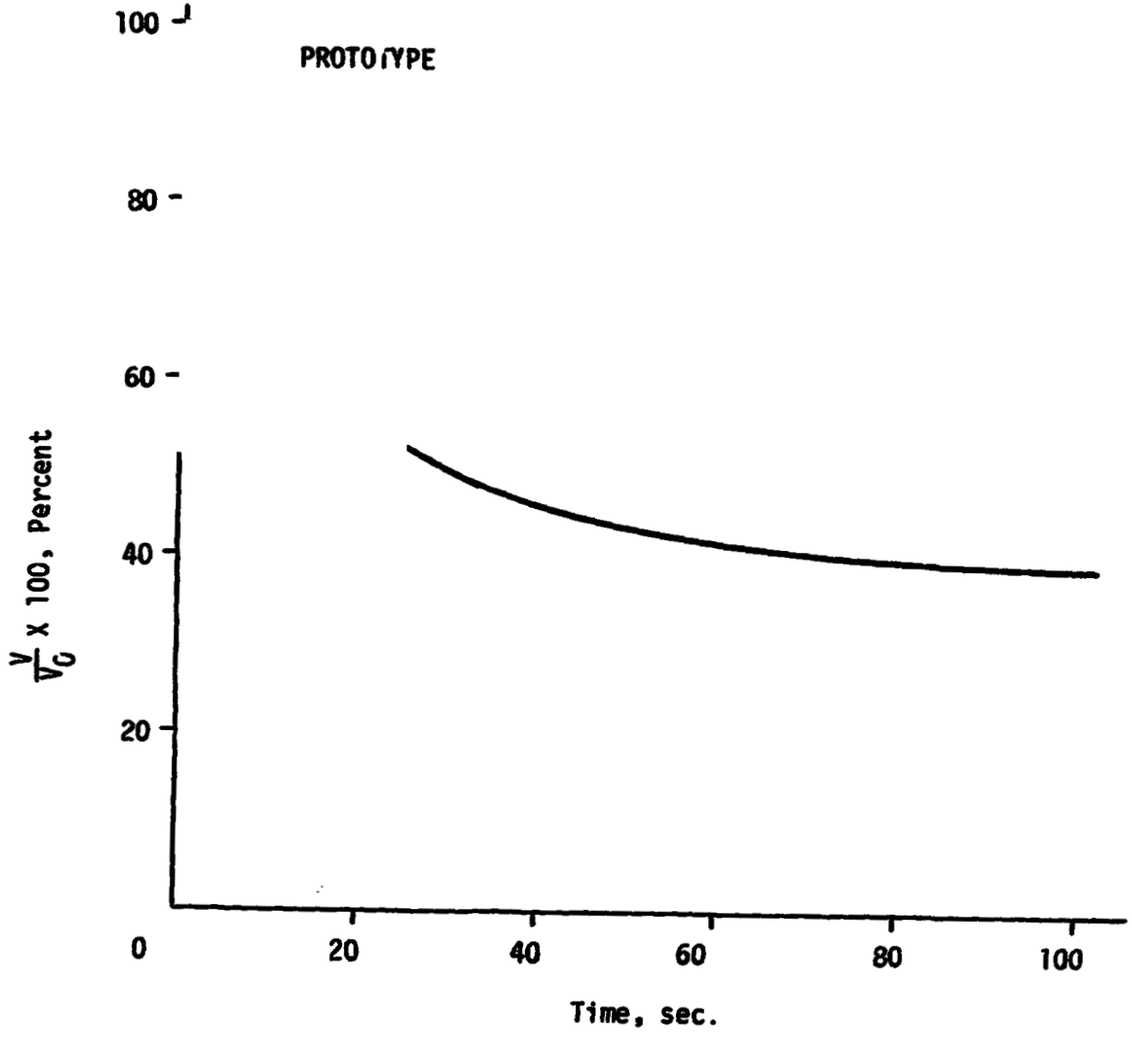

Figure 127A Volume-Time Function of LH_2 in the S-II Stage.

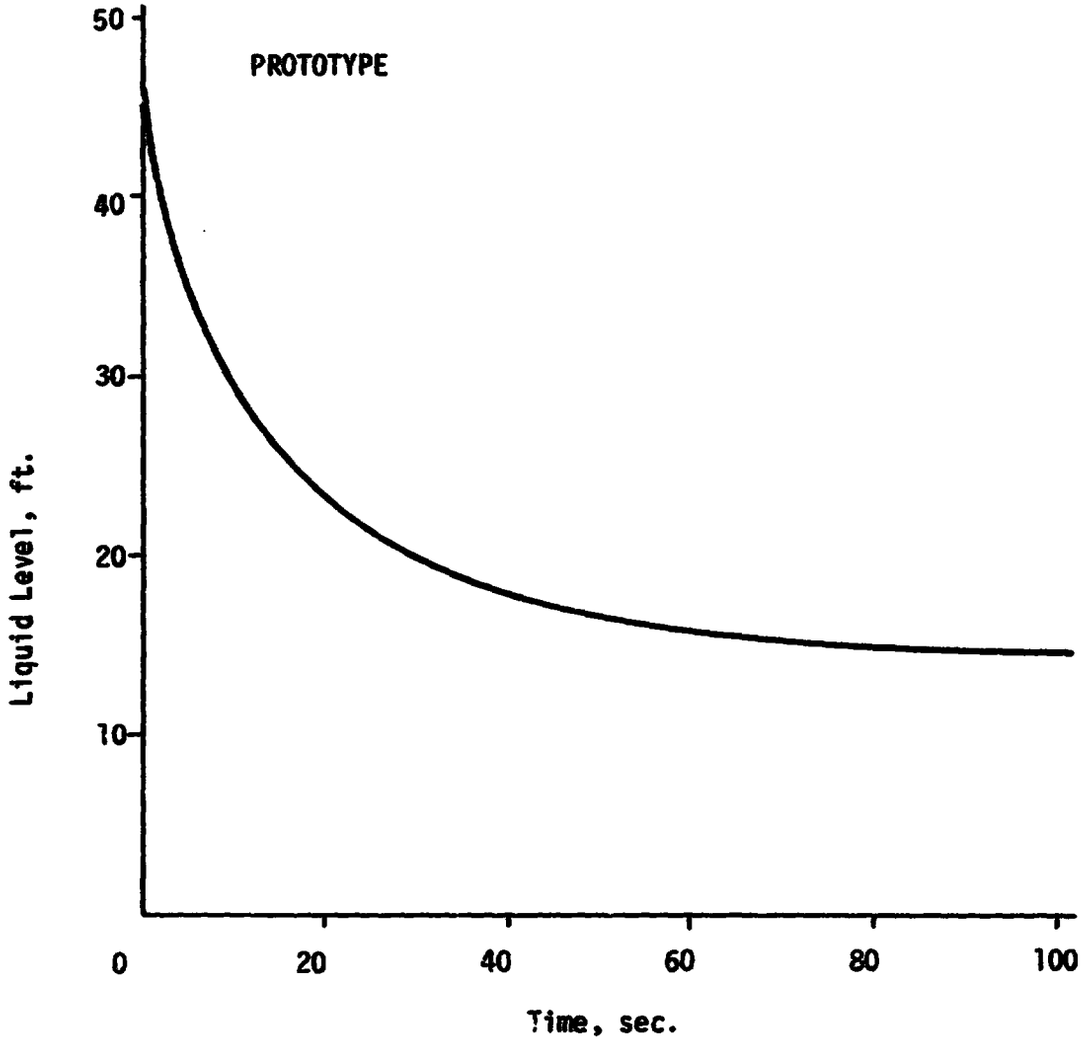

Figure 127B Liquid Level in S-II LH_2 Tank as a Function of Time.

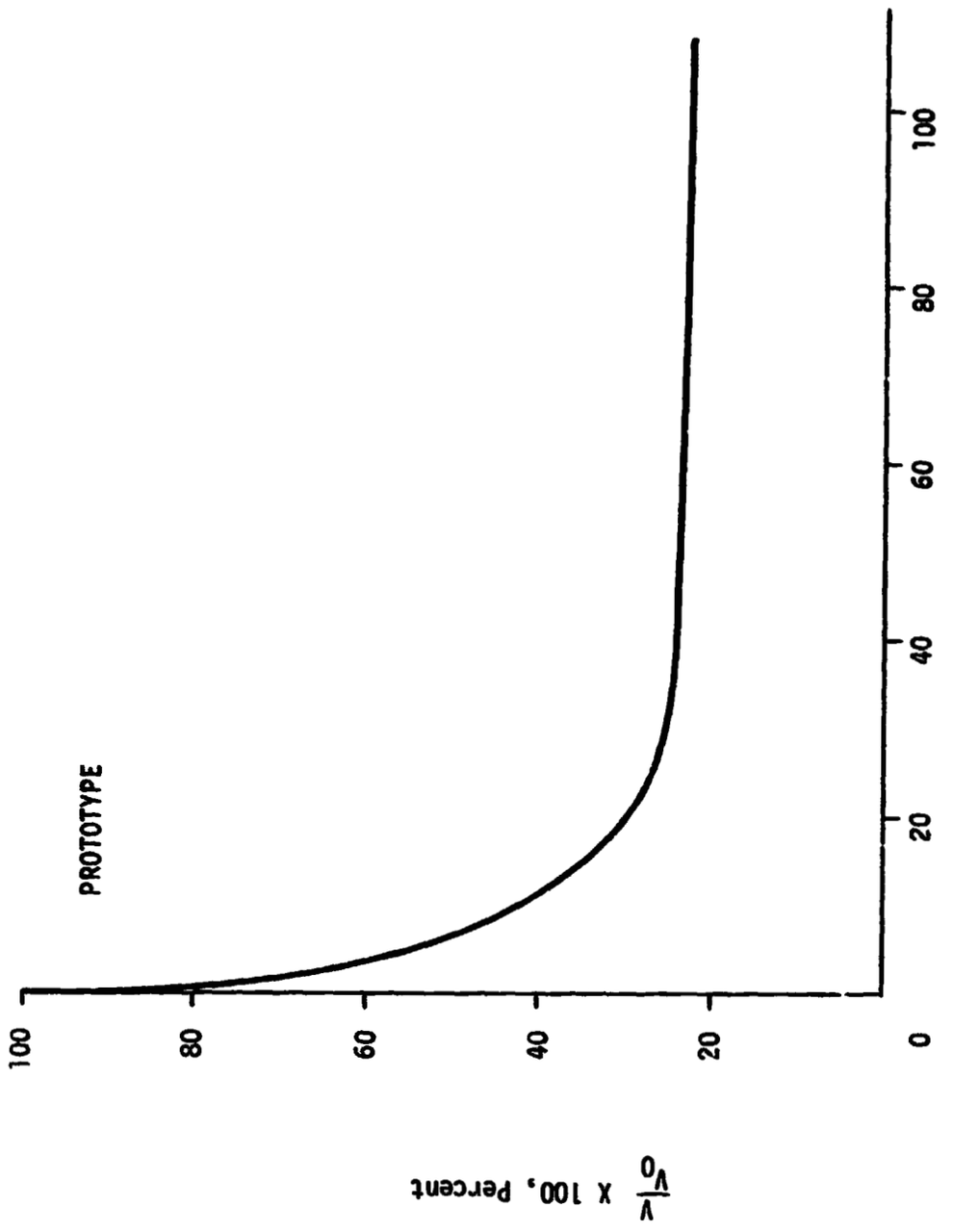

Figure 128A Volume-Time Function of LH_2 in the S-IVB Stage.

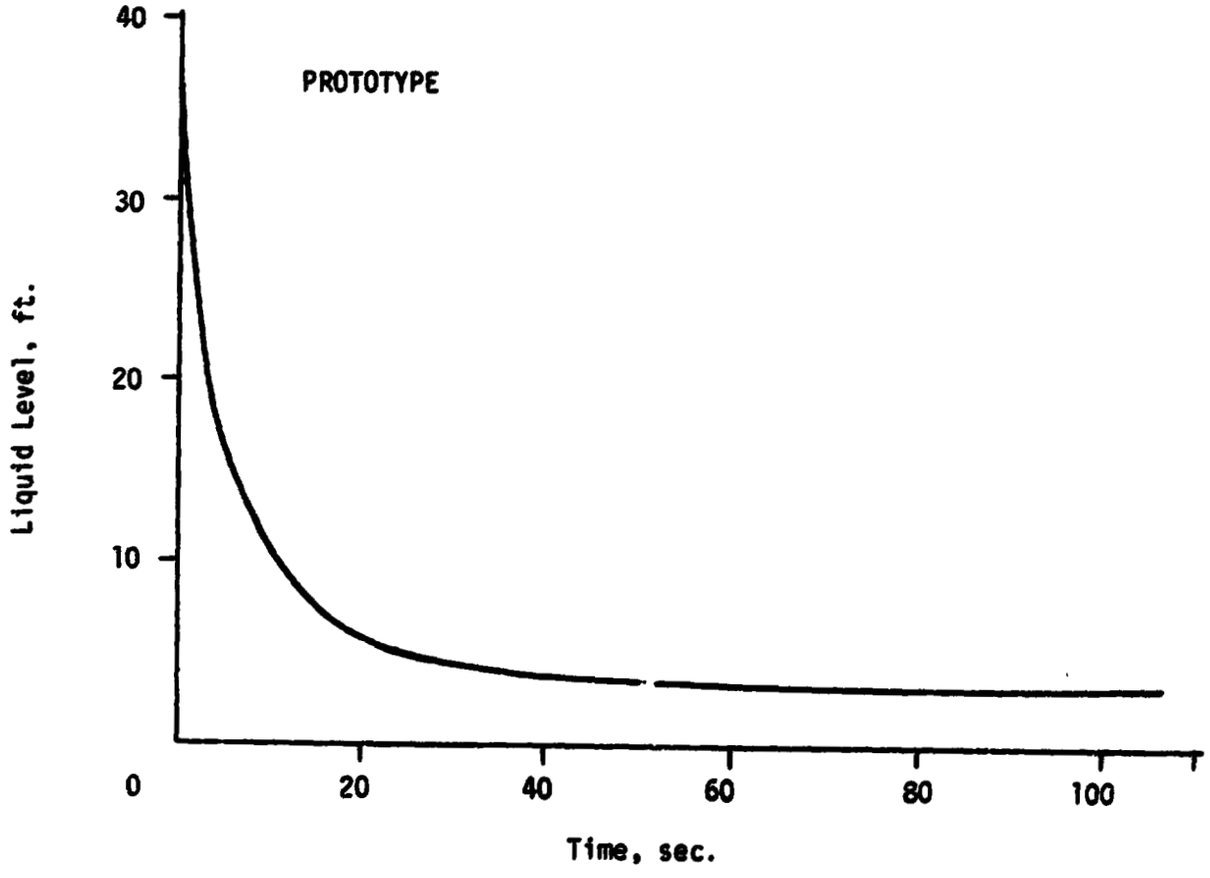

Figure 128B Liquid Level in S-IVB LH_2 Tank as a Function of Time

as based upon the failure information supplied by NASA. The LH_2 liquid levels are also given.

LOX Escape From the S-IVB Stage:

The action of the destruct system according to NASA information will cut a 47 inch diameter hole into the bottom of the LOX tank. This will allow the LOX to drain out into the thrust cone supporting the engine. Figure 129 gives information as to the volume and liquid level of LOX in the tank as a function of time.

Forces on the Thrust Cone:

With LOX pouring out under the influence of pressure and gravity through the 47 inch diameter hole in the bottom of the S-IVB LOX tank after initiation of the Saturn V destruct system, tremendous forces are produced on the thrust cone supporting the engine. The LOX jet, the pressure behind it due to evaporization of LOX in the LOX tank, not even considering the impact load of the jet, will produce a loading on the thrust cone in tension of about 700,000 lbs. The impact will considerably increase this value.

Figure 129 shows maximum amount of LOX in the S-IVB LOX tank during the expansion process and while filling the thrust cone.

Strength of the Thrust Cone and Engine and Puncturing of the S-II LH_2 Dome:

The thrust cone carrying the S-IVB rocket engine is attached to the bottom of the LOX tank by 96 bolts which have to carry the entire load in tension. To determine the strength of this configuration we took a number of the bolts and tested them in our laboratory

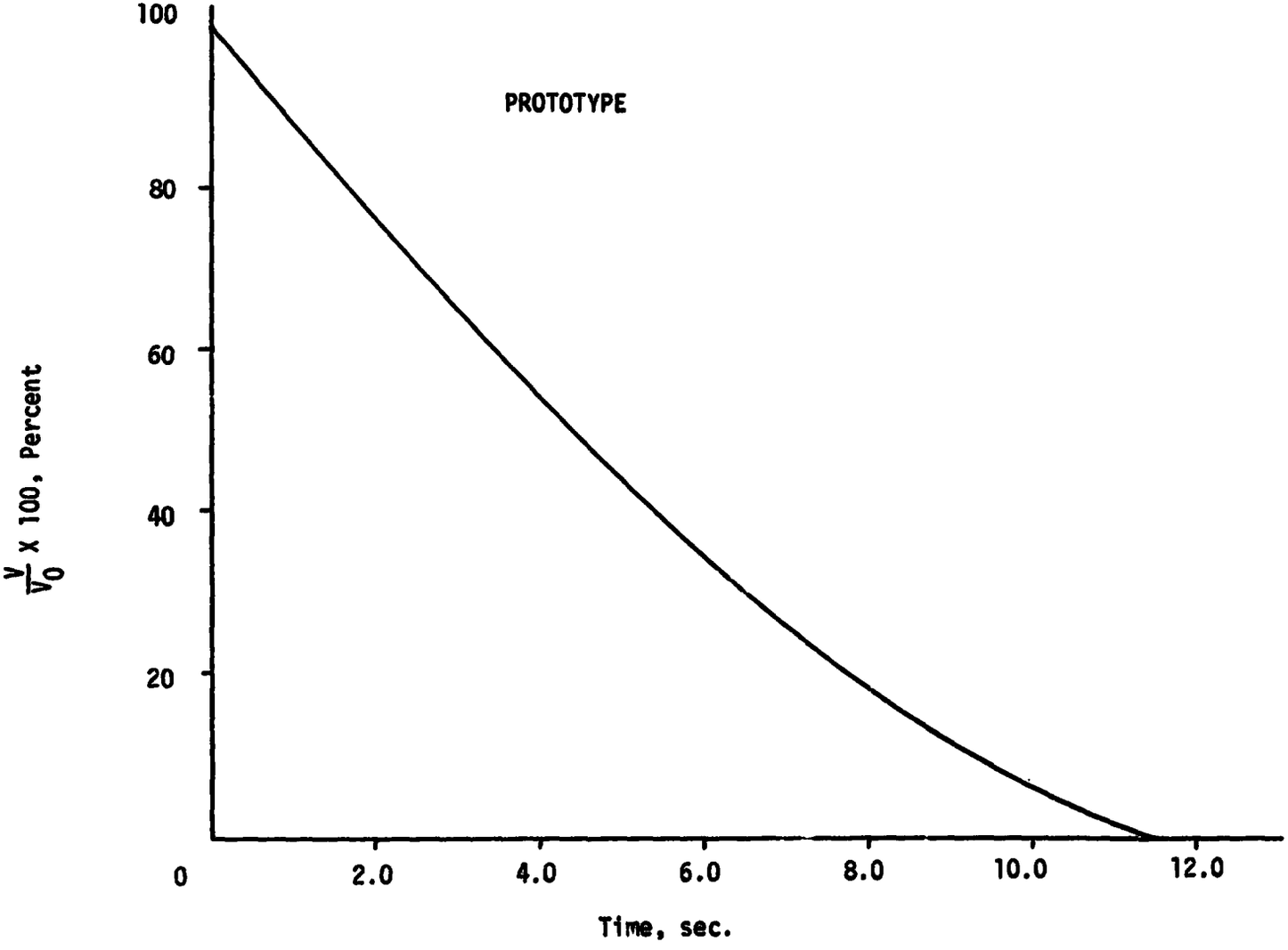

Figure 129A LOX Volume-Time Function in the S-IVB Stage

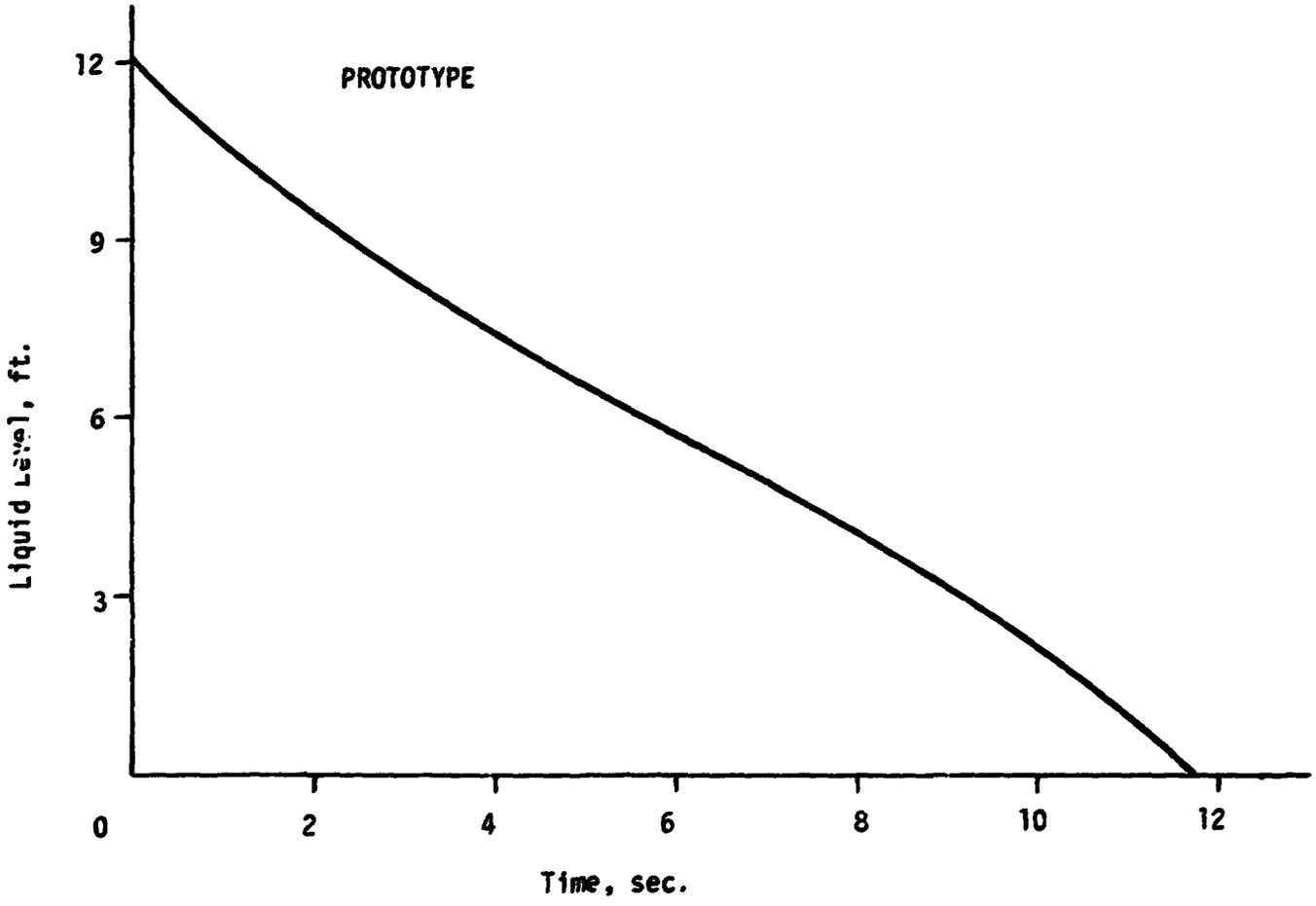

Figure 129B Liquid Level in S-IVB LOX tank as a Function of Time.

both at room and LN_2 temperatures. The results of these tests are shown in Figure 130.

The combined strength of these bolts and thus the system under uniformly distributed loading (which is very unlikely because of the violence of the LOX jet) is less than the force produced upon this system even when only static loading is considered. Thus it must be concluded with certainty that the thrust cone assembly will tear loose from the bottom of the LOX tank and drop, partially guided by the fuel and oxidizer lines.

The sequence of events likely to follow the failure of the bolts is shown and described in Figure 131, both schematically and pictorially based upon model studies.

Dropping of the Thrust Cone and Engine and Penetration of the S-II LH_2 Tank Dome:

As discussed above, it can be concluded with mathematical certainty that the engine and thrust cone will drop. After movement of only a few inches the rim of the expansion nozzle of the engine will contact the dome of the S-II LH_2 tank causing tremendous stress concentrations, which will cut a hole into this dome letting the engine penetrate into the S-II LH_2 tank. LOX running through the holes in the thrust cone, down the engine, and spilling over the edge of the thrust cone will thus enter the S-II LH_2 tank mixing with LH_2 below the engine and thrust cone assembly.

Primary Mixing of LOX and LH_2

All the events leading up to this point happened in a very

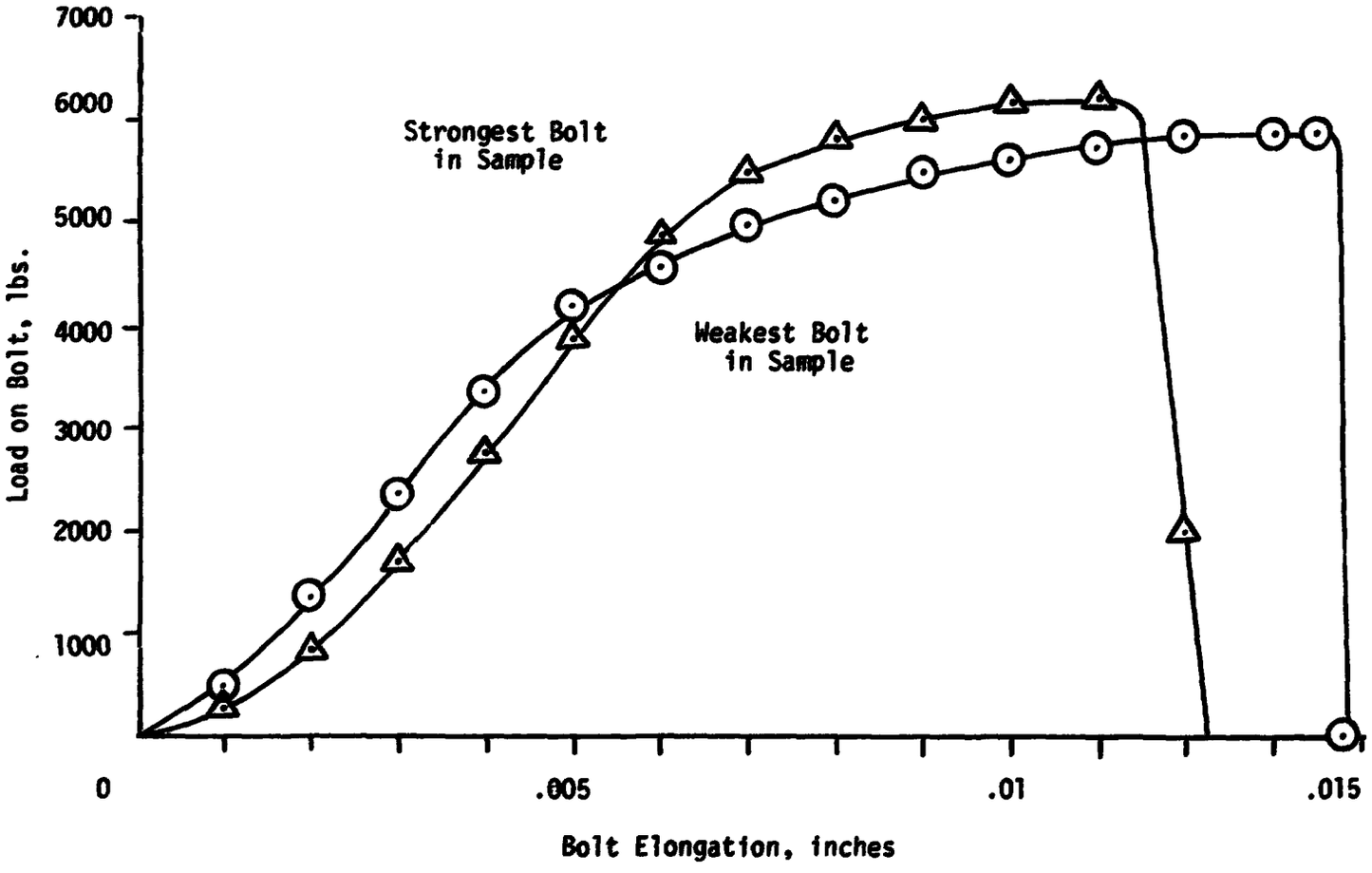

Figure 130A Strength of S-IVB Thrust Cone Anchor Bolts. (At room temperature)

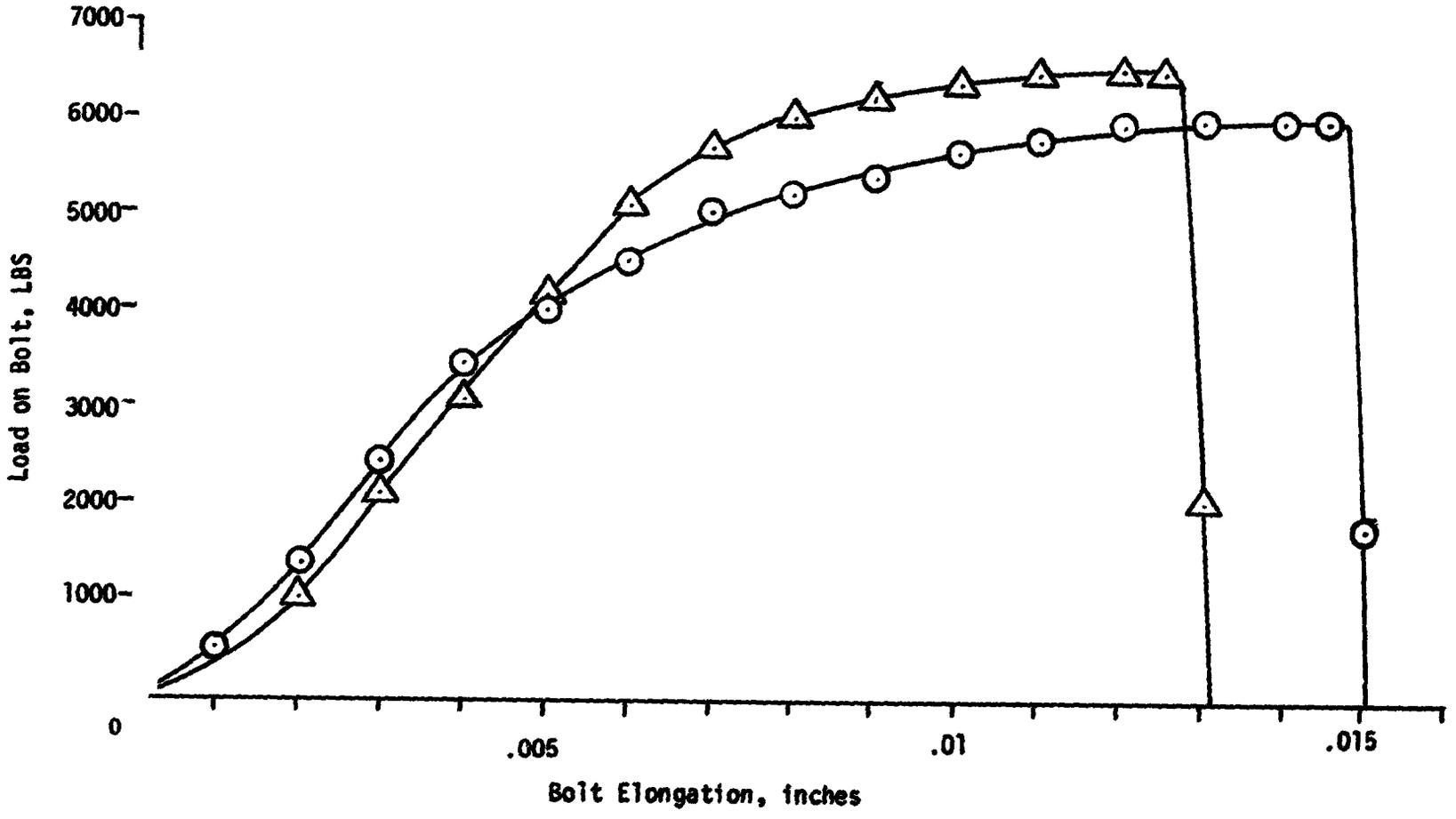

Figure 130B Strength of S-IVB Thrust Cone Anchor Bolts. (At LN_2 temperature)

(a)

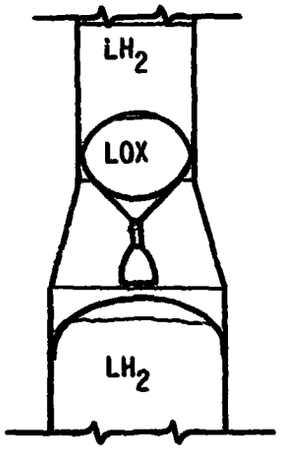

Schematic configuration prior to initiation of destruct system.

(b)

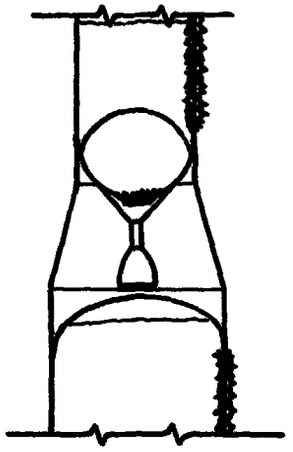

Destruct system initiated; slots blown in LH_2 tanks and circular hole blown in bottom of LOX tank.

(c)

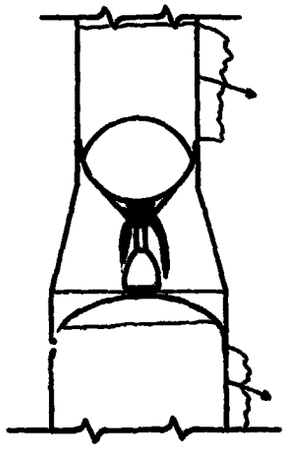

LOX pours into thrust cone. Some LOX escapes through openings (for pipes) from thrust cone.

Figure 131A

Possible Sequence of Events

(d)

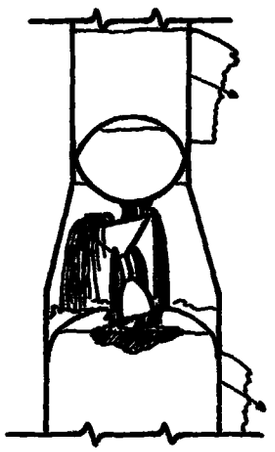

Weight and impact of LOX in thrust cone breaks mounting bolts and entire engine assembly falls. Engine penetrates upper bulkhead of S-II LH_2 tank, LOX flows into LH_2 tank to start primary mixing.

(e)

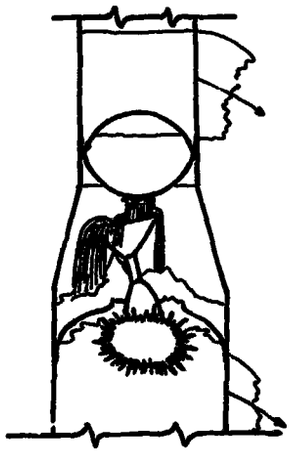

Primary explosion occurs in LH_2 tank.

(f)

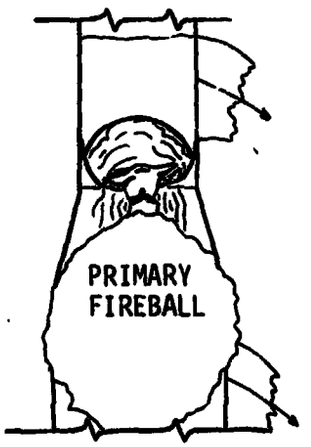

Engine assembly is driven explosively through lower bulkhead of LOX tank-primary fireball expands.

Figure 131A Continued

Possible Sequence of Events

(g)

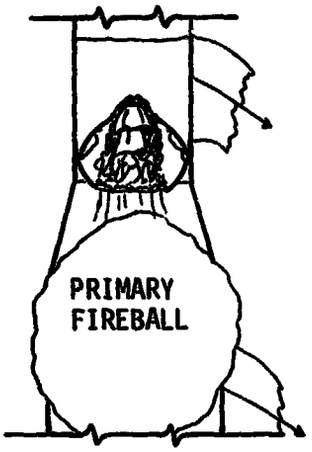

Thrust cone-engine assembly continues forward, penetrating upper bulkhead of LOX tank, introducing LOX into LH_2 tank of S-IVB.

(h)

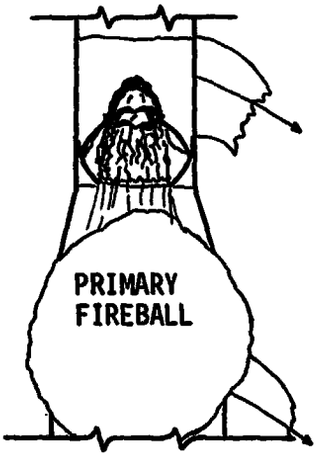

Engine continues through LH_2 tank producing further mixing.

(i)

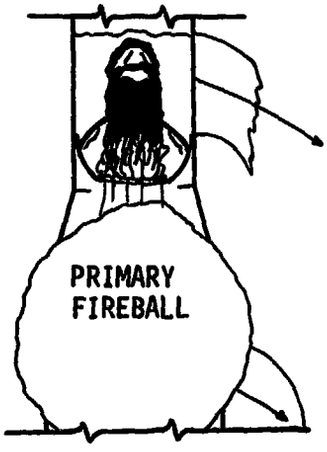

Extreme turbulence and large amounts of LOX introduced into LH_2 tank produces extensive mixing.

Figure 131A Continued

Possible Sequence of Events

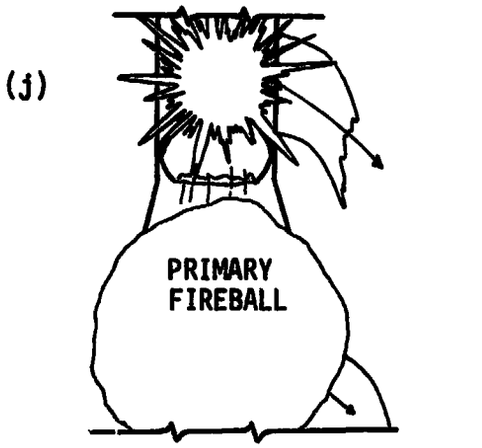

Violent secondary explosion occurs in LH_2 tank of S-IVB.

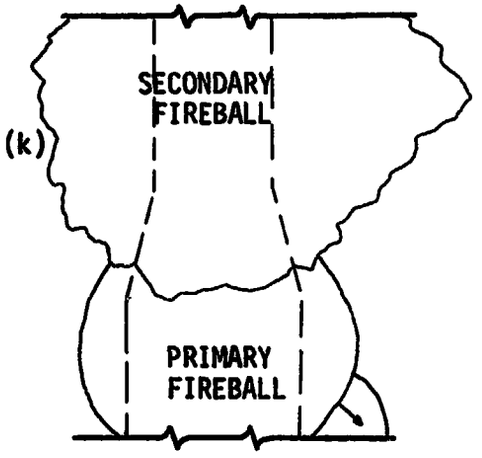

Secondary explosion fireball expands destroying S-IVB Stage.

Figure 131A Continued

Possible Sequence of Events

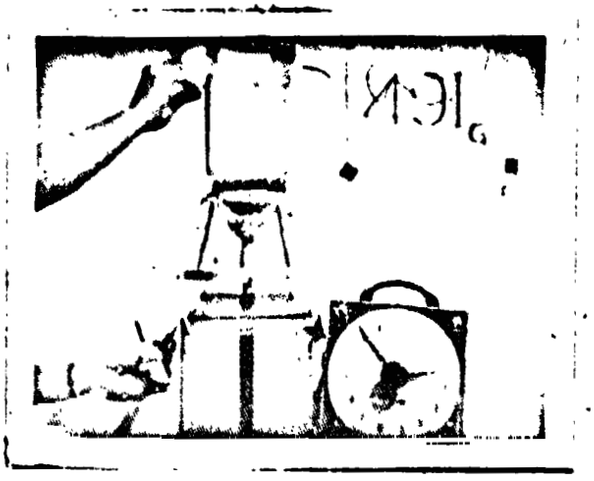

(a)

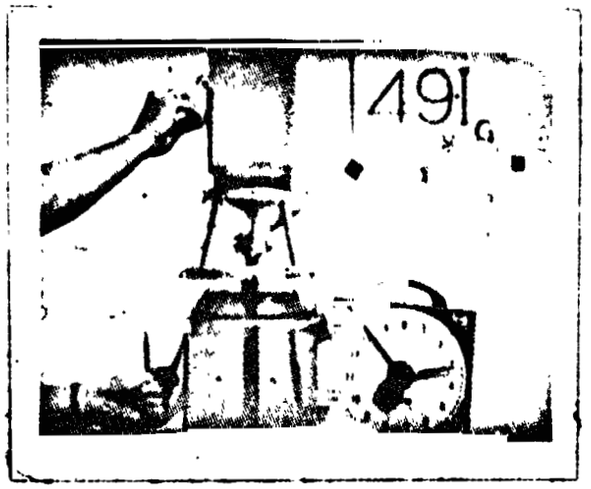

(d)

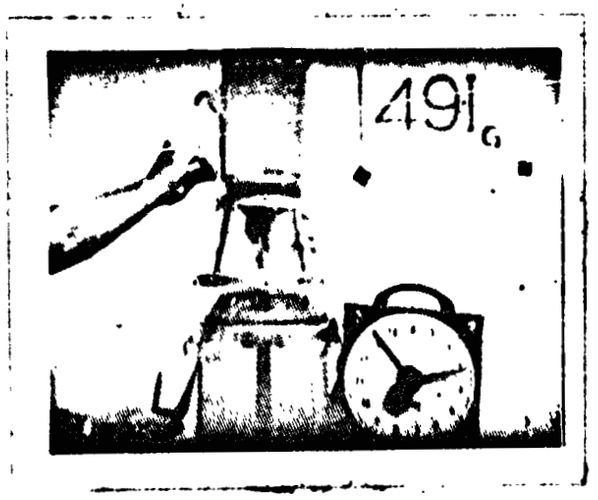

(e)

Figure 131BPossible Sequence of Events.
Letter notations correspond to sketches in Fig.

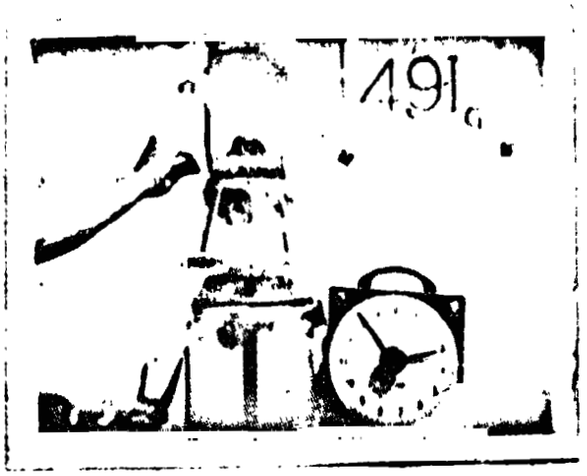

(g)

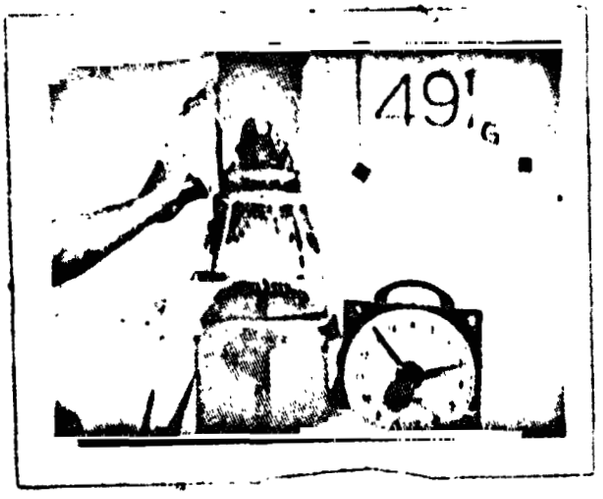

(h)

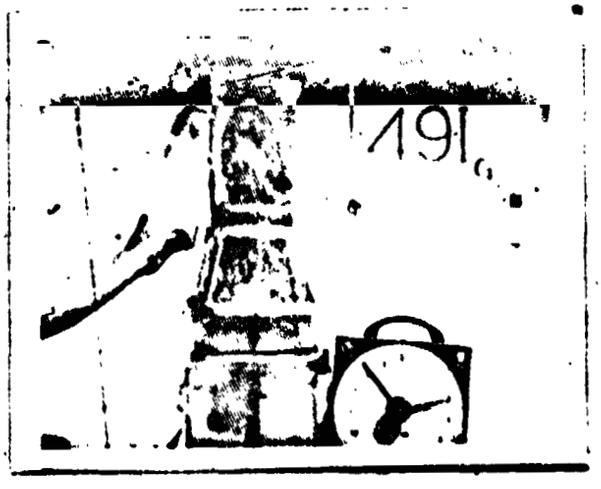

(i)

Figure 131B Continued
Possible Sequence of Events

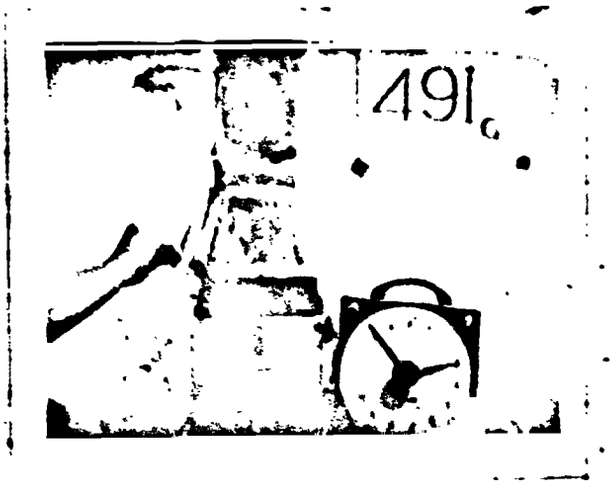

(j)

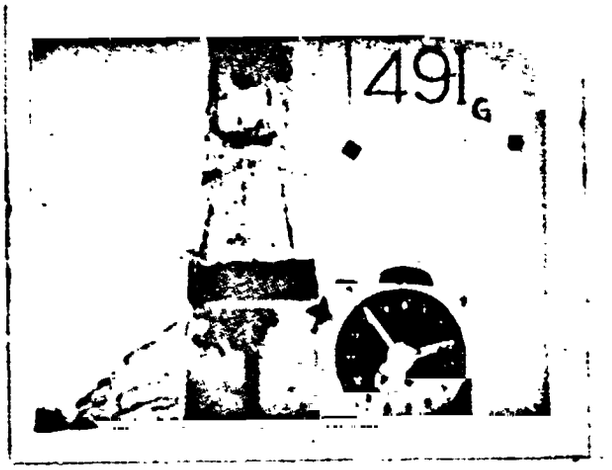

(k)

Figure 131B Continued
Possible Sequence of Events

short time. LOX from the S-IVB and LH_2 from the S-II will continue to mix until ignition occurs producing the primary explosion. A typical curve for the amounts mixed as a function of time is presented in Figure 132 for both the models which were used in simulating the events and for the prototype based upon correlation analysis.

These curves represent the amount mixed as a function of time if ignition does not occur. When ignition occurs, it will terminate the curve at the time of ignition.

Ignition and Predicted Yield for the Primary Explosion:

Based upon the theoretical investigations of ignition phenomena[75,124,125,126], it can be concluded that ignition of the mixture would occur rather early during the mixing phenomenon and thus result in a relatively low yield. Experience also supports this.

The type of failure involved in this case has been covered by the University of Florida investigation[79,15,75,124,125] as well as by Project PYRO[22,119]. The S-IV test[22,119] with an explosive yield of about four percent seems to be applicable in this case. Also, the thoroughly instrumented 25,000 lb. explosion experiments[79,75,124,125] correlate well with the low yield prediction.

Effect of Primary Explosion Upon Engine and Thrust Cone Assembly:

The primary explosion, occurring essentially below the thrust cone engine assembly, will, based upon vector analysis, be propelled upward or forward carried by the shock and reaction front of the explosion at velocities of up to several thousand feet per second. Velocities of this magnitude were verified through analysis of high-speed movie

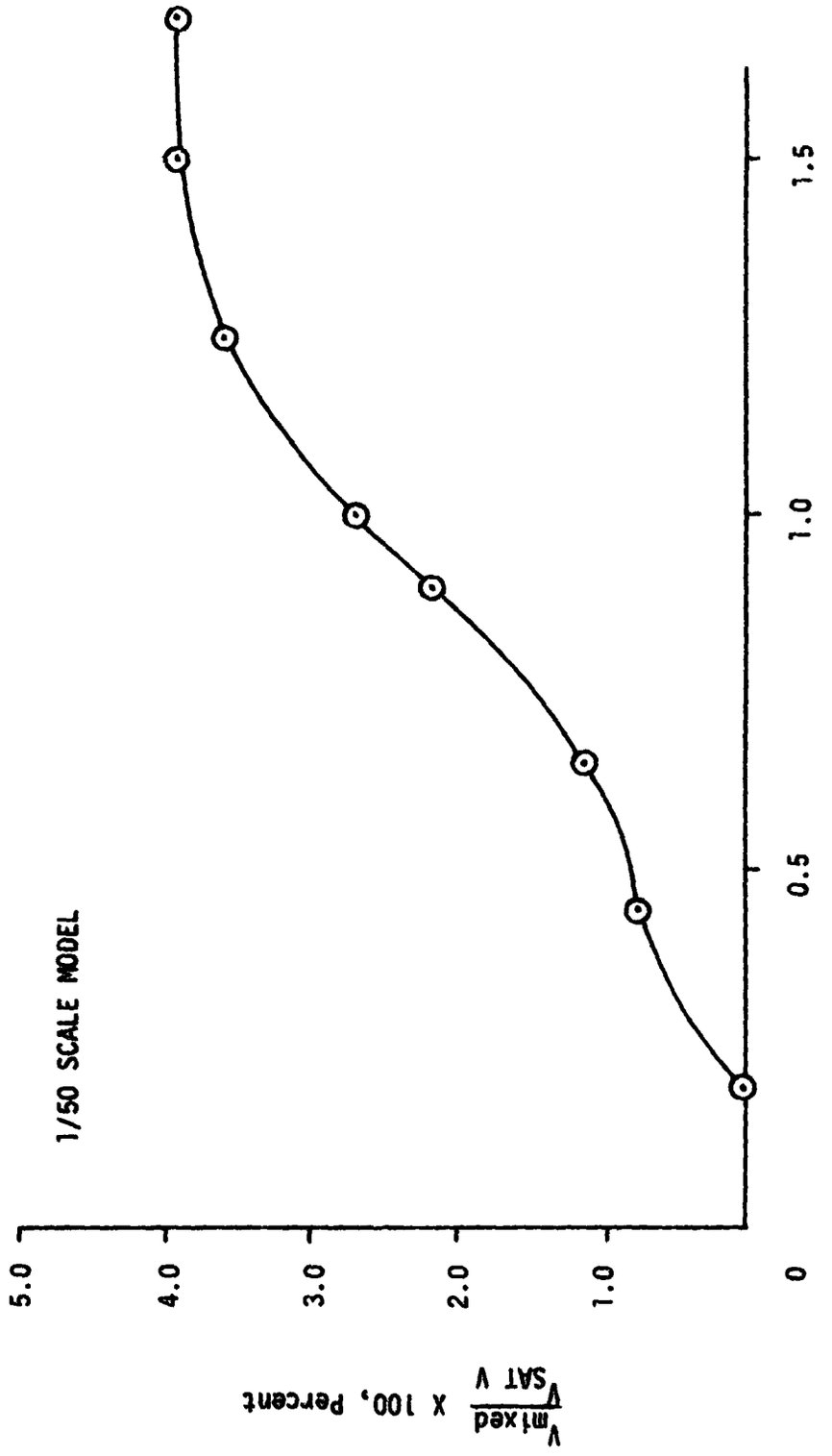

Figure 132A Mixing Function for the S-II LH_2 Tank Using a 1/50 Scale Model.

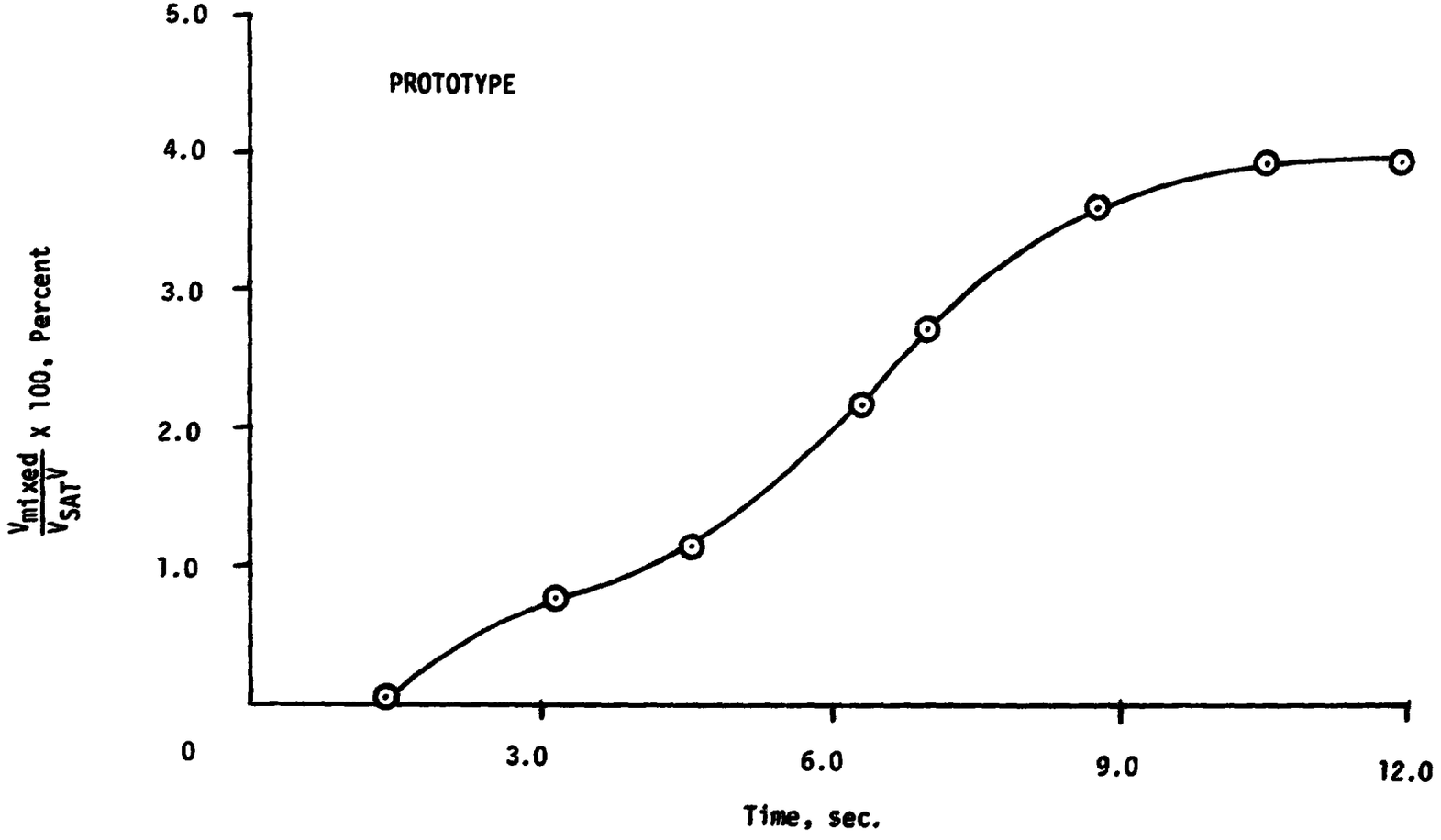

Figure 132B Predicted Mixing Function for the Prototype S-II LH_2 Tank Forming the Basis for the Primary Explosion.

film coverage of liquid rocket propellant explosions both in the ADL experiments[6] and the PYRO experiment where trajectories of large pieces of metal can be traced, giving their motion, velocities, etc.

The engine thus moving forward penetrates the lower bulkhead of the S-IVB LOX tank then the upper one which is common with the LH_2 in the S-IVB.

Failure of the LOX Tank (Hole or Shattering):

The impact of the thrust cone and engine assembly upon the LOX tank lower and upper bulkheads causes penetration of the thin metal walls. The minimum effect will be penetration by the thrust cone and engine, which will become mangled in the process. The maximum effect will be the shattering of the bulkheads. Both opinions have been advanced with, however, no experimental support of how the material of the S-IVB stage will react to such severe impact conditions.

The amount of mixing of LOX and LH_2 will depend on the size of the hole produced and the subsequent amount of motor penetration into the LH_2 tank. Again experimental determination of the material behavior could narrow the range of results predicted.

Secondary Mixing in the S-IVB Stage:

Depending upon the size of the primary explosion and the time at which it occurs, partial or complete penetration of the thrust cone and engine into the LH_2 tank of the S-IVB can be expected. This phenomenon, producing violent mixing, is referred to in our work as the EXPLOSIVE MIXING MODE. This mixing mode produced by an explosion, ramming the propellants and oxidizers together with extreme velocities

and violence, was simulated in our modeling studies and showed that due to the extreme mixing rates very high explosive yields can be expected.

None of the other experiments with liquid rocket propellants such as the ADL experiments, Project PYRO, and the work of Mr. Fletcher covered EXPLOSIVE MIXING MODES and therefore cannot be used to make predictions about the explosive yields obtainable from such a mode of failure. Our work of simulation through model studies covered this mode as well as the others and indicated the much higher explosive yields obtainable.

Even though the other works cited above did not cover the EXPLOSIVE MIXING MODE, they indicated that the higher the energy supplied for the bringing together of the propellants such as dropping, firing into concrete walls, etc., the higher the yield obtainable. The EXPLOSIVE MIXING MODE is one of the extreme cases of energy supply for the mixing process

Figure 133 presents the mixing function for the secondary explosion produced by a one tenth of one percent primary explosion.

Ignition of Secondary Mix and Resulting Explosive Yield:

Previous work has shown that the mixing energy affects the delay time before ignition less than the amount of fuel and oxidizer mixed. Thus, the greater the amount of energy supplied, the more mixing which will be accomplished before ignition occurs, and thus, the higher the explosive yield obtained.

In the EXPLOSIVE MIXING MODE the size of the primary explosion, up to a value where maximum secondary mixing can be obtained, is

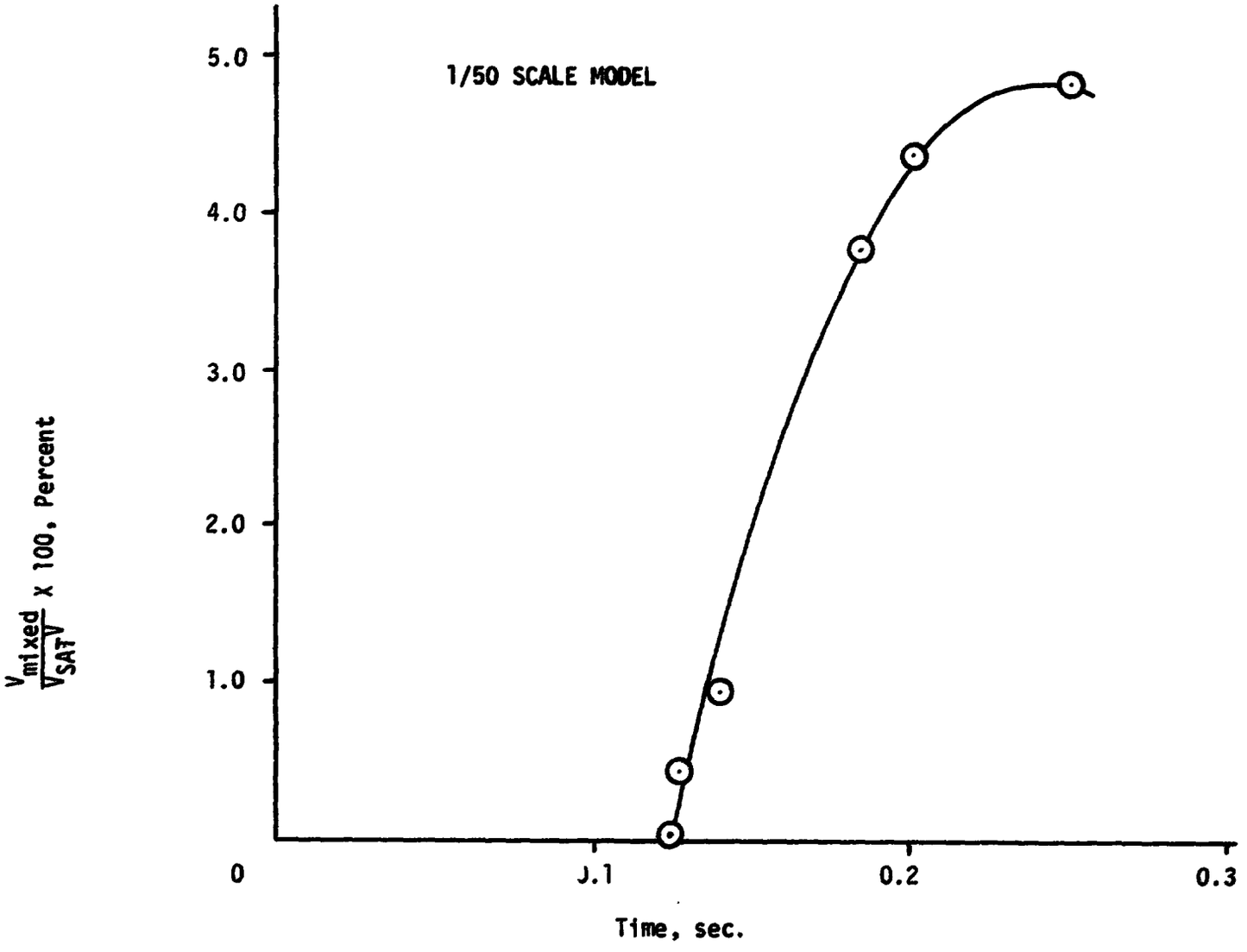

Figure 133A Mixing Function for the S-IVB LH_2 Tank Using a 1/50 Scale Model.

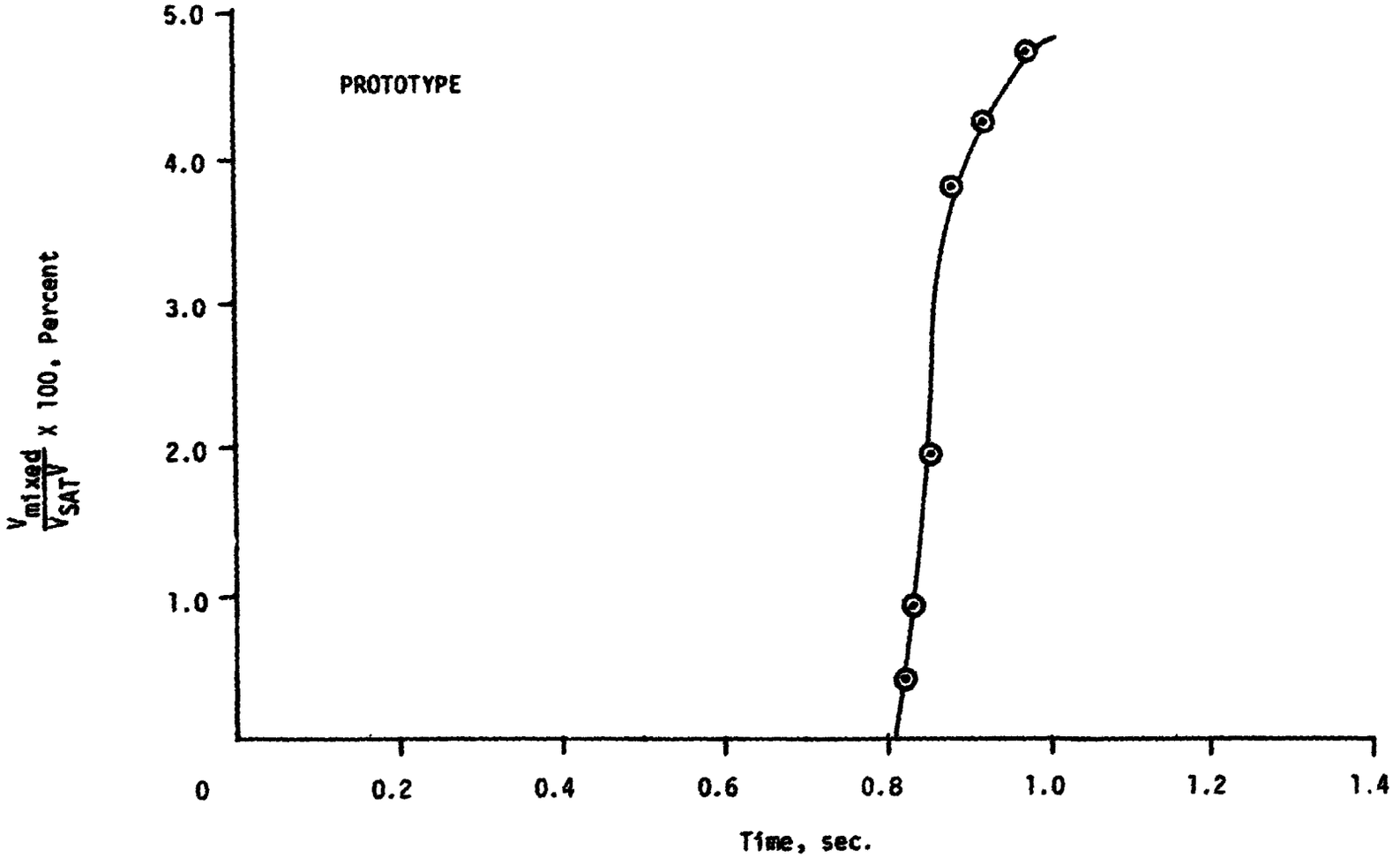

Figure 133B Predicted Mixing Function for the Prototype S-IVB LH_2 Tank Forming the Basis for the Secondary Explosion.

important. If the primary explosion is larger than this value it consumes part of the LOX which otherwise would be available for the secondary explosion, resulting in a decrease in the total yield.

Figure 134 presents the theoretical maximum explosive yield of the secondary explosion based upon the primary explosive yield. It can be seen that for very low primary explosive yields the secondary yields produced are also low. With a yield increase of the primary explosion the secondary maximum yield increases and then decreases again depending upon the delay time involved before the primary explosion. Finally, if the primary yield is rather large the secondary explosion is smaller since not much oxidizer was left for this reaction.

Figure 135 presents the experimentally predicted primary yield as a function of ignition time after destruct initiation. This figure also presents the secondary explosive yield resulting from an approximate 0.1% primary explosion.

Had the primary explosive yield increased (in the modeling studies) the resulting secondary explosion yield curve would have been shifted with the maximum value moving up and to the left.

Results of the above analysis and phenomena following a destruct initiation, which can produce the S-II/S-IVB interaction, are summarized in Figure 136. It presents theoretical primary and secondary explosive yields and experimental primary yield predictions. It also presents experimental secondary explosive yield predictions based upon an approximate 0.1% primary explosive yield. A higher primary explosive yield shifts the secondary explosive yield curve up and to the left.

Figure 134 Theoretical Prediction of Maximum Yield as a Function of Time After Destruct.

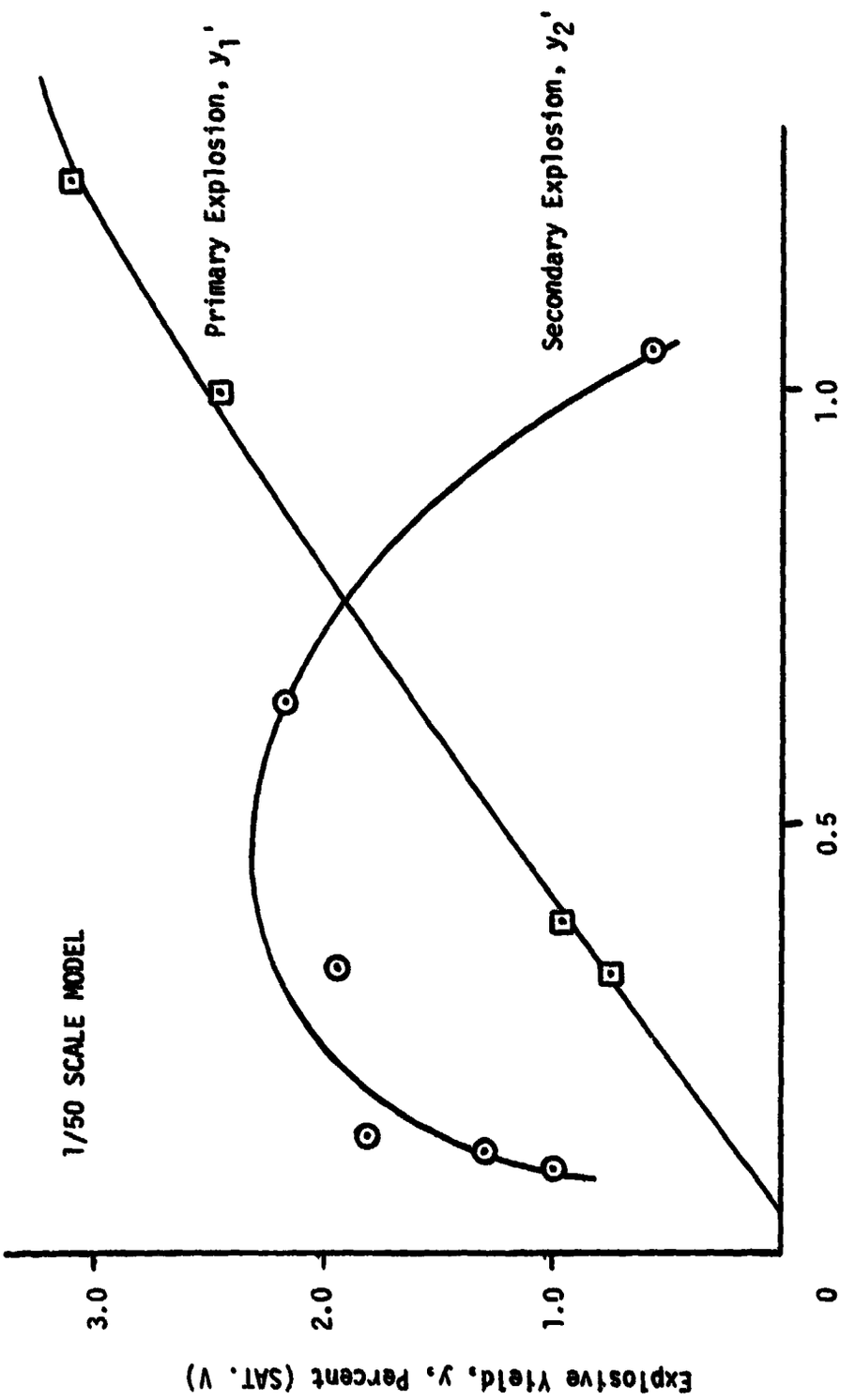

Figure 135A Experimental Prediction of Maximum Yield as a Function of Time

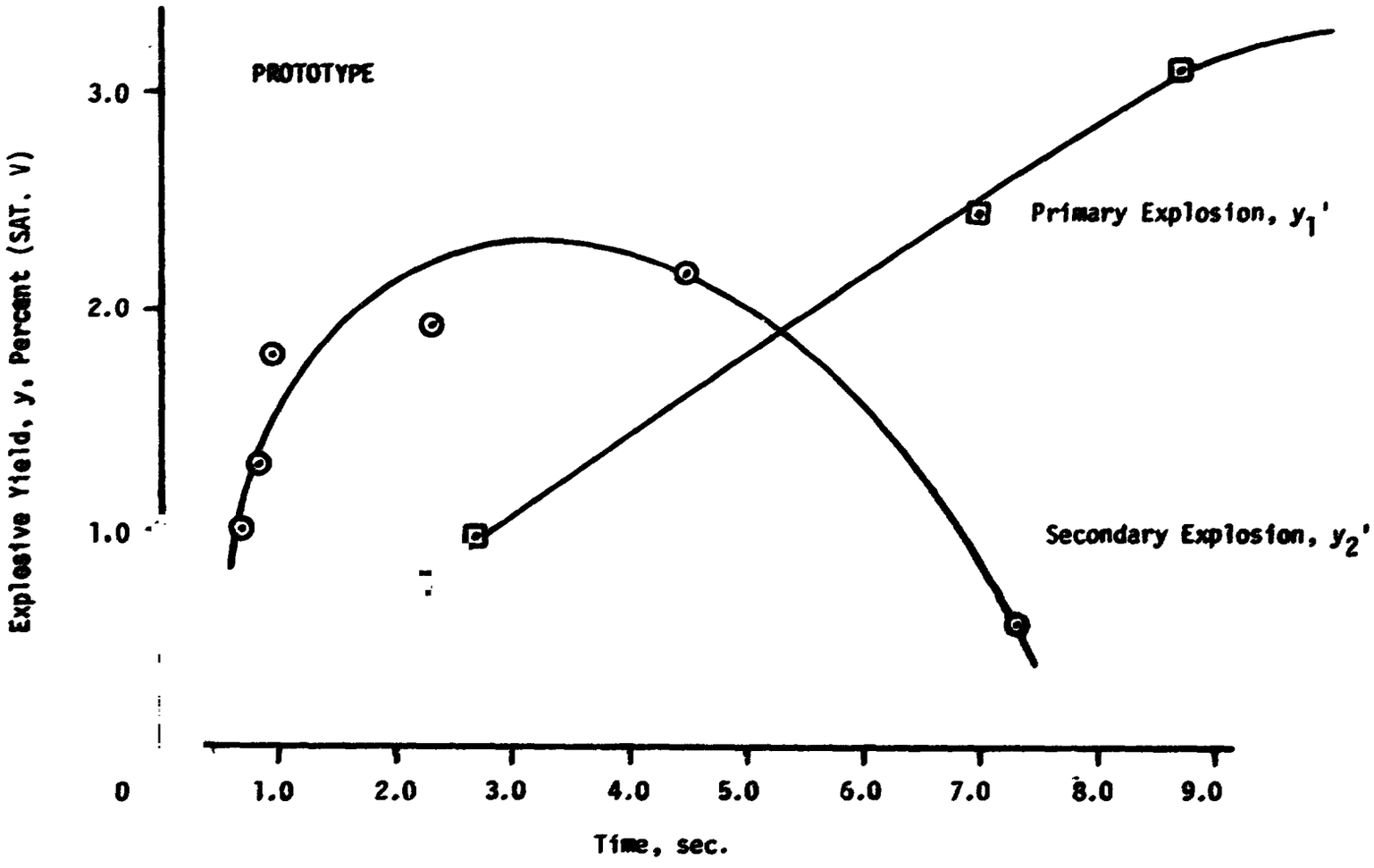

Figure 135B Experimental Prediction of Maximum Yield as a Function of Time

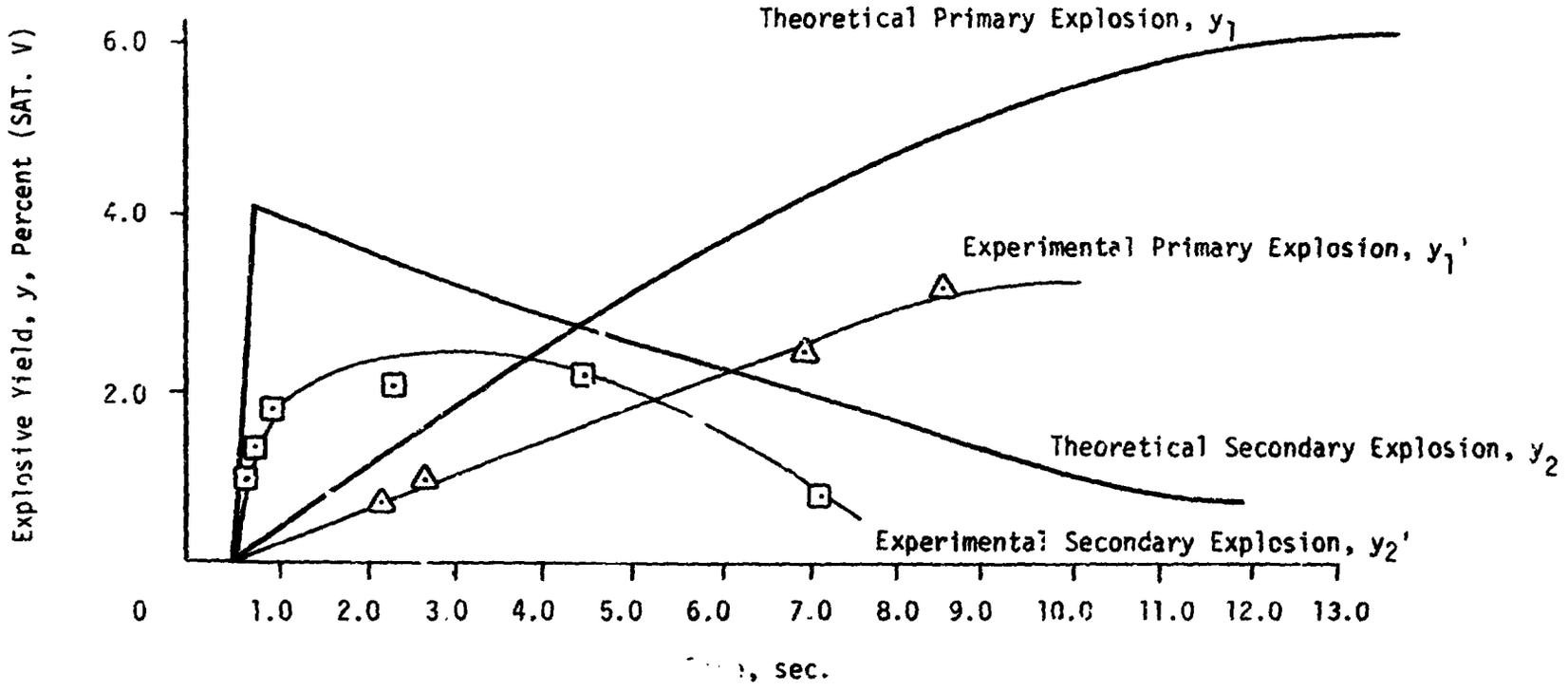

Figure 136 Comparison of Theoretical and Experimental Maximum Yields

There may be some desire to establish the exact "likelihood" of the events described above. It does not seem too important to establish this. Theoretical studies and the modeling, both two and three dimensional, simulating the primary explosions, show that these events will happen. The initiation of the destruct system may well be necessary, causing a sequence of events such as described above. The reported explosion on the pad of the Russian 10-14 million pound thrust super rocket during the summer of 1969 is a case in point.

In the case at hand the problem of the S-II/S-IVB interstage failure is self imposed through the design of the destruct system. The above problem can be eliminated by removing the ring charge from the S-IVB LOX tank resulting in a simpler, better, and safer Saturn V destruct system.

Recommended Action for Preventing the S-IVB/S-II Interstage Failure

The detailed analysis of the destruct system reported elsewhere, is believed to be able to function more or less as intended except for the S-II/S-IVB interstage failure.

The sequence of events as analyzed and discussed in this paper are triggered by the setting off of the destruct charge on the S-IVB LOX tank. For this reason it seems that, from a technical point of view, the removal of the ring charge would prevent the occurrence of this sequence of events.

Everyone with whom this problem was discussed, at Huntsville and Cape Kennedy, agrees that we would have a better destruct system with

that charge removed.

If, however, positive destruct of the LOX tank is required, pancake charges could possibly be used to accomplish this without letting the S-IVB and S-II interact as discussed.

Conclusions

It is believed that upon the foregoing work the following conclusions can be made:

1. The methods previously developed by Dr. Farber's group regarding liquid rocket propellant explosions seemed well-suited for the detailed analysis of the Saturn V destruct system.
2. A considerable amount of uncertainty still exists regarding the actual effect of the destruct system upon the Saturn V tankage configuration. Our recommendation of several years ago concerning experimental verification of the various opinions is still valid.
3. An S-IVB/S-II interaction caused by the initiation of the destruct system can happen, and in our opinion, based upon theoretical and experimental modeling studies, is likely to happen.
4. This S-IVB/S-II interaction can produce a primary explosion of the size predicted by other works, and in turn a much larger secondary explosion produced by the explosive mixing mode not previously investigated.
5. The sequence of events described in this paper can be prevented by removing the ring charge on the S-IVB LOX tank, preventing the occurrence of a high yield explosion in this manner.

6. If positive destruct of the S-IVB LOX tank is required this can possibly be done by using pancake charges, thus preventing the above sequence of events which lead to a high secondary yield explosion.

S-IVB Pancake Charge Destruct Analysis

Because of the possible difficulties with the destruct system as it was designed and intended to be used, opening a hole in the bottom of the LO_2 tank of the third stage, which in turn can produce a primary explosion leading to a larger secondary explosion in a critical region, alternative destruct methods were investigated.

This seemed to be necessary if positive destruct of the tanks was to remain a definite requirement.

For this reason the possibility of rupturing the tanks of the third stage, especially the LO_2 tank, was studied. This tank does not have actual contact with the outside skin and thus cannot be ripped open like the other tanks for propellant dispersal. This could be done by the proper design and placement of pancake charges.

The pancake charges were simulated in both two and three dimensional models, see Figures 137, 138, by several methods.

1. Pressurized air, blowing one propellant into the other.
2. An air rifle which produces a blast opening the tanks and allowing the components to mix.
3. A 22 caliber blank which acts similarly to the air gun but has a sharper and more powerful blast.

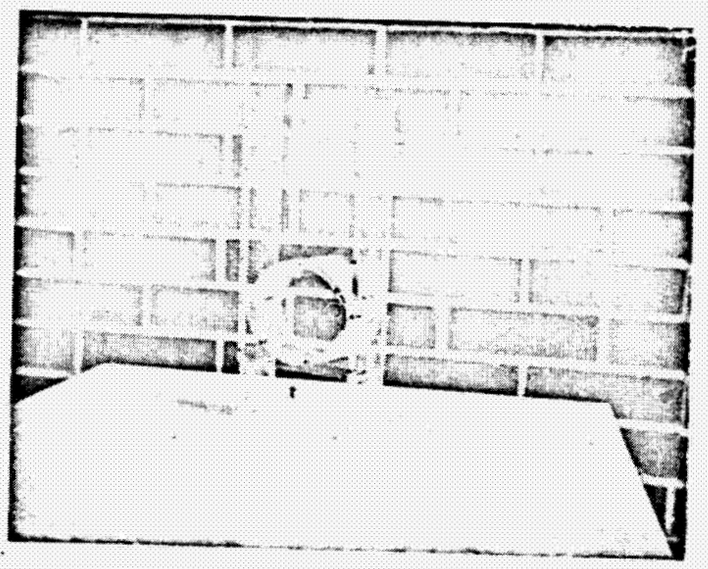

Figure 137 Two Dimensional Pancake Charge Model

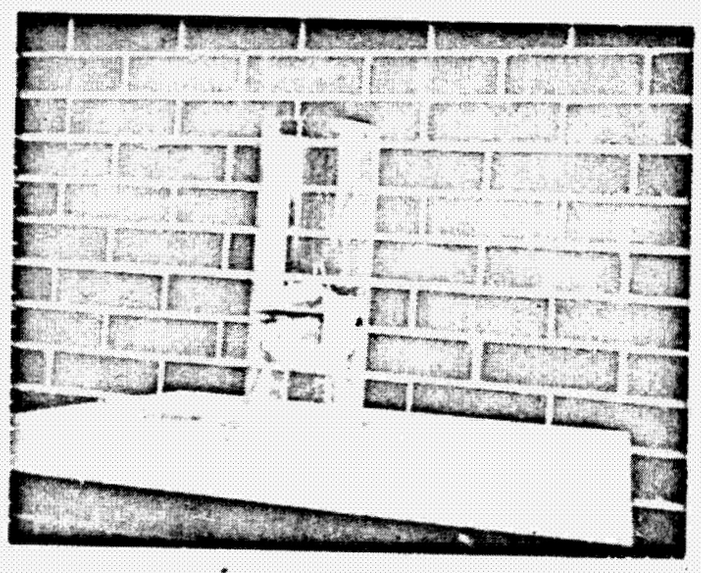

Figure 138 Three Dimensional Pancake Charge Model

4. The pressurization of the tanks so when the openings are made manually one liquid is propelled into the other by the pressure in the tank.
5. Pressurized, unpressurized and vented systems were analyzed and compared.

Again depending upon the design of the charge different results can be obtained. If the shaped pancake charge is to basically blow a hole into the walls of both the LH_2 tank and the LO_2 tank and both of them are pressurized, relatively little mixing is produced and with the liquids streaming out of the hole an external H_2 fire may be produced.

If, however, the shaped charge blows one constituent into the other backed by the pressure in the tank, then considerable mixing can occur.

It might be observed that the size of the pancake charge in the modeling was relatively larger than would be used in the comparable prototype since true scaling would not have produced much effect on the models. The models used here were again 1/50 scale.

The actual explosive yield even for the worst case is only a small fraction of the maximum of the total theoretical maximum for the Saturn V.

The position, however, may be critical and it may be better to produce a small explosion, or not to destruct the tank at all, if this is admissible for actual operation.

Figure 139 presents the progression of the mixing process by showing a number of frames of the high-speed movie film.

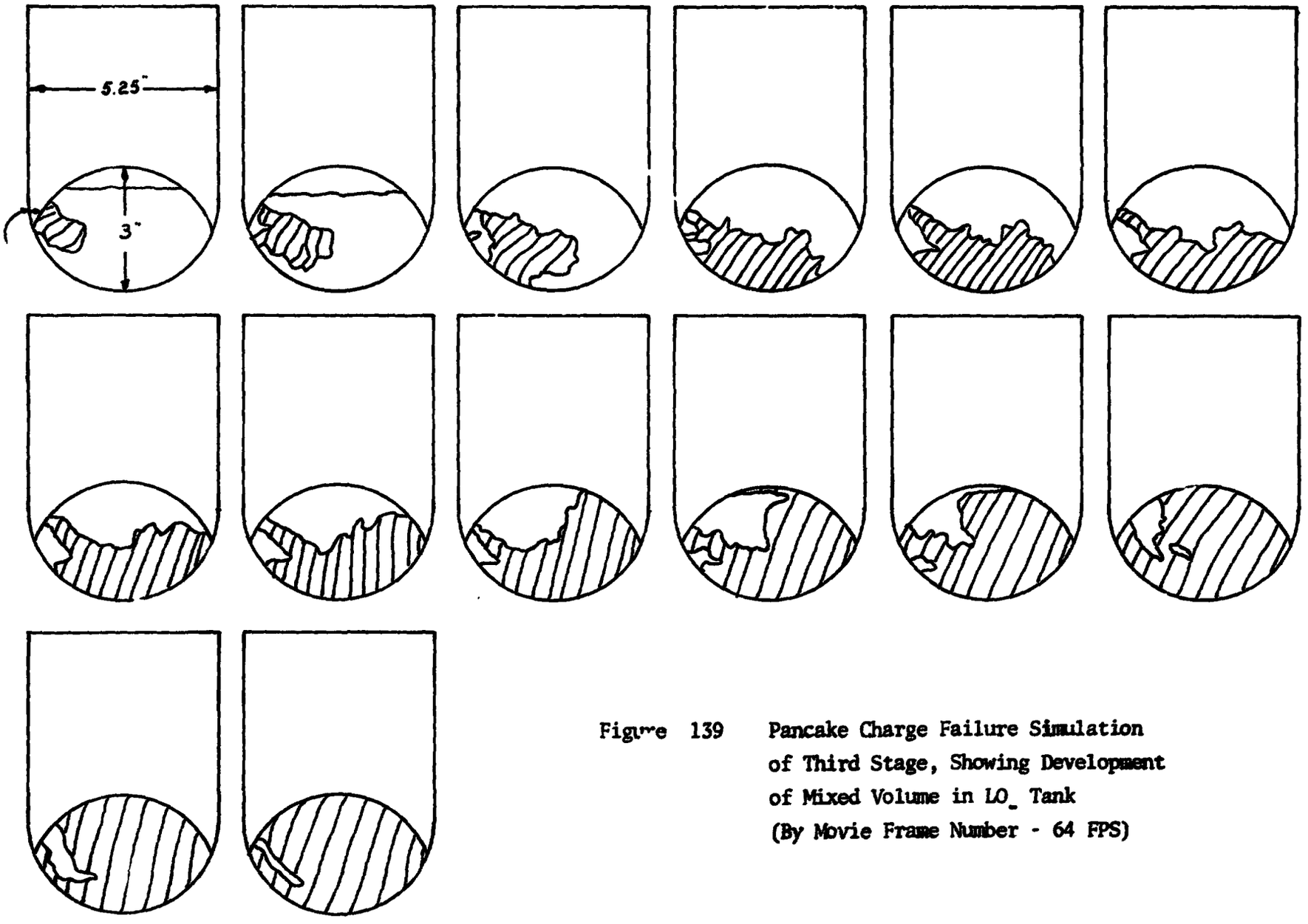

Figure 139 Pancake Charge Failure Simulation of Third Stage, Showing Development of Mixed Volume in LO_2 Tank (By Movie Frame Number - 64 FPS)

An analysis of the records, frame by frame, results in a mixing function and expected yield as shown in Figure 140, and it can be seen that by this method of failure the mixing and thus the explosive yield will always be a small fraction of the theoretical possible for the Saturn V. Thus in the over-all picture the pancake charge destruct does a nice job in producing low yield but the location near the payload, nuclear packages, or the personnel capsule may be cause for some concern.

On the last Figure, 141, in this section several typical yield functions are presented mostly to indicate the various possibilities of modeling.

The fastest rising curve is the result of a glass model which was partly shattered by a 22 caliber blank which was used to simulate the pancake charge. Because of the shattering and the large contact area the mixing progressed rather rapidly in this case.

The next curve over is essentially the same experiment repeated but with a plastic model which had a predrilled hole which was covered by tape and the tape was blown in with a 22 blank. Because of the smaller hole and therefore less contact surface the mixing progressed more slowly.

The next curve presented gives the results when a plug is removed in the plastic model to open up the holes which otherwise would be produced by the pancake charge. Since the action is much less violent, the mixing which occurs is much slower.

When an air gun is used instead of the 22 blank or the plug, the

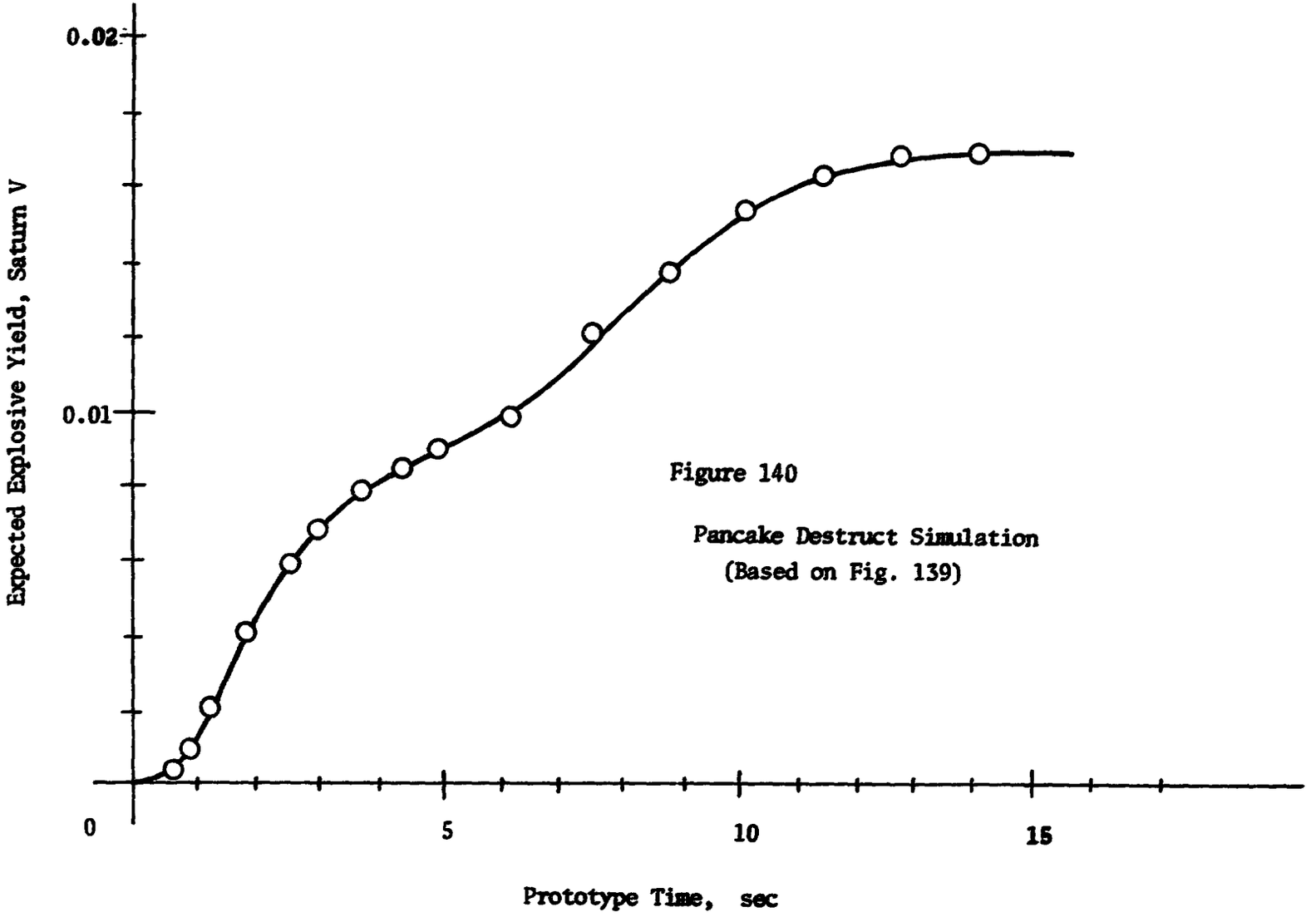

Figure 140

Pancake Destruct Simulation
(Based on Fig. 139)

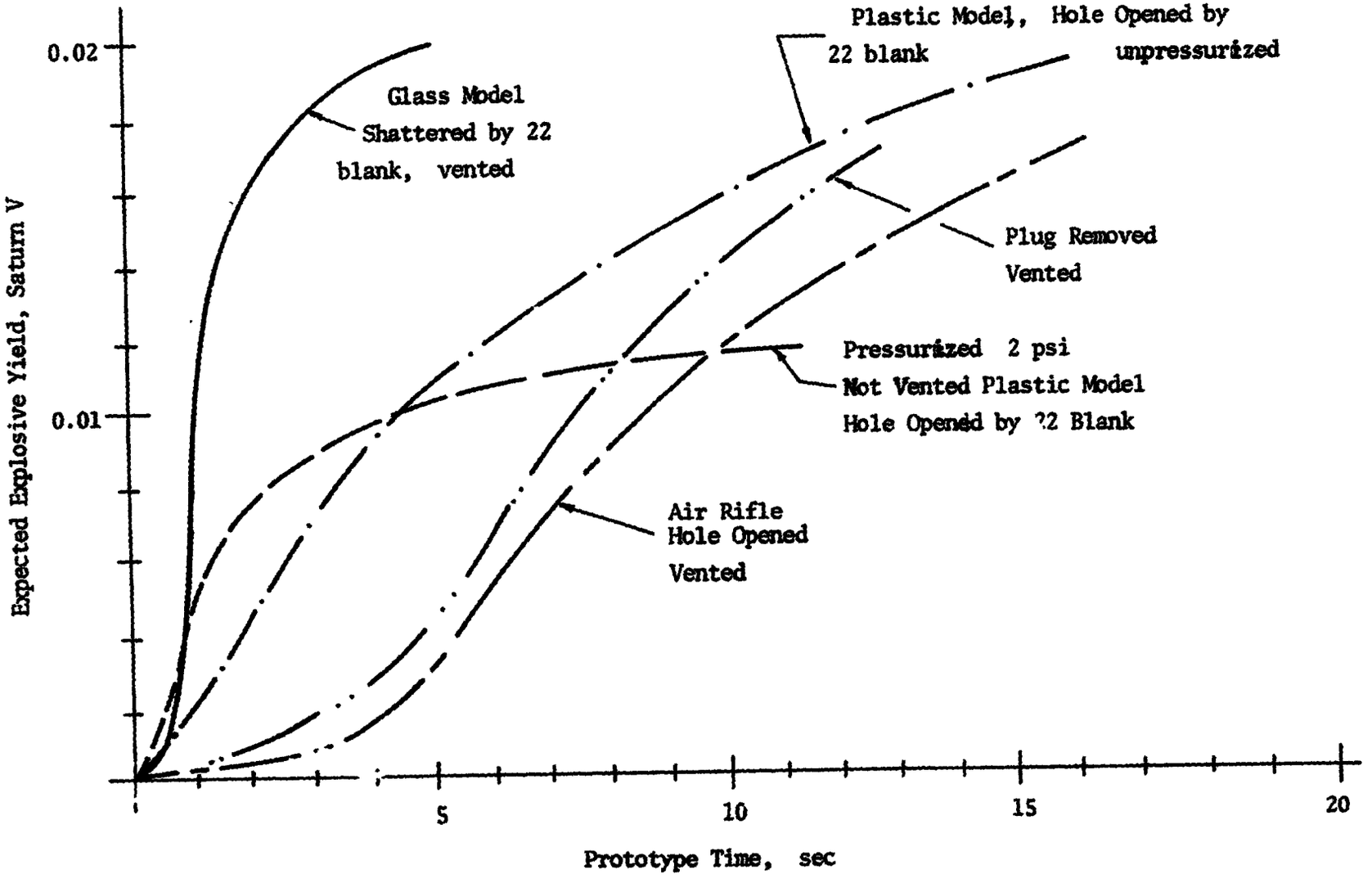

Figure 141 Comparison of Various Pancake Charge Produced Failures

tape over the hole absorbed much of the energy and the mixing is still slower. It does not seem as good a simulation to the pancake charge effect.

The last curve presented is that of the LO_2 tank pressurized and not vented or opened up by the pancake charge. This makes it difficult to have the simulated LH_2 to flow into the LO_2 tank except for an initial surge and the mixing never reached the completion it did in the other simulations.

In all cases the mixing and thus the resulting explosive yield was a small fraction of the total potential of the Saturn V.

Since this type of destruct system was not seriously considered, the work was not carried out as completely as in the others. It is of interest, however, since the type of failure and the subsequent mixing phenomena are different.

*This work is presented late in the report since it represents an application of the theories and methods developed under this contract. It was actually carried out in 1968.

Part IV Space Shuttle Analyses (Early Configurations)

Introduction

Since methods had been developed earlier that proved to be reliable for predicting the explosive yield, it was decided to apply the same procedure of analysis to the various configurations of the Space Shuttle and its most probable modes of failure. This information then became available parallel to the development of the shuttle rather than after the designs and configurations had become hardened, as proved to be the case with the Saturn V.

It is much easier to use information,if available,for guidance and decision making than to use that same information for making changes later.

The early configurations were of the all liquid type with a booster and two different types of orbiters, the Delta Wing Orbiter and the 200 Mile Orbiter.

Again, 50th scale models were constructed from wire frames and plastic to simulate the tankage configurations and then they were mounted on the pad and in flight configurations so that with high speed photography various modes of failure can be studies. See Figs. 142-145.

With these models available the following modes of failure were studied and the mixing functions obtained:

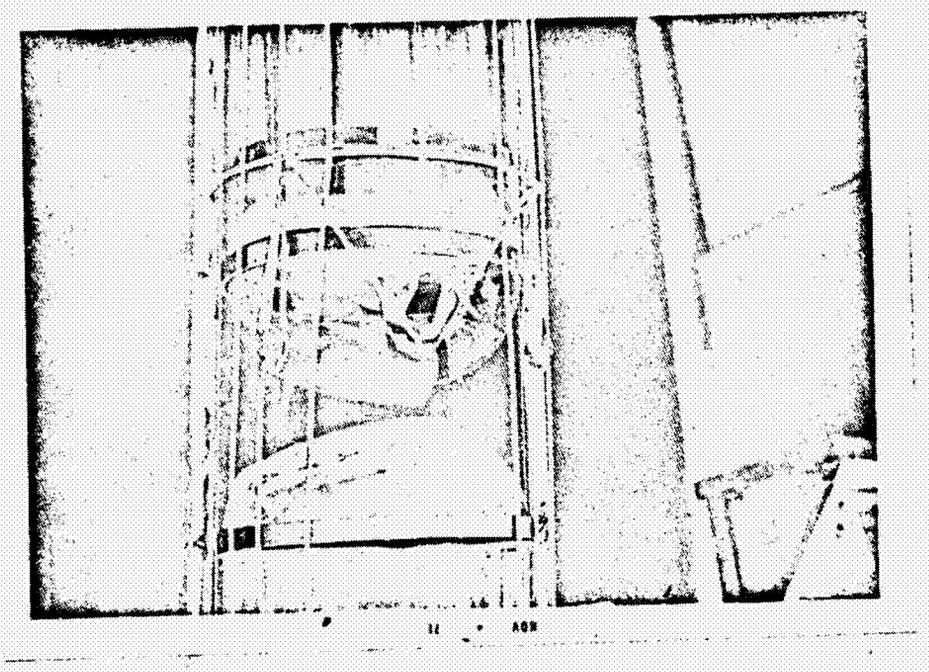

Figure 142 Space Shuttle Booster - Bulkhead Type Failure.

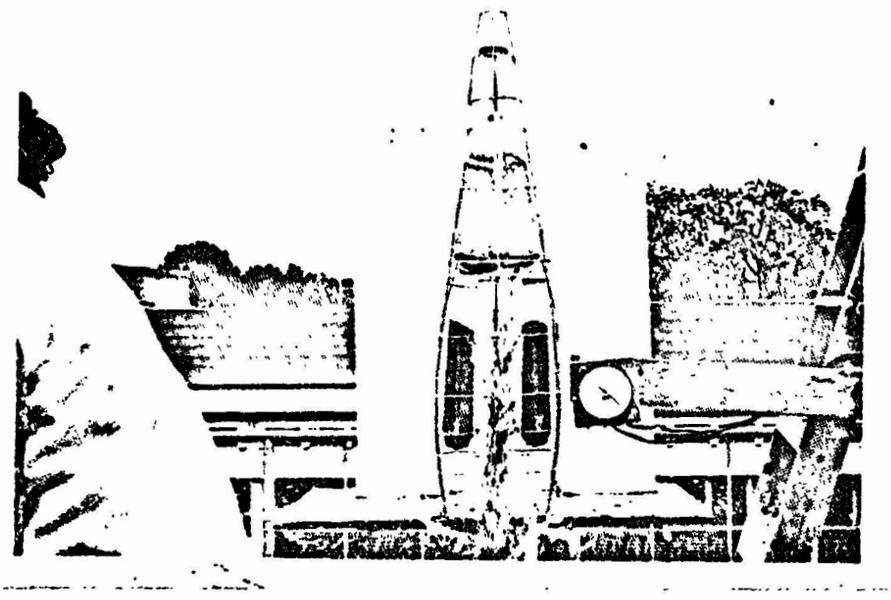

Figure 143 Space Shuttle Delta Wing Orbiter Bulkhead Type Failure

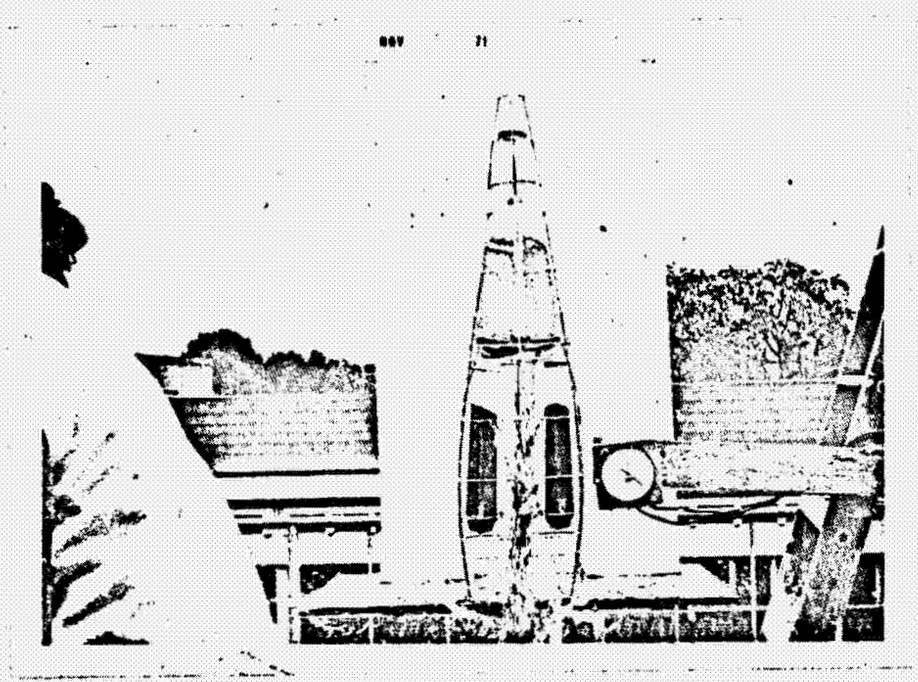

Figure 143 Space Shuttle Delta Wing Orbiter Bulkhead Type Failure

Figure 144 Space Shuttle 200 Mile Orbiter
Bulkhead Type Failure

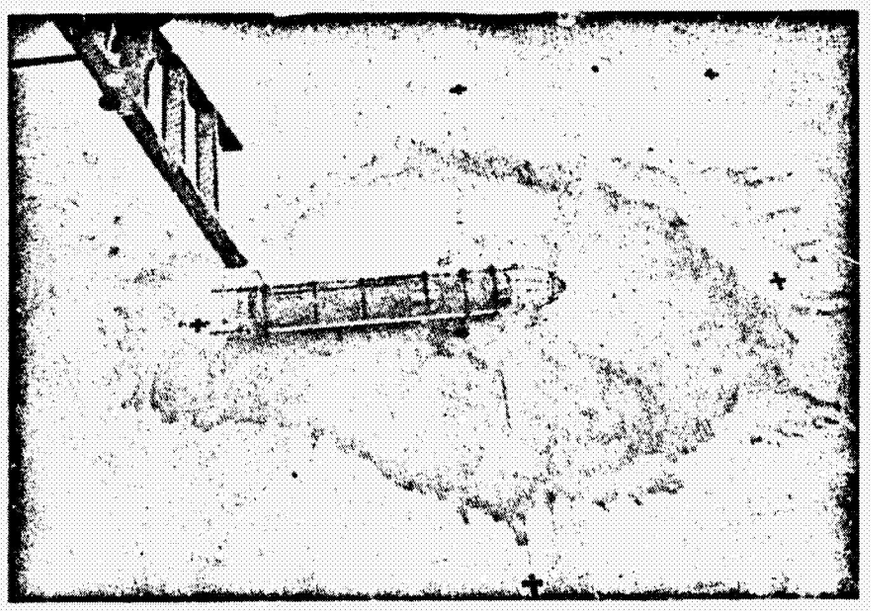

Figure 145 Space Shuttle Booster - Fall Over on Pad

A. Bulkhead Type Failures

Booster

Delta Wing Orbiter

200 Mile Orbiter

B. Toppling on Pad

Booster

Delta Wing Orbiter and 200 Mi Orbiter
Drop Off & Fall Over

Booster Plus Delta Wing Orbiter

Booster Plus 200 Mi Orbiter

c. Crash Landing

Booster

Delta Wing Orbiter

200 Mi Orbiter

Other configurations and a number of different modes of failure could have been used, but the above were chosen as the most probable ones both by our group and an independent study made by the Aero-Space Corporation.

The results of the studies are shown below and the discussion of the analyses, which are essentially the same as those used for the Saturn V, are not repeated.

The crash landing dynamic tests were simulated by hanging the space shuttle models on chains and letting them swing down from different heights to simulate different landing speeds, and letting them

fly into the ground at different angles. A dashpot constructed from a 55 gallon oil drum made it possible to stop the models in distances and times realistic for the modeling of actual crashes and crash landings.

Again, High-speed photography was used in recording the events, and the analysis of the mixing frame by frame produced the results for these different configurations and modes of failure.

Since the actual configuration of the Space Shuttle now has taken on a Solid-Liquid combination, the modeling results discussed here have value mostly in showing how the modeling and analyses procedures can be applied to almost any real system once the configurations are known and the most likely modes of failure selected.

A. Bulkhead Type Failures

These types of failures are probably the most likely ones and are investigated in this section.

Booster

On Pad Failure - He or RP Tank Explosion Rupturing Main LO_2 and LH_2 Tanks:

The booster model was in vertical or launch position and holes were precut into the tanks and then covered by duct tape.

At time zero the duct tape was ripped of remotely and the simulated liquid propellants were allowed to mix while high speed cameras recorded the processes.

In deciding upon the damage done to the propellant tanks and the hole sizes, it was assumed that the He tank explosion progresses

spherically outward and the intersection of it with the tanks produces holes in the respective tanks allowing the fuel and oxidizer to flow out and mix.

The frame by frame analysis, translated into prototype time as explained and executed earlier, gives the mixing function for the Space Shuttle Booster of this configuration.

Five different failure modes are presented here with their respective results:

1. He Tank Explosion, Small Concentric Holes:

A He tank explosion cuts holes into the LO_2 and the LH_2 tanks one concentrically above the other and both of them 2.6 inches in diameter. It was assumed that the He tank explosion produces a spherical shock wave which cuts the holes into the main propellant tanks.

The LO_2 exiting from the top hole falls into the hole in the LH_2 tank and mixing progresses. Translated into prototype time the mixing function is obtained for this case and this mode of failure. Fig. 146

2. He Tank Explosion, Small Off-Set Holes:

This case is similar to the first discussed above except that the two holes in the main tanks are off-set by one radius.

When the LO_2 stream falls into the hole in the LH_2 tank off center, it allows some of the LH_2 to splash out, giving more room on the ullage space for the LO_2 to enter. More mixing is obtained than was possible in the first case. Again with the same frame by frame analysis the

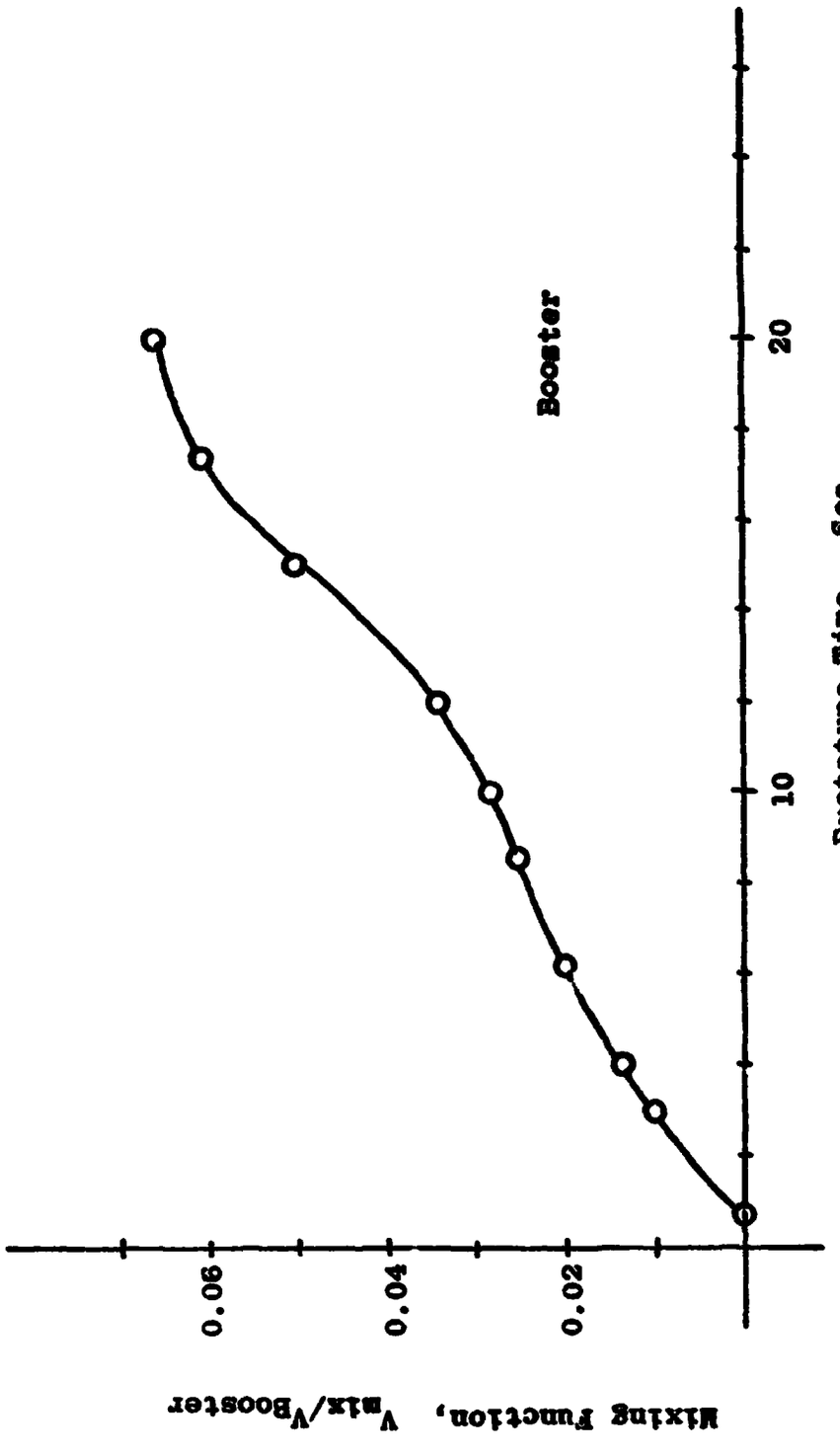

Fig. 146 He Tank Explosion, Small Concentric Holes

mixing function is obtained as presented in Fig. 147

3. He Tank Explosion, Large Holes

Case 3 is similar to case 1 except that it is assumed that the explosion of the He tank is more powerful and produces considerably larger holes in the main propellant tanks than were produced before.

The simulated hole size in this case was 4.5 inches in diameter.

While in the first two cases most of the mixing occurs inside the tanks, in this case a considerable portion of the total mixing occurs external to the tanks where the two liquids from both the LO_2 and LH_2 tanks come together.

The results from this mode of failure and configuration are shown in Fig. 148

4. Kidney Shaped J P Tank Explosion (No Skin)

The next case analyzed was that of the kidney shaped J P tank exploding and again cutting holes into the main propellant tanks of the Booster.

For this particular case it was assumed that the skin of the Booster was damaged or removed allowing the propellants to flow to the ground. The propellants were mixing as the streams were flowing together before they hit the ground and further mixing occurred after impact and puddling on the ground.

Again making the frame by frame analysis and determining the mixing

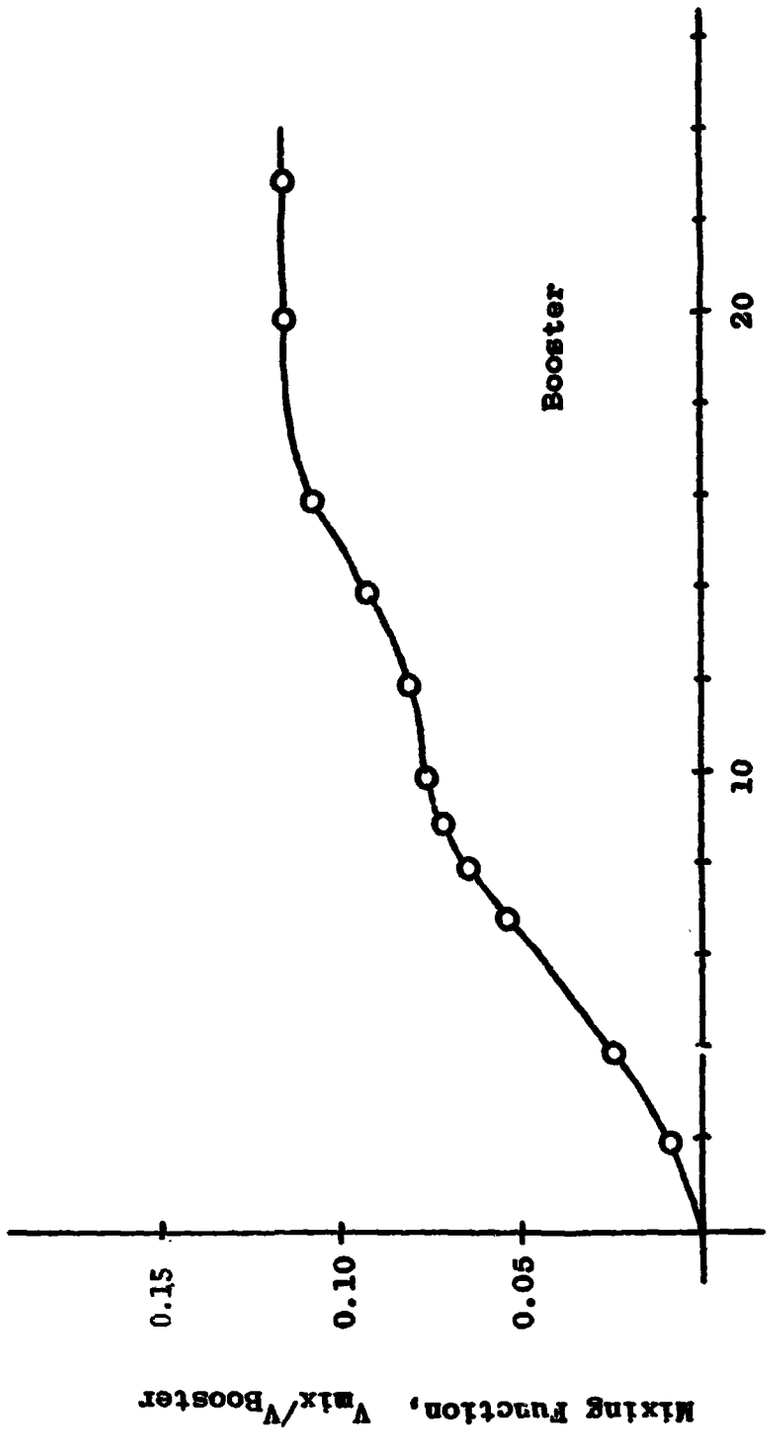

Fig. 147 He Tank Explosion, Small Off-Set Between Holes

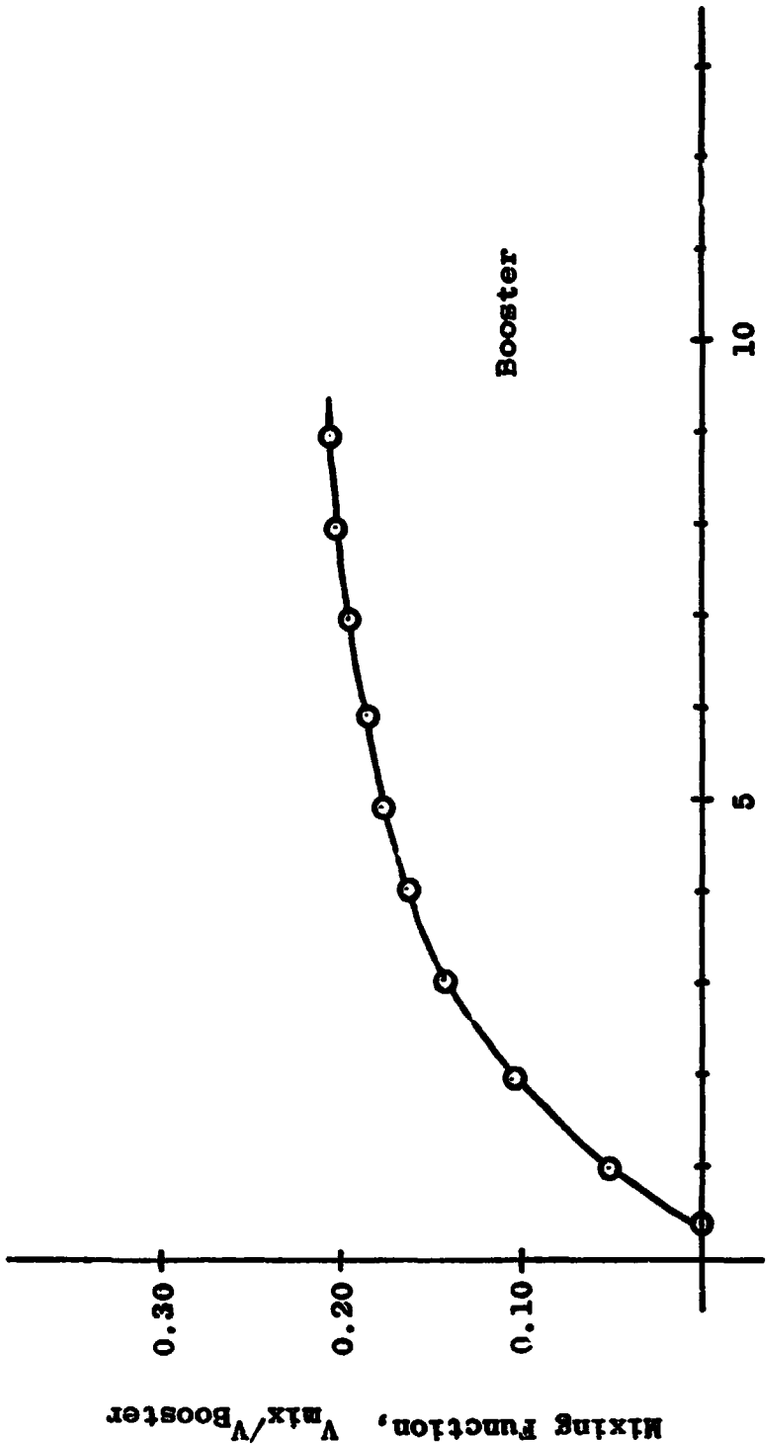

Fig. 148 He Tank Explosion, Large Holes

in the impacting streams and then on the ground, the mixing function for the prototype Space Shuttle Booster is obtained. Fig. 149

5. Kidney Shaped J P Tank Explosion (With Skin)

The last case simulated and discussed here on the Space Shuttle Booster is similar to case 4 except that the assumption was made that the skin of the Booster was left intact by the explosion and the LO_2 and LH_2 are confined by the vehicle.

Due to confinement and less chance for the propellants to spread out and disperse, the mixing produced is considerably higher and the mixing function again for the prototype is shown in Fig. 150

Delta Wing Orbiter

Two cases are taken up here. They are both on-pad failures due to He tank explosions. In the first case the He tank explosion blows holes into the main propellant tanks allowing the fuel and oxidizer to mix. In tne second case the He tank explosion produces a seam failure which opens a much larger hole and therefore the mixing is much greater.

The results from the analysis are again presented after frame by frame analysis and prototype time correlation.

Case 1 Holes produced in the tanks give the results shown in Fig. 151 .

Case 2. A seam failure gives the results shown in Fig. 152

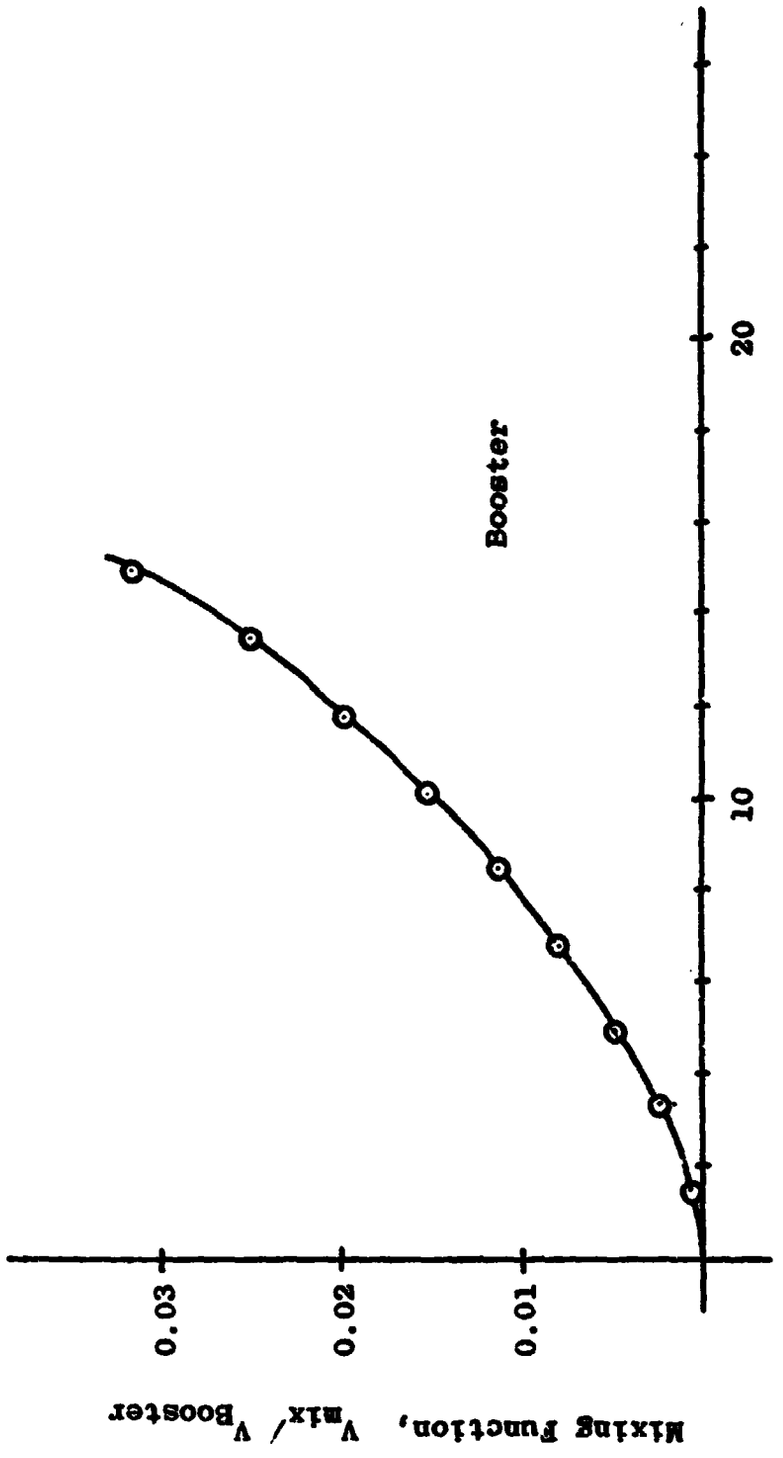

Fig. 149 Kidney Shaped JP Tank Explosion, No Skin

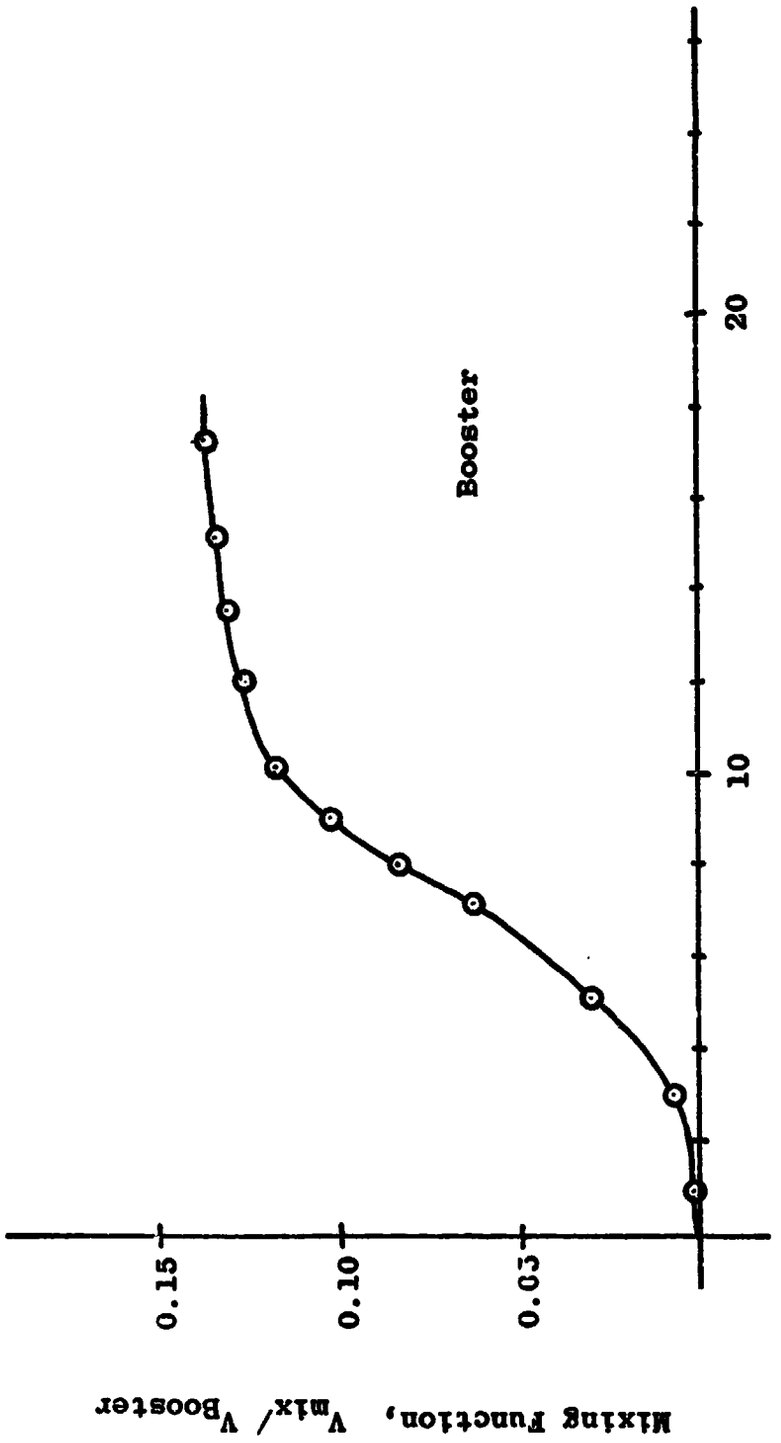

Fig. 150 Kidney Shaped JP Tank Explosion, With Skin

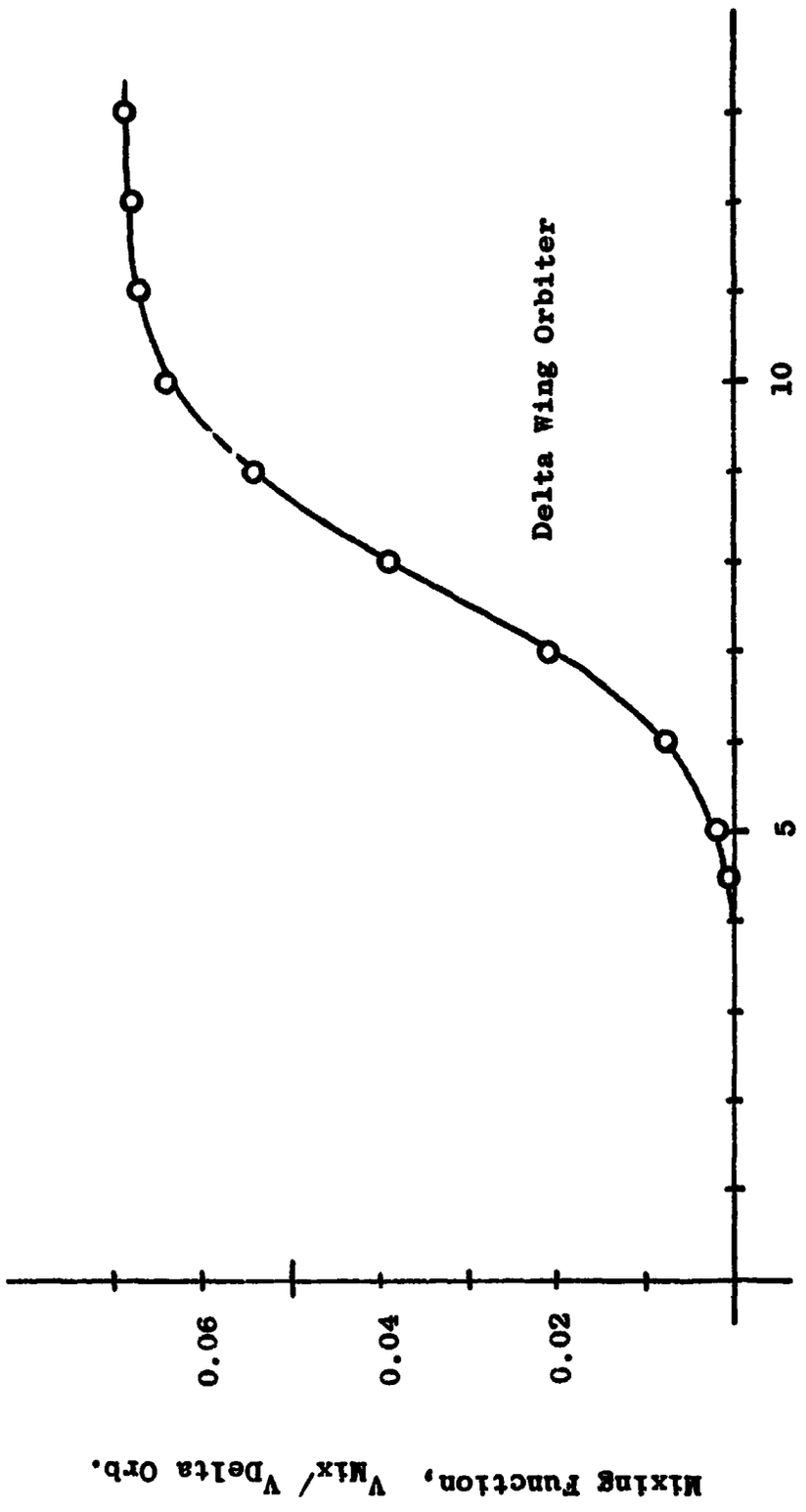

Fig. 151 He Tank Explosion in Delta Wing Orbiter

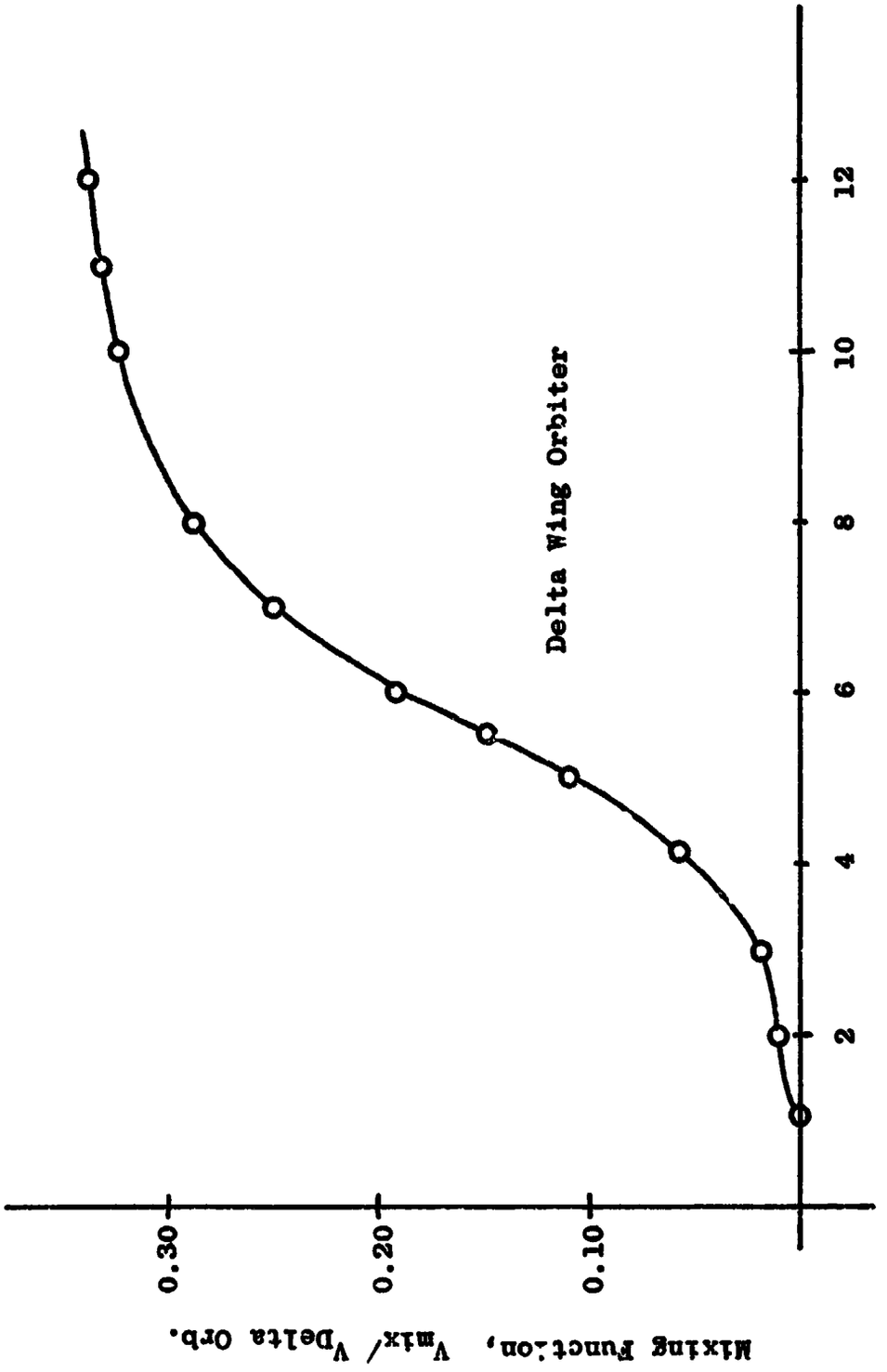

Fig. 152 He Tank Explosion in Delta Wing Orbiter, Seam Failure

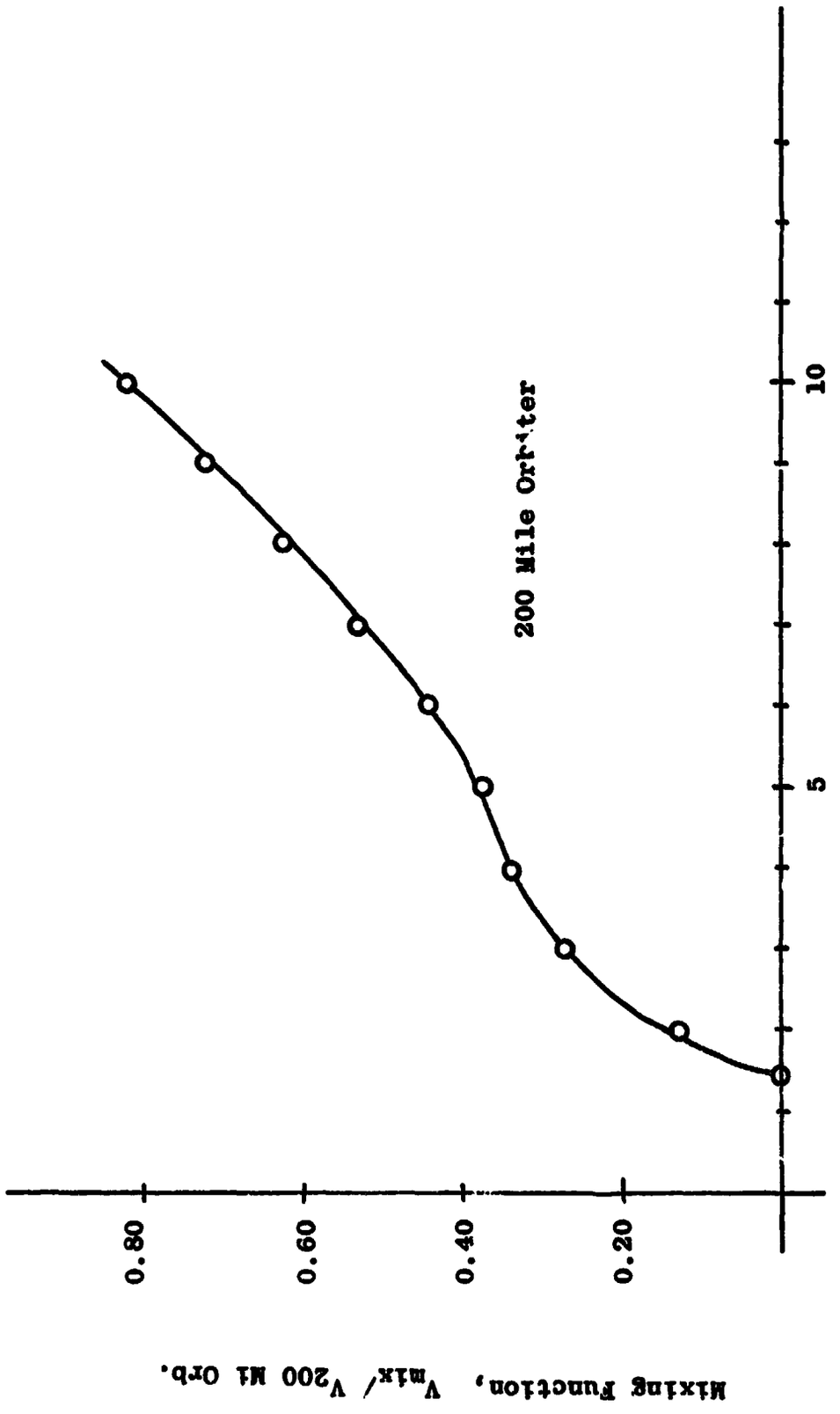

Fig. 153 ...e Tank Explosion in 200 Mile Orbiter

200 Mile Orbiter

The case analyzed for the 200 mile orbiter is a He tank explosion which opens holes in both the LO_2 and the LH_2 tanks with subsequent mixing.

Again this failure occurs on the pad with the orbiter in vertical position.

With the mixing occurring both inside and external to the tanks, rather high values are obtained at the end of the mixing process. Naturally, as was pointed out earlier, the "critical mass" will be reached quickly, not letting the mixing process progress very far, resulting in a low explosive yield. The mixing function, however, since not terminated in the modeling, can proceed undisturbed right to the end.

The results from this analysis are shown in Fig. 153.

B. Toppling on the Pad

In this section cases are taken on which may occur if the booster or the orbiter or the combined Space Shuttle configuration should topple over on the pad.

Again, these modes of failure have been considered among the more likely ones and for this reason they have been modeled.

Booster

The toppling of the booster alone has been divided into two cases, one where, due to the toppling, the seams fail in the tank and the tanks split open, and two where the bulkheads fail or the ends of the tanks come open.

1. Seam Failure

In this simulation the booster was allowed to tip over when at the same time the seams were opened by rip tape procedure. All this was done on a crosshatched platform so that the high speed records of the phenomena could be analyzed accurately and carefully.

The results from this series of experiments are shown in Fig. 154

2. Tank Bulkhead End Failure

The second case was essentially the same as the first but with different damage resulting to the tanks, namely the heads were allowed to come off the tanks.

This failure allowed the liquids to splash forward and a certain amount of mixing occurred. Fig. 155 gives the results from the detailed film analysis.

Delta Wing Orbiter

The Delta Wing Orbiter in this series of experiments was allowed to topple over and at the same time the seams were split open simulated by rip-tapes.

The resulting splash patterns as recorded by high speed photography were analyzed and resulted in the mixing function presented in Fig. 156

200 Mile Orbiter

The experiments carried out with the 200 mile orbiter were identical to those of the delta wing orbiter, but due to the different internal configuration of the tankage, the mixing patterns and the

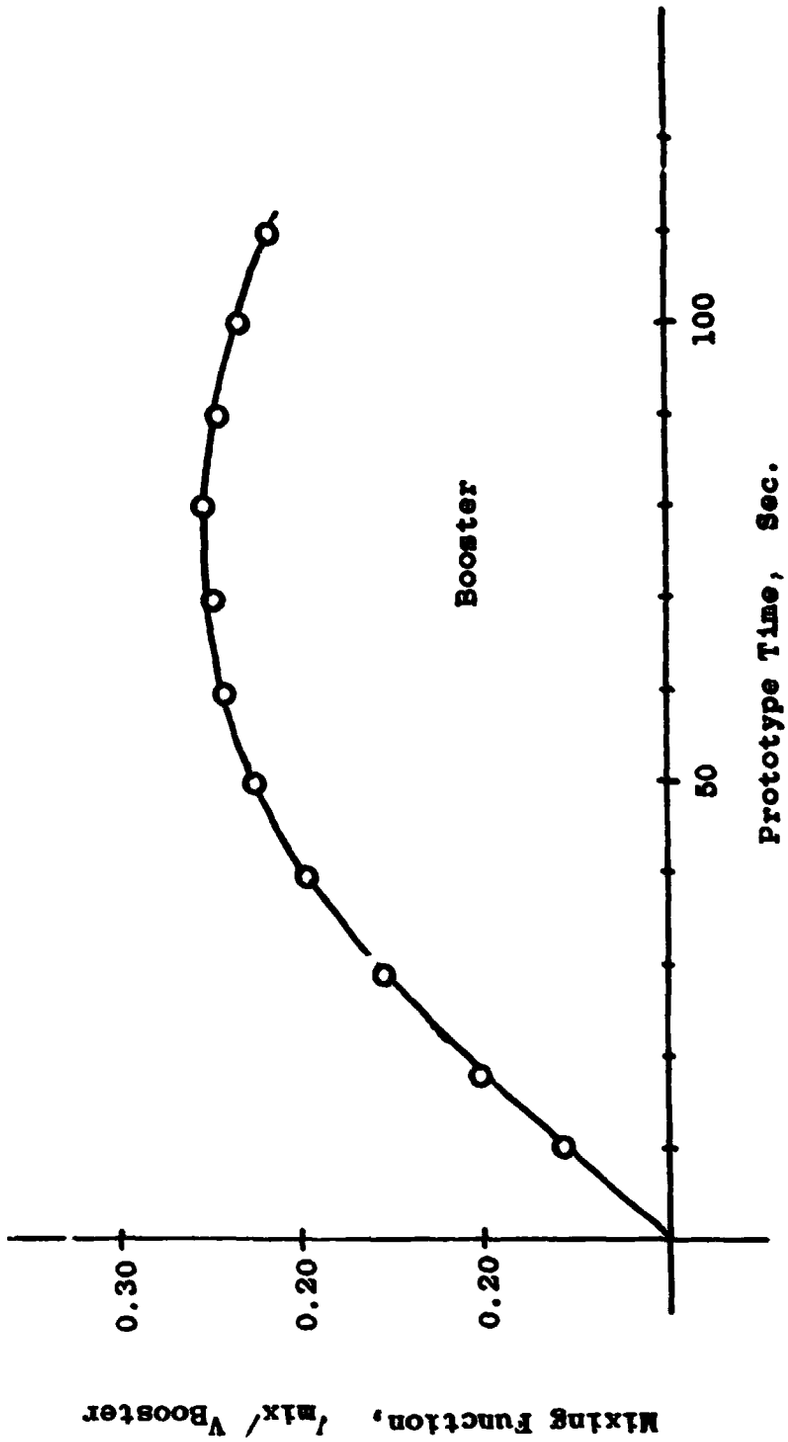

Fig. 154 Toppling on Pad, Seam Failure

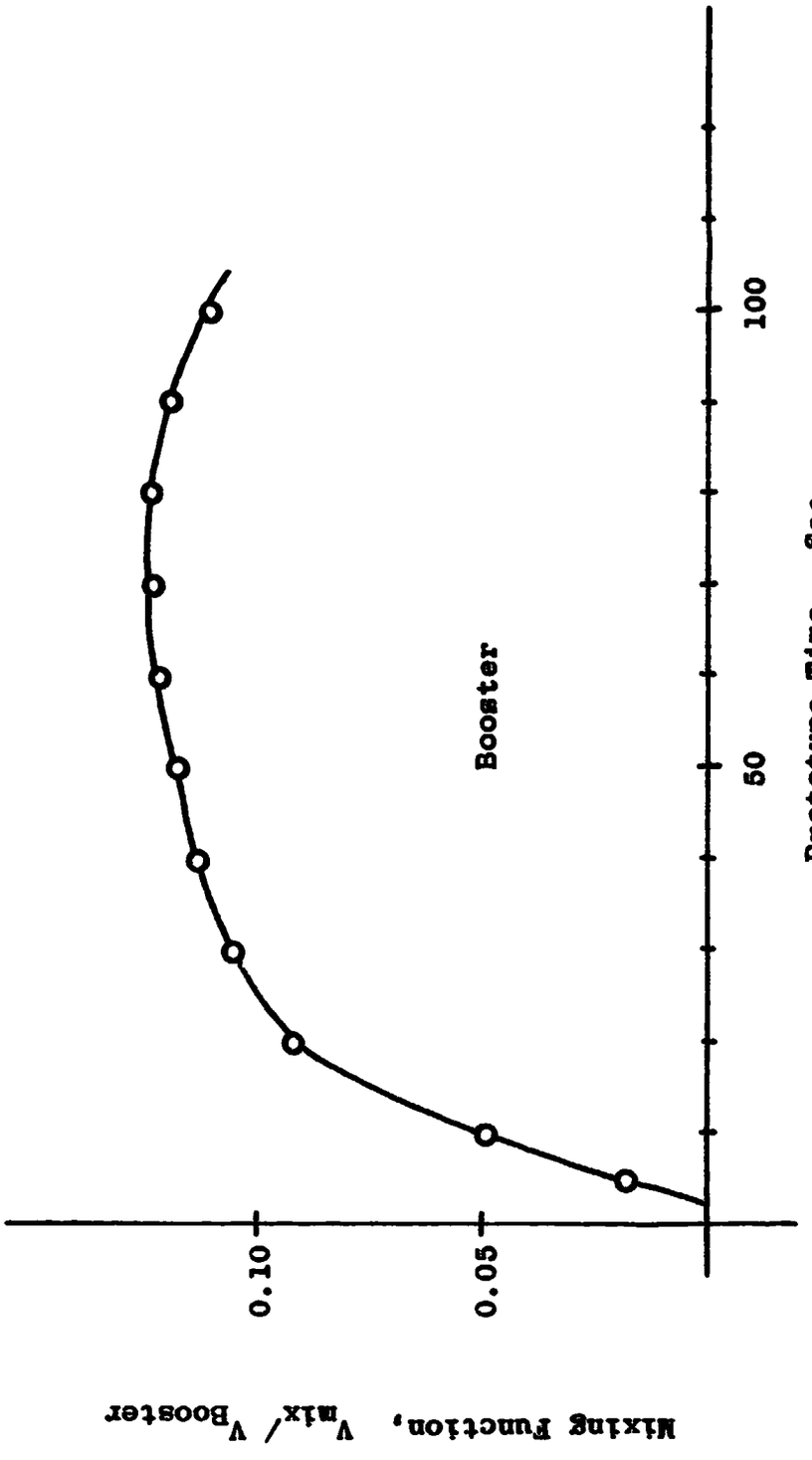

Fig. 155 Booster Toppling Over on Pad, Bulkhead End Failure

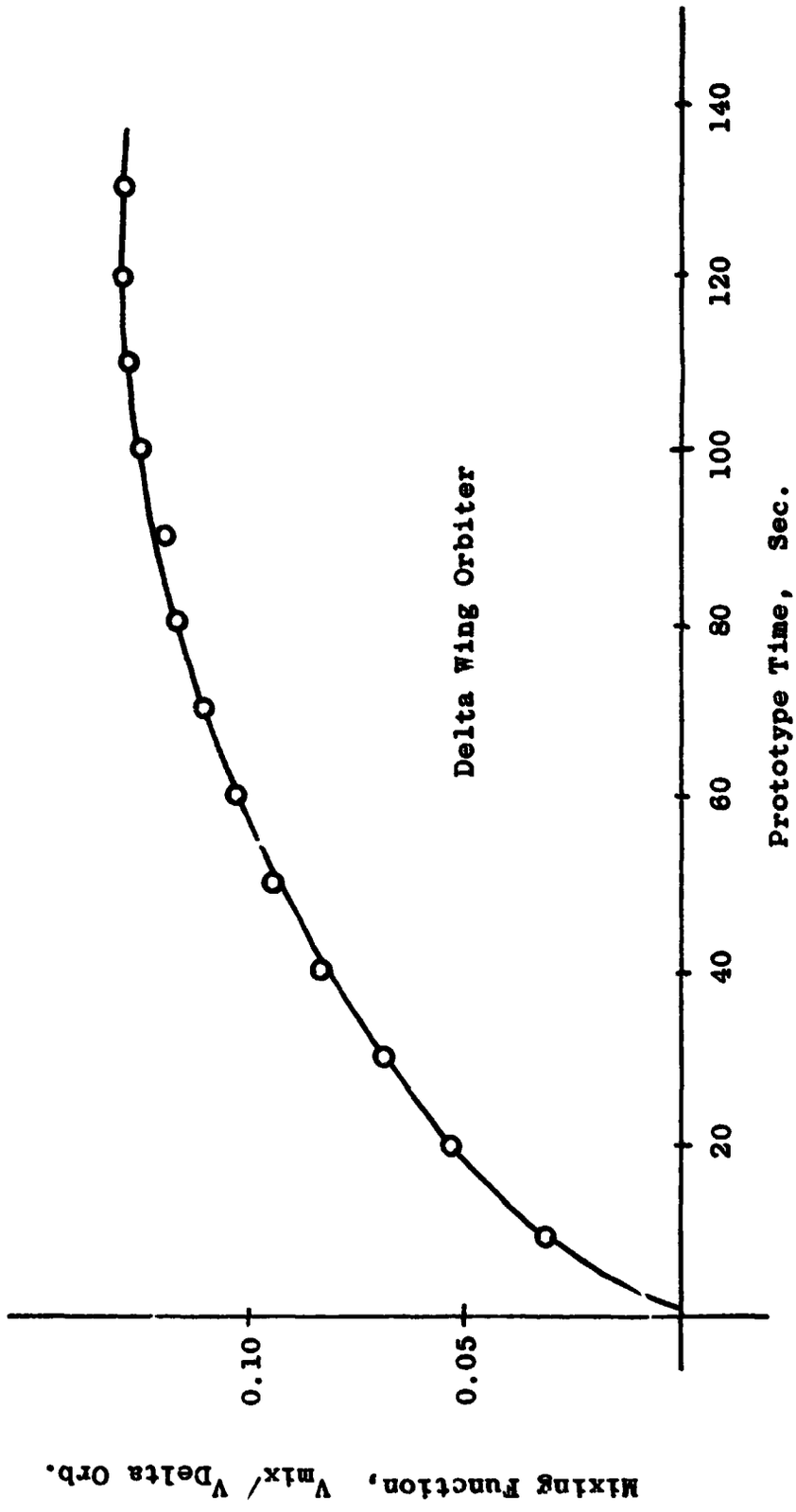

Fig. 156 Delta Wing Orbiter Toppling Over on Pad, Seam Failure

resulting mixing function looked different. Fig. 157.

Booster and Delta Wing Orbiter

In these series of experiments the combination of the booster and the delta wing orbiter were allowed to topple over on the pad and while they fell the tanks were opened with rip-tapes simulating the failure of the tankage. The booster and orbiter separated upon impact, leaving an ever increasing splash and mixing area which was faithfully recorded by high speed photography and later analyzed frame by frame to obtain the mixing function. Fig. 158.

Booster and 200 Mile Orbiter

These experiments were carried out very much like the ones for the booster and delta wing orbiter and the results were obtained in exactly the same manner.

Again the mixing function is obtained which represents the results of this mode of failure and this combined configuration. Fig. 159.

C. Crash Landing

In this, the last, series of experiments on Space Shuttle Configurations under consideration at the time, the experiments carried our included dynamic systems. Investigated were primarily the crash landings of the booster, and each of the orbiters, separately.

To simulate these conditions, a physical system was set up to allow the booster or orbiters to be suspended by thin chains. In this

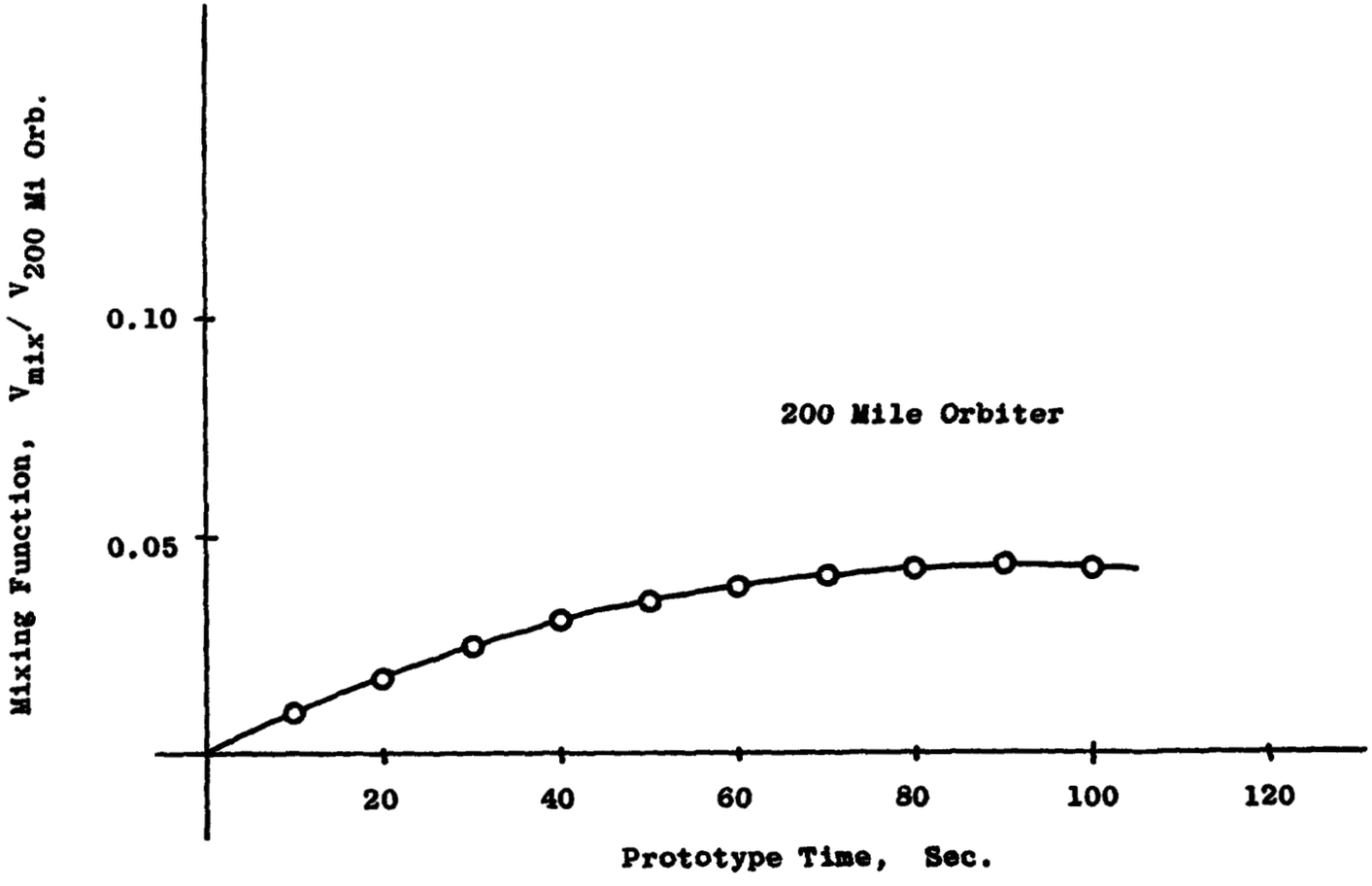

Fig. 157 200 Mile Orbiter Toppling Over on Pad

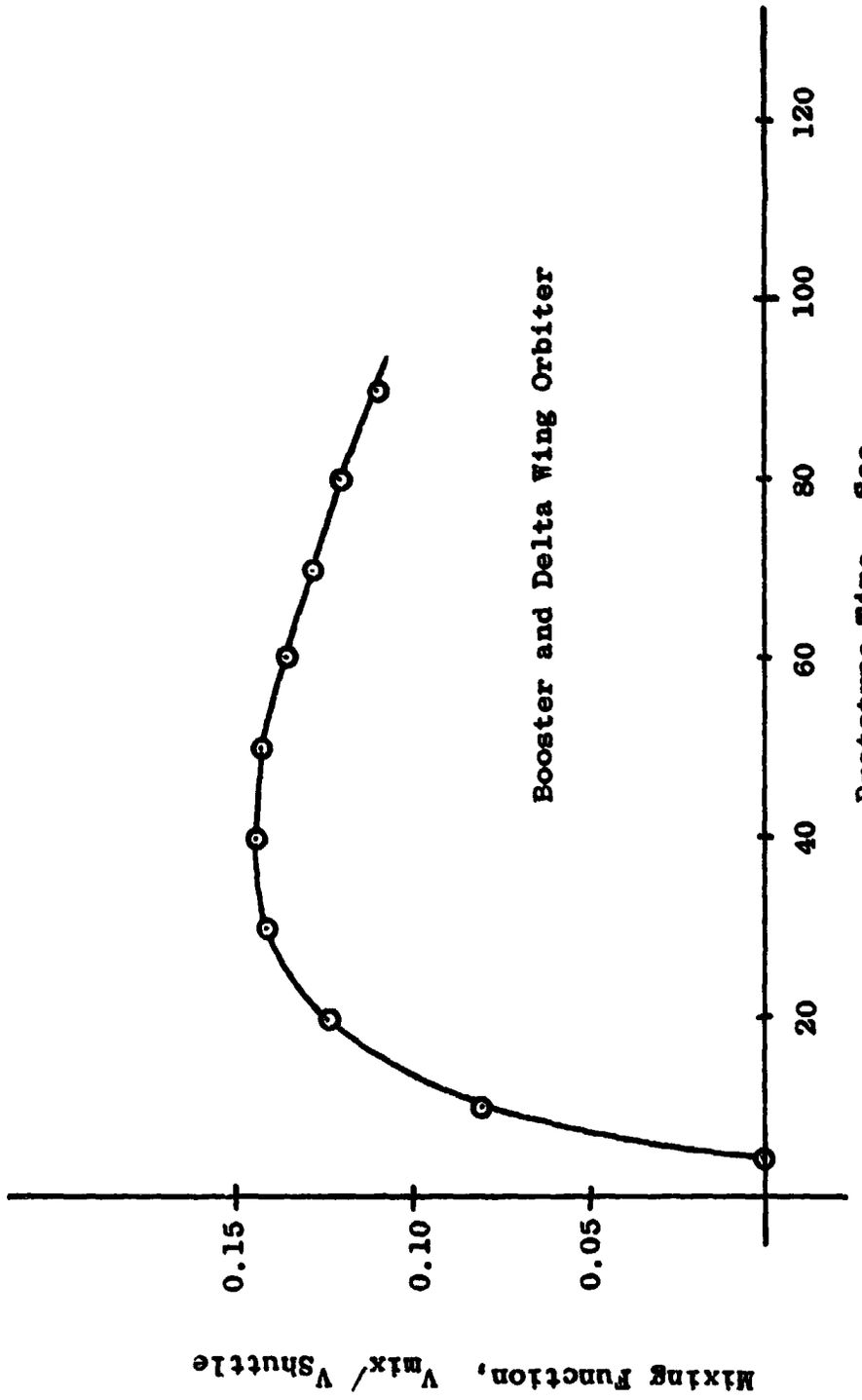

Fig. 158 Booster and Delta Wing Orbiter Toppling Over on Pad

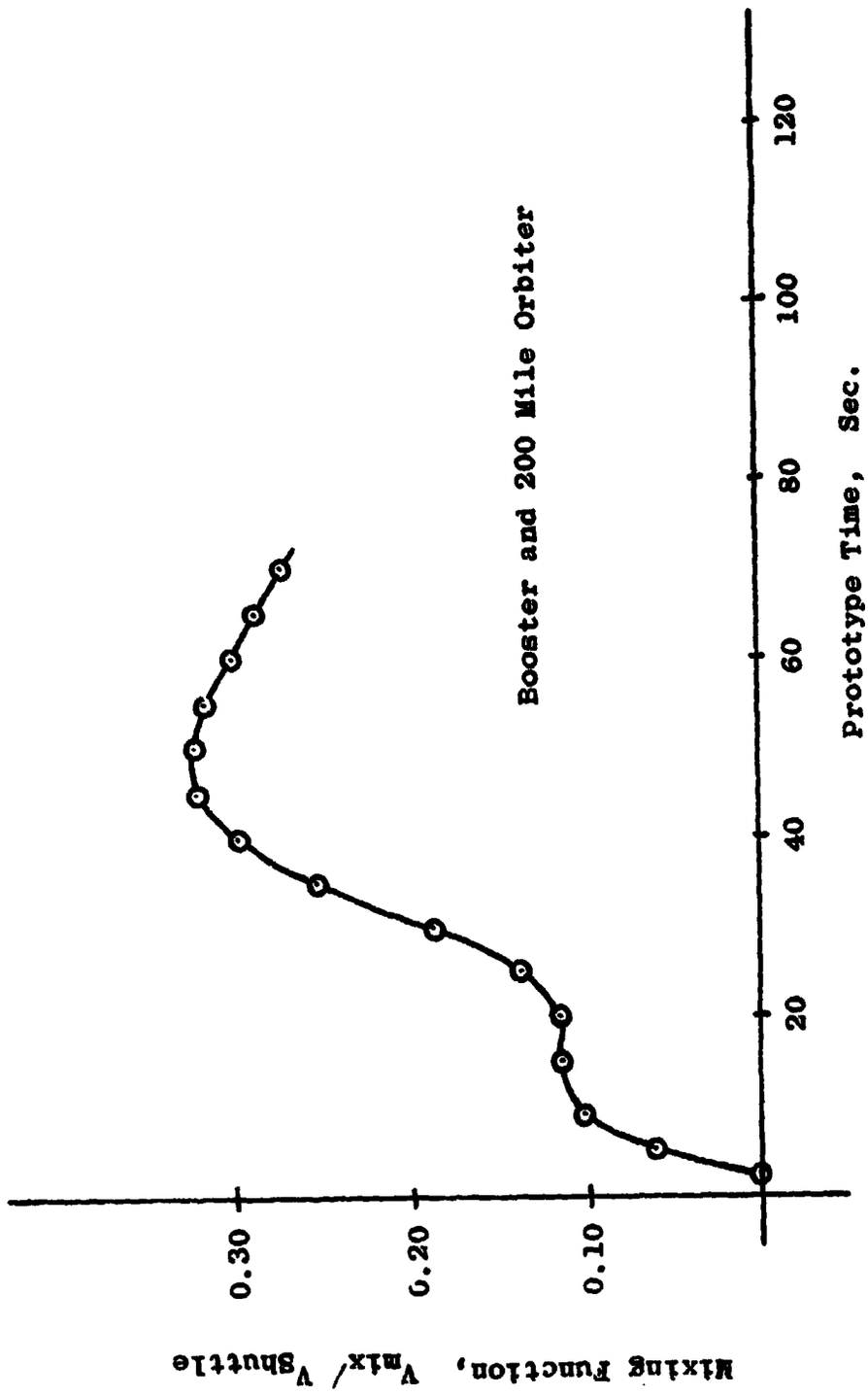

Fig. 159 Booster and 200 Mile Orbiter Toppling Over on Pad

manner the models could swing from various heights simulating different landing velocities and could allow, by varying the length of the chains, different landing or crash angles.

To prevent bouncing of the models and to stop them, simulating the actual cases, a large dashpot made from a 55 gallon drum was attached to the models. This stopped them at different and predetermined rates of deceleration. Rip-tapes were also attached to the models and they were automatically removed as the model simulated the crash landing.

Again, the complete procedures and series of events were documented on high-speed films which were later used for analysis and the determination of the mixing functions.

More trials were needed for this procedure, until the right velocity simulation and dash-pot deceleration values were obtained. After this method was perfected the results obtained were reproducible.

Booster

The booster model with rip-tapes and the braking or dash pot system attached was filled with the simulated propellants. Then the model was allowed to swing down from a predetermined height and to impact at a shallow angle upon the landing surface.

As it landed, the rip tapes were pulled, opening the tankage, and the braking system stopped the forward motion rather sharply.

The resulting splash patterns were recorded with high-speed photography and then analyzed frame by frame by tracing and then planimetering the various areas, (total, splash, and mixing).

From the analysis the following results are obtained. Fig. 160

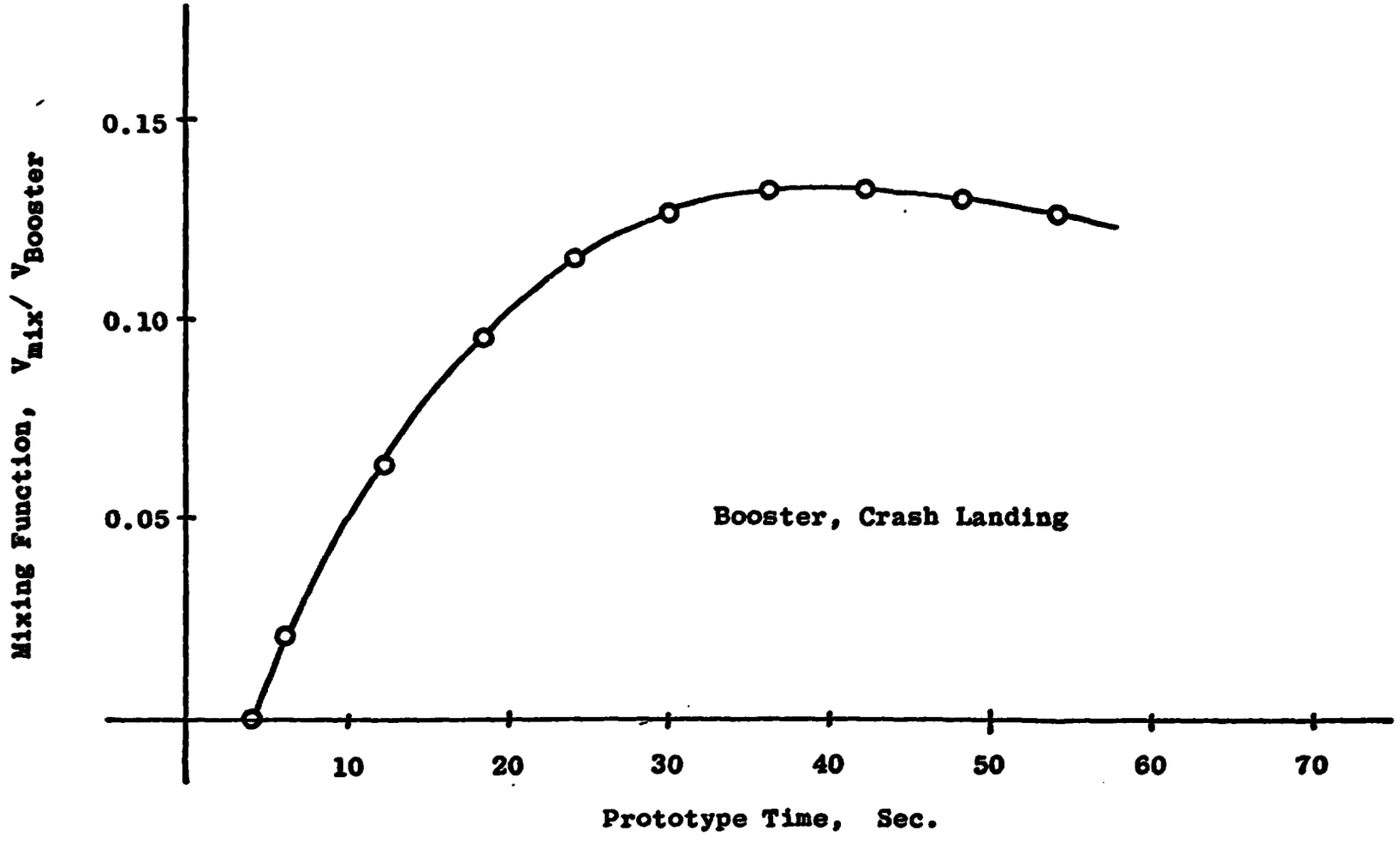

Fig. 160 Crash Landing of Space Shuttle Booster

Delta Wing Orbiter

The crash landing simulation was repeated for the delta wing orbiter, and except for the configuration and the braking system and rip-tape attachment, the experiments were carried out the same as for the booster.

The analysis of the high-speed photographic records again allowed the determination of the mixing function for this type of experimental simulation.

The results are shown in Fig. 161.

200 Mile Orbiter

The last in the series of experiments of the early Space Shuttle Configurations was the crash landings of the 200 mile orbiter.

The experiments were carried out in the same manner as those with the booster and the delta wing orbiter. The 200 mile orbiter after being filled with simulated fuel and oxidizer was allowed to swing down and crash land on the simulated landing platform. The resulting splash patterns, again recorded with high-speed photography, were then analyzed giving the results reported in Fig. 162.

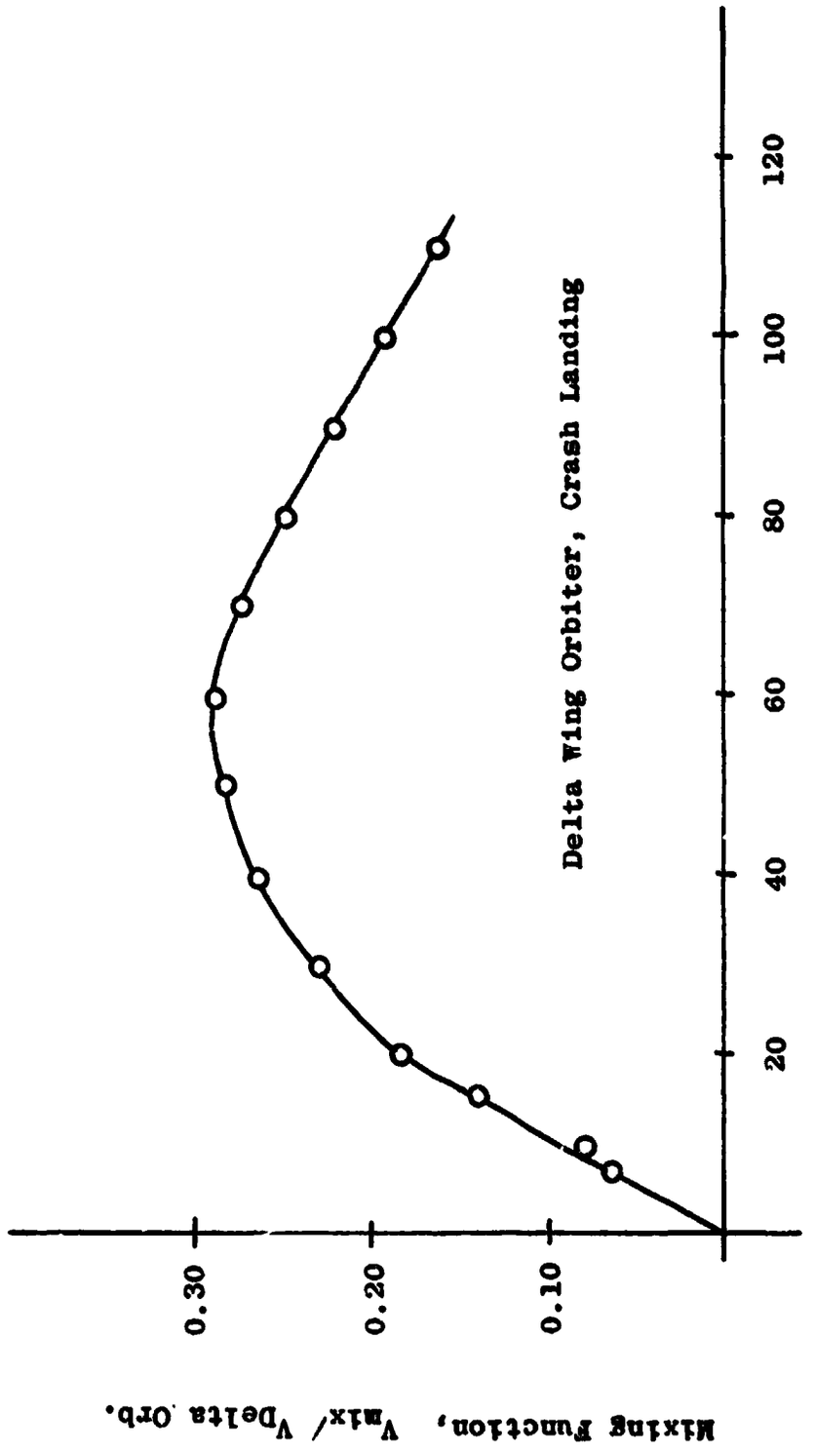

Fig. 161 Crash Landing of Space Shuttle Delta Wing Orbiter

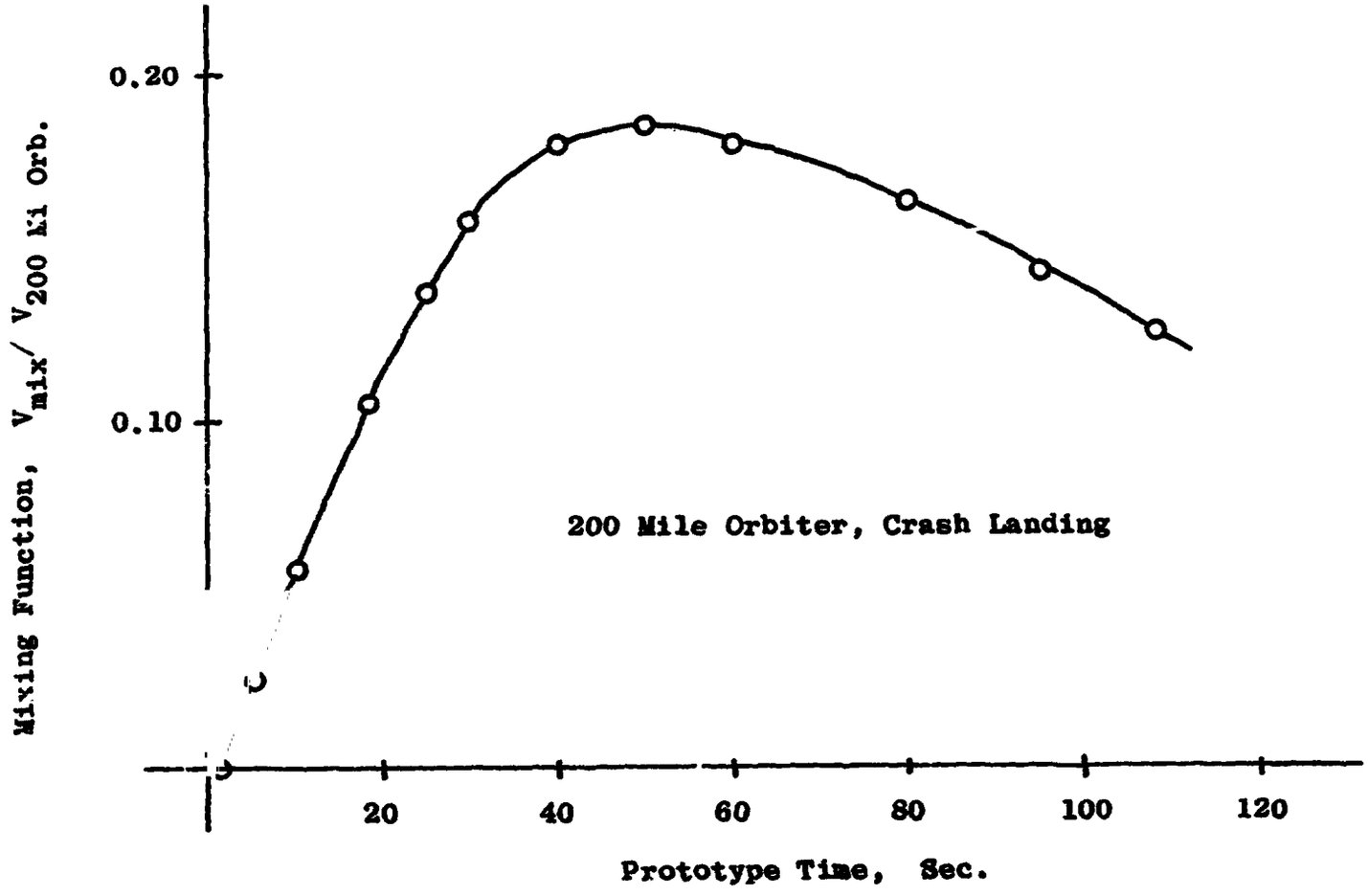

Fig. 162 Crash Landing of the Space Shuttle 200 Mi Orbiter

Final Closure

The foregoing discussions and presentation of results cover a large amount of both theoretical and experimental work.

A number of new concepts are presented, and verified experimentally, to give several new approaches for the evaluation of liquid rocket propellant phenomena, and to allow their analyses with regard to mixing characteristics, basic behavior and explosive yield predictions.

For the first time, data were taken inside exploding missiles, measuring mixing characteristics, location of ignition points, shock front and reaction front behavior and velocities, etc.

Three methods for determining explosive yield were developed and verified in the laboratory and field and then used for analyses and prediction. They are the

1. Mathematical Model
2. Seven Chart Approach
3. Critical Mass Analysis

These methods, although quite different in approach and independent from each other, give the same results when used for analysis of a particular problem.

It is believed that this work as presented here is a valuable contribution to Space Technology, and Liquid Fuel Technology in general, and a significant step in making Space travel and Industrial processes safer.

BIBLIOGRAPHY

1. Farber, E. A., et al. "Feasibility Study to Explore the Explosive Effects of Liquid Propellants to Define the Mathematical Behavior of Physical Processes Involved," Final Report, Phase I, Contract No. NAS10-1255, University of Florida, February, 1965.

2. Farber, E. A., "A Mathematical Model for Defining Explosive Yield and Mixing Probabilities of Liquid Propellants," Third Space Congress Proceedings, March 1966 (Preceding paper).

3. "Thermocouple Grid Analysis of Two 25,000-lb LOX/RP Liquid Propellant Explosion Experiments," E. A. Farber, Technical Paper No. 396, Florida Engineering and Industrial Experiment Station, Vol. XXI, No. 11, November, 1967.

4. "Explosive Yield Estimates for Liquid Propellant Rockets Based Upon a Mathematical Model," E. A. Farber, Technical Paper No. 415A, Florida Engineering and Industrial Experiment Station, Vol. XXII, No. 7, July, 1968.

5. "Interpretation of Explosive Yield Values Obtained from Liquid Rocket Propellant Explosions," E. A. Farber, Technical Paper No. 415B, Florida Engineering and Industrial Experiment Station, Vol. XXII, No. 7, July, 1968.

6. Arthur D. Little, Inc. "Summary Report on a Study of the Blast Effect of a Saturn Vehicle," February, 1962.

7. Wilks, S. S., Mathematical Statistics, John Wiley & Sons, Inc., New York, 1962.

8. Serret, "Cours de Calcul Differential et Integral," Paris, 1907.

9. Gradshteyn and Ryshik, Tablitsy Integralov, Moscow, 1963.

10. Wald, A., Annals of Mathematical Statistics, 11, 1940.

11. "Handbook of Mathematical Functions with Formulas, Graphs, and Mathematical Tables," U. S. Department of Commerce, NBS Applied Mathematics Series -55, 1964.

12. Jahnke, Emde, Lösch, "Tables of Higher Functions," McGraw-Hill Book Company, Inc., New York, 1960.

13. "Preliminary Final Report of Project PYRO." Received incomplete copy April 17, 1968.

14. Information obtained from Lou Ullian, AFETR through informal correspondence and relayed by J H. Deese.

Bibliography (Continued)

15. E. A. Farber and R. L. San Martin, "Studies and Analyses of the Mixing Phenomena of Liquid Propellants Leading to a Yield-Time Function Relationship," Proceedings of the New York Academy of Sciences Explosives Symposium, November, 1966.

16. Farber, E. A., et al., "Fireball Hypothesis Describing the Reaction Front and Shock Wave Behavior in Liquid Propellant Explosions," New York Academy of Sciences, Explosives Symposium Proceedings, 1967. Available as Technical Paper 387, Florida Engineering and Industrial Experiment Station.

17. Welch, J. E., et al., "The MAC Method," Los Alamos Scientific Laboratory LA-3425, New Mexico, March, 1966.

18. Eichel, F. G., "Electrostatics," Chemical Engineering, March 13, 1967.

19. Van Dolah, R. W. and Burgess, D. S., "Explosion Problems in the Chemical Industry," American Chemical Society, 1968.

20. Van Nice, L. J., et al., "Thermal Radiation from Saturn Fireballs," Volume I, Analysis, TRW Systems, December, 1965.

21. Van Nice, L. J., et al., "Thermal Radiation from Saturn Fireballs," Volume II, Appendices F, G, and H, TRW Systems. December, 1965.

22. Project PYRO, "Monthly and Quarterly Progress Reports," 1963 to present.

23. Huff, V. N., et al., "General Method and Thermodynamic Tables for Computation of Equilibrium Composition and Temperature of Chemical Reaction," NACA TR 1037, U. S. Govt. Printing Office, Washington, D. C., 1951.

24. Houston Research Institute, Inc., "Blast and Fireball Comparison of Cryogenic and Hypergolic Propellants," Contract NAS-93506, August, 1964.

25. Smith, M. L., et al., "Fuels and Combustion," McGraw-Hill Book Company, New York 1952.

26. Goodman, H. J., "Compiled Free-Air Blast Data on Bare Spherical Pentolite," BRL Report No. 1092, Aberdeen Proving Ground, MD. February 1960.

27. Shaffer, A., Rouseau, J., "THermodynamical Properties of 24.4K Equilibrium Hydrogen," Airesearch Manufacturing Company, Los Angeles, California, October 1961.

Bibliography (Continued)

28. Deese, J. H., "A Correlation and Hypothesis of LH_2/LO_2/RP-1 Blast Data," Unpublished, January 1963.

29. Stewart, R. B., Timmerhaus, K. D., "Thermodynamic Properties of Cryogenic Fluids," NBS, Boulder, Colorado, 1963.

30. Linde Corp., "Physical Property Equivalents of Some Cryogenic Fluids," 1963.

31. Facilities Engineering and Construction Division, KSC, "Study of Degree of Risk to Launch Area Due to Spilling, Mixing, and Ignition of Cryogenic Propellants," Unpublished, January 1964.

32. Gayle, J. B., "Investigation of S-IV All Systems Vehicle Explosion," MSC, Huntsville, Alabama, NASA TM X-53039, April 27, 1964.

33. Aerojet-General Corp., "Blast and Fireball Comparison of Cryogenic and Hypergolic Propellants," Contract NAS9-2055, June 26, 1964.

34. Foust, A. S., and others, "Principles of Unit Operations," John Wiley & Sons, Inc., New York, New York, 1960.

35. Information obtained from J. H. Deese through informal corresponde e.

36. Edwards, J. W. Integral Calculus, MacMillan Company, London, 1896.

37. Mechanical Engineers' Handbook, edited by T. Baumeister, McGraw-Hill Book Company, Inc., 6th Edition, New York, 1958.

38. Obert, E. F., Internal Combustion Engines, International Textbook Company, Second Edition, Pennsylvania, 1960.

39. Seader, J. D., et al., "Boiling Heat Transfer for Cryogenics," Final Report, Rocketdyne R-5598, May 11, 1964.

40. ASHRAE Guide and Data Book 1961, American Society of Heating, Refrigeration and Air-Conditioning Engineers, Inc., 1961.

41. Handbook of Engineering Fundamentals, edited by O. W. Eshbach, John Wiley and Sons, Inc., Second Edition, New York, 1958.

42. Handbook of Chemistry and Physics, edited by C. D. Hodgman, Chemical Rubber Publishing Company, Forty-First Edition, Ohio, 1960.

43. Chemical Engineers' Handbook, edited by J. H. Perry, McGRaw-Hill Book Company, Inc., Third Edition, New York, 1958.

Bibliography (Continued)

44. Technical Data on Fuel, edited by H. M. Spiers, The British National Committee World Power Conference, Fifth Edition, London, 1952.

45. Fuels and Combustion Handbook, edited by A. J. Johnson, McGraw-Hill Book Company, Inc., New York, 1951.

46. Nelson, W. L., Petroleum Refinery Engineering, McGraw-Hill Book Company, Inc., New York, 1936.

47. Farber, E. A. and Deese, J. H., "A Systematic Approach for the Analytical Analysis and Prediction of the Yield from Liquid Propellant Explosions," Proceedings of the Third Space Congress, March, 1966.

48. "Blast and Fireball Comparison of Cryogenic and Hypergolic Propellants," Aerojet General Corp., Contract No. NAS 9-2055, Final Report, June 1964.

49. Farber, E. A. and Richardson, M. R., "The Gamma Ray Densitometer and Concentration Meter," Proceedings of Annual Meeting of Instrument Society of America, April, 1957.

50. Farber, E. A., "200 A Thorium Oxide Slurry Test Loop Density and Concentration Data," Oak Ridge National Laboratory Report, January, 1957.

51. Farber, E. A., "Bubble and Slug Flow in Gas-Liquid and Gas (Vapor) - Liquid-Solid Mixtures," Oak Ridge National Laboratory Report, May 1957.

52. Farber, E. A., "Bubble and Slug Flow in Circulating Gas-Liquid and Gas-Liquid-Solid Mixtures," Oak Ridge National Laboratory Report, February, 1958.

53. ASME and ASCE "Symposium on Water Hammer," Proceedings, 1933.

54. Boering, Burkhardt, "Beitraege zur Theorie der Detonation," Deutsche Luftfahrtforschung, No. 1939, April 1944.

55. Farber, E. A., et al., "Fireball and Post-Fireball Composition and Atmospheric Chemistry of Fuel/Oxygen-Fluorine Propellants," NASA report, Contract NAS10-1255, July 1967.

56. Farber, E. A., et al., "A Bibliography of Authoritative Sources Defining the Physical and Chemical Properties of Fluorine and Its Oxidizing Mixtures and Compounds," Part I, Contract NAS10-1255, University of Florida, April 1965.

57. Farber, E. A., et al., "A Bibliography of Authoritative Sources Defining the Physical and Chemical Properties of Fluorine and Its Oxidizing Mixtures and Compounds," Part II, Confidential, Contract NAS10-1255, University of Florida, April 1966.

Bibliography (Continued)

58. Farber, E. A., et al., "Thermocouple Grid Method Applied to Studying Liquid Mixing," Contract NAS10-1255, University of Florida, March 1966.

59. High, R. W., "The Saturn Fireball," New York Academy of Sciences, Explosives Symposium Proceedings, 1967.

60. Fletcher, R. F., "Characteristics of Liquid Propellant Explosions," New York Academy of Sciences, Explosives Symposium Proceedings, 1967.

61. Information obtained from Lou Ullian, AFETR through informal correspondence and relayed by J. H. Deese.

62. Information obtained from J. H. Deese through informal correspondence.

63. NASA/USAF Liquid Propellant Blast Hazards Program, Project Pyro Monthly Progress Report for Period Ending 31 July 1965, AF Rocket Propulsion Laboratory, Research and Technology Division, Edwards, California.

64. Obert, E. F., Internal Combustion Engines, International Textbook Company, Second Edition, Pennsylavnia, 1960.

65. Seader, J. D., et al., "Boiling Heat Transfer for Cryogenics," Final Report, Rocketdyne R-5598, May 11, 1964.

66. Farber, E. A. and Deese, J. H., "A Systematic Approach for the Analytical Analysis and Prediction of the Yield from Liquid Propellant Explosions," Proceedings of the Third Space Congress, March 1966. (Paper No. II in this series).

67. ASME and ASCE "Symposium on Water Hammer," Proccedings, 1933.

68. Van Nice, L. J., Carpenter, J. H., "Thermal Radiation from Saturn Fireballs," TRW Systems Reports, Vol. I and II, December 1965.

69. Goodman, H. J., "Compiled Free-Air Blast Data on Bare Spherical Pentolite," BRL Report, No. 1092, February 1960.

70. Boering, Burkhardt, "Beitraege zur Theorie der Detonation," Deutsche Luftfahrtforschung, No. 1939, April 1944.

71. Farber, E. A., et al., "A Systematic Approach for the Analytical Analysis and Prediction of the Yield from Liquid Propellant Explosions," Third Space Congress Proceedings, March 1966. Available as Technical Paper No. 347, Florida Engineering and Industrial Experiment Station.

72. Farber, E. A., et al., "Fireball Hypothesis Describing the Reaction Front and Shock Wave Behavior in Liquid Propellant Explosions," New York Academy of Sciences, Explosives Symposium Proceedings, 1967. Available as Technical Paper 387, Florida Engineering and Industrial Experiment Station.

Bibliography (Continued)

73. Farber, E. A., et al., "Fireball and Post-Fireball Composition and Atmospheric Chemistry of Fuel/Oxygen-Fluorine Propellants," NASA Report, Contract NAS10-1255, July 1967.

74. Farber, E. A., "A Mathematical Model for Defining Explosive Yield and Mixing Probabilities of Liquid Propellants," Technical Paper Series No. 346, Florida Engineering and Industrial Experiment Station, Vol. XX, No. 3, March 1966.

75. Farber, E. A., et al., "Prediction of Explosive Yield and Other Characteristics of Liquid Propellant Rocket Explosions," Final Report, Contract No. NAS10-1255, University of Florida, October 31,1968.

76. Farber, E. A., et al., "A Systematic Approach for the Analytical Analysis and Prediction of the Yield from Liquid Propellant Explosions," Annals of the New York Academy of Sciences, Vol. 152, Art. 1, pp. 645-665.

77. Farber, E. A., et al., "Studies and Analyses of the Mixing Phenomena of Liquid Propellants Leading to a Yield-Time Function Relationship," Annals of the New York Academy of Sciences, Vol. 152, Art. 1, pp. 654-684.

78. Paper (77) reprinted as Technical Paper No. 386, Florida Engineering and Industrial Experiment Station, Vol. XXI, No. 8, August 1967.

79. Farber, E. A., "Thermocouple Grid Analysis of Two 25,000 lb LOX/RP Liquid Propellant Explosions Experiments," Technical Paper NO. 396, Florida Engineering and Industrial Experiment Station, Vol. XXI, No. 11, November 1967.

80. Farber, E. A., "Explosive Yield Estimates for Liquid Propellant Rockets Based Upon the Mathematical Model," Technical Paper No. 415A, Florida Engineering and Industrial Experiment Station, Vol. XXII, No. 7, July 1968.

81. Farber, E. A., "Interpretation of Explosive Yield Values Obtained from Liquid Rocket Propellant Explosions," Technical Paper No. 415B, Florida Engineering and Industrial Experiment Station, Vol. XXII, No. 7, July 1968.

82. Farber, E. A., et al., "Fireball and Post-Fireball Composition and Atmospheric Chemistry of Fuel/Oxygen-Fluorine Propellants," NASA report, Contract NAS10-1255, July 1967.

83. Farber, E. A., Klement, F. W. and Bonzon, C. F., "Prediction of Explosive Yield and Other Characteristics of Liquid Propellant Rocket Explosions," University of Florida, Contract No. NAS10-1255, Final Report, October, 1968.

Bibliography (Con inued)

84. "Liquid Propellant Explosive Hazards," Project PYRO, AF RPL, Final Report, December 1968.

85. Klinkerberg, A., and Van der Minne, J. L., Electrostatics in the Petroleum Industry, Elsevier Publishing Co., 1958.

86. Helmholtz, H., "Studien ueber Electrische Grenzschichten," Annalen der Physik und Chemie, Vol. 243, No. 7, pp. 337-382, July 1879.

87. Cooper, W. F., "The Electrification of Fluids in Motion," Static Electrification, a Symposium held by the Institute of Physics in London on March 25, 26, and 27, 1953, British Journal of Applied Physics, Vol. 4, Supplement No. 2, pp. S 11-15, 1953.

88. Elton, G. A. H. and Peace, J. B. M., "Sedimentation Potentials. Part I. The Measurement of Sedimentation Potentials in Some Aqueous and Non-Aqueous Media," Journal of the Chemical Society (London), Vol. 53, No. 1, pp. 22-26, January 1956.

89. Booth, F., "Sedimentation Potential and Velocity of Solid Spherical Particles," The Journal of Chemical Physics, Vol. 22, No. 12, pp. 1956-1968, December 1954.

90. Henry, D. C., "The Cataphoresis of Suspended Particles. Part I. The Equation of Cataphoresis," Proceedings of the Royal Society of London, Series A., Vol. 133, No. 821, pp. 106-129, September 1931.

91. Summer, C. G. and Henry, D. C., "Cataphoresis. Part II. A New Experimental Method and a Confirmation of Smoluchouski's Equation," Proceedings of the Royal Society of London, Series A., Vol. 133, No. 821, pp. 130-140, September 1931.

92. Overbeek, J. T. G.. "Electrokinetic Phenomena," Colloid Science, Vol. I, H. R. Kruyt (ed.), Elsevier Publishing Company, Amsterdam, Chap. V, pp. 194-244, 1952.

93. Rutgers, A. J., De Smet, M. and De Moyer, G. "Influence of Turbulence on Electrokinetic Phenomena; Experimental Determination of the Thickness of the Diffuse Part of the Double Layer," Transactions of the Faraday Society, Vol. 53, Part 3, No. 411, pp. 393-396, March 1957.

94. Rutgers, A. J., De Smet, M. and De Moyer, G. "Influence of Turbulence on Electrokinetic Phenomena; Experimental Determination of the Thickness of the Diffuse Part of the Double Layer," Experentia, Vol. 12, No. 10, p. 371, October 1956.

95. Bocquet, P. E., Sliepcevich, C. M., and Bohr, D. F., "Effect of Turbulence on the Streaming Potential," Industrial and Engineering Chemistry, Vol. 48, No. 2, pp. 197-200, February 1956.

96. Arthur D. Little, Inc., "Electrostatic Hazards Associated with the Transfer and Storage of Liquid Hydrogen," Final Report, Contract No. AF 18(600)-1687, May 1961.

Bibliography (Continued)

97. Farber, E. A. and Gilbert, J. S., "Fireball Hypothesis Describing the Reaction front and Shock Wave Behavior in Liquid Propellant Explosions," Technical Paper No. 387, Florida Engineering and Experiment Station, Vol. XXI, No. 8, August 1967.

98. Air Products, Inc., "Static Charge Generation," Project I, Contract No. AF 18(600)-1771, February 1959.

99. Loeb, L. B., "Static Electrification," Progress in Dialectrics, Vol. 4, Academic Press Inc., pp. 249-309, 1962.

100. Workman, E. J. and Reynolds, S. E., "Freezing Potentials," Physics Review, 78, p. 254, 1950.

101. Welch, J. E., et al., "The MAC Method," Los Alamos Scientific Laboratory Report LA-3425, March 1966.

102. San Martin, R. L., "A Theoretical Investigation and Experimental Verification of the Mixing of Insoluble Liquids," Ph.D. Dissertation, University of Florida, March 1969.

103. Willoughby, A. B., et al., Problems Involved in Assessing the Explosive Hazards of Liquid Bipropellant Systems," Project PYRO, Contract No. AF 04(611)-9558, September 1964.

104. Farber, E. A., "Prediction of Explosive Yield and Other Characteristics of Liquid Propellant Rocket Explosions," Technical Paper NO. 448, Part VIII, Florida Engineering and Industrial Experiment Station, Vol. XXIII, No. 11, November 1969.

105. Eichel, F. G., "Electrostatics," Chemical Engineering March 13, 1967.

106. Yates, G. B. and Perl, A. R., "Spark Ignition Parameters for Cryogenic Hydrogen in Oxygen and Nitrogen Mixtures," Advances in Cryogenic Engineering, Vol. 10, 1967.

107. Bonzon, C. F., "Generation of Static Electricity Caused by the Mixing of Insoluble Fluids," Ph.D. Thesis, University of Florida, December 1970.

108. Ernsberger, F. M., "Mechanism of Frictional Electrification of Dialectric Liquids," Journal of Applied Physics, Vol. 27, No. 4, pp. 418-419, April 1956.

109. Quist, J. D., and Washburn, E. R., "A Study in Electrokinetics," Journal of the American Chemical Society, Vol. 62, No. 11, pp. 3169-3172, November 1940.

Bibliography (Continued)

110. Bemant, A., "Electrical Properties of Hydrocarbons," in A. Farkas, Physical Chemistry of Hydrocarbons, Vol. I, Academic Press, Inc., New York, Chap. VI, pp. 215-240, 1950.

111. Goodwin, D. W. and Macfadyen, K. A., "Electrical Conduction and Breakdown in Liquid Dielectrics," Proceedings of the Physical Society (London) Section B, Vol. 66, No. 2, pp. 85-96, February 1952.

112. Meek, J. M. and Craggs, J. D., Electric Breakdown of Gases, Oxford University Press, London, 1953.

113. Lewis, B. and Von Elbe, G., Combustion, Flames and Explosions of Gases, Academic Press, Inc., New York, 1951.

114. MacKeown, S. S. and Wouk, V., "Electrical Charges Produced by Flowing Gasoline," Industrial and Engineering Chemistry, Vol. 34, No. 6, pp. 659-664, June 1942.

115. Loeb, L. B., Static Electrification, Springer-Verlag, Berlin, 1958.

116. Farber, E. A., "Critical Mass (Hypothesis and Verification) of Liquid Rocket Propellants," Report No. IX contract no. NAS10-1255, University of FLorida, September 14, 1971.

117. Deese, J. H., "Test Conductors Damage Assessment Report on Auto-Ignition LO_2/LH_2 Mixing Test Experimental Explosions of March 2, 1972, Vols. 1 and 2. Systems Engineering Division, Design Engineering Director, J. F. K. Space Center NASA, March 23, 1972.

118. Farber, E. A., et al., "Electrostatic Charge Generation and Auto-Ignition Results of Liquid Rocket Propellants Experiments," NASA Report, Contract NAS10-1255, October 1972.

119. Project PYRO Final Reports, December 1968, "Liquid Propellant Explosive Hazards," Vols. 1, 2, and 3. AFRPL-TR-68-92; URS 652-35. Prepared under contract AF04(611)10739 for Air Force Rocket Propulsion Lab. Air Force Systems Command USAF Edwards, California.

120. Letter from H. K. Weidner (Marshall Space Flight Center) to G. M. Preston (Kennedy Space Center), November 22, 1968.

121. "Ordinance Systems Saturn V Launch Vehicle," George C. Marshall Space Flight Center, Huntsville, Alabama. Final Report Contract No. SE005-003-2H.

122. Farber, E. A. and San Martin, R. L., "Part III. Studies and Analysis of the Mixing Phenomena of Liquid Propellants Leading to a Yield-Time Function Relationship." Available as Technical Paper 386, Florida Engineering and Industrial Experiment Station.

Bibliography (Continued)

123. Farber, E. A. and Gilbert, J. S., "Part IV. Fireball Hypothesis Describing the Reaction Front and Shock Wave Behavior in Liquid Propellant Explosive." Available as Technical Paper 387, Florida Engineering and Industrial Experiment Station.

124. Farber, E. A., "Part VIII. Prediction of Explosive Yield and Other Characteristics of Liquid Propellant Rocket Explosions." Available as Technical Paper 448, Florida Engineering and Industrial Experiment Station.

125. Proceedings Eleventh Explosive Safety Seminar, Armed Forces Explosive Safety Board, Washington, D.S., September 1969.

126. Generation of Static Electricity Caused by the Mixing of Insoluble Fluids," C. F. Bonzon, Ph.D. Dissertation, December 1969, University of Florida.

127. "Statistical Analysis of Project PYRO Liquid Propellant Explosion Data," P. Gunter, G. R. Anderson, Bell Comm, Inc., July 1969.

Appendix

Computer Programs for the Solution of Equations (156) and (172)

EQUATION (2.6) WITH SIDE FORCES


```
/JOB (114818,3,6),E. STEWART
C DESTRUCT SPILL PATTERN (CIRCULAR HYDRAULIC JUMP)
C R0,Y0,F0 = RADIUS,DEPTH,FROUDE NO AT BEGINNING OF JUMP
C R1,Y1,F1 = RADIUS,DEPTH,FROUDE NO AT END OF JUMP
C R ,Y ,F  = RADIUS,DEPTH,FROUDE NO DOWNSTREAM OF JUMP
C RR1=R/R1,RR0=R1/R0,DR0=Y1/Y0,DR1=Y/Y1
      DIMENSION F0(10),RR0(15),RR1(10)
      READ(5,10)(F0(J),J=1,10)
      READ(5,11)(RR0(J),J=1,15)
      READ(5,10)(RR1(J),J=1,10)
      DO 6 I=1,10
      WRITE(6,12)
      WRITE(6,13)
      WRITE(6,14)
      WRITE(6,15)
      FN=6.*F0(I)**2
      DO 6 J=1,15
      A2=-(RR0(J)-1.)/(2.*RR0(J)+1.)
      A1=-(RR0(J)+FN+2.)/(2.*RR0(J)+1.)
      A0=FN/(RR0(J)*(2.*RR0(J)+1.))
      X1=F0(I)
    1 X=X1
      EQN=X**3+A2*X**2+A1*X+A0
      DERIV=3.*X**2+2.*A2*X+A1
      Z=EQN
      D=DERIV
      X1=X-(Z/D)
      IF(ABS(X-X1)-0.0005)2,2,1
    2 ROOT1=X1
      B=A2+ROOT1
      AC=-A0/ROOT1
      D=B**2-4.*AC
      IF(D)4,3,3
    3 ROOT2=(-B+D**0.5)/2.
      ROOT3=(-B-D**0.5)/2.
      GO TO 5
    4 ROOT2=0.
      ROOT3=0.
      WRITE(6,16)F0(I),RR0(J),ROOT1,ROOT2,ROOT3
      GO TO 6
    5 WRITE(6,17)F0(I),RR0(J),ROOT1,ROOT2,ROOT3
    6 CONTINUE
      DO 112 J=1,10
      F1=1.05
      WRITE(6,18)
      WRITE(6,19)
      WRITE(6,14)
      WRITE(6,20)
      DO 112 I=1,20
      F1=F1-0.05
      FN=6.*F1**2
      A2=-(RR1(J)-1.)/(2.*RR1(J)+1.)
      A1=-(RR1(J)+FN+2.)/(2.*RR1(J)+1.)
      A0=FN/(RR1(J)*(2.*RR1(J)+1.))
      X1=F1
    7 X=X1
      EQN=X**3+A2*X**2+A1*X+A0
      DERIV=3.*X**2+2.*A2*X+A1
```

```
      X1=X-(7/D)
      IF(ABS(X-X1)-0.0005) 8,8,7
    8 ROOT1=X1
      B=A2+ROOT1
      AC=-A0/ROOT1
      D=B**2-4.*AC
      IF(D)110,9,9
    9 ROOT2=(-B+D**0.5)/2.
      ROOT3=(-B-D**0.5)/2.
      GO TO 111
  110 ROOT2=C.
      ROOT3=0.
      WRITE(6,21)   F1,RR1(J),ROOT1,ROOT2,ROOT3
      GO TO 112
  111 WRITE(6,22)   F1,RR1(J),ROOT1,ROOT2,ROOT3
  112 CONTINUE
   10 FORMAT(10F6.1)
   11 FORMAT(15F5.2)
   12 FORM/ (///,10X,23HCIRCULAR HYDRAULIC JUMP )
   13 FORMAT(/,6X,41HFROUDE  RADIUS          DEPTH RATIO (Y1/Y0) )
   14 FORMAT(6X,36HNUMBER  RATIO              THREE ROOTS )
   15 FORMAT(7X,45H(F0)   (R1/R0)     ROOT 1     ROOT 2     ROOT 3 )
   17 FORMAT(5X,F6.1,3X,F5.2,4X,F9.4,1X,F9.4,1X,F9.4)
   16 FORMAT(5X,F6.1,3X,F5.2,4X,F9.4,9HIMIGINARYI2,9HIMAGINARYI2)
   18 FORMAT(///,12X,28HDOWNSTREAM OF HYDRAULIC JUMP )
   19 FORMAT(/,6X,40HFROUDE  RADIUS          DEPTH RATIO (Y/Y1)  )
   20 FORMAT(7X,45H(F1)    (R/R1)     ROOT 1     ROOT 2     ROOT 3  )
   21 FORMAT(5X,F6.2,3X,F6.1,4X,F7.4,1X,9HIMAGINARYI2,9HIMAGINARYI2)
   22 FORMAT(5X,F6.2,3X,F6.1,4X,F7.4,1X,F9.4,1X,F9.4)
      STOP
      END
```

CIRCULAR HYDRAULIC JUMP

FROUDE NUMBER (FO)	RADIUS RATIO (R1/RO)	DEPTH RATIO (Y1/YO) THREE ROOTS ROOT 1	ROOT 2	ROOT 3
200.0	1.00	282.3430	0.9999	-283.3428
200.0	1.05	277.7756	0.9523	-278.7114
200.0	1.10	273.4229	0.9089	-274.3005
200.0	1.15	269.2686	0.8695	-270.0923
200.0	1.20	265.2979	0.8333	-266.0723
200.0	1.25	261.4980	0.7999	-262.2263
200.0	1.30	257.8569	0.7692	-258.5425
200.0	1.35	254.3637	0.7407	-255.0098
200.0	1.40	251.0089	0.7143	-251.6179
200.0	1.45	247.7835	0.6896	-248.3577
200.0	1.50	244.6794	0.6666	-245.2209
200.0	2.00	218.9406	0.5000	-219.2405
200.0	2.50	199.9267	0.4000	-200.0767
200.0	3.00	185.1421	0.3333	-185.1897
200.0	4.00	163.3431	0.2500	-163.2595

CIRCULAR HYDRAULIC JUMP

FROUDE NUMBER (FO)	RADIUS RATIO (R1/RO)	DEPTH RATIO (Y1/YO) THREE ROOTS ROOT 1	ROOT 2	ROOT 3
100.0	1.00	140.9222	1.0000	-141.9221
100.0	1.05	138.6547	0.9524	-139.5908
100.0	1.10	136.4930	0.9091	-137.3708
100.0	1.15	134.4295	0.8695	-135.2535
100.0	1.20	132.4566	0.8333	-133.2311
100.0	1.25	130.5683	0.8000	-131.2958
100.0	1.30	128.7585	0.7692	-129.4442
100.0	1.35	127.0219	0.7407	-127.6680
100.0	1.40	125.3539	0.7142	-125.9628
100.0	1.45	123.7499	0.6896	-124.3241
100.0	1.50	122.2061	0.6666	-122.7477
100.0	2.00	109.3976	0.5000	-109.6976
100.0	2.50	99.9285	0.4000	-100.0784
100.0	3.00	92.5620	0.3333	-92.6095
100.0	4.00	81.6955	0.2500	-81.6122

CIRCULAR HYDRAULIC JUMP

FROUDE NUMBER (FO)	RADIUS RATIO (R1/RO)	DEPTH RATIO (Y1/YO) THREE ROOTS ROOT 1	ROOT 2	ROOT 3
50.0	1.00	70.2124	1.0000	-71.2124
50.0	1.05	69.0949	0.9523	-70.0311
50.0	1.10	68.0290	0.9090	-68.9069
50.0	1.15	67.0109	0.8695	-67.8350
50.0	1.20	66.0372	0.8333	-66.8117

50.0	1.25	65.1048	0.7999	-65.8332
50.0	1.30	64.2107	0.7691	-64.8965
50.0	1.35	63.3526	0.7406	-63.9986
50.0	1.40	62.5.80	0.7142	-63.1369
50.0	1.45	61.7349	0.6896	-62.3091
50.0	1.50	60.9712	0.6666	-61.5128
50.0	2.00	54.6284	0.4999	-54.9283
50.0	2.50	49.9320	0.3999	-50.0819
50.0	3.00	46.2748	0.3332	-46.3223
50.0	4.00	40.8750	0.2499	-40.7915

CIRCULAR HYDRAULIC JUMP

FROUDE NUMBER (FO)	RADIUS RATIO (R1/RO)	DEPTH RATIO (Y1/YO) THREE ROOTS ROOT 1	ROOT 2	ROOT 3
25.0	1.00	34.8589	1.0000	-35.8589
25.0	1.05	34.3168	0.9523	-35.2530
25.0	1.10	33.7991	0.9090	-34.6769
25.0	1.15	33.3041	0.8694	-34.1280
25.0	1.20	32.8301	0.8331	-33.6044
25.0	1.25	32.3758	0.7997	-33.1041
25.0	1.30	31.9399	0.7689	-32.6255
25.0	1.35	31.5211	0.7404	-32.1670
25.0	1.40	31.1185	0.7139	-31.7272
25.0	1.45	30.7309	0.6893	-31.3048
25.0	1.50	30.3576	0.6663	-30.8988
25.0	2.00	27.2486	0.4996	-27.5482
25.0	2.50	24.9391	0.3996	-25.0887
25.0	3.00	23.1370	0.3329	-23.1842
25.0	4.00	20.4712	0.2496	-20.3874

CIRCULAR HYDRAULIC JUMP

FROUDE NUMBER (FO)	RADIUS RATIO (R1/RO)	DEPTH RATIO (Y1/YO) THREE ROOTS ROOT 1	ROOT 2	ROOT 3
20.0	1.00	27.7887	1.0000	-28.7887
20.0	1.05	27.3619	0.9523	-28.2980
20.0	1.10	26.9539	0.9089	-27.8316
20.0	1.15	26.5636	0.8693	-27.3875
20.0	1.20	26.1898	0.8330	-26.9639
20.0	1.25	25.8312	0.7996	-26.5593
20.0	1.30	25.4870	0.7688	-26.17..
20.0	1.35	25.1562	0.7402	-25.8018
20.0	1.40	24.8380	0.7138	-25.4465
20.0	1.45	24.5316	0.6891	-25.1053
20.0	1.50	24.2363	0.6661	-24.7774
20.0	2.00	21.7746	0.4993	-22.0739
20.0	2.50	19.9427	0.3993	-20.0920
20.0	3.00	18.5118	0.3326	-18.5587
20.0	4.00	16.3930	0.2494	-16.3090

CIRCULAR HYDRAULIC JUMP

FROUDE NUMBER (FO)	RADIUS RATIO (R1/RO)	DEPTH RATIO (Y1/YO) THREE ROOTS ROOT 1	ROOT 2	ROOT 3
15.0	1.00	20.7191	1.0000	-21.7191
15.0	1.05	20.4077	0.9522	-21.3437
15.0	1.10	20.1097	0.9087	-20.9872
15.0	1.15	19.8243	0.8690	-20.6479
15.0	1.20	19.5506	0.8327	-20.3245
15.0	1.25	19.2879	0.7993	-20.0157
15.0	1.30	19.0355	0.7684	-19.7205
15.0	1.35	18.7927	0.7399	-19.4380
15.0	1.40	18.5590	0.7134	-19.1671
15.0	1.45	18.3339	0.6887	-18.9072
15.0	1.50	18.1168	0.6656	-18.6575
15.0	2.00	16.3027	0.4988	-16.6015
15.0	2.50	14.9488	0.3988	-15.0975
15.0	3.00	13.8893	0.3321	-13.9357
15.0	4.00	12.3178	0.2489	-12.2333

CIRCULAR HYDRAULIC JUMP

FROUDE NUMBER (FO)	RADIUS RATIO (R1/RO)	DEPTH RATIO (Y1/YO) THREE ROOTS ROOT 1	ROOT 2	ROOT 3
10.0	1.00	13.6510	1.0000	-14.6510
10.0	1.05	13.4555	0.9519	-14.3913
10.0	1.10	13.2679	0.9083	-14.1449
10.0	1.15	13.0877	0.8684	-13.9106
10.0	1.20	12.9145	0.8319	-13.6875
10.0	1.25	12.7479	0.7984	-13.4749
10.0	1.30	12.5876	0.7674	-13.2717
10.0	1.35	12.4331	0.7388	-13.0773
10.0	1.40	12.2842	0.7122	-12.8911
10.0	1.45	12.1405	0.6875	-12.7125
10.0	1.50	12.0018	0.6644	-12.5412
10.0	2.00	10.8365	0.4973	-11.1338
10.0	2.50	9.9612	0.3973	-10.1084
10.0	3.00	9.2735	0.3306	-9.3184
10.0	4.00	8.2500	0.2474	-8.1641

CIRCULAR HYDRAULIC JUMP

FROUDE NUMBER (FO)	RADIUS RATIO (R1/RO)	DEPTH RATIO (Y1/YO) THREE ROOTS ROOT 1	ROOT 2	ROOT 3
7.0	1.00	9.4121	1.0000	-10.4121
7.0	1.05	9.2869	0.9514	-10.2222
7.0	1.10	9.1661	0.9074	-10.0423
7.0	1.15	9.0497	0.8672	-9.8714
7.0	1.20	8.9373	0.8304	-9.7089
7.0	1.25	8.8288	0.7967	-9.5540
7.0	1.30	8.7241	0.7655	-9.4063
7.0	1.35	8.6229	0.7367	-9.2653
7.0	1.40	8.5251	0.7100	-9.1299
7.0	1.45	8.4306	0.6852	-9.0004

7.0	1.50	8.3392	0.6620	-8.8761
7.0	2.00	7.5648	0.4945	-8.8593
7.0	2.50	6.9775	0.3944	-7.1219
7.0	3.00	6.5135	0.3279	-6.5557
7.0	4.00	5.8198	0.2448	-5.7313

CIRCULAR HYDRAULIC JUMP

FROUDE NUMBER (FO)	RADIUS RATIO (R1/R0)	DEPTH RATIO (Y1/Y0) THREE ROOTS ROOT 1	ROOT 2	ROOT 3
4.0	1.00	5.1709	1.0000	-6.1789
4.0	1.05	5.1265	0.9494	-6.0598
4.0	1.10	5.0748	0.9037	-5.9472
4.0	1.15	5.0238	0.8621	-5.8405
4.0	1.20	4.9738	0.8243	-5.7392
4.0	1.25	4.9248	0.7896	-5.6429
4.0	1.30	4.8768	0.7577	-5.5512
4.0	1.35	4.8300	0.7283	-5.4637
4.0	1.40	4.7843	0.7010	-5.3801
4.0	1.45	4.7398	0.6758	-5.3001
4.0	1.50	4.6963	0.6522	-5.2235
4.0	2.00	4.3174	0.4833	-4.6007
4.0	2.50	4.0203	0.3833	-4.1536
4.0	3.00	3.7816	0.3170	-3.8129
4.0	4.00	3.4196	0.2348	-3.3210

CIRCULAR HYDRAULIC JUMP

FROUDE NUMBER (FO)	RADIUS RATIO (R1/R0)	DEPTH RATIO (Y1/Y0) THREE ROOTS ROOT 1	ROOT 2	ROOT 3
2.0	1.00	2.3723	1.0000	-3.3723
2.0	1.05	2.3805	0.9379	-3.3023
2.0	1.10	2.3839	0.8837	-3.2364
2.0	1.15	2.3838	0.8358	-3.1742
2.0	1.20	2.3811	0.7930	-3.1153
2.0	1.25	2.3763	0.7545	-3.0594
2.0	1.30	2.3700	0.7197	-3.0064
2.0	1.35	2.3625	0.6880	-2.9560
2.0	1.40	2.3541	0.6590	-2.9079
2.0	1.45	2.3450	0.6323	-2.8620
2.0	1.50	2.3354	0.6078	-2.8182
2.0	2.00	2.2292	0.4366	-2.4658
2.0	2.50	2.1285	0.3390	-2.2175
2.0	3.00	2.0411	0.2757	-2.0311
2.0	4.00	1.9018	0.1984	-1.7668

DOWNSTREAM OF HYDRAULIC JUMP (WITH SIDE FORCES)

FROUDE NUMBER (F1)	RADIUS RATIO (R/R1)	DEPTH RATIO (Y/Y1) THREE ROOTS ROOT 1	ROOT 2	ROOT 3

0.55	1.1	-1.8529	1.1814	0.7028
0.90	1.1	0.6707	1.1503	-1.7897
0.85	1.1	0.6347	1.1236	-1.7270
0.80	1.1	0.5951	1.1011	-1.6649
0.75	1.1	0.5525	1.0823	-1.6035
0.70	1.1	0.5075	1.0667	-1.5429
0.65	1.1	0.4607	1.0538	-1.4833
0.60	1.1	0.4129	1.0431	-1.4248
0.55	1.1	0.3645	1.0343	-1.3676
0.50	1.1	0.3163	1.0270	-1.3120
0.45	1.1	0.2687	1.0209	-1.2583
0.40	1.1	0.2224	1.0159	-1.2071
0.35	1.1	0.1781	1.0118	-1.1586
0.30	1.1	0.1366	1.0084	-1.1137
0.25	1.1	0.0987	1.0057	-1.0732
0.20	1.1	0.0655	1.0036	-1.0378
0.15	1.1	0.0379	1.0020	-1.0087
0.10	1.1	0.0173	1.0009	-0.9859
0.05	1.1	0.0044	1.0002	-0.9733

DOWNSTREAM OF HYDRAULIC JUMP

FROUDE NUMBER (F1)	RADIUS RATIO (R/R1)	DEPTH RATIO (Y/Y1) THREE ROOTS ROOT 1	ROOT 2	ROOT 3
1.00	1.5	1.3403	0.4484	-1.6638
0.95	1.5	1.3036	0.4303	-1.6089
0.90	1.5	1.2690	0.4106	-1.5546
0.85	1.5	-1.5008	1.2365	0.3893
0.80	1.5	-1.4478	1.2063	0.3664
0.75	1.5	-1.3955	1.1784	0.3420
0.70	1.5	1.1529	0.3162	-1.3441
0.65	1.5	0.2891	1.1296	-1.2937
0.60	1.5	0.2610	1.1085	-1.2445
0.55	1.5	0.2320	1.0897	-1.1956
0.50	1.5	0.2025	1.0729	-1.1504
0.45	1.5	0.1730	1.0581	-1.1061
0.40	1.5	0.1438	1.0453	-1.0641
0.35	1.5	0.1156	1.0342	-1.0248
0.30	1.5	0.0888	1.0248	-0.9887
0.25	1.5	0.0643	1.0171	-0.9553
0.20	1.5	0.0426	1.0108	-0.9285
0.15	1.5	0.0247	1.0061	-0.9057
0.10	1.5	0.0112	1.0027	-0.8889
0.05	1.5	0.0028	1.0007	-0.8785

DOWNSTREAM OF HYDRAULIC JUMP

FROUDE NUMBER (F1)	RADIUS RATIO (R/R1)	DEPTH RATIO (Y/Y1) THREE ROOTS ROOT 1	ROOT 2	ROOT 3
1.00	3.0	1.3153	0.1796	-1.2092
0.95	3.0	1.2865	0.1711	-1.1718
0.90	3.0	1.2587	0.1620	-1.1350
[illegible]	3.0	1.2321	0.1525	-1.0988
[illegible]	[illegible]	[illegible]	[illegible]	[illegible]

7.0	1.50	8.1392	0.6620	-8.6701
7.0	2.00	7.5648	0.4945	-7.8593
7.0	2.50	6.9775	0.3944	-7.1219
7.0	3.00	6.5135	0.3279	-6.5557
7.0	4.00	5.8198	0.2448	-5.7313

CIRCULAR HYDRAULIC JUMP

FROUDE NUMBER (FO)	RADIUS RATIO (R1/R0)	DEPTH RATIO (Y1/YC) THREE ROOTS ROOT 1	ROOT 2	ROOT 3
4.0	1.00	5.1789	1.0000	-6.1789
4.0	1.05	5.1265	0.9494	-6.0598
4.0	1.10	5.0748	0.9037	-5.9472
4.0	1.15	5.0238	0.8621	-5.8405
4.0	1.20	4.9738	0.8243	-5.7392
4.0	1.25	4.9248	0.7896	-5.6429
4.0	1.30	4.8768	0.7577	-5.5512
4.0	1.35	4.8300	0.7283	-5.4637
4.0	1.40	4.7843	0.7010	-5.3801
4.0	1.45	4.7398	0.6758	-5.3001
4.0	1.50	4.6963	0.6522	-5.2235
4.0	2.00	4.3174	0.4833	-4.6007
4.0	2.50	4.0203	0.3833	-4.1536
4.0	3.00	3.7816	0.3170	-3.8129
4.0	4.00	3.4196	0.2348	-3.3210

CIRCULAR HYDRAULIC JUMP

FROUDE NUMBER (FO)	RADIUS RATIO (R1/R0)	DEPTH RATIO (Y1/YC) THREE ROOTS ROOT 1	ROOT 2	ROOT 3
2.0	1.00	2.3723	1.0000	-3.3723
2.0	1.05	2.3805	0.9379	-3.3023
2.0	1.10	2.3839	0.8837	-3.2364
2.0	1.15	2.3838	0.8358	-3.1742
2.0	1.20	2.3811	0.7930	-3.1153
2.0	1.25	2.3763	0.7545	-3.0594
2.0	1.30	2.3700	0.7197	-3.0064
2.0	1.35	2.3625	0.6880	-2.9560
2.0	1.40	2.3541	0.6590	-2.9079
2.0	1.45	2.3450	0.6323	-2.8620
2.0	1.50	2.3354	0.6078	-2.8182
2.0	2.00	2.2292	0.4366	-2.4658
2.0	2.50	2.1285	0.3390	-2.2175
2.0	3.00	2.0411	0.2757	-2.0311
2.0	4.00	1.9018	0.1984	-1.7668

DOWNSTREAM OF HYDRAULIC JUMP (WITHOUT SIDE FORCES)

FROUDE NUMBER (F1)	RADIUS RATIO (R/R1)	DEPTH RATIO (Y/Y1) THREE ROOTS ROOT 1	ROOT 2	ROOT 3
1.0	1.1	1.1168	0.9813	-1.0698

0.95	1.1	1.0827	0.8575	-1.6069
0.90	1.1	1.0547	0.8223	-1.5437
0.85	1.1	1.0325	0.7812	-1.4804
0.80	1.1	0.0324	1.1525	-1.4515
0.75	1.1	0.9349	1.1414	-1.3929
0.70	1.1	0.8351	1.1330	-1.3353
0.65	1.1	0.7439	1.1283	-1.2789
0.60	1.1	0.6322	1.1250	-1.2239
0.55	1.1	0.5804	1.1232	-1.1702
0.50	1.1	0.5292	1.1225	-1.1183
0.45	1.1	0.4791	1.1236	-1.0684
0.40	1.1	0.4306	1.1235	-1.0208
0.35	1.1	0.3844	1.1248	-0.9760
0.30	1.1	0.3413	1.1265	-0.9345
0.25	1.1	0.3020	1.1284	-0.8971
0.20	1.1	0.2677	1.1303	-0.8646
0.15	1.1	0.2392	1.1320	-0.8379
0.10	1.1	0.2178	1.1334	-0.8179
0.05	1.1	0.2045	1.1343	-0.8055

DOWNSTREAM OF HYDRAULIC JUMP

FROUDE NUMBER (F1)	RADIUS RATIO (R/R1)	DEPTH RATIO (Y/Y1) THREE ROOTS ROOT 1	ROOT 2	ROOT 3
1.00	1.5	1.0875	0.6025	-1.3566
0.95	1.5	1.0525	0.5846	-1.3038
0.90	1.5	1.0203	0.5641	-1.2510
0.85	1.5	0.9909	0.5408	-1.1984
0.80	1.5	0.9644	0.5148	-1.1459
0.75	1.5	0.9409	0.4860	-1.0935
0.70	1.5	0.9201	0.4546	-1.0414
0.65	1.5	0.9020	0.4208	-0.9895
0.60	1.5	-1.1898	1.3193	0.2039
0.55	1.5	0.8729	0.3473	-0.8869
0.50	1.5	0.2352	1.0222	-0.9241
0.45	1.5	0.2008	1.0153	-0.8828
0.40	1.5	0.1669	1.0101	-0.9436
0.35	1.5	0.1341	1.0062	-0.8070
0.30	1.5	0.1031	1.0035	-0.7733
0.25	1.5	0.0746	1.0018	-0.7431
0.20	1.5	0.0496	1.0008	-0.7170
0.15	1.5	0.0287	1.0003	-0.6957
0.10	1.5	0.0131	1.0001	-0.6798
0.05	1.5	0.0033	1.0000	-0.6700

DOWNSTREAM OF HYDRAULIC JUMP

FROUDE NUMBER (F1)	RADIUS RATIO (R/R1)	DEPTH RATIO (Y/Y1) THREE ROOTS ROOT 1	ROOT 2	ROOT 3
1.00	3.0	0.8614	0.3084	-0.8365
0.95	3.0	0.8333	0.3006	-0.8006
0.90	3.0	0.8063	0.2919	-0.7648
0.85	3.0	0.7806	0.2820	-0.7293
0.80	3.0	0.7563	0.2710	-0.6939

EQUATION (2.22)

```
/JOB (114818,3,6),JOHN MILLER
C     HYDRAULIC JUMP IN RADIAL FLOW
C     TO GENERATE A FAMILY OF CURVES OF FJ VS Y1/RJ FOR SEVERAL VO/VJ
C     Y1 = DEPTH OF FLOW AT THE END OF JUMP
C     RJ = RADIUS OF IMPINGING JET
C     FJ = FROUDE NUMBER OF IMPINGING JET
C     VO = VELOCITY BEFORE THE JUMP
C     VJ = VELOCITY OF IMPINGING JET
C     A = Y1/RJ
C     SA = VO/VJ
C
C     INITIALIZATION OF DATA
C
      DATA B,C/-0.672,0.245/
      SA = 0.1
      DO 90 N = 1,12
      IF(N .EQ. 1) GO TO 1
      IF(N .EQ. 4) GO TO 1
      IF(N .EQ. 7) GO TO 1
      IF(N .EQ. 10) GO TO 1
      WRITE(6,100)
  100 FORMAT(///,T12,'VO/VJ',T24,'Y1/RJ',T36,'FJ')
      WRITE(6,101)
  101 FORMAT('+',T11,'_____',T23,'_____',T35,'____',/)
      GO TO 2
    1 WRITE(6,102)
  102 FORMAT('1',T12,'VO/VJ',T24,'Y1/RJ',T36,'FJ')
      WRITE(6,101)
    2 A = 0.5
      DO 10 M = 1,14
      R = 20.0*(A**2.0)*SA
      S = (32.0*(A**2.0)*SA*C)-(2.0*A*C)-(3.0*C/4.0*A*SA)
      T = (8.0*(A**2.0)*(C**2.0))+(4.0*(C**2.0)/SA)
      U = 4.0*A*(C**3.0)/SA
      V = 6.0*(SA**2.0)/A
      W = (3.0*SA*C/(A**2.0))-24.0*(SA**2.0)*C
      X = 3.0*A*SA/C
      FJ = 200.0
      K = 1
   20 K = K+1
      IF(K-10)50,50,80
   50 RES = (R*(FJ**3))+(S*(FJ**(2.0*B)))+(T*(FJ**(3.0*B)))-(U*(FJ**(4.0
     $*B)))-(V*(FJ**(2.0+B)))+(W*(FJ**(2.0*(1.0+B))))+X
      DER = B*R*FJ**(B-1.0)+2.0*B*S*FJ**(2.0*B-1.0)+3.0*B*T*FJ**(3.0*B-
     $1.0)-4.0*B*U*FJ**(4.0*B-1.0)-(2.0+B)*V*FJ**(1.0+B)+2.0*(1.0+B)*W*
     $FJ**(1.0+2.0*B)
      IF(ABS(RES)-0.001)80,80,12
C     USING NEWTON'S METHOD OF NUMERICAL SOLUTIONS
   12 FJ = FJ - RES/DER
C     DER = FIRST DERIVATIVE OF RES
      GO TO 20
   80 WRITE(6,60)SA,A,FJ
   60 FORMAT(' ',T13,F4.2,T25,F3.1,T34,F6.2)
      A = A+0.5
   10 CONTINUE
      SA = SA+0.02
   90 CONTINUE
      STOP
      END
```

VO/VJ	Y1/RJ	EJ
0.10	0.5	7.18
0.10	1.0	12.39
0.10	1.5	20.82
0.10	2.0	31.12
0.10	2.5	42.90
0.10	3.0	56.00
0.10	3.5	70.28
0.10	4.0	85.64
0.10	4.5	102.03
0.10	5.0	119.36
0.10	5.5	137.60
0.10	6.0	156.71
0.10	6.5	176.64
0.10	7.0	197.36

VO/VJ	Y1/RJ	EJ
0.12	0.5	5.92
0.12	1.0	10.70
0.12	1.5	18.15
0.12	2.0	27.20
0.12	2.5	37.55
0.12	3.0	49.05
0.12	3.5	61.57
0.12	4.0	75.05
0.12	4.5	89.42
0.12	5.0	104.63
0.12	5.5	120.62
0.12	6.0	137.37
0.12	6.5	154.85
0.12	7.0	173.02

VO/VJ	Y1/RJ	EJ
0.14	0.5	5.05
0.14	1.0	9.47
0.14	1.5	16.18
0.14	2.0	24.29
0.14	2.5	33.57
0.14	3.0	43.86
0.14	3.5	55.08
0.14	4.0	67.15
0.14	4.5	80.01
0.14	5.0	93.62
0.14	5.5	107.94
0.14	6.0	122.94
0.14	6.5	138.58
0.14	7.0	154.84

VO/VJ	Y1/RJ	EJ
0.16	0.5	4.41
0.16	1.0	8.53
0.16	1.5	14.65
0.16	2.0	22.04
0.16	2.5	30.47
0.16	3.0	39.83
0.16	3.5	50.03
0.16	4.0	61.00
0.16	4.5	72.68
0.16	5.0	85.05
0.16	5.5	98.06
0.16	6.0	111.69
0.16	6.5	125.90
0.16	7.0	140.67

VO/VJ	Y1/RJ	EJ
0.18	0.5	3.53
0.18	1.0	7.79
0.18	1.5	13.43
0.18	2.0	20.23
0.18	2.5	27.59
0.18	3.0	36.59
0.18	3.5	45.97
0.18	4.0	56.05
0.18	4.5	66.79
0.18	5.0	78.16
0.18	5.5	90.11
0.18	6.0	102.64
0.18	6.5	115.70
0.18	7.0	129.28

VO/VJ	Y1/RJ	EJ
0.20	0.5	3.55
0.20	1.0	7.19
0.20	1.5	12.43
0.20	2.0	18.75
0.20	2.5	25.94
0.20	3.0	33.93
0.20	3.5	42.62
0.20	4.0	51.97
0.20	4.5	61.94
0.20	5.0	72.48
0.20	5.5	83.57
0.20	6.0	95.18
0.20	6.5	107.29
0.20	7.0	119.88

VO/VJ	Y1/RJ	EJ
0.22	0.5	3.24
0.22	1.0	6.68
0.22	1.5	11.60
0.22	2.0	17.50
0.22	2.5	24.23
0.22	3.0	31.69
0.22	3.5	39.81
0.22	4.0	48.55
0.22	4.5	57.86
0.22	5.0	67.70
0.22	5.5	78.06
0.22	6.0	88.91
0.22	6.5	100.22
0.22	7.0	111.98

VO/VJ	Y1/RJ	EJ
0.24	0.5	2.99
0.24	1.0	6.26
0.24	1.5	10.89
0.24	2.0	16.44
0.24	2.5	22.76
0.24	3.0	29.78
0.24	3.5	37.41
0.24	4.0	45.62
0.24	4.5	54.37
0.24	5.0	63.63
0.24	5.5	73.36
0.24	6.0	83.55
0.24	6.5	94.18
0.24	7.0	105.24

VO/VJ	Y1/RJ	EJ
0.26	0.5	2.78
0.26	1.0	5.89
0.26	1.5	10.27
0.26	2.0	15.52
0.26	2.5	21.50
0.26	3.0	28.12
0.26	3.5	35.34
0.26	4.0	43.09
0.26	4.5	51.36
0.26	5.0	60.10
0.26	5.5	69.29
0.26	6.0	78.92
0.26	6.5	88.96
0.26	7.0	99.40

VO/VJ	Y1/RJ	EJ
0.28	0.5	2.60
0.28	1.0	5.58
0.28	1.5	9.74
0.28	2.0	14.72
0.28	2.5	20.39
0.28	3.0	26.68
0.28	3.5	33.52
0.28	4.0	40.88
0.28	4.5	48.72
0.28	5.0	57.01
0.28	5.5	65.73
0.28	6.0	74.86
0.28	6.5	84.38
0.28	7.0	94.29

VC/VJ	Y1/RJ	EJ
0.30	0.5	2.44
0.30	1.0	5.30
0.30	1.5	9.26
0.30	2.0	14.01
0.30	2.5	19.41
0.30	3.0	25.40
0.30	3.5	31.92
0.30	4.0	38.92
0.30	4.5	46.38
0.30	5.0	54.28
0.30	5.5	62.58
0.30	6.0	71.27
0.30	6.5	80.34
0.30	7.0	89.77

VC/VJ	Y1/RJ	EJ
0.32	0.5	2.30
0.32	1.0	5.05
0.32	1.5	8.84
0.32	2.0	13.38
0.32	2.5	18.54
0.32	3.0	24.26
0.32	3.5	30.49
0.32	4.0	37.18
0.32	4.5	44.31
0.32	5.0	51.85
0.32	5.5	59.78
0.32	6.0	68.08
0.32	6.5	76.74
0.32	7.0	85.74

NFILE TIME= 1.38 SEC. EXECUTION TIME= 19.10 SEC. OBJECT CODE= 2784 BYTES.

332 LINES PRINTED-- 0 CARDS PUNCHED-- CHARGES 20.50 SEC